

Mechanical phenotyping of single cells using shear and inertial microfluidics

Fern Jordan Armistead

University of Leeds

Department of Physics and Astronomy

September 2019

Submitted in accordance with the requirements for the degree of

Doctor of Philosophy

Intellectual Property and Publication Statements

The candidate confirms that the work submitted is their own, except where work which has formed part of jointly authored publications has been included. The contribution of the candidate and the other authors to this work has been explicitly indicated below. The candidate confirms that appropriate credit has been given within the thesis where reference has been made to the work of others.

The work in Chapters 4 and 5 of the thesis has appeared in publication as follows:

Armistead, F. J., Gala De Pablo, J., Gadêlha, H., Peyman, S. A., & Evans, S. D. (2019). Cells Under Stress: An Inertial-Shear Microfluidic Determination of Cell Behavior. *Biophysical Journal*, 116(6), 1127-1135. doi:10.1016/j.bpj.2019.01.034. [1]

- F.J.A. performed research and collected all experimental data, analysed the datasets and wrote the manuscript.
- J.G.D.P. helped with cell culture maintenance and provided code for data processing. H.G. also provided analytical tools for image analysis of deformation events. S.A.P. and S.D.E. helped to design the experimental plan and with manuscript review.

The work in Chapter 6 of the thesis will appear in publication as follows

Armistead, F. J., Gala De Pablo, J., Gadêlha, H., Peyman, S. A., & Evans, S. D. (2019). Physical biomarkers of disease progression: on-chip monitoring of changes in mechanobiology of colorectal cancer cells. [**under review, submitted 2/8/2019**].

- F.J.A. performed research including all deformation cytometry experiments, analysed the majority of data and wrote the manuscript.
- J.G. provided code for data processing and performed LDA analysis. H.G. also provided analytical tools. S.A.P. and S.D.E. helped with development of the experimental plan and provided constructive discussion.

Other publications co-authored during the course of this studentship include:

The results in this publication are discussed and compared to results within the thesis in the Conclusions section (chapter 8).

Julia Gala de Pablo, Fern J. Armistead, Sally A. Peyman, David Bonthron, Michael Lones, Stephen Smith, and Stephen D. Evans. Biochemical Fingerprint of Colorectal Cancer Cell Lines Using Label-Free Live Single-Cell Raman Spectroscopy. *Journal of Raman Spectroscopy* 49(8):1323-32, aug 2018. ISSN 03770486. doi:10.1002/jrs.5389. [2]

- F.J.A. helped with cell culture maintenance.

Microfluidic deformation experiments performed for QD uptake reported in chapter 7 were led by Abiral Tamang, with microfluidic design, fabrication and deformation cytometry expertise provided by Fern Armistead. This work is currently in preparation to be published in a joint author publication.

Experiments reported in chapter 5 were performed using cells and materials provided by Elizabeth Evans.

This copy has been supplied on the understanding that it is copyright material and that no quotation from the thesis may be published without proper acknowledgement. The right of Fern Jordan Armistead to be identified as Author of this work has been asserted by her in accordance with the Copyright, Designs and Patents Act 1988.

In some parts of the thesis, figures have been reproduced from publications with permission from the copyright holder:

1. Figure 1.2: permission from Elsevier, License: 4644770582075, 09/08/2019.
2. Figure 1.3: permission from Elsevier, License: 4644770748041, 09/08/2019.
3. Figure 1.5: permission from Springer Nature, License: 4644771027210, 09/08/2019.
4. Figure 2.1: permission from Elsevier, License: 4644711424610, 09/08/2019.
5. Figure 2.2: permission from Springer Nature, License: 4644720236771, 09/08/2019.
6. Figure 2.5: permission from Springer Nature, License: 4718241428233, 29/11/2019.

For Mum, Dad, Grandma and Grandad

Acknowledgments

I must start by thanking my supervisor Prof Stephen Evans for his support and guidance throughout the past four years, particularly through the traumatising 18 month period of writing my first paper. Thanks also to Dr Sally Peyman for the great advice, encouragement and optimism that I definitely needed at times. Both of you had confidence in me when I had no confidence in myself, and even though the struggle continues I think you somehow turned me into a “scientist”.

A huge thanks must go to Julia Gala De Pablo, my long-time science companion and housemate. A lot of this thesis would not have been achieved without her immense amount of knowledge. Thanks for putting up with me when I was my most annoyed and frustrated at science. Also a shout out to Lucien Roach for being on this PhD journey with me since day one, thanks for always being helpful and up for a coffee break.

I would also like to thank my collaborator Dr Hermes Gadêlha for all his help towards the work in this thesis, and for his incredible enthusiasm for science. Thanks to Dr Ben Johnson for sorting out the microscope in my first year, without which most of the data could not have been collected. Huge thanks to Abiral Tamang for providing the best side project and being a great travel buddy in Tokyo.

I would like to acknowledge anyone who attended the BioNano summer school in Hirscheegg 2013 (particularly Julia, Twig, Adam and Victoria). I was a very shy undergraduate on summer placement, but this was my first taste of academia and definitely inspired me to do a PhD. This leads me to thanking my original MNP besties Victoria Mico and Adam Churchman, thanks for being my science big siblings in the first half of my PhD and now being my good friends for life #creative #inspiring.

A general thanks to the entire MNP group past and present, especially if you ever bought me a pint at the Fenton, accompanied me to Charcos (where food is good), shared an elf faro pizza with me, or consoled me during one of my many emotional breakdowns. To mention a few, thanks to Twig, Ellen, Jamie, Liam, Ash, Shajeth and Holly. I feel very fortunate to have spent time in such a sociable and inclusive research group.

Special thanks to Samuel Moorcroft for making misery corner slightly less miserable, and always providing great gossip. Thanks to Grace Porter for singing country roads with me at microTAS 2017, and making me laugh with her twisted sense of humour #TheVoid. Also thanks to Grace Blake (my first ever physics friend) for continuing to invite me out for tea even when I am rubbish at replying to messages.

Damien Batchelor deserves many thanks for his constant support and patience with me during this time, and for making me “not sad”. Also thanks for cooking me nice food, putting up with my nonsense, sending me good/bad tweets, and for being my best friend for some time. Meeting you was a highlight of my PhD, you are alright.

My final and biggest thanks goes to my family, the most generous people I know. Thanks to my Grandparents Dot and John for always being proud of me and being my number 1 fans. Thank you to my parents Jeanette and Roy for always being willing to help me with absolutely anything. Without your support and encouragement I would not have made it here, thank you so much.

Abstract

Disease induced changes to subcellular components leads to measurable changes in whole cell deformability. Thus, mechanical phenotyping offers potential as a diagnostic tool. Cells undergo physical and biological changes during cancer progression and understanding these changes is a major challenge in developing new diagnosis and treatment methods.

High-throughput mechanophenotyping methods are required to account for cell heterogeneity, which arise due to cell-cycle stage and biological noise. Here, a high-throughput microfluidic technique called deformation cytometry was used to deform cells in an extensional flow using a cross-slot geometry. Cells are viscoelastic and their mechanical response to an applied stress depends on the magnitude and timescale of application. Two distinct flow regimes were studied where either shear or inertial forces dominated the system. In the inertia-dominant regime cell response showed yield stress behaviour and subsequent cell structural failure at high stresses, whilst the shear-dominant regime required lower applied stress to achieve high cell strains. The different regimes proved able to expose subtle changes attributed to specific subcellular changes, tested by treating cells with drugs to disrupt the actin, microtubule, and nuclear structure. Deformation and recovery were tracked as a function of time, with various deformation and relaxation parameters found to be useful markers to distinguish cell types.

Deformation cytometry was also applied to studying colorectal cancer progression. Colorectal cancer is the third most common cancer in the UK and the five year survival rate drops from ~93% with early stage diagnosis to ~7% for late stage diagnosis. The deformability of three colorectal cancer cell lines was investigated using both flow regimes. SW480, HT29 and SW620 cell lines offered a model of metastatic progression from primary to metastatic and were compared to the leukaemia cell line HL60. Results indicated increased deformability associated with metastatic progression, and relaxation parameters showed significant changes between different cell types. Additional work showed that hydrodynamic deformation can be used to increase non-endocytic uptake of quantum dots into cells, due to the applied shear force forming transient pores in the cell membrane. Successful delivery of quantum dots into the cytosol will allow them to be used to measure the cell redox environment, which is a marker of disease state including metastatic progression.

Results showed the potential for deformation cytometry as a cell mechanophenotyping tool with high sensitivity, including multiparameter characterisation for improved accuracy in detecting disease stage. This work shows that mechanical measurements on a single cell level offer insight into heterogeneity, allowing distinctions to be made between different phenotypes. Future work could use the method for detection of rare events or subpopulations, particularly those arising during disease progression.

List of Abbreviations

AFM Atomic Force Microscopy	OT Optical Tweezers
CA4 Combretastatin A4	PBS Phosphate Buffered Saline
CRC Colorectal cancer	PBS-MC PBS with Methyl Cellulose
CytoD Cytochalasin D	PCA Principal Component Analysis
CV Coefficient of Variation	PDMS Polydimethyl Siloxane
D_c Circularity	QD Quantum Dot
DC Deformation Cytometry	RBC Red Blood Cell
DEP Dielectrophoresis	Re Reynolds number
DI Deformation Index	RS Raman Spectroscopy
DMEM Dulbecco's Modified Eagle Medium	RT-DC Real time deformation cytometry
DMSO Dimethyl sulfoxide	SD Standard Deviation
DNA Deoxyribonucleic acid	SE Standard Error
E Elastic Modulus	TSA Trichostatin A
ECM Extracellular matrix	ε Strain
EMT Epithelial-to-Mesenchymal transition	ε₀ Initial strain
FBS Foetal Bovine Serum	ε_∞ Final strain
F_C Compressive force	ε_{max} Maximum strain
F_S Shear force	σ Stress
F_T Total force	τ_d Deformation time
FWHM Full width half maximum	τ_r Relaxation time
IPA Isopropanol	
LatA Latrunculin A	
LDA Linear Discriminant Analysis	
MA Micropipette Aspiration	
MC Methyl Cellulose	
MTC Magnetic Twisting Cytometry	

Table of Contents

Acknowledgments	v
Abstract	vii
List of Abbreviations	ix
List of Figures	xiv
List of Tables	xx
1 Introduction	1
1.1 Overview	1
1.2 Background: Mechano-phenotyping and Single Cell Analysis	1
1.3 Biophysical characterisation techniques	2
1.3.1 Overview.....	2
1.3.2 Microfluidics.....	5
1.4 Deformation Cytometry Applications	10
1.4.1 Detecting diseased states.....	10
1.4.2 Sensitivity to subcellular changes	11
1.4.3 DC for non-endocytic uptake of nanoparticles	12
1.4.4 Combining DC and fluorescence measurements	14
1.5 Scope of project and thesis outline	15
2 Theory and Background	17
2.1 Cell Structure	17
2.1.1 Overview.....	17
2.1.2 The Cell Membrane	18
2.1.3 The Cytoskeleton	18
2.1.4 The Nucleus	22
2.1.5 The Cell Cycle	23
2.2 Cancer cell progression and mechanical changes	26
2.2.1 Cancer and Metastasis.....	26
2.2.2 Colorectal Cancer.....	26
2.2.3 Model System	28
2.2.4 Mechanical phenotype of malignant cells.....	29
2.3 Biomechanics of Cells	31
2.3.1 Viscoelasticity.....	31
2.3.2 Linear-Spring and Dashpot models.....	33
2.3.3 Overview of Models of Cell Mechanics	36
2.3.4 Kelvin-Voigt Model.....	39
2.3.5 Cell Plasticity	40
2.4 Microfluidics Background	42

2.4.1	Navier-Stokes equation	42
2.4.2	Reynolds number	43
2.4.3	Flow Resistance	44
2.5	Microfluidic Cell Deformation.....	45
2.5.1	Structure induced deformation.....	45
2.5.2	Flow induced deformation	45
2.5.3	Shear and Inertial Forces.....	47
3	Experimental Methods	50
3.1	Microfluidic Device Fabrication	50
3.1.1	Master Fabrication	50
3.1.2	PDMS Device Fabrication	51
3.2	Device designs.....	52
3.2.1	Cross-slot	52
3.2.2	Serpentine	53
3.3	Deformation Cytometry Procedure.....	54
3.4	Microscopy Techniques	55
3.4.1	Bright Field Microscopy	55
3.4.2	High Speed Microscopy.....	55
3.4.3	Phase Contrast Microscopy.....	56
3.4.4	Confocal Fluorescence Microscopy	57
3.5	Automated Image Analysis	58
3.5.1	ImageJ particle tracking	58
3.5.2	Matlab particle tracking	61
3.5.3	Parameter definitions	63
3.6	Cell Culture	65
3.6.1	HL60	65
3.6.2	Colorectal Cancer Cell Lines	65
3.6.3	MCF-7.....	66
3.6.4	HEK-293 T-REx and Piezo1 T-REx.....	66
3.6.5	Concentration and Viability Measurements.....	68
3.7	QD uptake in Cells	68
3.7.1	Quantum Dots	68
3.7.2	Microfluidic Uptake Protocol	69
3.7.3	Analysis of QD uptake.....	69
4	Cell deformation in shear and inertial flows	70
4.1	Cross-slot optimisation	70
4.1.1	Tracking particles in flow	70

4.1.2	Varying Flow Rate	73
4.1.3	Varying Velocity Threshold.....	75
4.1.4	Varying Channel Dimensions	77
4.2	Cell deformation across flow regimes	81
4.2.1	Varying suspension buffer viscosity	81
4.2.2	Inertial Regime.....	83
4.2.3	Deformation as a function of force	84
4.3	Cell viability after deformation	85
4.3.1	Shear Regime	85
4.3.2	Inertial Regime.....	86
4.4	Tracking cell deformation and recovery.....	88
4.4.1	Single cell tracking in the shear regime	88
4.4.2	High strain recovery in the shear regime	93
4.4.3	High strain recovery in the inertial regime	97
4.4.4	Summary of section 4.4	100
4.5	Discussion.....	101
5	The sensitivity of DC to subcellular alterations	105
5.1	Treating cells with Latrunculin A	105
5.1.1	Drug treatment and observations	106
5.1.2	Deformation Cytometry in the shear regime.....	110
5.1.3	Deformation Cytometry in the inertial regime.....	114
5.1.4	Deformation traces and SCA	116
5.1.5	Discussion	120
5.2	Treating cells with Combretastatin A4.....	122
5.2.1	Drug treatment and observations	123
5.2.2	Deformation Cytometry in the shear regime.....	127
5.2.3	Deformation Cytometry in the inertial regime.....	130
5.2.4	Viability Assays	132
5.2.5	Deformation traces and SCA	137
5.2.6	Discussion	141
5.3	Treating cells with Trichostatin A	145
5.3.1	Drug treatment and observations	145
5.3.2	Deformation Cytometry in the shear regime.....	147
5.3.3	Deformation Cytometry in the inertial regime.....	148
5.3.4	Discussion	150
5.4	Chapter Overview	152
6	Changes to mechanical phenotype with colorectal cancer progression	154

6.1	Colorectal cancer cell lines	154
6.1.1	Initial morphology.....	154
6.1.2	Nucleus size	155
6.2	Deformation Cytometry	157
6.2.1	Shear-dominant regime	157
6.2.2	Inertia-dominant regime.....	161
6.2.3	Cell width and height	164
6.3	Deformation and Recovery	167
6.3.1	Strain trace multiparameter analysis	167
6.3.2	Single Cell Analysis.....	170
6.3.3	Linear Discriminant Analysis	172
6.4	Discussion and Chapter Overview	174
7	Other applications of Deformation Cytometry	179
7.1	Non-Endocytic uptake of Quantum Dots	179
7.1.1	Shear Regime	180
7.1.2	Inertial Regime.....	183
7.1.3	Constriction channel control	186
7.1.4	Uptake by incubation	189
7.1.5	Discussion	192
7.2	DC for probing the mechanoresponse of Piezo1	195
7.2.1	Yoda1 activation	197
7.2.2	Shear Regime Deformation.....	199
7.2.3	Strain Traces	202
7.2.4	Discussion	206
8	Conclusions and Future Work	210
8.1	Chapter by Chapter Overview	210
8.2	MRC Project	215
8.3	Next Steps	216
8.3.1	Further optimisation.....	216
8.3.2	DC to study other subcellular alterations	217
8.3.3	DC for studying Piezo1	218
8.3.4	DC and high speed fluorescence	219
Appendix		221
References		228

List of Figures

Figure 1.1 Schematic representations of the types of experimental techniques used for biomechanical characterisation of cells.	4
Figure 1.2 The typical ranges of forces (a) and displacements (b) probed by various biomechanical assays.....	5
Figure 1.3 A graphical representation of the “precision” of different biomechanical methods for probing cells compared to the “speed” (i.e. throughput).....	6
Figure 1.4 The principles of deformability cytometry.....	8
Figure 1.5 (a) An example scatter plot of deformation against initial size (cross sectional area) for a HL60 cell sample.....	9
Figure 1.6 Constriction microfluidics for increased QD uptake in cells.....	13
Figure 1.7 Details of the inertial microfluidic cell hydroporator for intracellular delivery of nanoparticles.....	14
Figure 2.1 A fluorescent image of a cell with labelled cytoskeletal filaments	18
Figure 2.2 A simplified schematic of the structure of the three cytoskeletal filaments: actin filaments, microtubules and intermediate filaments	19
Figure 2.3 Schematic showing the main structure of the eukaryotic cell nucleus	22
Figure 2.4 (a) A simplified schematic of the four main phases of the cell cycle.	24
Figure 2.5 Schematic describing progression from normal epithelial crypts through to colorectal adenocarcinoma to metastasis.....	27
Figure 2.6 A schematic outlining the model system for CRC progression.....	29
Figure 2.7 Graphical schematic of the stress-strain loading and unloading curves of an elastic vs a viscoelastic material.	32
Figure 2.8. Schematic describing the three simplest spring-dashpot models and their responses over time to a step-wise applied stress σ and strain ϵ	34
Figure 2.9 Simplified schematics showing some of the main conceptual models of cell mechanics. ..	38
Figure 2.10: (a) Cross-slot velocity profile found using COMSOL	39
Figure 2.11 A schematic showing the different microfluidic geometries that can be used to deform single cells	46
Figure 2.12: Variation of Reynolds number with flow rate in a cross-slot device for two viscosities ..	48
Figure 2.13: Plots of equations 2.23 and 2.24 as a function of flow rate. Changing the viscosity μ of the fluid determines whether the system is inertia or shear dominant.	49
Figure 3.1. Schematic summarising the production steps for fabrication of an SU-8-silicon master ...	51
Figure 3.2. Schematic summarising the production steps for fabrication of microdevices using PDMS	52
Figure 3.3. (a) Cross-slot device designed using AutoCAD, with inlets and outlets labelled and arrows used to show the direction of flow.....	53
Figure 3.4. Serpentine device designed using AutoCAD, with inlets and outlets labelled and arrows used to show the direction of flow.....	54
Figure 3.5. (a) Schematic of the microfluidic apparatus used for deformation cytometry.	55
Figure 3.6 Simplified schematic of the optical set-up of a phase contrast microscope.....	56
Figure 3.7 Simplified schematic of a confocal microscope.	57
Figure 3.8. An example image of a cell deforming at the stagnation point of a microfluidic device. ..	60

Figure 3.9. An example of particle tracking used to analyse the deformation of a HL60 cell deformation in a cross-slot device	61
Figure 3.10. Example of precision particle tracking using Matlab. The code is used to track the position and shape of a cell passing through an extensional flow junction.	63
Figure 3.11. Schematic describing how the deformation parameters DI, ϵ and DC change when a cell begins to deviate from a perfect circle (Shape A).	64
Figure 4.1 Comparison of the trajectory of a cell in a cross-slot microfluidic device compared to a polystyrene bead.....	71
Figure 4.2 COMSOL simulations of flow in a cross-slot microfluidic device.	72
Figure 4.3 The velocity (m/s) as a function of flow rate ($\mu\text{l}/\text{min}$) of polystyrene beads and HL60 cells travelling through a rectangular channel.	73
Figure 4.4 Density scatter plots of DI as a function of initial diameter of HL60 cells deformed at various flow rates.....	74
Figure 4.5: A plot of the average $DI \pm SE$ of HL60 cells deformed over a range of flow rates in a shear-dominant flow regime ($\mu \cong 33$ cP).....	74
Figure 4.6 The velocity profile of a HL60 cell as it passes through the extensional flow junction of a cross-slot microfluidic device	75
Figure 4.7 (a) The average $DI \pm SE$ of HL60 deformed at 40 $\mu\text{l}/\text{min}$ in 0.24% methyl cellulose buffer, as a function of Δv threshold.	77
Figure 4.8 Bright field images of HL60 cells deforming at $DI \cong DI_{\text{max}}$ in a shear-dominant flow regime ($\mu \cong 33$ cP).....	78
Figure 4.9 HL60 cells were deformed in microfluidic cross-slot devices at a range of flow rate. The flow regime was shear-dominant ($\mu \approx 33$ cP) and device dimensions are labels channel width W by channel height H (W x H μm).	79
Figure 4.10 A plot of $DI_{\text{max}} \pm SE$ of HL60 cells deformed in microfluidic cross-slot devices with different channel dimensions.	80
Figure 4.11 Bar graphs showing the percentage number of cell events with $\Delta v > 0.75$ when HL60 cells were deformed microfluidically at a range of flow rates, for different channel dimensions.	81
Figure 4.12 DI as a function of Q for HL60 cells in four different suspension buffers with viscosity ranging from 1 to 33 cP.....	82
Figure 4.13 A graph of the extrapolated value DI_{max} associated with the deformability of HL60 cells as a function of flow rate for four different viscosities of suspension buffer.	83
Figure 4.14 The average $DI \pm SE$ of HL60 cells versus Q, in an inertial-dominant flow regime ($\mu = 1$ cP).	84
Figure 4.15 The DI of HL60 cells as a function of applied force (μN), where FT is the sum of the shear force (Fs) and inertial force (FC).	85
Figure 4.16 The viability of HL60 cells after being deformed on-chip over a range of flow rates, where the flow regime was shear dominant ($\mu \cong 33$ cP).....	86
Figure 4.17 The viability of HL60 cells after microfluidic deformation at a range of flow rates Q (blue) in the inertial regime ($\mu = 1$ cP)	87
Figure 4.18 Shape analysis of HL60 post-deformation.	88
Figure 4.19 (a) Strain, ϵ , as a function of time, averaged over 50 HL60 cells, with the standard error shown in gray. Q was fixed at 5 $\mu\text{l}/\text{min}$, and the suspension medium viscosity was 33 cP.	89
Figure 4.20 (a) The average velocity profile of N=50 HL60 cells as they pass through the SP of the cross flow.	90
Figure 4.21 Examples of 4 strain traces of HL60 cells deforming in the extensional flow junction of a microfluidic cross-slot device.	91

Figure 4.22 Histograms of the single cell parameters extracted from strain traces of N=50 HL60 cells	93
Figure 4.23 Schematic and bright field images of cell recovery after deformation at the SP of a cross-slot device.	94
Figure 4.24 The $DI \pm SE$ of HL60 cells as a function of position in a cross-slot device ($\mu \cong 33$ cP) ...	95
Figure 4.25 Histograms of the DI of HL60 cells at various positions in a cross-slot microfluidic device which were deformed in a shear-dominant regime ($\mu \cong 33$ cP)	97
Figure 4.26 Example bright field images of cells in the cross-slot device at the different positions, where the flow rate was 600 μ l/min and the flow regime was inertia-dominant ($\mu \approx 1$ cP).....	98
Figure 4.27 The $DI \pm SE$ of HL60 cells as a function of position in a cross-slot device ($\mu \cong 1$ cP)	99
Figure 4.28 Histograms of the DI of HL60 cells at various positions in a cross-slot microfluidic device which were deformed in an inertia-dominant regime ($\mu \cong 1$ cP).....	100
Figure 4.29 The $DI \pm SE$ of HL60 cells as a function of time in a cross-slot device as cells recover through the outlet after deformation at the SP	101
Figure 5.1 Measurement of the size and shape of HL60 cells compared to those treated with 1 μ M of LatA:.....	106
Figure 5.2 Measurement of the size and shape of SW480 cells compared to those treated with 1 μ M of LatA:.....	107
Figure 5.3 Confocal fluorescence images of control HL60 cells and HL60 treated with 0.01 μ M, 0.1 μ M and 1 μ M of LatA, stained for actin (red) and DNA (blue).	108
Figure 5.4 Confocal fluorescence images of control SW480 cells and SW480 treated with 0.01 μ M, 0.1 μ M and 1 μ M of LatA.	109
Figure 5.5 Confocal fluorescence images of control SW480 cells and SW480 treated with 0.01 μ M, 0.1 μ M and 1 μ M of LatA.	109
Figure 5.6 The nuclear diameter of HL60 and SW480 cells was measured using confocal fluorescence images with DNA staining.....	110
Figure 5.7 (a) The deformation index DI of HL60 cells treated with 1 μ M of LatA as a function of flow rate, compared to a control sample. Cells were deformed in a shear-dominant regime where $\mu \cong 33$ cP.	111
Figure 5.8 (a) The deformation index DI of SW480 cells treated with 1 μ M of LatA as a function of flow rate, compared to an untreated sample. Cells were deformed in a shear-dominant regime where $\mu \cong 33$ cP.	112
Figure 5.9 Histograms of the DI of SW480 treated with 1 μ M of LatA compared to an untreated sample.	113
Figure 5.10 (a) The deformation index DI of HL60 cells treated with 1 μ M of LatA as a function of flow rate, compared to a control sample. Cells were deformed in an inertia-dominant regime where $\mu \cong 1$ cP.....	114
Figure 5.11 (a) The deformation index DI of SW480 cells treated with 1 μ M of LatA as a function of flow rate, compared to an untreated sample. Cells were deformed in an inertia-dominant regime where $\mu \cong 1$ cP.....	115
Figure 5.12 The averaged strain trace for SW480 (N = 56) and SW480 treated with 1 μ M LatA	117
Figure 5.13 Strain traces of SW480 and SW480 treated with LatA fitted with the Kelvin voigt model, accompanied by velocity profiles fitted with a sine function.	117
Figure 5.14 SCA was performed on strain traces of SW480 treated with LatA and a control sample to extract multiple parameters.....	119
Figure 5.15 Histograms showing the maximum strain ϵ_{max} , final strain ϵ_{∞} and relaxation time τ_r of SW480 treated with LatA (N=30), compared to an untreated control sample (N=56).	120

Figure 5.16 Measurement of the size and morphology of HL60 treated with 100 nM of CA4, compared to a control sample	124
Figure 5.17 Measurement of the size and morphology of SW480 cells treated with 100 nM of CA4, compared to a control sample.....	125
Figure 5.18 Confocal fluorescence images of control HL60 cells and HL60 treated with 10 nM, 50 nM and 100 nM of CA4, stained for tubulin (red) and DNA (blue).	126
Figure 5.19 Confocal fluorescence images of control SW480 cells and SW480 treated with 10 nM, 50 nM and 100 nM of CA4	126
Figure 5.20 DNA stained images were used to measure the nuclear diameter of HL60 and SW480 treated with CA4	127
Figure 5.21 (a) The deformation index DI of HL60 cells treated with 100 nM of CA4 as a function of flow rate, compared to a control sample. Cells were deformed in a shear-dominant regime where $\mu \cong 33$ cP.	128
Figure 5.22 Histograms of the DI of HL60 treated with 100nM of CA4 (N=890) and a control sample (N=853), cells were deformed at 60 μ l/min in a shear dominant regime ($\mu \cong 33$ cP).....	129
Figure 5.23 (a) The deformation index DI of SW480 cells treated with 100 nM of CA4 as a function of flow rate, compared to a control sample. Cells were deformed in a shear-dominant regime where $\mu \cong 33$ cP.	130
Figure 5.24 (a) The deformation index DI of HL60 cells treated with 100 nM of CA4 as a function of flow rate, compared to untreated cells. Cells were deformed in an inertia-dominant regime where $\mu \cong 1$ cP.	131
Figure 5.25(a) The deformation index DI of SW480 cells treated with 100 nM of CA4 as a function of flow rate, compared to untreated cells.....	132
Figure 5.26 The viability of HL60 cells treated with CA4 was tested up to 48 hr of incubation with the drug.	133
Figure 5.27 The circularity of HL60 cells treated with CA4 was measured using Dc up to 48 hr of incubation with the drug.....	135
Figure 5.28 (a) The viability of SW480 cells after incubation with 100 nM of CA4 for 2 hr and 48 hr was measured using a Trypan blue assay.	136
Figure 5.29 The normalised fluorescence intensity of SW480 and HL60 using an AlamarBlue assay after 4 hr incubation with different concentrations of CA4.....	137
Figure 5.30 The averaged strain trace for HL60 (N = 50) and HL60 treated with 100 nM LatA (N = 30) as a function of time	138
Figure 5.31 The averaged strain trace of N=38 HL60 cells treated with CA4, the Kelvin-Voigt model was fitted, shown in red. The average velocity profile of the same 38 cells is shown and fitted with a sine function, shown in red.	139
Figure 5.32 SCA performed on strain traces of HL60 treated with CA4 and a control sample.	140
Figure 5.33 Histograms showing the maximum strain ϵ_{max} , relaxation time τ_r and final strain ϵ_{∞} of HL60 treated with CA4 (N=38), compared to an untreated control sample (N=50).....	141
Figure 5.34 Confocal fluorescence images of control HL60 cells and HL60 treated with 100 nM of CA4	144
Figure 5.35 Measurement of the size and shape of HL60 cells compared to those treated with 1 μ M of TSA	146
Figure 5.36 Confocal fluorescence images of control HL60 cells and HL60 cells treated with 0.1 μ M and 1 μ M of TSA	147
Figure 5.37(a) The deformation index DI of HL60 cells treated with 1 μ M of TSA as a function of flow rate, compared to a control sample. Cells were deformed in a shear-dominant regime where $\mu \cong 33$ cP.	148

Figure 5.38 (a) The deformation index DI of HL60 cells treated with 1 μM of TSA as a function of flow rate, compared to untreated cells. Cells were deformed in an inertia-dominant regime where $\mu \cong 1 \text{ cP}$.	149
Figure 5.39 Histograms of DI of HL60 at various flow rates, comparing cells treated with 1 μM of TSA to a control sample.	150
Figure 6.1 Phase contrast images of HL60, SW480, HT29 and SW620	154
Figure 6.2 Confocal fluorescence images of detached (a) SW480, (b) HT29 and (c) SW620 cells	156
Figure 6.3 Bar graph showing the Nuclear Ratio of HL60, SW480 and SW620 cells	157
Figure 6.4 DI of SW480, HT29 and SW620 cell lines over a range of flow rates Q ($\mu\text{l}/\text{min}$). The flow regime was shear dominant ($\mu \approx 33 \text{ cP}$).	158
Figure 6.5 Histograms of the DI of the CRC cells lines deformed at 5 $\mu\text{l}/\text{min}$ in a shear-dominant regime ($\mu \approx 33 \text{ cP}$).	159
Figure 6.6 Histograms of the DI of the CRC cells lines deformed at 80 $\mu\text{l}/\text{min}$ in a shear-dominant regime ($\mu \approx 33 \text{ cP}$).	160
Figure 6.7 The initial size normalised deformation index DI/A of three colorectal cancer cell lines over a range of flow rates Q ($\mu\text{l}/\text{min}$).	161
Figure 6.8 DI of SW480, HT29 and SW620 cell lines over a range of flow rates Q ($\mu\text{l}/\text{min}$). The flow regime was inertia dominant ($\mu \approx 1 \text{ cP}$).	162
Figure 6.9 Histograms of the DI of the CRC cells lines deformed at 300 $\mu\text{l}/\text{min}$ in the inertia-dominant regime ($\mu \approx 1 \text{ cP}$).	163
Figure 6.10 Histograms of the DI of the CRC cells lines deformed at 600 $\mu\text{l}/\text{min}$ in the inertia-dominant regime ($\mu \approx 1 \text{ cP}$).	163
Figure 6.11 DI/A of three colorectal cancer cell lines over a range of flow rates ($\mu\text{l}/\text{min}$), in an inertia dominant regime ($\mu \approx 1 \text{ cP}$).	164
Figure 6.12 Cells were deformed at the SP of a cross-slot device, the width (W) and (height) of the cell were measured at their maximum deformed state at the SP ($\mu \approx 33 \text{ cP}$).	165
Figure 6.13 Cell were deformed at the SP of a cross-slot device, the width (W) and (height) of the cell were measured at their maximum deformed state at the SP ($\mu \approx 1 \text{ cP}$).	166
Figure 6.14 Strain ϵ was tracked for SW480, HT29 and SW620 cells as a function of time	168
Figure 6.15 The average strain trace of SW480, HT29 and SW620 cells fitted with the Kelvin-Voigt function accompanied by the velocity profile fitted with a sine function (shown in red).	169
Figure 6.16 A bar graph of the Elastic moduli of HL60, SW480, HT29 and SW620 cells.	170
Figure 6.17 Multiparameter analysis of HL60, SW480, SW620 and HT29 cell populations using statistical t-tests	171
Figure 6.18 Linear discriminant analysis of 5 parameter datasets for HL60, SW480, HT29 and SW620	173
Figure 7.1 Schematic describing the passive diffusion of quantum dots through transient membrane pores in cells, due to deformation at the stagnation point of a cross-slot microfluidic device.	180
Figure 7.2 The deformation index DI of MCF7 cells as a function of flow rate in a shear-dominant regime ($\mu \cong 33 \text{ cP}$)	181
Figure 7.3 QD uptake analysis of MCF7 cells microfluidically deformation whilst suspended with 100 nM of QDs in a shear-dominant regime ($\mu \approx 33 \text{ cP}$).	182
Figure 7.4 Confocal fluorescence images of MCF7 cells with QD uptake, showing	183
Figure 7.5 The deformation index DI of MCF7 cells as a function of flow rate. Cells were deformed in an inertia-dominant regime where $\mu \sim 1 \text{ cP}$.	184
Figure 7.6 Uptake of QDs in MCF7 cells deformed in a cross-slot device whilst suspended in media ($\mu \sim 1 \text{ cP}$) with 100 nM QDs	185

Figure 7.7 Analysis of uptake of MCF7 cells deformed in a cross-slot whilst suspended with 100 nM of QDs ($\mu \approx 1$ cP).....	186
Figure 7.8 Shape analysis of cells deformed in a constriction channel.	187
Figure 7.9 Uptake of QDs into MCF7 cells deformed in a constriction channel	188
Figure 7.10 Analysis of uptake of QDs in MCF7 cells deformed in a constriction channel whilst suspended with 100 nM of QDs	189
Figure 7.11 Confocal images of QD uptake in MCF7 cells of the inertial and shear controls	190
Figure 7.12 (a) Histograms of the fluorescence per cell for the inertial control and the shear control, showing the distribution of QD uptake in MCF7 cells.....	191
Figure 7.13 Simplified schematic showing the mechanosensitive ion channel Piezo1 which resides in the cell membrane.	196
Figure 7.14 (a) Phase contrast images of HEK293 T-REx and Piezo1 T-REx cell lines adhered to a culture flask, scale bars are 20 μm	197
Figure 7.15 The drug Yoda1 was used to activate the mechanosensitive ion channel Piezo1.	199
Figure 7.16 The deformation index DI of HEK293 T-REx and Piezo1 T-REx as a function of flow rate.	200
Figure 7.17 (a) The fluorescence intensity Lm1/Lm2 of HEK293 T-REx and Piezo1 T-REx cell lines as a function of flow rate through a cross-slot microfluidic device.....	201
Figure 7.18 The averaged strain trace for HEK293 T-REx (N = 95) and Piezo1 T-REx (N=60) as a function of time	203
Figure 7.19 Averaged strain traces and velocity profiles of (a) N=95 HEK293 T-Rex cells and (b) N=60 Piezo1 T-Rex cells	203
Figure 7.20 SCA was performed on individual strain traces of HEK293 T-Rex and Piezo1 T-REx.	205
Figure 7.21 Histograms showing the final strain ϵ_{∞} of HEK293 T-REx (N=95) and of Piezo1 T-REx (N=60).....	206
Figure 8.1 Schematic showing structural information that could be gained from combining deformation cytometry and fluorescence imaging.....	220

List of Tables

Table 4.1 Multiple characteristic parameters extracted from the strain traces of N=50 cells.	91
Table 4.2 A summary of the strain rate and relaxation time of HL60 cells after deformation at the SP of an extensional flow	101
Table 4.3 A table summarising the different values of elastic modulus reported for HL60 cells using a range of techniques.	103
Table 5.1 Multiple characteristic parameters extracted from the strain traces of N=56 SW480 cells and N=30 SW480 cells treated with LatA.	118
Table 5.2 Multiple characteristic parameters extracted from the strain traces of N=50 HL60 cells and N=38 HL60 cells treated with CA4.	140
Table 5.3 Summary of DI results w between untreated HL60 cells and those treated with TSA.	150
Table 6.1 The average nuclear diameter of HL60, SW480, HT29 and SW620 cells (measured using confocal images), and the nuclear ratio of each cell line ($A_{\text{nucleus}}/A_{\text{cell}}$).	157
Table 6.2 Summary of parameters associated with cell width W and H during deformation at the SP over a range of flow rates.	166
Table 6.3 Multiple characteristic parameters extracted from the strain traces of N=56 SW480 cells, N=49 HT29 and N=50 SW620 cells.	169
Table 6.4 Characteristic parameters of HL60, SW480, HT29 and SW620 cell lines, found using single cell analysis	170
Table 6.5 Summary of p-values comparing properties of HL60, SW480, SW620 and HT29 cell populations	172
Table 6.6 k-fold validation tests to classify the four cell lines (5-fold).	174
Table 7.1 Multiple characteristic parameters extracted from the strain traces of N=95 HEK293 T-REx cells and N=60 Piezo1 T-REx cells	204
Table 8.1 Confusion Matrix of PCA/LDA results from Raman spectra of the three CRC cell lines ..	216

1 Introduction

1.1 Overview

This PhD project was part of a larger collaboration to design a microfluidic platform with combined assays to mechanically, chemically and electrically phenotype single cells. The proposed assays were Deformation Cytometry (DC) for mechanical phenotyping, Surface Acoustic Wave (SAW) dielectrophoresis (DEP) for electrical phenotyping and Raman Spectroscopy for biochemical phenotyping. The main application of the platform would be to distinguish between healthy and diseased cells within a population, in a non-destructive manner. Traditional genomic and transcriptomic analytical methods are costly and time-consuming, as well as being inherently destructive, making it impossible to determine both a cell's mutational load, its biological behaviour and therapeutic response. The integrated microfluidic platform, indicated above, would provide a unique cell characterisation system capable of discerning between normal and pathological states on a single-cell level. The on-chip measurements leave the cells viable, permitting subsequent destructive genetic sequencing. Further, the platform could aid understanding of disease progression and with assessment of treatment success. The three assays were to be first developed and optimised separately; this project worked towards development of DC to mechanically phenotype single cells using a microfluidic device.

1.2 Background: Mechano-phenotyping and Single Cell Analysis

The deformability of a cell is the result of a complex interplay between its biological constituents at the subcellular level. Disease can induce changes to subcellular constituents (including the cytoskeleton, nucleus and cytoplasm), making cell deformability a biophysical marker for disease. The aim of the project is to mechanically phenotype cells in order to identify diseased populations in a sample and understand how the mechanical phenotype changes with disease progression.

The mechanical properties of biological materials can be measured on various length scales, including submicron protein filaments and micron ranging single cells, scaling up to tumours or entire organs. A challenge in cancer research is understanding how biological changes relate to pathology, hindered by finding appropriate methods to map tumours across all length scales. Comparisons between cell genotype and phenotype commonly come from averaged measurements of a population of cells. These measurements are useful, however cell populations are heterogeneous and averaging cannot assess individual responses. Cell heterogeneity derives from the active nature of cells, which involves biochemical reactions driving processes such as the cell-cycle, signalling, motility and differentiation. Further, "biological noise" occurs such that genetically identical cells, exposed to the same

environment, show stochastic gene expression resulting in phenotypic changes. Detailed reviews of biological noise can be found [3], [4]. Thus, an average study may show significant changes between two populations, however a single-cell analysis may produce further information on heterogeneity as well as sub-populations in mixed samples. For example, a study on mechanical changes induced by a drug treatment may only affect a small fraction of the cells which would not be deduced by averaging. Therefore, to properly characterise a system the individual components must be understood.

Common downfalls of single-cell analysis techniques are that they are time-consuming and require large numbers of cells to gain statistical significance. Flow cytometry is a high-throughput technique, able to analyse thousands of cells per second, to measure physical and chemical properties of cells [5]. Cells flow single file through a laser beam, scattered light is collected and used to infer information about the cells. Physical properties such as size and morphology can be deduced from scattering without fluorescent labelling, however fluorescent labelling is required for study of the chemical content (e.g. DNA stain to study cell cycle stage). Traditional flow cytometry offers no mechanical information, and thus current methods do not combine mechanical and chemical phenotyping at the single-cell level.

Many techniques exist for mechanical phenotyping of single cells (described in more detail in the next section), but are often plagued by being time-consuming and low-throughput. Microfluidics offers a high-throughput alternative for biophysical characterisation. Microfluidics constrains fluid flow to the micronscale, and involves flow through channels with dimensions on the 10s of microns scale. Fluids can be carefully manipulated with devices requiring low-volume of sample (picolitres to nanolitres). Advantages of microfluidic techniques include; low reagent, low cost, biocompatibility, integration capability and high-throughput potential. Additionally, on-chip measurements leave the cells viable and permits subsequent destructive genetic sequencing.

1.3 Biophysical characterisation techniques

1.3.1 Overview

Many experimental techniques have been developed for studying the mechanical properties of cells, these are summarised by schematics in Figure 1.1, and can be separated into three types; localized probing which deforms a small area of the cell, whole cell deformations, and simultaneously applying stress to a population of cells (10^2 - 10^4 cells) [6].

Localized deformation techniques include atomic force microscopy (AFM) and magnetic twisting cytometry (MT). In AFM, a local deformation is induced on the surface of cell through contact with a sharp tip at the end of a flexible cantilever (Figure 1.1a). The deflection of the cantilever tip, detected by a photodiode, is used to estimate the applied force. The force

range in AFM is 10^{-12} - 10^{-6} N, and capable of small displacements less than 1 nm [7]. This technique has been used to explore elastic deformation of cells and their subcellular components, such as the cytoskeleton, but is limited to measurements on cells that can adhere tightly to a substrate. Mechanical measurements are not optical and thus its combination with fluorescent labelling and chemical disruption of cytoskeletal filaments was used to show that actin filaments contribute more to cell stiffness than microtubules [8]. AFM data analysis requires application of elastic models, commonly the Hertz model, which rely on assumptions that do not account for the time-dependent and non-linear behaviour seen in cell mechanics. A more thorough review of the use of AFM for cell biomechanics can be found in Kumar *et al.* 2012 [9]. Magnetic twisting cytometry (MT) involves functionalised attachment of magnetic beads to the cell surface, a magnetic field is then applied to deform the cell via a twisting moment (Figure 1.1d). The applied forces and displacement are similarly small like in AFM (10^{-12} - 10^{-6} N, <1 nm) [7], with bead diameters of 250 nm to 5 μ m [10]. This method was first developed by Crick *et al.* (1949), and has since been used to study the cytoplasm, cell membrane and cytoskeleton [11]. MT has been used to study cyclic loading experiments, frequency range 0.2-400 Hz [12], to develop further insight into cell viscoelasticity.

Whole cell deformations can be induced by Optical Trapping (OT) and micropipette aspiration (MA). Optical tweezers (laser trapping) involves aiming a laser beam at a dielectric bead of high refractive index attached to a cell, an attractive force between the bead and laser beam pulls the bead to the focal point of the trap (Figure 1.1c). For cell deformations, two variations of OT exist. First, two beads can be attached to opposite ends of a cell and trapped by two laser beams which induces cell stretching. Second, a single bead can be trapped at one end of the cell whilst the other end of the cell is attached to a glass plate. Induced forces are typically on the 10s to 100s of pN range [7]. Biological objects probed by this method must be sufficiently compliant that the required laser power is enough to deform the object without imparting radiation damage, thus OT is typically limited to cells in fluid suspension (e.g. blood cells). Also, non-uniform stress distributions arise from the inherent point loading at the bead attachment area which creates challenges when calculating mechanical parameters. An advancement of traditional OT is the optical stretcher OS which does not require cells to be attached to beads or glass [13]. Here, two lasers are diametrically shone on opposite sides of the cell. The laser spots are unfocused in this plane, thus high laser powers can be used without cell damage [10].

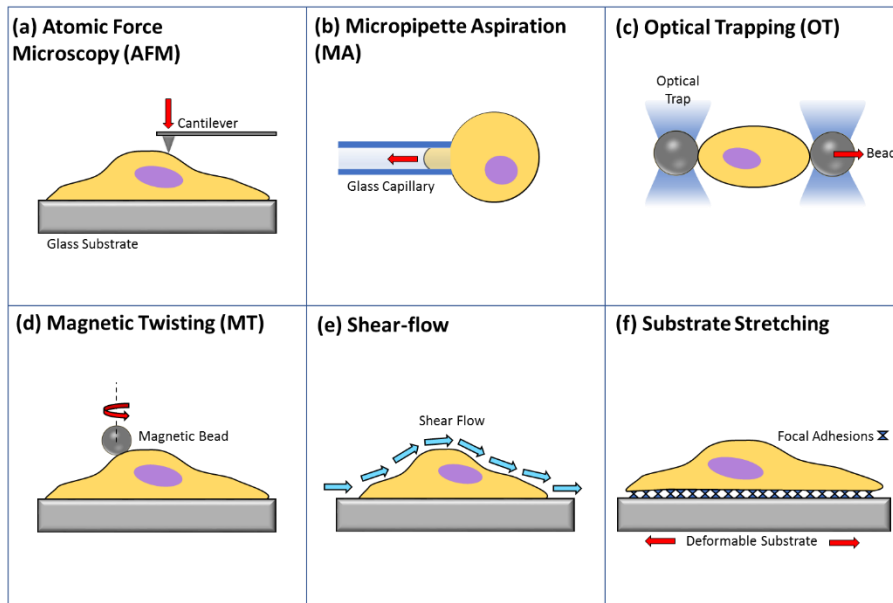


Figure 1.1 Schematic representations of the types of experimental techniques used for biomechanical characterisation of cells. Including atomic force microscopy (a), micropipette aspiration (b), optical trapping (c), magnetic twisting (d), shear-flow (e) and substrate stretching (f).

Micropipette aspiration (MA) uses extracellular pressure for time-dependent studies of cell deformation (Figure 1.1b). An aspiration pressure (suction) is used to draw a cell into a glass tube (micropipette), with an inner diameter smaller than the initial cell diameter [14]. Applied aspiration pressure typically ranges 0.1-1000 Pa [15]. The micropipette is coated with 1% agar to prevent cell adhesion and pressure is maintained over a specific time period and deformation is monitored by optical microscopy. Models can be applied to obtain mechanical parameters such as elastic modulus, apparent viscosity and relaxation constants. However, the values derived of these parameters are very model dependent.

The biomechanics of a population of cells can be simultaneously studied using shear-flow (Figure 1.1e) and substrate stretching (Figure 1.1f). Shear-flow is used to monitor the biomechanical response of cells by their resistance to fluid flow. This is conducted using either a cone-and-plate viscometer (a stationary flat plate below an inverted cone where laminar and turbulent flows are applied), or by parallel-plate flow where laminar flow is applied [16]. Substrate stretching involves adhering cells to polymeric substrates through focal adhesion complexes, the compliant substrate can be deformed and cell spreading, deformation and migration can be studied [17]. Here, forces are on the 10-100 nN range and displacements can be up to the mm range [7]. Additionally, the effect of changing the mechanical properties of the substrate on the cell response can be studied. A downfall of cell population studies, including shear-flow and substrate stretching, is that cell heterogeneity is largely unaccounted for. Single-cell properties cannot be easily decoupled from the entire population response.

A more in-depth description of these biomechanical techniques can be found in these review papers [6], [7], [10]. Figure 1.2 shows a representation of the range of forces and displacements cells are exposed to using the previously discussed techniques, and also provides comparison to relevant biological processes. The forces range from 10^{-14} to $\sim 10^{-7}$ N, with the lowest forces imparted using optical tweezers and largest forces via substrate deformation. The displacement ranges from 10^{-10} to $\sim 10^{-3}$ m, with AFM nanoindentation resulting in the smallest displacement and substrate stretching the largest displacement.

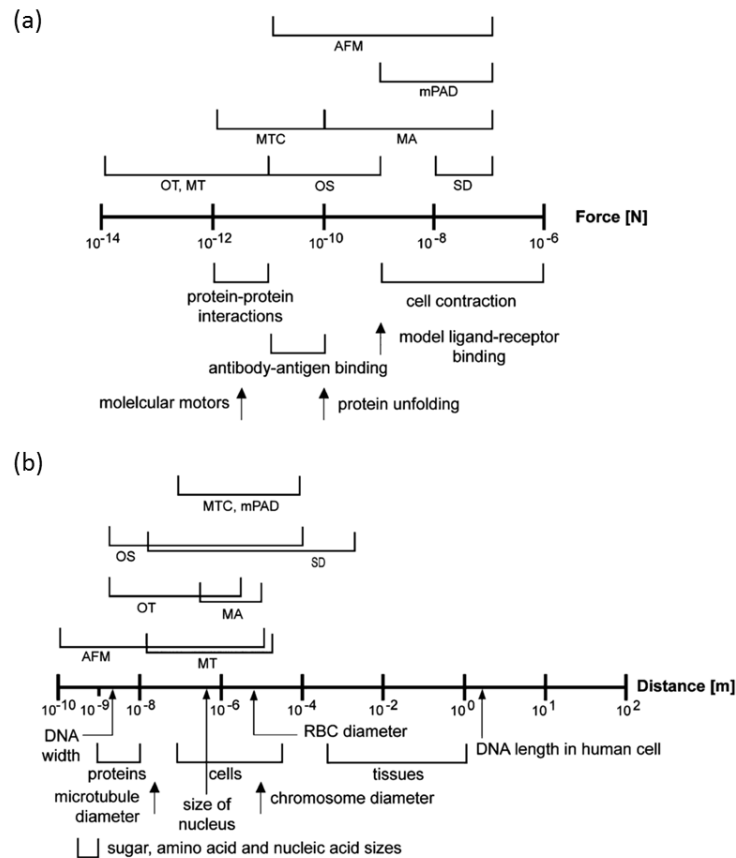


Figure 1.2 The typical ranges of forces (a) and displacements (b) probed by various biomechanical assays, compared to biological cell and molecular interactions and length-scales. Included are; atomic force microscopy (AFM), optical tweezers (OT), optical stretching (OS), magnetic twisting cytometry (MTC), micropipette aspiration (MA) and substrate deformation (SD). Figure taken from Suresh et al. 2007 [7].

1.3.2 Microfluidics

The previously discussed biomechanical techniques are often limited by being low-throughput, where measurements are performed one cell at a time which can be time-consuming, often resulting in a small number of cells being probed. Commonly used techniques such as AFM, MA and OT are well established and offer high precision measurements, however higher “speed” techniques are required for accurate characterisation and classification of heterogeneous cell populations. Thus, probing cells under continuous

flow (using microfluidics) allows for automated event capture (no preselection) and improved measurement throughput. Figure 1.3, taken from a review by Wyss 2015 [18], shows a graphical summary of biomechanical methods based on their “precision” and “speed”.

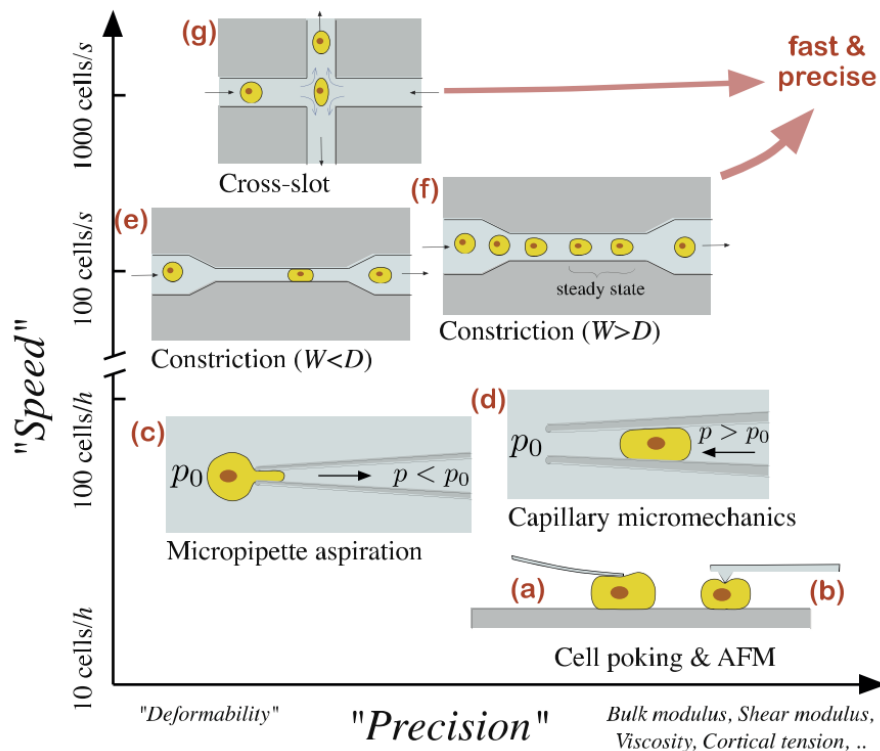


Figure 1.3 A graphical representation of the “precision” of different biomechanical methods for probing cells compared to the “speed” (i.e. throughput). Figures (e)-(f) depict microfluidic methods where the arrows indicate the direction of flow. Figure taken from Wyss 2015 [18].

Cell deformation using microfluidic techniques can be categorised as either: structure-induced deformation or fluid-induced deformation [19]. Structure-induced deformation involves passing a cell through a constriction channel with a width W smaller than the cell diameter D ($W < D$) (Figure 1.3e). From this, parameters such as cell elongation, transit time and recovery can be used to quantify cell stiffness. Structure-induced deformation is particularly useful for the study of red blood cells (RBCs) as the constriction channels mimic *in vivo* capillaries. Shelby *et al.* 2003 first used constriction ($W < D$) channels to deform malaria infected RBCs [20]. These type of devices can also be paired with impedance measurements, first demonstrated by Zheng *et al.* 2012 [21], eliminating the need for image analysis and instead using electric signals to infer mechanical properties. This allowed improved throughputs of ~ 100 cells/s and parameters such as transit time, impedance amplitude ratio and impedance phase increase were found. Abkarian *et al.* 2006 correlated pressure drop due to the presence of a cell in a constriction channel to its stiffness by measuring the fluid-fluid interface displacement downstream. Measurement throughput using constriction channels ($W < D$) has reached ~ 800 cells/min [22]. However, this method is also affected by cell volume and

adhesion between the cell membrane and channel walls. Larger and stickier cells will have a longer transit time, making it difficult to infer changes to stiffness. Additionally, the small channel diameters in such devices makes them susceptible to clogging which limits experimental throughput.

Fluid-induced deformation occurs when cells are deformed by a shear or extensional hydrodynamic force rather than by structural confinement [23], [24], which is not affected by friction or adhesion between the cell and channel walls. Constriction channels with widths slightly larger than the cells diameter ($W > D$) can be used to induce shear fluid stress (Figure 1.3g). Zheng *et al.* 2013 used a straight channel with $W > D$ to deform RBCs and found shear fluid stress can cause stretching, tumbling and recoiling [25], showing that chemically fixed RBCs are less deformable. Functionally, RBCs are required to squeeze through narrow capillaries in the body so are naturally highly deformable. Therefore, fluid-induced shear stress is often not enough to deform other cell types in these geometries. Lee *et al.* 2009 showed that extensional flow was more efficient for deforming cells than shear flow [26]. Extensional flow is due to a velocity gradient between a larger chamber and a contraction area in a microfluidic device. RBCs were deformed using a hyperbolic converging channel to create an extensional flow, they found that the same stress in extensional flow induced a higher degree of deformation compared to purely shear flow.

Extensional flow deformation can also be achieved using a cross-slot geometry, consisting of a junction with two opposing inlets and outlets (Figure 1.3g). An extensional flow is generated and cells are hydrodynamically deformed at the stagnation point (SP) at the centre of the junction. This geometry can be used to induce high strains on cells (>50%) [27]. This method often requires cells to be focused to a central streamline before entering the junction, to ensure they are exposed to the same stress field. This can be achieved via inertial focusing [28] or viscoelastic focusing [29]. A technique called Deformability Cytometry (DC) has been developed by the Di Carlo group, utilising inertial focusing and a cross-slot geometry to mechanically phenotype cells, first introduced in Gossett *et al.* 2012 [27]. The experimental set-up, cell deformation and analysis of the technique is summarised by Figure 1.4. This technique showed a significant increase in throughput in continuous mechanical phenotyping, the largest reported as 20,000 cells/s [30], [31]. The applied stress field is also dependent on initial cell size and shape, thus initial cell size and deformability are measured independently and used for classification [32]. They defined deformability as a simple ratio of the major (a) and minor (b) axis (Figure 1.4e), density scatter plots of deformability vs initial size were used to visualise collected data (Figure 1.4f).

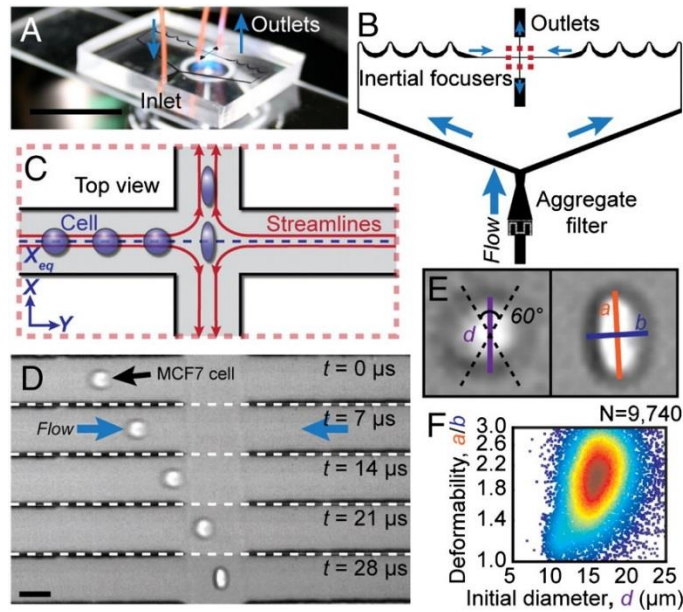


Figure 1.4 The principles of deformability cytometry. (a) Image of the device set up. (b) Schematic of the cross-slot device with inertial focusers. (c) A schematic of deformation at the stagnation point (SP) of the cross-slot. (d) Example high-speed image of a deformation event. (e) Definition of shape parameters for measuring deformability. (f) Example density scatter plot of deformability measurements. Reprinted from Gossett et al. 2012 with permission from PNAS [27].

Microfluidics techniques such as DC use high speed imaging to collect 1000s of cell deformation events, which in turn generates large amounts of data. This can require significant computational time between data collection and finished analysis. Real-Time Deformability Cytometry (RT-DC) was developed by the Guck group (first published in [33]), where microfluidic deformations are acquired continuously and analysis occurs in real-time. Comparatively, DC requires ~15 mins before results are available. RT-DC uses constriction deformations ($W > D$) where cells are suspended in high viscosity suspension buffers to increase the wall proximity induced shear forces. Cells deform to a bullet-like shape due to the strong velocity gradient within the channel. The throughput of RT-DC is 100 cells/s, however RT-DC has analysed total populations of >100,000 cells whereas DC only a few thousand despite the faster rate [19]. The deformations in RT-DC are relatively low compared to DC and are antisymmetric making the shape harder to characterise.

RT-DC operates in the laminar flow regime where the Reynolds number $Re \approx 0.1$. To find the associated flow fields in this system the Navier-Stokes equation must be solved, at $Re \ll 1$ the inertial terms can be ignored making the problem linear and time-independent. Comparatively, DC operates in a regime of $Re \approx 50$, here inertia has a significant effect and flow field calculation is a challenging non-linear and time dependant problem [34]. Mietke *et al.* 2015 produced an analytical model of RT-DC and related elastic parameters back to cell deformation [34], combining theory with simulations and experiments. As deformations are

measured under a steady state, the surface stresses on an isotropic and incompressible sphere in a cylindrical channel were found and used as a boundary condition to solve linear elasticity theory. Results agreed well with experiments using a rectangular channel (common for microfluidic fabrication) with identical channel pressure drop, and cells were modelled as an elastic sphere, a sphere with a thin elastic shell, and with added surface tension.

They were able to calculate the elastic modulus E of cells, decoupling size from deformation. However, the model is only valid for small deformations. Figure 1.5 shows an example density scatter plot of deformability against initial size for a given cell line, overlaid isoelasticity lines on the scatter plot are used to divide it into areas of equal stiffness. The model was in good agreement with experiments on agar beads of known stiffness, however the elastic modulus of HL60 measured using RT-DC was $E = 1.48 \pm 0.51 \text{ kPa}$ which is ~ 9 fold bigger than using AFM. They discussed that the shorter timescale of RT-DC ($\sim 1 \text{ ms}$) was responsible for the difference, or that the shell properties (membrane and cytoskeletal cortex) dominate the system. This work shows progress in using high-speed techniques whilst also improving measurement precision by extracting known mechanical properties.

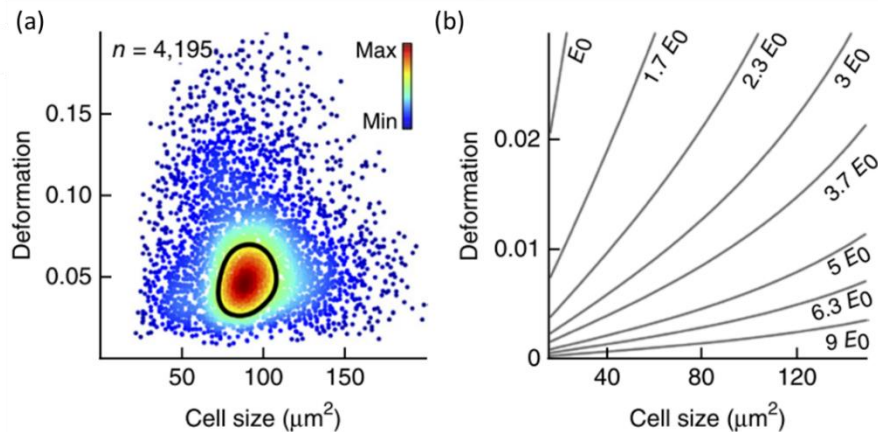


Figure 1.5 (a) An example scatter plot of deformation against initial size (cross sectional area) for a HL60 cell sample. (b) Isoelasticity lines can be used to divide the scatter plot into areas of identical stiffness as multiples of Elastic Modulus E_0 . Figure taken from Otto et al. 2015 [33].

Guillou et al. 2016 used a cross-slot device to deform cells at low strain ($0.01 < \epsilon < 0.18$, where ϵ is the strain defined in section 3.5.3) and at low Reynolds number ($Re < 0.2$), allowing them to apply an analytical model to extract mechanical parameters [35]. A viscoelastic two-parameter power law model was used to predict the shear modulus of cells, results were further validated using micropipette aspiration and by comparing to dextran particles. Here, cells were small compared to channel size and the model was only valid for small deformations. Cells which did not pass through the stagnation point of the device were discarded, resulting in low event numbers for each flow condition tested ($10 \leq n \leq 30$).

Integration of traditional “precise” techniques with microfluidics may be capable of producing a system that is high-throughput and outputs mechanical properties. For instance, Guck *et al.* 2005 combined continuous flow of cells through a microchannel with optical stretching measurements [36]. The trapping and stretching of cells using this method requires precise alignment of two laser fibres on each side of the microchannel, adding complexity to this method. Micropipette aspiration also lends itself to integration with microfluidics as a way to increase throughput and extract properties such as elastic modulus [37]. However, microchannels are commonly rectangular in shape which may reduce the validity of applying traditional MA models. Additionally, throughput is limited compared to other microfluidic techniques (such as DC and RT-DC). More detailed reviews discussing the advantages and disadvantages of different biomechanical assays can be found in [18], [19], [31], [38].

1.4 Deformation Cytometry Applications

1.4.1 Detecting diseased states

A principal application of mechanical phenotyping is disease diagnostics, i.e. identifying diseased cells based on their mechanical properties. Deformability changes have been identified in diseases such as cancer, sepsis [39], malaria [40], diabetes [41] and sickle cell anaemia [42]. Cancer is a common target of investigation as studies repeatedly show that malignant phenotypes have reduced stiffness than their healthy counterparts [7]. This is thought to be caused by a more disorganised cytoskeletal so that cancerous cells can more easily invade surrounding tissue and metastasise. The stiffness/softness of cells can be quantified in a number of ways such as measuring strains induced by an applied force, to extracting mechanical parameters such as elastic modulus (where a reduced modulus indicates cell softening). Cross *et al.* 2007 showed that malignant cells were >70% softer than cells from normal tissue by using AFM to extract single cell elastic moduli [43]. Often, diseased cells can equate to a small population of a sample and thus high-throughput screening is required for mechanical phenotyping. Microfluidic mechanical phenotyping has been able to distinguish cells with a variety of diseases.

Tse *et al.* 2013 used DC to identify disseminated tumour cells in pleural effusion samples from patients. Scatter plots of initial diameter against deformability showed two distinct regions corresponding to healthy leukocytes and malignant pleural cells. From these plots, a diagnostic scoring system was developed to categorise deformability. Cells were allocated a number from 1-10 based on their position on the graph, 1 indicates least likely to be malignant and 10 indicates most likely to be malignant. Regions 1-6 and 9-10 contained 63% of the cell population and identified the cell type with 100% accuracy, cells in region 7-8 were more difficult to diagnose and would need a different technique to be accurately identified [32]. Che

et al. 2017 combined microfluidic vortex trapping and *DC* to isolate and characterise rare circulating tumours cells (CTCs) from patient blood samples. Compared to samples from healthy patients, cancerous samples showed a cell population with increased size and deformability confirmed as CTCs by immunofluorescence.

Microfluidic studies have also been used to identify differences in deformability of malignant cell lines and those from different stages of cancer progression. This includes; breast cancer cell lines [36], [44], prostate cancer cell lines [44], pancreatic cancer cell lines [45], bone cancer [46] and brain cancer cells [47].

1.4.2 Sensitivity to subcellular changes

The sensitivity of *DC* has been tested by using various drugs to alter the internal structure of the cell, which includes destabilising or enhancing various cytoskeletal filaments, disrupting nuclear structure and inhibiting motor proteins. Microfluidic techniques have been used to probe the effect of deformability due to changes in; actin [27], [35], [48]–[50], microtubules [27], [50], intermediate filaments [27], [30], nuclear chromatin [48], [49], [51], and inhibition of motor proteins including Myosin II [27], [32], [50], [52].

Some studies were able to detect specific subcellular changes whereas some were not, showing that different microfluidic assays may be more/less sensitive to specific internal changes. Gossett *et al.* 2012 used *DC* (inertia-dominant and high strain deformations) to show deformability increases due to lymphocyte activation and stem cell pluripotency, states that are characterised by loose open chromatin structures [27]. However, no changes in deformability were detected due to treatment with several cytoskeletal altering drugs. Guillou *et al.* 2016 also used a cross-slot device but in a shear-dominant and low strain regime. This regime was able to detect increased cell deformability due to actin destabilisation using the drug cytochalasin D [35]. Otto *et al.* 2015 used RT-*DC* (shear-dominant and low strain) constriction induced deformations ($W > D$) and found significant deformability changes due to cytoskeletal alterations [33]. They also saw no significant changes in deformability due to nuclear structural changes. Thus, the sensitivity of microfluidic deformation cytometry is highly dependent on the device geometry used and the flow regime utilised.

Previous works limit the measurement range to either low or high relative strains, or apply stresses dominated by either shear force or inertial force [29], [35], [53], [54]. The scope of this thesis investigates the sensitivity of *DC* from low to high strain in shear and inertial flows using a single device geometry [1]. Compared to previous microfluidics assays, by probing over a wide range of conditions we could infer more physical understanding of how subcellular changes are coupled to whole cell mechanics. This would identify which conditions are optimum for distinguishing certain cell types leading to deformation assays

being tailored towards their application. The shear-regime was also used to introduce new parameters to describe cell response, allowing improved multiparameter characterisation on a single-cell level which can infer heterogeneous responses.

1.4.3 DC for non-endocytic uptake of nanoparticles

Cell deformation may also affect the cell membrane such that stretching can induce transient membrane pores, allowing materials to flow in and out of the cell. This phenomenon can be utilised for intracellular delivery of macromolecules and nanoparticles (NPs). This has a range of applications, including; RNA and DNA delivery for gene therapy [55], protein delivery [56], various NPs for cancer therapies [57], intracellular labelling [58], [59], and single-molecule tracking [60]. For example, Quantum Dots (QDs) are colloidal semiconducting nanoparticles with a range of uses in the fields of bioimaging and biosensing. Their size-tunable broad absorption spectra, narrow emission profiles, photostability and brightness compared to traditional fluorophores, makes them appealing. However, usually the cell membrane is mostly impermeable to nanoparticles and their uptake into cells occurs predominantly via endocytosis.

Methods exist to either release QDs from enclosed endosomes, or to deliver them directly to the cytosol. Labelling QDs with cell-penetrating peptides can facilitate direct uptake [61], however this requires successful dual conjugation. Electroporation involves exposing cells to an electric field to increase membrane permeability, and has shown cytosolic uptake of QDs [62]. However, the electric field can cause QDs to aggregate and reduce cell viability. Sonoporation is a similar technique utilising ultrasound instead of electric fields, and has been used for macromolecule and nanoparticle delivery [63]. Microinjection can directly deliver QDs to the cytoplasm, however this technique is extremely low throughput [64].

More recently, various types of microfluidic DC assays have achieved non-endocytic macromolecule and NP uptake. Langer and Jensen pioneered this technique, first using microfluidic constriction channels ($W < D$) to achieve cytosolic delivery of QDs to cells [65]. This cell squeezing method creates transient membrane pores which facilitate passive diffusion, the initial study found ~35% delivery efficiency whilst maintaining 80-90% cell viability. Figure 1.6 shows their experimental set-up and initial results for increased QD uptake for smaller constriction channels. They have since used this method to deliver a range of materials into 11 cell types [66], [67], including carbon nanotubes, proteins and siRNA. Sharei *et al.* 2013 showed increased delivery efficiency with increased cell speeds, reduced constriction dimensions, and increased number of constrictions. Additionally, 3kDa dextran beads were added at varying time points after microfluidic treatment showing that 70-90% of delivery occurs within the first minute.

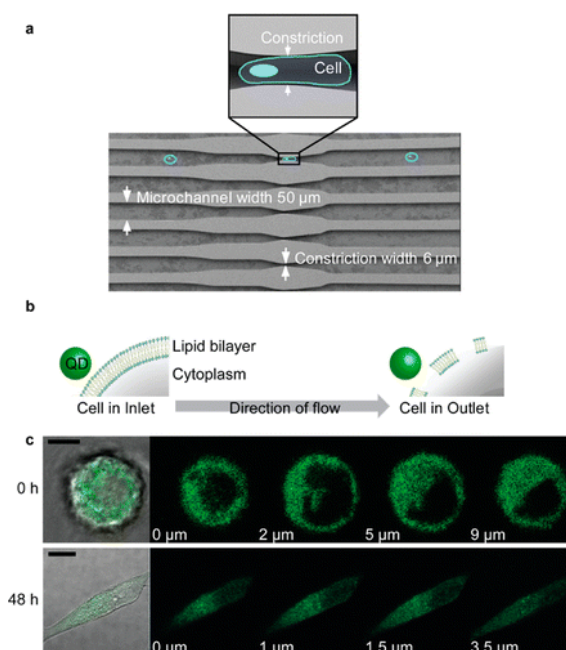


Figure 1.6 Constriction microfluidics for increased QD uptake in cells. (a) Schematic of the device. (b) Schematic of theorised method of uptake due to transient pore formation. (c) Confocal fluorescence images of cells deformed through different microfluidic constrictions with QDs. Reprinted from. Reprinted with permission from Lee et al. 2012 [65]. Copyright (2019) American Chemical Society.

Chung's group adapted their inertial microfluidic cell stretcher (iMCS) for intracellular delivery, here cells are deformed by contact with the device wall at a T-junction in an inertial flow regime ($Re > 100$) [54]. A sharp tip was added to the contact area of the T-junction wall, to increase the uptake efficiency [68]. Figure 1.7 shows images of the microfluidic device and results for increased uptake of 3 kDa dextran particles using the iMCS. Uptake of 3kDa and 70kDa beads was successfully demonstrated to mimic protein delivery. They also showed successful cytosolic uptake of various DNA origami structures achieving between 30% and 55% delivery efficiencies. More recently, this group have opted to use a cross-slot device in an inertial flow regime (similar to DC by the Di Carlo group) which they refer to as a *Hydroporator*. They achieved delivery of many macromolecules to 10 cell types, with up to 90% delivery efficiency and a throughput > 1.6 million cells/min. This included testing various sizes of Dextran beads and achieving $\sim 60\%$ delivery efficiency even at 2000 kDa (~ 50 nm). DNA origami structures were successfully delivered and maintained structural integrity for ~ 1 hr afterwards.

Deformation cytometry can achieve cytosolic uptake of macromolecules and nanoparticles of various shapes and sizes. The advantages of deformation cytometry include; high-throughput, label-free, non-endocytic, maintains viability and requires no external electric fields or high frequency ultrasound.

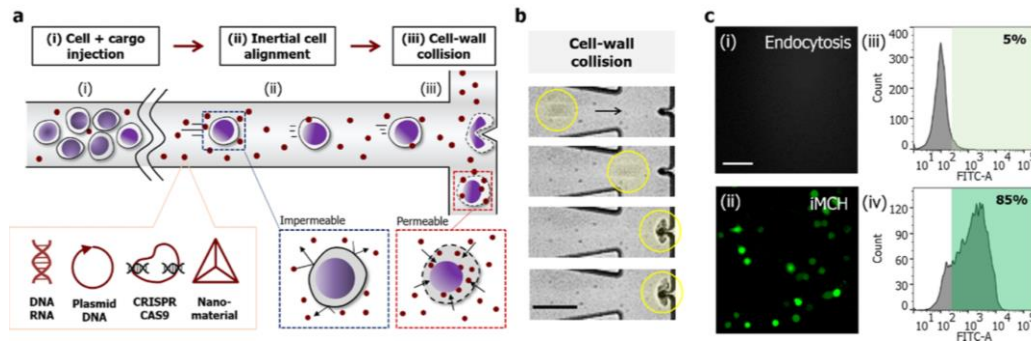


Figure 1.7 Details of the inertial microfluidic cell hydroporator for intracellular delivery of nanoparticles (a) Schematic of the T-junction chip design. (b) Bright field image of a cell deforming in the device. (c) Successful delivery of fluorescent dextran into cells using the system. Figure taken from. Reprinted with permission from Deng *et al.* 2018 [68]. Copyright (2019) American Chemical Society.

1.4.4 Combining DC and fluorescence measurements

DC has shown high-throughput and sensitivity to subcellular and pathological changes. However, using bright-field imaging alone does not provide the same specificity as traditional flow cytometers which can detect specific molecular markers using fluorescent labelling. Recent studies are working to combine mechanical phenotyping using DC with fluorescence measurements to identify how substructure affects whole cell deformation, and for improved classification rates by multiparameter analysis [69].

Hodgson *et al.* 2017 combined constriction channel deformation ($W < D$) with nuclear staining to study the nuclear deformability of embryonic stem cells [49]. Cells were imaged before, during and after compression using frame rates of 30-100 fps, and the traverse and axial strain of the cell nucleus was found. They also studied changes in nuclear deformability due to treatment with actin depolymeriser Cytochalasin D (CytoD) and chromatin decondenser Trichostatin A (TSA). The Guck group recently combined RT-DC with 1D imaging-fluorescence (RT-FDC) [69]. Lasers excite in a light sheet perpendicular to the channel axis such that cells pass through the light-sheet at constant speed, this allows measure of subcellular distribution of fluorophores in the direction of flow in the channel. Cells deform through a constriction ($W > D$) and pass through a 3 μm wide light sheet at constant speed, being excited by three lasers with photodiodes to measure fluorescence. This method allows identification of subpopulations, such as mitotic cells, and direct correlation to deformability. This method only measured fluorescence in 1D and no 2D or 3D (z-stack) fluorescence image accompanies the bright field image. Recently, the Goda research group have made progress in combining high speed confocal and light-sheet fluorescence of cells travelling up to >1 m/s [70], [71]. Confocal fluorescence imaging cytometry has been demonstrated for cells travelling up to 2 m/s, with two fluorescent channels including a DNA stain [70]. This allows multiple parameter analysis to occur including whole cell and nucleus shape and morphology parameters.

Traditional imaging flow cytometers have much lower throughput than non-imaging, using light-sheet excitation they improved fluorescence intensity 10 fold and achieved throughput of ~10,000 cells/s [71]. However, these techniques are yet to incorporate deformation studies which would elucidate further biomechanical information and potentially improve classification rates.

1.5 Scope of project and thesis outline

The scope of the project was to investigate the use of deformation cytometry using a cross-slot device for characterisation of cell mechanical properties in shear and inertial flow regimes. This included assays on cells treated with various drugs to alter the substructure and a colorectal cancer model system. Additional applications were also explored, such as the ability of DC for cytosolic uptake of quantum dots into cells.

Chapter 2 of this thesis includes theoretical background and **Chapter 3** the methodologies used to undertake the research. The deformation cytometry results are next reported in **Chapters 4 to 7**. Finally, **Chapter 8** provides a conclusion and discusses future work such as integration of *DC* with other phenotyping techniques. This includes a comparison of Raman Spectroscopy data performed on the same CRC model system. Below is a short description of each results chapter.

Chapter 4 describes the optimisation of the cross-slot device, including defining shear and inertial regime deformations using HL60 (human leukaemia) cells. Cell deformations were tracked as a function of time allowing multiple deformation and relaxation parameters to be extracted. A Kelvin-Voigt model was fitted to the strain curve to extract an elastic modulus. The advantages of bulk-averaging vs single cell analysis are also explored using the multiparameter dataset.

Chapter 5 involves probing mechanical changes due to subcellular alterations in the shear and inertial regimes. This includes; actin destabilisation using Latrunculin A (LatA), microtubule destabilisation using Combretastatin A4 (CA4), and chromatin decondensation using Trichostatin A (TSA). Deformation tracking and single cell analysis optimised in Chapter 4 were also applied to the datasets.

Chapter 6 focuses on mechanical changes due to colorectal cancer progression. This is done using a model system of three CRC cell lines (SW480, HT29 and SW620) representing different stages of disease progression. Deformation cytometry assays were performed in shear and inertial regimes, and deformation tracking was used for single-cell multiparameter analysis. Statistical tests were also used to test the abilities of mechanical parameters for cell type classification.

Chapter 7 explores other applications of microfluidic cell deformation. Firstly, cytosolic uptake of quantum dots (QDs) into MCF7 cells is probed as a function of flow rate in shear and inertial flow regimes. Secondly, preliminary results are presented for using microfluidic deformation to activate the mechano-sensitive ion channel *Piezol*.

2 Theory and Background

In this thesis, deformation cytometry is used primarily for mechanical phenotyping of single cells. This includes studying the effects of subcellular perturbations to whole cell mechanical response, and mechanical changes as a function of colorectal cancer progression. The introduction chapter provided a general introduction to advantages of microfluidics for mechanical phenotyping compared to other techniques, as well as a literature review on the diagnostic applications of mechanical phenotyping.

This chapter includes a deeper background into subcellular structure and metastatic progression, and how these relate to mechanical phenotype. The principles and main equations relating to microfluidics are also described. Finally, an overview of models of cell mechanics is provided as well as details of the Kelvin-Voigt model used throughout the thesis.

2.1 Cell Structure

2.1.1 Overview

The cell is considered the basic biological unit which makes up all living organisms. The two main types of cell are prokaryotic and eukaryotic. Prokaryotes are usually single living cells and have the simplest internal structure. They are thought to have been the oldest living organisms, the two types of prokaryote are archaea and bacteria which are usually between 1 μm and 10 μm in size. Eukaryotic cells are vastly more complex, generally bigger, capable of forming multicellular organisms (unlike most prokaryotes) and include fungi, plant and animal cells. For example, the human body is made up of ~ 37.2 trillion cells of ~ 200 different kinds of cells. Individually many cell types have a size of ~ 10 - $20 \mu\text{m}$, however can be even smaller such as red blood cells 6 - $8 \mu\text{m}$, and much larger such as female egg cells (oocytes) $\approx 120 \mu\text{m}$.

All cells are enclosed by the cell membrane, which keeps the key cellular components internalised. The cell membrane consists of a lipid bilayer with embedded membrane proteins, and controls movement of ions and molecules in and out of the cell. Eukaryote structure is more complex due to the presence of additional internal lipid membranes which enclose “organelles” from the rest of the internal cytoplasm. Additionally, eukaryotes contain a nucleus where DNA is contained and arranged into chromosomes. The material contained within a cell, apart from the nucleus, is referred to as the cytoplasm. The aqueous component of the cytoplasm, where all the organelles are suspended, is referred to as the cytosol. Prokaryotes do not contain a nucleus or enclosed organelles, any DNA and proteins are found within the cytosol and contained by the cell membrane. The other main organelles within eukaryotic animal cells are mitochondria and the Golgi apparatus.

2.1.2 The Cell Membrane

Cell membranes mainly consist of a phospholipid bilayer typically ~7 nm thick, held together mainly by non-covalent interactions and are dynamic fluid structures with the lipids able to diffuse freely within the plane of the membrane. The other main components of the membrane are various lipids, cholesterol and embedded proteins. The three main types of membrane protein are: integral proteins, peripheral proteins, and lipid-anchored proteins, which are important for a variety of biological activities [72]. Integral proteins span the membrane and are anchored within it, one example of a function of integral proteins are ion channels which can be chemically or mechanically triggered to allow ions to cross the membrane. Lipid anchored proteins are covalently bonded to lipid molecules which anchor the protein and are located on either side of the membrane surface. Peripheral proteins are attached to integral membrane proteins or the lipid bilayer periphery but interactions are temporary.

Through membrane proteins, the cell membrane anchors to the cytoskeleton which provides cell shape and integrity, and also attaches cells to the extracellular matrix (ECM) and other cells to form tissues. The membrane itself is a viscous fluid-like substance contributing to cell viscosity, bending resistance and incompressibility. However, as discussed in the next section the cytoskeleton is thought to be the main contributor to cell mechanics [73].

2.1.3 The Cytoskeleton

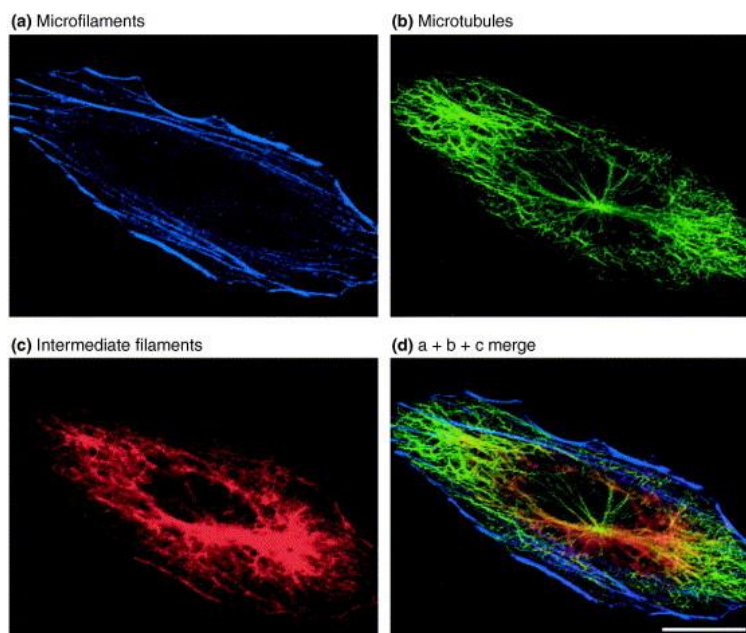


Figure 2.1 A fluorescent image of a cell with labelled cytoskeletal filaments: actin filaments (blue), microtubules (green) and intermediate filaments (red), Scale bar 10 μm . Image taken from [74].

The cell membrane alone does not provide enough structural integrity to maintain cell shape and structure or allow cell motility. A complex network of protein filaments which pervade

the cytoplasm, known as “the cytoskeleton”, are responsible for maintaining cell shape, internalised organisation of organelles, cell division and cell movement.

The cytoskeleton is highly dynamic and constantly reorganises itself to change the shape and arrangement of the cell. This depends on the environment; various signalling pathways can trigger restructure of the cytoskeleton. An example of this is the continuous cell cycle in which DNA is replicated and cells divide. The cytoskeleton also plays a key role in cell movement, vital for tissue development and wound healing. Until recently it was thought that the cytoskeleton was only present in eukaryotic cells, however some bacteria have been found to have primitive cytoskeletal components [75]. The cytoskeleton of eukaryotic cells consists of three types of filament; microtubules, intermediate filaments and actin filaments. Figure 2.1 shows an example fluorescent image of the three filaments. The three filaments play different mechanical and functional roles within the cell, discussed in the following sections.

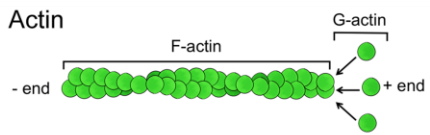
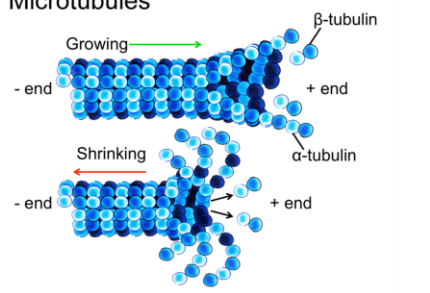
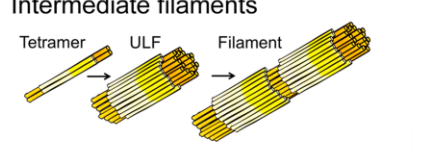
Filament Structure	Diameter	Persistence Length
A Actin 	~7 – 10 nm	3 – 17 μm
B Microtubules 	~25 nm	4 – 8 mm
C Intermediate filaments 	8 – 10 nm	200 nm – 1 μm

Figure 2.2 A simplified schematic of the structure of the three cytoskeletal filaments: actin filaments, microtubules and intermediate filaments. Image taken from [76] under the Creative Commons Attribution License.

Microfilaments

Microfilaments are also referred to as actin filaments of F-actin, they have a diameter of 7-10 nm, which is the smallest of the three cytoskeletal filaments in eukaryotic cells. Actin filaments are formed by polymerisation of actin monomers (G-actin which is ~42 kDa) which self-assembles into a double-helix structure with a pitch ~72 nm (the schematic of the structure

is shown by Figure 2.2a). Actin filaments have polarity, the two ends of a filament are labelled the barbed (or +) and pointed (or -) ends. The barbed end has preferential addition of G-actin and the pointed end preferential dissociation [77]. When the rate of polymerisation at the barbed end matches the rate of depolymerisation at the pointed end, the filaments are referred to as “treadmilling” with the appearance of moving forward.

The persistence length l_p is used to define the stiffness of cytoskeletal polymer filaments. If the filament has a length below the l_p it can be modelled as a flexible/elastic rod, whereas if the length is above the l_p it can only be modelled statistically as a 3D random walk. The persistence length of F-actin is $l_p = 3 - 17 \mu\text{m}$, which is more than for intermediate filaments (200 nm-1 μm) and less than for microtubules (4-8 mm) [78]. However, microfilaments form bundles and networks which help to regulate cell shape and give cells structural rigidity. Many types of actin binding cross-linkers facilitate the orientation and spacing of bundles and networks, mainly found at the cell periphery (Figure 2.1). Myosin motor proteins are ATP dependent and move along actin filaments, they are able to exert tension in the cell and transport intracellular vesicles. For instance, stress fibers are actin bundles with a highly regulated acto-myosin structure able to provide contractile forces for functions such as cell adhesion, motility and morphogenesis.

Actin microfilaments also form a cortex at the cell periphery, referred to as the cell cortex or actin cortex, which is ~100 nm thick [79]. The cortex consists of a network of microfilaments and myosin motors which are attached to the lipid membrane via membrane-anchoring proteins. This structure is mechanically rigid and provides cell shape, however the membrane fluidity results in rapid turnover of protein constituents so the cortex is also plastic in nature. Thus, the lipid membrane composition and microfilaments are coupled and changes to either can result in whole cell mechanical changes.

Microtubules

Microtubules have a diameter of 25 nm and their length can vary from 0.2 μm to 25 μm , they have the largest diameter of the three cytoskeletal filaments. These filaments consist of α and β tubulin dimers which polymerise end-to-end to form a helical filament structure, with a pitch of approximately 13 dimers [80]. Figure 2.2b shows a schematic of a microtubule where protofilaments self-assemble to form the cylindrical filament.

Figure 2.1b shows that microtubules radiate away from the cellular nucleus, this helps maintain cellular structure and provides transport mechanisms from the nucleus to the rest of the cell. An organelle called the centrosome is the primary microtubule organising centre, allowing the characteristic radial growth. Transport along the microtubules is facilitated

mainly by two motor proteins: kinesin and dynein [81]. Both motor proteins can only move along the filament in one direction. The direction is inherently controlled by filament polarity, the ends of each protofilament have either α or β subunits.

Microtubules are the stiffest of the three cytoskeletal filaments, with $l_p = 4 - 8 \text{ mm}$ [78]. However, they are still thought to be less important to whole cell mechanics compared to microfilaments. Microtubules are individually stiffer, but microfilaments can be highly cross-linked providing more mechanical rigidity.

Intermediate Filaments

Intermediate filaments have a diameter of 10-24 nm (“intermediate” in size compared to the other two cytoskeletal filaments). Microfilaments and microtubules consist of single types of proteins (G-actin and tubulin), whereas 70 different genes have been identified for coding various intermediate filament proteins. Six subcategories of intermediate filaments exist based on their amino acid sequence and protein structure. Their final structure consists of eight protofilaments arranged in a rope-like structure (Figure 2.2c). They are assembled to form antiparallel tetramers, resulting in them not having distinct plus and minus ends (unlike microfilaments and microtubules which are highly polar).

Intermediate filaments are less dynamic than microfilaments and microtubules and do not illustrate “treadmilling”, they are generally more stable and uninvolved in cell motility. However, phosphorylation regulates their assembly and disassembly. They have various roles within the cell including supporting the cell membrane and fixing organelles in place within the cytosol. Vimentin and keratin are examples of cytoplasmic intermediate filaments. Lamin is an example of a nuclear dwelling intermediate filament, a fibrous protein which provides the nucleus with structure and mechanical rigidity. These filaments are disassembled and reorganised during mitosis.

The persistence length of intermediate filaments in $l_p = 200 \text{ nm} - 1 \mu\text{m}$, the lowest of all the cytoskeletal filaments [78]. However, microfilaments and microtubules are more brittle and rupture under strains $\sim 10\%$ whereas intermediate filaments can withstand strains of $\sim 200\%$ [82]. This behaviour is attributed to the hierarchical structure of intermediate filaments that permits unfolding of subunits without rupturing the filament. Figure 2.1 shows that actin filaments are located at the cell periphery forming a cortex, which is mainly responsible for resisting stresses, the nature of the cortex allows cytoplasmic flow above a critical strain. Intermediate filaments maintain cell integrity in such cases by being sufficiently flexible to allow deformations without making the cytoskeleton too rigid or brittle, whilst still preventing excessive deformations [83].

2.1.4 The Nucleus

Most eukaryotic cells have a nucleus containing nearly all of the cells' genetic material, a small amount is contained in the mitochondria. The nucleus is the largest organelle and its mechanical properties can influence measurements of whole cell stiffness. The diameter of most mono-nucleated mammalian cells is 5-20 μm [84]. The nucleus is bound by two lipid bilayers, known as the nuclear envelope. The space between the layers is $\sim 20\text{-}40$ nm and known as the perinuclear space. The nuclear envelope isolates the contained genetic material from the cytoplasm and prevents passage of large molecules. Nuclear pores are embedded across both membranes and regulate transport of molecules across the envelope. The nuclear lamina is a fibrous network containing lamins (an intermediate filament) and membrane proteins, located on the inner surface of the inner nuclear membrane. An internal network provides the nucleus with mechanical support and helps to regulate DNA replication and mitosis. A looser external network forms outside of the nuclear envelope, providing additional support by binding to the cytoskeleton. The nuclear lamina is part of the nuclear matrix, which is the network within the nucleus which is comparable to the whole cell cytoskeleton.

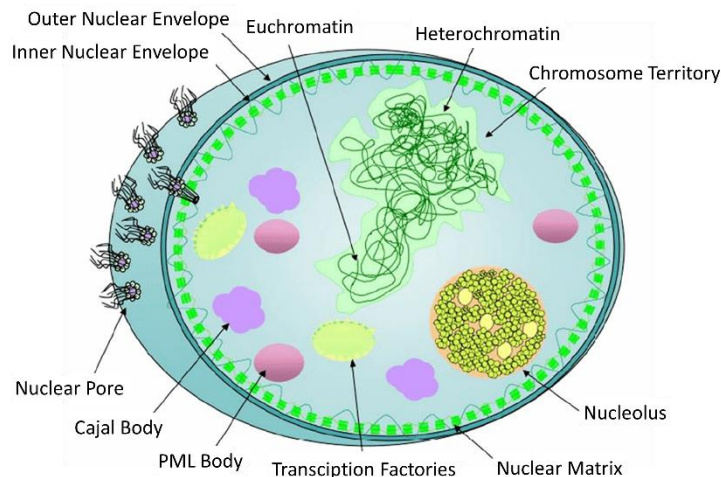


Figure 2.3 Schematic showing the main structure of the eukaryotic cell nucleus. Taken from [85].

Chromosomes are organised as DNA-protein complexes called chromatin. There are two types of chromatin: euchromatin which is less compact and contains frequently used genes, and heterochromatin which is denser and contains infrequently transcribed genes. Nuclear stiffness is known to be mostly dependent on the structure of nuclear lamins and chromatin. Many membraneless structures also reside within the nucleus, called nuclear bodies, the largest being the nucleolus which synthesises rRNA and assembles ribosomes.

The mechanical properties of cells is dominated by the nucleus during physiological deformations, such as cell migration and movement through narrow capillaries. The nuclear envelope, nuclear lamina and nuclear interior (consisting of chromatin, matrix and nuclear

bodies) all affect the stiffness. For example, during differentiation stem cells increase expression of proteins in the nuclear envelope and modify chromatin structure leading to increased stiffness [86]. Also, drugs such as Trichostatin A lead to decondensed chromatin which softens the nucleus [49], [87], [88]. The structure of the nucleus is also coupled to the cytoskeleton, loss of nuclear lamins has led to changes in cytoskeletal structure and reduced stiffness [89]. During interphase the nucleus can be 2-10 fold stiffer than the cytoplasmic areas of the cell, with measured elastic moduli between ~1-10 kPa (values vary due to cell type and experimental technique) [90], [91]. Under an applied stress, nuclear stiffness is mediated by the structure of lamins (generally closer to nuclear periphery) and the nuclear interior (chromatin structure and nuclear matrix). The nuclear lamina behaves like an active element whereas the nuclear interior a compressible viscoelastic material, also exhibiting strain-stiffening under compression [92].

The main techniques used to probe nuclear stiffness are atomic force microscopy (AFM), micropipette aspiration (MA) and microrheology [93], [94]. Both AFM and MA can be performed on isolated nuclei although the structure can be damaged during the initial isolation process. The techniques can also be performed on intact cells, however results can be skewed by the surrounding cytoplasm. Intact cells can also be used with a disrupted cytoskeleton to more accurately capture nuclear properties [92]. Tensile forces can transmit stress onto the nucleus via the cytoskeleton so this method loses that information. Comparatively, microrheology can be used to study local properties from within the nuclear interior. Active measurements involved inserting ~500-1000 nm magnetic beads into the nucleus, then applying a controlled force and inferring properties from the bead displacement. Downsides of this are that microinjection of these relatively large beads can disrupt the nuclear structure. Passive measurements use smaller beads (~100 nm) to compensate this, and measure the Brownian motion of the beads due to thermal fluctuations to infer stiffness. The smaller beads are less disruptive, however measurements are highly subject to local variations (i.e. a bead less embedded in the matrix will move more).

2.1.5 The Cell Cycle

The cell cycle is the process within a cell where DNA is replicated and the cell contents are divided onto two daughter cells. The cell cycle of eukaryotic cells has two basic parts called mitosis and interphase [95]. Mitosis is the process of nuclear division and eventual cell division (known as cytokinesis), interphase is the period between mitosis events where cell growth and DNA replication occur. A complete cell cycle is typically 24 hr (depending on cell type) and the mitosis phase ~1 hr, meaning dividing cells are in interphase 95% of the time. During interphase, cells grow at a steady rate and usually double in size between mitosis. DNA

synthesis occurs during one portion of interphase, meaning the cell cycle can be described by four distinct phases, summarised by the schematic in Figure 2.4a.

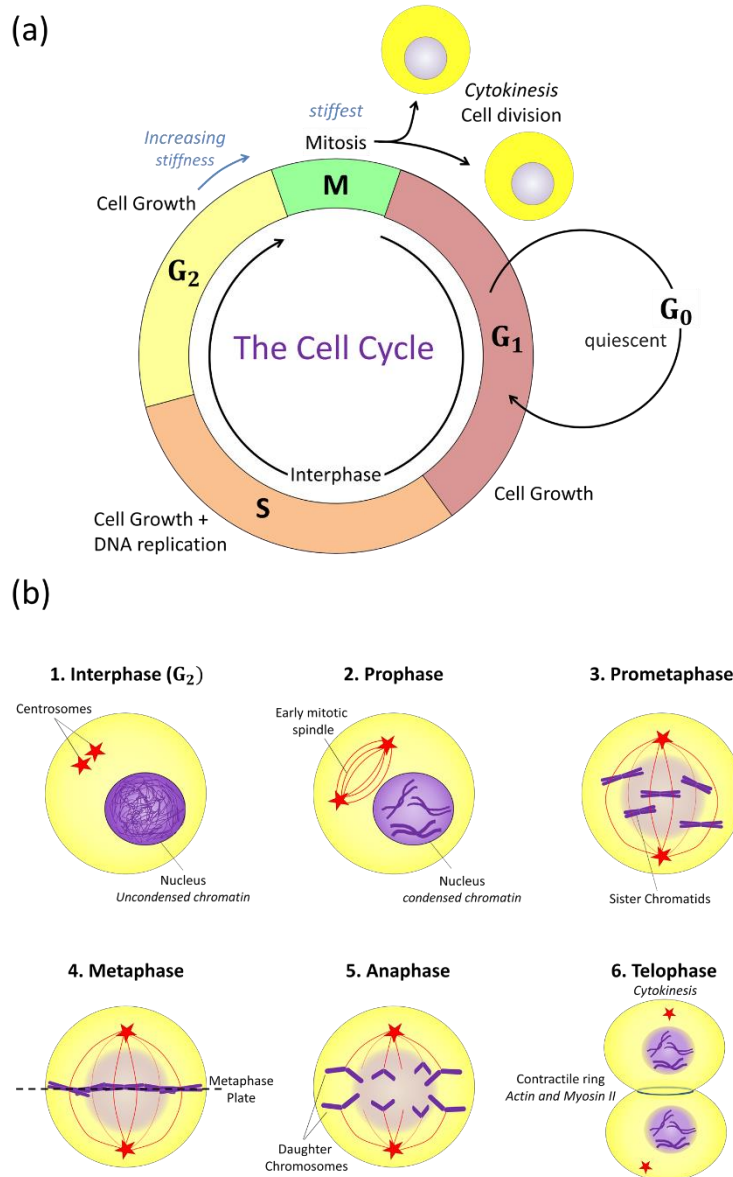


Figure 2.4 (a) A simplified schematic of the four main phases of the cell cycle. (b) A schematic of the subphases during mitosis which results in cell division (cytokinesis).

G₁ (gap 1) phase is the gap between cytokinesis (end of mitosis phase) and the beginning of DNA replication, however the cell remains metabolically active and growth occurs. Next is the S (synthesis) phase, this is when DNA replication occurs. The G₂ (gap 2) phase signals the completion of DNA synthesis, the cell continues to grow and proteins are synthesised in preparation for mitosis. G₁, S and G₂ occur during interphase and the time spent in each phase is cell dependent. The M phase (mitosis) is described by subphases, summarised by the schematic in Figure 2.4b. Immediately after interphase ends, the cell enters *prophase* and chromatic condenses into chromosomes. Next, in *prometaphase* the nuclear envelope breaks

down allowing microtubules to invade the nuclear space and form the mitotic spindle. The mitotic spindle is a cytoskeletal structure (composed mostly of microtubules and other proteins) which works to separate sister chromatids (identical copies of chromosomes). The cell then enters *metaphase*, the two centrosomes (located at opposite ends of the spindle) work to pull the chromosomes to opposite ends of the cell. The chromosomes align along the “metaphase plate” at the midline of the cell. *Anaphase* then results in the chromatids being cleaved and separated so that a copy of each chromosome is at opposite ends of the cell, *Telophase* then signals the nuclear membrane to reform into two nuclei within the cell. Finally, *cytokinesis* occurs via Myosin II and actin forming a ring which contracts to cleave the cell into two daughter cells.

Many adult eukaryotic cells cease division (e.g. nerve cells) or divide occasionally via signalling pathways when new cells are required to replace lost or damaged cells (e.g. skin fibroblasts). These cells exit the G_1 phase and enter the G_0 phase, which is a quiescent (dormant) stage where cells remain metabolically active but do not proliferate. The cell cycle is regulated by extracellular growth factors as opposed to availability of nutrients.

Figure 2.4 shows that the subcellular structure of cells is altered greatly throughout the cell cycle, particularly during mitosis. This results in changes in cell stiffness depending on cell cycle phase. Otto et al. 2015 chemically synthesised HL60 cells at the four phases and used microfluidic RT-DC to measure the cell deformability [96]. They found that cell size and deformability could distinguish the four phases, particularly cells in G_2 had increased deformability compared to M. Similar deformability's were found for M, G_1 and S, with M being the stiffest, however the cell size halves after mitosis (M-S) and then increases again (S \rightarrow G_1). Fluorescence-activated cell sorting (FACS) has traditionally been unable to separate G_2 and M as it relies on DNA stain, and both phases have the same total DNA content. Therefore, deformation cytometry shows promise as a label free method for studying the cell cycle.

Discussion of the cell cycle often focuses on structural changes in microtubules (mitotic spindle formation) and nucleus (condensing chromatin and nuclear division), however the actin structure also changes significantly. Actin has a key role in early mitosis, it initiates cell rounding by forming a cortex (adherent cells must become rounded in order to divide during cytokinesis) [97]. Also, Matze et al. 2001 used AFM to study the actin stiffness before and after formation of the cleavage furrow, the actin-Myosin II contractile ring which forms to cleave the cell during cytokinesis. They showed a significant increase of actin in this region during the onset of furrowing compared to interphase, with a 10-20 fold increase in stiffness during cytokinesis.

2.2 Cancer cell progression and mechanical changes

2.2.1 Cancer and Metastasis

The staple of a cancerous cell is uncontrolled continuous proliferation, whereas a normal cell has controlled proliferation. This continuous proliferation arises due to mutations in genes, however multiple specific mutations are required for a cell to become cancerous. Two basic types of mutation are required, firstly in systems which promote cell growth and secondly in safeguarding systems preventing unwanted cell growth. During mitosis DNA is replicated and mistakes naturally occur, causing mutations. However, the relative number of mistakes is extremely low and cells have safeguarding mechanisms to repair DNA. Usually, if cell DNA is irreparably damaged then cell death is triggered (apoptosis). Environmental factors (carcinogens) and genetic factors cause mutations. Hence, the likelihood of the multiple mutations required for cancer increases with age.

Once mutations occur in multiple genes associated with cell growth and multiple genes associated with safeguarding genes, which would usually induce apoptosis, a cancerous growth (primary tumour) will occur. Another requirement for tumour growth, is access to a blood supply. For a mass of cancer cells to continue growing, additional mutations must occur to promote the growth of new blood vessels or else the cells will starve (necrosis). Cancer next becomes metastatic when cells from the primary tumour are able to enter the blood stream or the lymphatic system. This leads to secondary cancerous growths in other regions of the body.

For metastases to occur, a cancerous cell must be able to break away from the primary tumour and move into a blood vessel or lymph node. This process is not well understood, theory suggests the cells may begin to produce an enzyme that destroys surrounding membranes and structures separating the tumour from the blood and lymph. Additionally, for cancerous cells to move to new locations their mechanical structure may change to increase their deformability. Therefore, cell deformability is a marker for cancer cell progression.

2.2.2 Colorectal Cancer

Colorectal cancer (CRC) is the third most common in the UK for both males and females, there are around 41,700 new cases each year in the UK [98], [99]. The five year survival rate for early stage diagnosis (where the primary tumour is contained within the bowel lining) is 93.2%, this drops drastically to 6.6% for late stage diagnosis when the tumour has metastasised to different parts of the body [100]. Therefore, improvements are needed for ensuring early stage diagnosis and also for treatment of advanced stages of CRC. This section will detail how a primary CRC tumour forms and eventually metastasises to a secondary location.

The interior of the colon is covered in “crypts”. The surface is covered by a single layer of epithelial cells that facilitates salt and water absorption. Epithelial stem cells reside at the bottom of the crypts, these cells proliferate in a controlled way and move toward the colon surface to replenish cells at the surface when they die. When mutations occur the epithelial cells may begin to proliferate continuously and form a mass called a polyp which protrudes into the interior of the colon. Most colon cancers originate from cells in polyps.

The majority of progressed colon cancers show examples of multiple mutations in genes associated with promotion of cell growth and safeguarding methods to prevent cell growth. The earliest mutations are found in both copies of the gene APC [101]. APC is responsible for a growth factor pathway, when both copies are mutated the APC proteins turn on growth factors even when no signalling occurs to signal proliferation being required. Cells in the epithelial lining begin to proliferate, forming a “nest” of pre-cancerous cells. Cells lacking APC protein also show many more mistakes being made during mitosis, therefore APC mutations lead to both growth advantage and an increase in subsequent genetic mutations.

However, APC mutation alone is not enough to lead to cancer metastasis due to additional safeguarding systems. In half of polyps a second mutation called KRAS was responsible for progression from cell nest to polyp [102]. This mutation can cause growth factor pathways to be permanently on. Mutations in two APC genes and one KRAS can form a polyp. A polyp is still termed pre-cancerous and further mutations are required for tumour progression and metastasis. At least 7 mutations are required for most colon epithelial cancers to progress to a metastatic stage [103]. Figure 2.5 shows a schematic outlining the genetic mutations which can result in a pre-cancerous polyp developing into an adenocarcinoma and then metastasising.

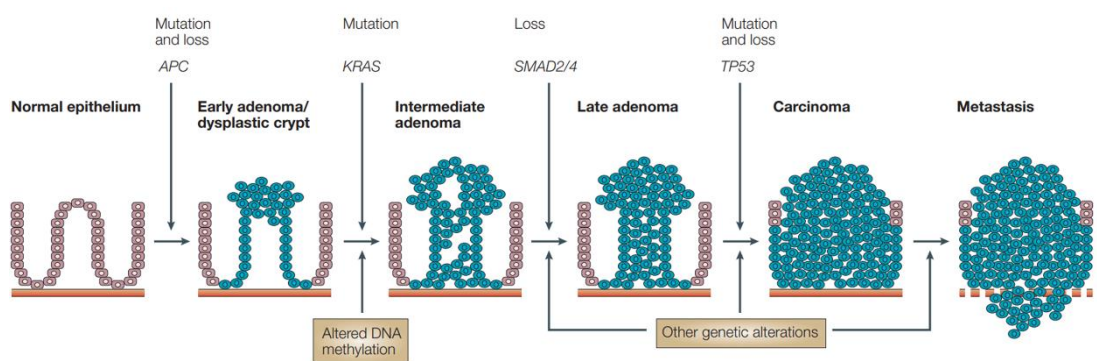


Figure 2.5 Schematic describing progression from normal epithelial crypts through to colorectal adenocarcinoma to metastasis, including common genetic mutations towards promotion of cell growth and loss of safeguarding methods which lead to CRC progression. Image taken from [104].

Colon cancer progression is described by the Dukes system, different stages are identified by accounting for: penetration depth of the cancer below the colon surface and whether the

tumour cells have entered the lymphatic system. Staging helps to determine what treatment is suitable i.e. surgical methods for polyp removal, chemotherapy and/or radiotherapy. The stages range from a polyp (Duke's stage A), to detectable metastasis stage (Duke's stage D).

The most common location for a secondary metastatic tumour is the liver. Chemotherapy and radiotherapy are widely used for treating advanced cancerous tumours, however the rapid mutations in cancer cells render some of them resistant to these treatments [105]. They do this by: blocking entry of a drug into the cell, enhancing systems that repair DNA damage and disabling enzymes required to activate the therapeutic drugs.

2.2.3 Model System

Three colorectal cancer cell lines, originating from different tumour stages, were chosen to study changes in cell deformability due to CRC progression. Traditionally, the Duke's staging system is used to classify CRC stages but the TNM cancer staging system is used more widely for all cancer types. TNM provides three numbers to classify the stage: T refers to the size of the primary tumour, N the number of nearby cancerous lymph nodes and M the amount of metastasis. SW480 cells derive from a primary adenocarcinoma corresponding to Duke's stage B, which is equivalent to T2-3 N0 M0. SW620 cells derive from a secondary tumour from the lymph node of the same patient (Duke's stage C and T2-4 N1 M0). The SW480 cells were isolated in 1976 from the colon of a 50 year old male, with the SW620 cells isolated from the secondary lymph node tumour a year later [106]–[108]. These two cell lines are an ideal model of progression as they derive from one patient, eliminating any metastasis variability due to variations between patients.

HT29 was the third CRC cell line studied, it is a Duke's stage C human colon adenocarcinoma (T2-3 N1 M0) from a 44 year old female isolated in 1964 [109]. This cell line represents an intermediate stage between primary SW480 cells and the secondary SW620 cells, so the three together are ideal for studying progression. Ahmed *et al.* 2015 has a comprehensive study of the genetics and epigenetics of CRC cell lines, including those of SW480, SW620 and HT29 [110]. Figure 2.6 shows a schematic outlining the Duke's stages of the CRC adenocarcinoma model system.

Several works report that the secondary SW620 cells have up-regulated genes associated with cytoskeletal changes, which accompanied increased motility, enhanced invasion potential, reduced adhesion and higher proliferation compared to the primary SW480 [111]–[115]. Tsikritis *et al.* 2015 [116] and Palmieri *et al.* 2015 [117] both used AFM to study the mechanical properties of SW480 and SW620. They found that the progressed SW620 cells were softer and insinuated this may be due to changes in the actin cytoskeleton. Gala de Pablo *et al.* 2018 used Raman spectroscopy to biochemically phenotype CRC cell lines, including

the three for the model system studied here [2]. They found a correlation with stage advancement and lower lipid content and higher lactate content. To the best of our knowledge microfluidic deformation assays have not been previously used to mechanically phenotype SW480, HT29 and SW620 cells.

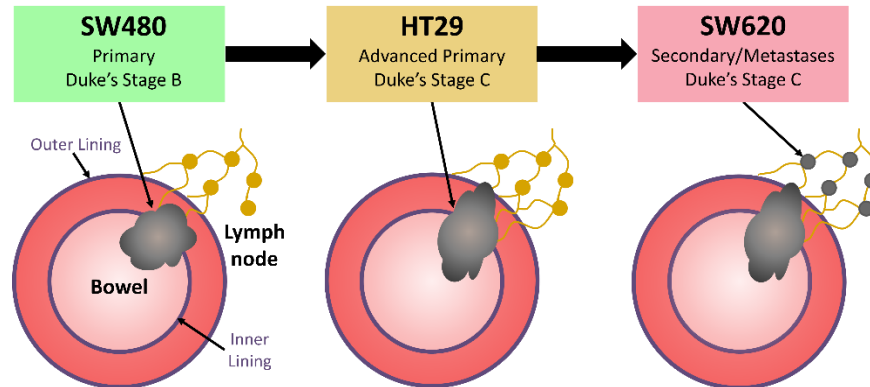


Figure 2.6 A schematic outlining the model system for CRC progression, which includes SW480, HT29 and SW260 cells.

2.2.4 Mechanical phenotype of malignant cells

A primary tumour is exposed to different types of mechanical interactions, including cell-cell and cell-ECM (extracellular matrix) interactions. The three types of mechanical stress include tensile stresses due to actomyosin contractility in response to the ECM stiffness, compressive forces due to rapid expansion caused by proliferation in a confined space, and shear stresses due to blood and interstitial flow. Mechanotransduction is the biochemical response of cells due to a mechanical stimulus. These same mechanical stimuli can elicit increased actomyosin contractility and ECM stiffening in transformed cancerous cells, which aids tumour progression [118], [119]. Further, the alteration of protein structures as cells become cancerous leads to changes in cell shape, stiffness and adhesion to the extracellular matrix. This results in enhanced motility of cancerous cells, which in turn allows them to escape the primary tumour and migrate to secondary sites. Generally, studies have shown a correlation between cell deformability and malignancy [7], [120], [121]. Specifically, changes to cytoskeletal structure have been noted in the Epithelial-to-Mesenchymal transition (EMT), associated with metastatic progression [122]. This transition involves cell phenotype changing from epithelial to mesenchymal and is known to facilitate metastasis by disrupting cell polarity, cell-cell adhesion and transforming well-organised cytoskeletal networks into fragmented arrangement. These changes aid migration and invasiveness of cells. Nuclear morphological changes have also been noted in cancer cells, including disrupted chromatin arrangements which may alter stiffness [123].

Guck *et al.* 2005 used a microfluidic optical stretcher to deform various breast cancer cell lines representative of different stages of metastatic progression: MCF10 (benign), MCF7 (primary adenocarcinoma) and modified MCF7 to increase invasiveness (metastasis) [36]. They found a correlation between increased deformability and disease progression, which they also related to an associated drop of ~30% in F-actin. Cross *et al.* 2007 used AFM to study metastatic cells from pleural fluids of patients with lung, breast and pancreas cancer [43]. They showed that metastatic cells are ~70% softer from different cancer origins. Metastatic cells had a common stiffness and their properties were less heterogeneous than benign cells. Xu *et al.* 2012 used AFM to study deformability as a function of ovarian cancer progression [124]. They showed that highly metastatic ovarian cells are softer (HEY A8) compared to the less invasive ovarian cancer cell (HEY), and further correlated metastatic potential to increased invasiveness. Gene expression analysis of the two cell lines indicates that stiffness reduction is related to changes in the actin cytoskeleton, a correlation was found between F-actin coalignment and Young's modulus with softer cells showing less organised F-actin arrangements. Additionally, Lekka *et al.* 1999 found decreased stiffness in cancerous bladder cells using AFM and suggested cytoskeletal reorganisation due to oncogenic transformation as the cause for this. It should be noted that these techniques (AFM and optical stretching) are low strain and mostly sensitive to cytoskeletal properties, other mechanical changes in the nucleus likely play a key role in cancer progression [118]. As the largest and stiffest organelle, a compliant nucleus coupled with contractile forces enables cells to squeeze through the vasculature to aid metastatic progression.

More recent studies have shown that correlation between metastatic progression and deformability may be dependent on cancer type. Ahmmed *et al.* 2018 used a microfluidic channel to deform cells under shear stress, and studied deformability changes of breast and prostate cancer cell lines at different stages of disease progression [44]. They found that strongly metastatic breast cancer cells had increased deformability, similar to the results by Guck *et al.* 2005 [36]. However, they found that prostate cells showed decreased stiffness with metastatic potential. Nguyen *et al.* 2016 studied the mechanical properties and invasiveness of pancreatic cancer cell lines using deformability cytometry, AFM and parallel microfiltration [45]. They showed that metastatic potential correlated with passive deformations using microfiltration, which is representative of invasiveness. However, AFM showed increased Young's modulus with metastatic potential. Cell transit time through a microfluidic constriction channel was weakly correlated to invasiveness. The use of AFM and microfluidics to deform cells in both adhered and suspended states shows how morphology can affect mechanical response. RNA sequencing was also performed and showed that Lamin A is strongly associated with the decrease in Young's modulus and increased invasiveness

compared to F-actin. Zhan *et al.* 2013 used a microfluidic constriction channel to study benign and cancerous brain cells [47]. They found that the cell types were indistinguishable using cell elongation, transit speed. They also measured the associated pressure drop due to passage of cells through the microchannel. Entry time into the microchannel was more sensitive than pressure drop when distinguishing the cell types. The cancerous cells took longer to squeeze into the constriction suggesting that cancerous cells have increased stiffness.

The general consensus suggests that cancerous cells tend to become softer to aid migration and invasiveness, however this may depend on cancer type. Mechanical properties have been shown to successfully distinguish cells based on disease state. However, different techniques and measured properties can be more/less sensitive to these changes, which shows that multiple parameter analysis offer a wider understanding of disease induced changes to mechanophenotype.

2.3 Biomechanics of Cells

Cells display viscoelastic response to an applied stress when probed using multiple techniques ranging across forces ($10^{-14} - 10^{-6} N$) and length scales ($\sim 10^{-10} - 10^{-4} m$) [125]. Many models exist which try to encompass the complex behaviour of cells and extract fundamental parameters. The elastic modulus is often used, which is a measure of the cells resistance to elastic deformation due to an applied stress (with units of Pa). However, reported values for the elastic moduli for the same cell type can vary by an order of magnitude depending on model and technique used. This section of the thesis gives an overview of the complexity of cell viscoelasticity, the main models used in cell mechanics and the model that was adapted toward the original work in this thesis.

2.3.1 Viscoelasticity

A viscoelastic material exhibits behaviour somewhere between an ideal solid and an ideal liquid. A purely elastic material does not dissipate energy when a stress is applied and removed. However, materials have a characteristic “yield stress”. Below the yield stress the deformation is termed reversible and once the stress is removed the material returns to its original shape (elastic deformation). Above the yield stress, the material undergoes a permanent deformation known as plastic deformation which results in energy loss. A viscoelastic material also loses energy when a stress is applied.

An ideal solid is modelled as a linear spring described by Hooke’s law (equation 2.1). The strain ϵ (amount that the spring stretches from equilibrium) is linearly proportional to the applied stress σ , where E is the elastic modulus which characterises the spring’s stiffness. Purely elastic materials are time independent, when stress is applied the strain is immediate and when the stress is removed, they immediately recover their original shape. Comparatively,

an ideal liquid is modelled by a dashpot where a plunger moves through a viscous Newtonian fluid. Equation 2.2 describes this behaviour, where the applied stress σ is proportional to strain rate $\dot{\epsilon}$ with a constant of proportionality η , which is the fluid viscosity. The material deforms at a constant rate until stress is removed, i.e. the material “flows”. The energy required to deform the material is dissipated and the strain is permanent (time dependent).

$$\sigma(t) = E\epsilon(t) \quad 2.1$$

$$\sigma(t) = \eta\dot{\epsilon}(t) \quad 2.2$$

For a material to be deemed viscoelastic it must have three properties: hysteresis in its stress-strain curve, exhibit stress relaxation and exhibit creep behaviour. Unlike an elastic material, a viscoelastic stress-strain curve will show hysteresis with the area of the loop equal to the energy loss during the loading-unloading cycle (Figure 2.7). This is due to it taking more energy to displace the material from equilibrium than to return it to its original shape, the energy consumed during loading is due to heat dissipation or molecular rearrangement. Stress relaxation is the reduction of stress as a function of time in a material which is undergoing a constant strain. Contrasting this, creep behaviour is the tendency of a material to continue deforming when a continuous stress is applied, the strain increases until the material reaches an equilibrium and the strain is constant.

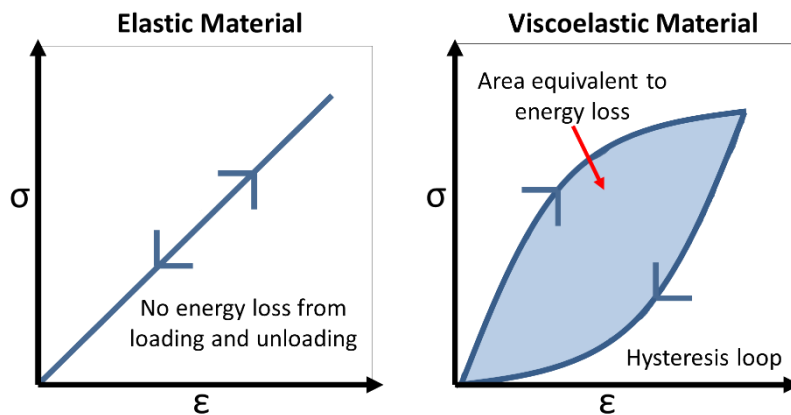


Figure 2.7 Graphical schematic of the stress-strain loading and unloading curves of an elastic vs a viscoelastic material. Where a viscoelastic material shows hysteresis where the area of the loop is equivalent to energy loss.

These characteristic viscoelastic behaviours can be modelled by arrangement of spring and dashpots as equivalent circuits [126]. Here, stress is equivalent to voltage and strain rate is equivalent to current. The elastic modulus of the spring corresponds to the capacitance as it stores energy, and the viscosity of the dashpot corresponds to the resistance because it dissipates energy. The next section discussed the different circuit arrangements and their ability to model creep and stress relaxation.

2.3.2 Linear-Spring and Dashpot models

Viscoelastic materials can be modelled by a circuit arrangement of linear springs and dashpots, and are often used to model cell mechanics [127]–[136]. The two simplest arrangements are the Maxwell model and the Kelvin-Voigt model. The Maxwell model consists of spring and dashpot arranged in series (Figure 2.8ai), governed by equation 2.3. Where $\sigma(t)$ is the applied stress, $\varepsilon(t)$ is the strain, E is the elastic modulus associated with the linear spring and η is the viscosity associated with the dashpot. If a material is subjected to an instantaneous force σ_0 , the solution of equation 2.3 is shown by equation 2.4. There is an instantaneous elastic deformation governed by E , and viscous flow deforming at constant rate governed by η (Figure 2.8aaii). When the force is removed at time t , the elastic deformation recovers instantly whereas the deformation of the viscous element is permanent. The Maxwell model can predict stress relaxation (Figure 2.8aiii) but not creep behaviour, this model is often used to model viscoelastic liquids.

The Kelvin-Voigt model consists of a spring and dashpot arranged in parallel (Figure 2.8bi), governed by equation 2.5. If an instantaneous force is applied (σ_0) the solution to equation 2.5 is shown by equation 2.6. Here, the strain response develops over time as the dashpot retards the response of the spring. The system initially behaves like a viscous liquid, over longer timescales the behaviour becomes more elastic as the spring stretches. Under constant stress the system tends towards the deformation of a purely elastic material, i.e. $\varepsilon(\infty) = \frac{\sigma_0}{E}$, characteristic creep behaviour (Figure 2.8bii). When the material is freed at time t , the spring retards the material back to its original shape with no deformation. The Kelvin-Voigt model successfully predicts creep behaviour, lending itself as a suitable model for viscoelastic solids, but not stress relaxation (Figure 2.8biii). It has been used to model the behaviour of cells [137], [138], however resolution was limited in early experiments and since then more complex systems have since shown to better fit cell response [129]–[132], [139], [140].

$$\sigma(t) = \eta \left(\frac{d\varepsilon(t)}{dt} - \frac{1}{E} \frac{d\sigma(t)}{dt} \right) \quad 2.3$$

$$\varepsilon(t) = \frac{\sigma_0}{E} + t \frac{\sigma_0}{\eta} \quad 2.4$$

$$\sigma(t) = E\varepsilon(t) + \eta \frac{d\varepsilon(t)}{dt} \quad 2.5$$

$$\varepsilon(t) = \frac{\sigma_0}{E} \left(1 - e^{-\frac{Et}{\eta}} \right) \quad 2.6$$

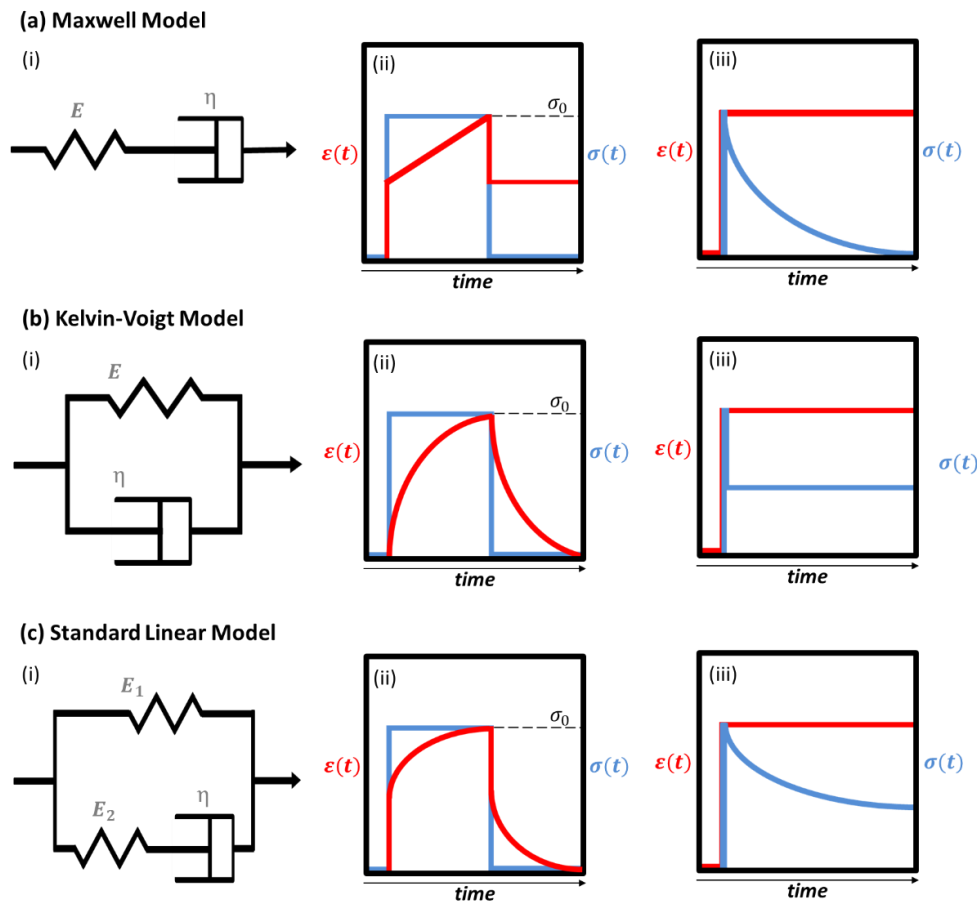


Figure 2.8. Schematic describing the three simplest spring-dashpot models and their responses over time to a step-wise applied stress σ and strain ϵ : (a) Maxwell Model consisting of a spring and dashpot in series (b) Kelvin-Voigt Model consisting of a spring and dashpot in parallel and (c) Standard Linear Model consisting of a Maxwell body in parallel with another spring.

Two principal phenomena seen in viscoelastic materials are creep/recovery and stress relaxation. The Maxwell model predicts stress relaxation but not creep behaviour, and vice versa the Kelvin-Voigt model predicts creep behaviour but not stress relaxation. The simplest spring-dashpot circuit model to predict both phenomena is the Standard Linear Solid (SLS) Model [134], consisting of a Maxwell body in parallel with a second spring Figure 2.8ci (modelled by equation 2.7). Figure 2.8cii shows the creep behaviour of this system which combines the responses of the Maxwell and Kelvin-Voigt Models. When an instantaneous stress (σ_0) is applied there is an instantaneous elastic deformation similar to a Maxwell body and due to the stretching of spring with E_2 , followed by a response similar to the Kelvin-Voigt model where the dashpot (η) retards the stretching of the second spring E_1 . Similarly, when the stress is removed instantaneously there is an associated instantaneous decrease in strain followed by a slower recovery. Figure 2.8ciii shows stress relaxation of the system under a constant strain, the system relaxes gradually but not completely and a permanent (plastic)

deformation remains. Overall, this model can accurately predict the shape of curves for many viscoelastic biological materials under instantaneous loading and long timescales [134]–[136].

$$\frac{d\varepsilon(t)}{dt} = \frac{\frac{E_2}{\eta} \left(\frac{d\sigma(t)}{dt} + \sigma(t) - E_1\varepsilon(t) \right)}{E_1 + E_2} \quad 2.7$$

Heterogeneous materials such as cells can have multiple associated relaxations, which are not predicted by the SLS model. A commonly used model which can predict creep behaviour, stress relaxation and multiexponent decays is the Generalised Maxwell model (GMM) [128], [133], [136], [141], [142]. GMM is an expansion of the SLS model and consists of N number of Maxwell bodies in parallel with an additional linear spring, also in parallel. The model accounts for the fact different subcellular components have different mechanical properties with varying relaxation times, more Maxwell body elements can be added to represent more complex distributions. However, as additional elements are added to spring-dashpot circuits they become less useful for extracting numerical values corresponding to real life parameters. Therefore, depending on experimental technique some still prefer to use the simpler Maxwell and Kelvin-Voigt models. For example, AFM used to perform stress relaxation measurements shows good agreement with Maxwell models and GMM [134], [136], [141], [142]. Whereas, techniques where the timescale of applied force is much less than the cell relaxation time show that Kelvin-Voigt is a suitable model [129]–[132], [134]. A simplified GMM model called the Zener mode, consisting two Maxwell body's in parallel with a linear spring, also shows good agreement with stress relaxation AFM measurements [128].

Bausch *et al.* 1998 used magnetic twisting microrheometry to apply 1 s pulses of force (500–2500) pN to cells, and a model consisting of the SLS Body in series with a dashpot was found to fit their experimental data [127]. This model shows a three phase response to an instantaneous force: an initial elastic response, a relaxation regime and viscous flow. This behaviour suggests at least two components of the cell exhibit an elastic response and at least two a viscous response. Once again, a downfall of this model is that it tells us nothing about which components of the cell are responsible for these responses. This model has a large number of parameters which are impossible to equate to real cellular components which makes the model ambiguous [126].

Overall, circuit arrangements of linear springs and viscous dashpots have been used to model the mechanical response of cells across a wide range of techniques. More simplistic models are more useful for extraction of viscoelastic parameters; however they do not account for cell heterogeneity and multiple relaxation times. More complex models have shown to accurately fit data; however the large number of fitting parameters offer no insight into the specific

mechanical responses of different subcellular components. Other mechanical models, discussed in the next section, have been developed to compensate these issues.

2.3.3 Overview of Models of Cell Mechanics

Early cell mechanics experiments had limited resolution and simple spring-dashpot models were sufficient to model viscoelastic creep and stress relaxation. As a wider range of timescales and frequencies were probed at improved resolutions, additional spring-dashpot elements were required to sufficiently fit data. The increasing number of model fit parameters made their mechanistic meaning ambiguous. The exponential relaxation behaviour modelled by linear viscoelasticity was previously favoured over power-law stress relaxation because it was seen as more intuitive [143]. However, a weak power-law dependence has now been found for a large number of cell types, using different experimental techniques and timescales [137], [144]–[146]. Cell rheology is typically characterised by sinusoidal deformations at a given frequency (ω), using the frequency-dependent complex shear modulus $G^*(\omega)$. The complex shear modulus of cells can be described using equation 2.8, validated across many studies [145]. Where $G'(\omega)$ is the storage modulus, $G''(\omega)$ is the loss modulus and β is the power law exponent.

$$\begin{aligned} G'(\omega) &= A \cos\left(\frac{\pi\beta}{2}\right) \omega^\beta + B \cos\left(\frac{3\pi}{8}\right) \omega^{3/4} \\ G''(\omega) &= A \sin\left(\frac{\pi\beta}{2}\right) \omega^\beta + B \sin\left(\frac{3\pi}{8}\right) \omega^{3/4} \\ |G^*(\omega)|^2 &= G'(\omega)^2 + G''(\omega)^2 \end{aligned} \quad 2.8$$

Equation 2.9 describes power-law behaviour from a creep experiment where a constant force F is applied to a material at $t = 0$, the material deformation over time is recorded where $J(t) = d(t)/F$ is known as the creep function. The power law exponent β describes the viscoelastic behaviour of the material. For a given system such as a cell type, j_0 and τ_0 are constants. The constant j_0 characterises the materials compliance, and τ_0 is an arbitrary timescale which does not affect β . This makes the behaviour timescale invariant. Power-law rheology manages to display cell responses to force with just one parameter. As β tends to 0, equation 2.9 reduces to Hooke's law (equation 2.1) and the material behaves elastically. As β tends to 1 equation 2.9 reduced to equation 2.2 and the material behaves as a viscous liquid. For cells, β commonly ranges between 0.1 and 0.5 and is stress dependent [143].

$$J(t) = \frac{d(t)}{F} = j_0 \left(\frac{t}{\tau_0}\right)^\beta \quad 2.9$$

The downfall of this is that cell behaviour is highly non-linear and power-law rheology offers no insight into characteristic timescales associated with cell relaxation. The dynamic

behaviour of the cytoskeleton makes cells inherently different from non-living material. Various cell types both stiffen and fluidize when undergoing an applied stress, known as the stiffening-softening paradox in cell mechanics [147]. Currently no model combines this stress-dependant cell response and weak power-law rheology, and no synthetic materials exhibit both of these behaviours. Thus, mechanistic values such as elastic modulus vary between experimental techniques making it difficult to compare between studies.

Several conceptual models have been suggested to explain the unique mechanical behaviour of cells. The “Sol-gel” model treats the cell like a gel, where polymer filaments pervade a fluid cytosol [148]. The filament lengths and amount of cross-linking proteins determines whether the response to stress is fluid-like (Sol-state) or solid-like (gel-state). More recently, data suggests that the cytoskeleton is better modelled as a glassy material. The Soft-glassy rheology (SGR) model describes a material existing close to a glass transition where disorder and metastability govern the mechanical response. This theory does well to explain the weak power-law behaviour of cells but does not explain the phenomenon of stress-induced stiffening [149]. The tensegrity model operates under the assumption that cell stiffness is proportional to intracellular stresses [150]. The cell is a prestressed structure with evidence suggesting that actin filaments are responsible for tensional forces and microtubules for compressional forces. This theory links the active and dynamic nature of a cell with its mechanical response, however it does not predict power-law rheology [151].

Linear-Viscoelasticity, Tensegrity and SGR are examples of “top-down” approaches, where the main principles are valid independently of microscopic substructure. “Bottom-up” models can be used instead which explain bulk properties of a system from its individual constituents. One examples is the Glassy Worm-Like (GWLC) chain model, which combines the worm-like (WLC) chain model from polymer physics with the SGR model. WLC describes polymer segments (in this case cytoskeletal filaments) as semi-flexible rods with successive segments pointing in roughly the same direction. Stretching of curved individual filaments reduced the number of available conformations, reducing entropy and generating prestress. SGR is combined with WLC by adding “sticky” interactions between filaments, retarding filament relaxation. GWLC can explain weak power-law behaviour and stress stiffening. However, “bottom-up” descriptions do not offer a quantitative cell shear modulus because the mesh size and filament length of cytoskeletal filaments are highly variable.

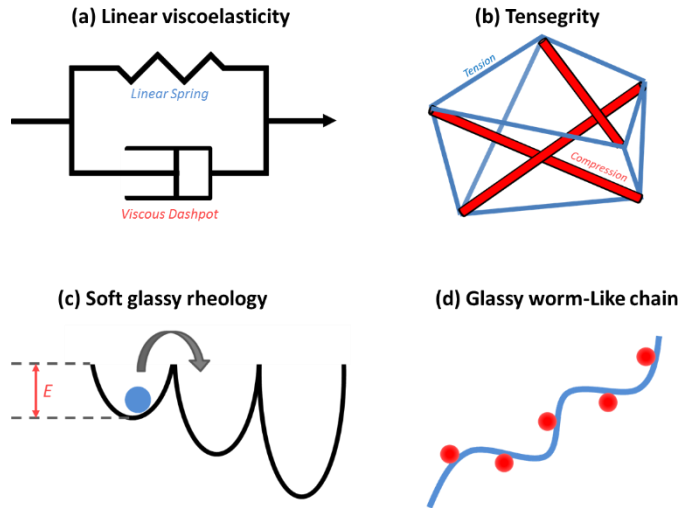


Figure 2.9 Simplified schematics showing some of the main conceptual models of cell mechanics.

None of these models account for dilatational (volume) changes in the cytoplasm. Living cells are constantly undergoing biochemical processes to remodel their internal structure. They can change their shape and volume without an external force. Examples include cell oscillations, blebbing and cell movement [152]. To have a complete understanding of cell rheology, shear and dilatational effects should be accounted for. Moeendarbary *et al.* 2013 introduced the poroelastic model of the cell cytoplasm, where a porous elastic solid meshwork (the cytoskeleton, organelles and macromolecules) is immersed in the fluid cytosol. The rate of deformation is governed by the rate at which the cytosol can pass through the holes in the porous meshwork [153]. Using AFM they found force-relaxation to be poroelastic at short timescales. Poroelastic behaviour can be characterised by the diffusion constant D_p . This is shown in Equation 2.10 where E is the elastic modulus, ζ is the pore radius, and μ is the cytosol viscosity. Equation 2.11 shows the timescale t_p for water movement through the pores, where L is a length scale associated with the amount of indentation. If the force application time t_r is shorter than the timescale for water movement ($t_r \ll t_p$) then poroelastic relaxation dominates. For longer timescales ($t_r \geq t_p$) power-law models were applicable.

$$D_p = \frac{E\zeta^2}{\mu} \quad 2.10$$

$$t_p \sim \frac{L^2}{D_p} \quad 2.11$$

Overall, the mechanical response of a cell is dependent on; the magnitude of the load, technique of application and the timescale. Different theories capture different aspects of cell mechanical behaviour and produce scaling laws which fit well to experimental data. A universal model does not currently exist and a complete understanding of the physical mechanisms behind these scaling laws is still to be determined.

2.3.4 Kelvin-Voigt Model

The Kelvin-Voigt model was introduced in section 2.3.2 as a simple model for a viscoelastic solid, and has been used widely in the field of cell mechanics. This model was used as it is applicable to measurements of whole-cell deformations and known to fit viscoelastic solid behaviour well. Equation 2.6 shows the solution to the differential equation 2.5 when an instantaneous step force is used. The work in this thesis used a cross-slot microfluidic device to deform cells at the SP of an extensional flow. Here, the force is not applied in a step-like fashion and is instead ramped from 0 to a maximum value occurring at the SP. In a shear dominant flow regime velocity scales linearly with force (equation 2.24). Calculation of the flow profile in the cross-slot device was used to characterise how the stress on a cell deforming at the SP varies with time.

The velocity profile in a shear-dominant regime was simulated using the finite element software COMSOL Multiphysics, with the fluid properties $\mu = 33 \text{ cP}$ and $\rho = 1005 \text{ kg/m}^3$. The simulation was 3D and the geometry mimicked the cross-slot geometry used experimentally, the channel widths were $35 \mu\text{m}$ and channel height was $25 \mu\text{m}$. A single-phase laminar flow model was used with the initial condition of incompressible fluid behaviour. The boundary conditions were inlet laminar inflow at a flow rate of $5 \mu\text{l/min}$, and at the outlet pressure of 0. An “extremely fine mesh” was used when running the simulation. Figure 2.10 shows the variation of flow velocity for an ideal cell deformation event, following a central path through the inlet/outlet and travelling through the SP. The position $(-40-0) \mu\text{m}$ is the inlet, position 0 is the stagnation point and $(0-40) \mu\text{m}$ is the outlet.

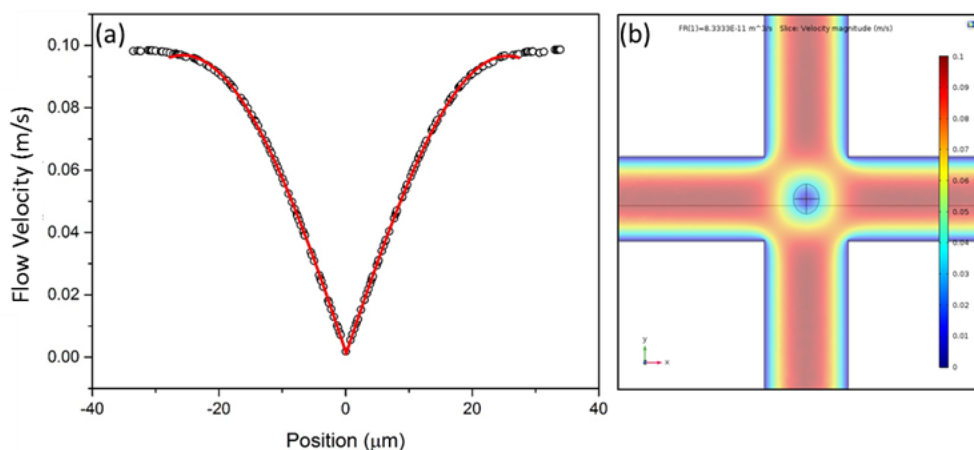


Figure 2.10: (a) Cross-slot velocity profile found using COMSOL where position 0 is the stagnation point of the cross-flow. The volumetric flow rate used was $5 \mu\text{l/min}$. (b) A velocity magnitude image generated by COMSOL.

The velocity profile shows an initial linear velocity in the inlet corresponding to the volumetric flow rate ($5 \mu\text{l/min}$) which ramps down to 0 at the SP, and then ramps up at the same rate. A

sine function is fitted to the velocity profile, shown in red ($R^2 = 0.99$). This suggests that $\sigma(t)$ varies approximately as a *sine* function, for a period T (where $\omega = \frac{2\pi}{T}$). Equation 2.12 shows the sine-varying stress $\sigma(t)$ as a function of time which is used to solve equation 2.5. The analytical solution is shown by equation 2.13. Here σ_0 is the peak value of the sine wave corresponding to the SP position, which was found by calculating the pressure drag and shear stress on a cell at the SP (described in section 2.5.2).

$$\sigma(t) = \sigma_0(1 + \sin(\omega t)) \quad 2.12$$

$$\varepsilon(t) = \frac{\sigma_0}{(\eta^2 \omega^2 + E^2)E} \left((\eta^2 \omega^2 - E\eta\omega + E^2)e^{-\frac{Et}{\eta}} - E\eta\omega \cos(\omega t) + \omega^2 \eta^2 + E^2 \sin(\omega t) + E^2 \right) \quad 2.13$$

This model is used throughout the thesis to fit data for cell deformation dynamics and extract an elastic modulus for various cell types. The addition of multiple spring and dashpot elements was considered, however the simpler Kelvin-Voigt fit well to experimental data. Multiple elements also produce more fitting parameters which cannot be correlated to specific responses, whereas Kelvin-Voigt produces an elastic modulus which can be easily compared to other studies.

2.3.5 Cell Plasticity

After a cell is deformed due to mechanical stress, the cell shape recovers. Studies have shown that this recovery is not always to the original undeformed shape, some cells do not recovery fully and show an apparent “permanent deformation”. Cells show viscoelastic behaviour, an elastic deformation would result in complete recovery (i.e. linear spring) whereas a viscous deformation would result in no recovery after stress removal (i.e. dashpot). However, “plastic” deformations can occur due to bond ruptures occurring within the cytoskeleton resulting in incomplete recovery, referred to as cell plasticity. The majority of cell mechanics research focuses on cell deformation due to an applied stress, with less focus on the cell-shape recovery once stress is removed [154]. However, incomplete shape recovery is an adaptive cell property as it reduces mechanical stress during cyclic deformations which can protect the cell from mechanical damage [155].

Bonakdar *et al.* 2016 used a multidirectional magnetic tweezer device to investigate the reversibility of deformation in cells, and found cells did not recover their initial shape [155]. Additionally, they used cyclic loading and showed that the magnitude of incomplete recovery increased with each cycle of force application and followed weak power law behaviour. They discussed that under cyclic loading tensed fibers become permanently stretched and compressed fibers buckle, leading to incomplete recovery. Pajerowski *et al.* 2007 studied the

developmental “plasticity” of the nuclei human embryonic stem cells compared to differentiated cells [86]. Developmental “plasticity” refers to the ability of cells to modulate their gene expression, but evidence of physical plasticity was seen in the undifferentiated stem cells. Micropipette aspiration showed that stem cells were ~6 fold softer than differentiated cells, and also did not recover their original shape after being deformed. Undifferentiated cells showed negligible traces of Lamin A/C and also decondensed chromatin. Fluidisation of chromatin and lack of Lamin A/C was attributed to the plasticity of stem cells.

Ho *et al.* 2018 devised a microfluidic device to impart cyclic deformations on cells, to test whether compression loading and unloading lead to plastic deformations [156] (as opposed to tensile or shear). They found no plasticity in MCF10A cells after 0.5 Hz cyclic compression for 6 min. These results show that plastic deformations are dependent on loading frequency, initial stress, experimental technique and could also be a property of specific cell type.

2.4 Microfluidics Background

Microfluidics is defined as the manipulation of fluid flows on the microscale. This scale offers many advantages due to the precise-control over the fluid compared to macroscopic scales due to the presence of laminar flow. This technology, known as lab-on-a-chip [157], utilises a device made of small channels typically etched into glass or a polymer. Microfluidic device fabrication is discussed in section 3.1.

The main advantages of microfluidics are the low volumes required, reducing the amount of reagents needed and thus the production cost. The scaled down systems also readily allow automation, device multiplexing, and high-throughput measurements. This section will give an overview of the governing equations which determine the nature of flow in microfluidic devices, and its interaction with suspended particles.

2.4.1 Navier-Stokes equation

The Navier-Stokes equation govern the motion of viscous fluid substances. An application of the equations is to model fluid flow in a pipe, including predicting flow behaviour in microfluidic devices. Equation 2.14 denotes the Navier-Stokes equation in the case of an incompressible and Newtonian fluid [158]. Where v is the fluid velocity, μ is the fluid viscosity, ρ is the fluid density and p is the fluid pressure. The different terms correspond to different force contributions, a is the inertial forces due to fluid acceleration. Term b is the pressure term representing the external pressure applied to the fluid, where fluid flows in the direction of the largest pressure change. Term c is the viscous forces, increasing viscosity acts to diffuse momentum. Finally, term d represents any external forces such as gravitational or electromagnetic.

$$\underbrace{\rho \left(\frac{\partial v}{\partial t} + v \cdot \nabla v \right)}_a = \underbrace{-\nabla p}_b + \underbrace{\mu \nabla^2 v}_c + \underbrace{F}_d \quad 2.14$$

$$\frac{\partial \rho}{\partial t} + \nabla \cdot (\rho v) = 0 \quad 2.15$$

Here, the Navier-Stokes equation represents the conservation of momentum. It is solved together with the continuity equation 2.15 which represents the conservation of mass. Under the assumption of fluid incompressibility, fluid density is assumed to be constant. Therefore, equation 2.15 reduces to $\nabla \cdot v = 0$. The Navier-Stokes equation can be simplified for certain flow regimes, whereas for others additional equations may be required. Flow regime can be characterised by various nondimensional numbers including the Reynolds number.

2.4.2 Reynolds number

The behaviour of fluid flows can be characterised by the Reynolds Number (Re) shown by equation 2.16 [159]. Re is the ratio of inertial to viscous forces, quantifying the relative importance of each force for given flow conditions. The hydraulic diameter D_H is dependent on the cross-sectional geometry of the channel the fluid flows through, the equation for a rectangular channel is given by equation 2.17 [160]. Where A is the cross-sectional area of the channel, P is the perimeter of the channel, w is the channel width and h is the channel height.

$$Re = \frac{\text{inertial forces}}{\text{viscous forces}} = \frac{\rho v D_H}{\mu} \quad 2.16$$

$$D_H = \frac{4A}{P} = \frac{2wh}{w+h} \quad 2.17$$

At low Re viscous forces dominate which is known as laminar flow, where fluid follows smooth continuous streamlines and particle velocity is not a random function of time [161]. As Re increases inertial forces begin to dominate and flow transitions from laminar to where the flow is chaotic and instabilities such as eddy currents and vortices will occur, making it impossible to predict the position of a particle in flow as a function of time [162]. This transition occurs at a critical Reynolds number. For flow in a pipe a critical value of $Re = 2300$ is often quoted in the literature, where flows with $Re < 2300$ remain laminar even with system disturbances such as surface roughness, vibration and heat transfer. The critical value changes for different geometries such as square or rectangular channels. Thus, the “transitional flow” regime between wholly laminar and turbulent flows is often quoted as occurring between $2300 < Re < 4000$ [163].

Equation 2.16 shows that a low Re requires a combination of low velocities, high viscosities and small length scales. Hence, microfluidic systems almost always operate in the laminar flow regime due to the microscale dimensions of the channels (usually 10’s of micrometres). In many cases, microfluidics achieves $Re \ll 1$, known as Stokes or creeping flow, where inertial effects are considered negligible [159]. Here, the inertial term can be removed from the Navier-Stokes (equation 2.14), and assuming no external forces, the equation simplifies to $\mu \nabla^2 v - \nabla p = 0$. The problem then becomes linear and time-independent, and the associated flow fields can be solved. Comparatively, at higher Re the inertial term cannot be ignored and the flow field calculation becomes more challenging due to non-linearity and time dependence. An intermediate regime exists ($\sim 1 < Re < \sim 100$) where inertia still has a notable effect and can be used to manipulate particle positions in flow [164]–[166].

Microfluidic systems often involve fluid flow with suspended particles, which are subject to additional drag and lift forces. Two variations of Reynolds number can be used to describe the

flow of particles through a channel. The channel Reynolds number R_c (equation 2.18) describes the unperturbed flow through the channel and is related to the Reynolds number by $Re = \frac{2}{3}R_c$, whereas the particle Reynolds number R_p (equation 2.19) has an additional dependence on the size of particle within the channel [167]. Where v_{max} is the maximal fluid velocity and a is the particle size. Particle flow is dominated by viscous forces at low particle Reynolds number ($R_p \ll 1$). Here, particles travel at the local fluid velocity due to viscous drag. Under these conditions neutrally buoyant particles do not migrate across streamlines and particle distribution is conserved. With increasing R_p ($R_p > 1$) particles become increasingly subject to “the wall effect” and “shear-induced” lift forces leading to migration across streamlines and particle focusing.

$$R_c = \frac{\rho v_{max} D_H}{\mu} = \frac{3}{2} Re \quad 2.18$$

$$R_p = R_c \frac{a^2}{D_H^2} \quad 2.19$$

2.4.3 Flow Resistance

Flow resistance must also be considered when designing microfluidic channels. This is calculated using equation 2.20, where ΔP is the pressure difference across a channel, Q is the volumetric flow rate and R_ϕ is the channel resistance. Microfluidics commonly uses volumetric flow rates Q (m^3/s) instead of linear velocity (m/s), as this value remains constant throughout the device whereas v changes with channel dimensions.

$$\Delta P = QR_\phi \quad 2.20$$

The fluid flow in a rectangular microchannel can be defined by equation 2.21 [168]. Where w is the channel width, h is the channel height, L is the length of the channel and μ is the fluid viscosity. β is the aspect of the channel ($\beta=h/w$), such that $0 < \beta < 1$ where $\beta=1$ represents a square channel. The function $f(\beta)$ (equation 2.22) shows a known polynomial of the aspect ratio β , which simplifies significantly for high aspect ratios (β tending toward 0) where the flow is confined in one dimension.

$$R_\phi = \frac{\Delta P}{Q} = \frac{f(\beta)\mu(2w + 2h)^2L}{32(wh)^3} \quad 2.21$$

$$f(\beta) = 96(1 - 1.3553\beta + 1.9467\beta^2 - 1.7012\beta^3 + 0.9564\beta^4 - 0.2537\beta^5) \quad 2.22$$

2.5 Microfluidic Cell Deformation

Microfluidics is an appealing technique for cells studies due to: small sample volume, low cost, biocompatibility, integration capability and potential for high throughput measurements. Cell deformation using microfluidics can be categorised as either: structure induced deformation or fluid induced deformation. Figure 2.11 summarises the different channel geometries that can be used to hydrodynamically deform single cells.

2.5.1 Structure induced deformation

Structure induced deformation involves passing cells through a channel which has at least one channel dimension that is smaller than the cell diameter (Figure 2.11a). Confinement by the channel walls requires the cells to deform as they are pushed through the channel at a set flow rate. Parameters such as cell elongation, transit time and recovery are used to quantify cell deformability [19]. Structure induced deformation is particularly useful for studying red blood cells (RBC) because the channels mimic in vivo capillaries [20], [22]. However, constriction-induced deformation is also affected by cell volume and adhesion between the cell membrane and channel walls. This means that larger and stickier cells will have a longer transit time. Additionally, the small diameters of constriction channels make them susceptible to clogging which limits experimental throughput.

2.5.2 Flow induced deformation

Fluid-induced deformation is where the cell is deformed by a shear or extensional force rather than by confinement structures [38]. Fluid-induced deformation is not affected by adhesion between the cell and the channel walls, and cell strain can be adjusted as a function of flow rate. Several geometries can be utilised for fluid-induced deformations (and are shown in Figure 2.11).

Channels with a diameter slightly larger than the cells diameter can be used to induce shear fluid stress, where the cells deform to a bullet-like shape due to the strong velocity gradient within the channel (b) [19], [34], [46], [52], [96], [169]. Here, the magnitude of shear stress is relatively small and only able to induce smaller strains. The entrance or exit of a constriction channel can also be used to generate an extensional flow, often more efficient for deforming cells [26]. Extensional flow is caused by a velocity gradient between a larger chamber and an area of contraction in a microfluidic device, a hyperbolic converging channel to deform cells in extensional flow is shown by (c) [23], [24].

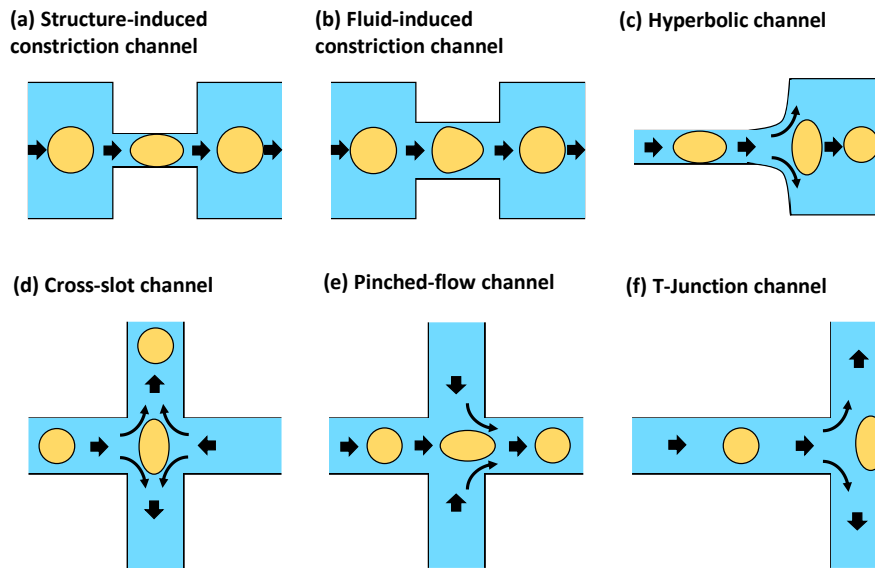


Figure 2.11 A schematic showing the different microfluidic geometries that can be used to deform single cells in a high-throughput and automated manner.

Figure 2.11 a-c show microfluidic geometries comprising of single channels which expand and contract to induce extensional or shear forces, geometries d-f have more than one channel. An extensional flow can also be generated using a cross-slot geometry (d). Cells are delivered to a junction of two orthogonal channels at a set flow rate Q , an extensional flow is generated due to the flow decelerating to $Q \cong 0$ at the stagnation point (SP) at the centre of the junction [27], [29], [32], [35], [48], [170], [171]. This geometry is capable of inducing high-strain cell deformations. However, unlike the single channel geometries (a-c) the cells need to be focused to the centre of inlet square/rectangular channels in order to deform at the SP. This requires an additional on-chip particle focusing mechanism, such as sheath or inertial focusing, which can be difficult to design and implement. Alternatively, particle tracking software can be used to only analyse the deformations of cells which passed through the SP and discarding cells which were close to channel walls.

A cell travelling down a straight channel can be hydrodynamically stretched by a pinched flow (d), where the cell is squeezed by the introduction of two opposite and perpendicular channels [30]. A T-Junction design combines fluid and structure induced deformation (f) [54]. Cells are delivered to a T-Junction where they collide with the channel wall, resulting in high-strain deformation. Similar to cross-slot channels, pinch-flow and T-junction deformations are also dependent on the cells position within the channel. Adding complexity to either device design or image analysis.

2.5.3 Shear and Inertial Forces

Hydrodynamic cell stretching is due to a combination of shear and inertial forces. The Reynolds number determines whether the regime is shear-dominant or inertia-dominant. The different regimes depend on device geometry, cell suspension viscosity and flow rate.

The majority of the studies in the thesis use a cross-slot geometry (Figure 2.11d), a geometry first designed to study extensional rheology of polymer solutions [172], [173]. This geometry was chosen as it can be used to induce low and high strains at a range of flow conditions. The shear and compressive force's acting on a cell deforming at the SP of a cross-slot device can be estimated using equations 2.23 and 2.24. The compressive force F_C , is due to the inertia of the fluid and the fact the cell is decelerating as it moves towards the SP, can be calculated using 2.23 [174]. Where ρ is the density of the suspension media, U is the fluid velocity, A_p is the cross sectional area of the cell and C_D is the drag coefficient. C_D is highly dependent on Re (equation 2.16), and was calculated using equation 2.25 which is the four-parameter drag correlation equation proposed by Brown *et al.* 2003 [175]. This equation was correlated to a 480 point data set of measured values of C_D , using the terminal velocity of falling spheres, over a large range of Re . The given equation best correlated the experimental data for $Re < 2 \cdot 10^5$ which fully encompasses the range of Reynolds numbers used in this thesis.

$$F_C \cong \frac{1}{2} \rho U^2 C_D A_p \quad 2.23$$

$$F_s \cong \dot{\gamma} \mu (4\pi r^2) = 2\pi U \mu r \quad 2.24$$

$$C_D = \frac{24}{Re} (1 + 0.150 Re^{0.681}) + \frac{0.407}{(1 + \frac{8710}{Re})} \quad 2.25$$

The shear force F_s , due to the viscosity of the suspension fluid imparting a frictional force on the cell, was determined by 2.24, where μ is the viscosity of the suspension media, r is the cell radius and $\dot{\gamma}$ is the strain rate [35], [174]. Flow rate and viscosity can be tailored to achieve a shear or inertia-dominant flow regime. This can be demonstrated by calculating Re (equation 2.16) for a range of flow rates and suspension medium viscosities. Figure 2.12 is a plot of Re as a function of flow rate at two viscosities of suspension medium, 1 cP (the same as water) and a high viscosity 33 cP. Where the unit cP (centipoise) is equivalent to 1 mPa-s. Calculations were done for devices with channel width of 35 μm and a height of 25 μm , matching the dimensions of the design most used in this thesis (described further in section 3.2). Figure 2.12 shows a linear increase of Re as a function of flow rate, and that increasing viscosity significantly decreases Re . Previous studies have shown that inertial effects start for

Re between 20-40, therefore $Re = 40$ was used as a boundary for the inertial regime [30], [176], [177]. For a solution with a viscosity of 1 cP, $Re > 40$ for flow rates $\geq 11 \mu\text{l}/\text{min}$. Therefore, low viscosities and high flow rates ensure an inertia-dominant regime. For $\mu = 33 \text{ cP}$, the Reynolds number is low ($Re < 6$) for the entire range of flow rates used in the body of work, a high viscosity and low flow rate are ideal for a shear-dominant regime.

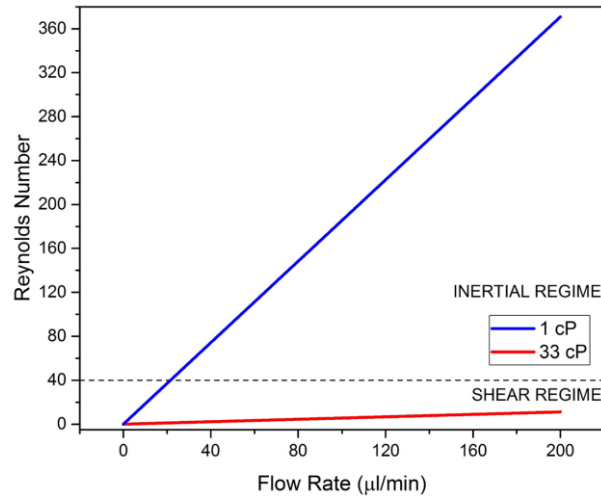


Figure 2.12: Variation of Reynolds number with flow rate in a cross-slot device for two viscosities, $\mu = 1 \text{ cP}$ and $\mu = 33 \text{ cP}$. The dashed line at $Re = 40$ represents the flow regime being defined as either shear- or inertia-dominant.

The total force F_T is the sum of the two force components, $F_T = F_S + F_C$. Figure 2.13 further describes the separate contributions to F_T by F_S and F_C as a function of flow rate and Reynolds number. Figure 2.13a shows plots of equations 2.23 and 2.24 as a function of flow rate for a suspension viscosity of $\mu = 1 \text{ cP}$. F_C is proportional to U^2 compared to F_S which is proportional to U . For flow rates $\sim 40 \mu\text{l}/\text{min}$ the compressive contribution F_C begins to surpass the shear contribution F_S . Here, $Re > 40$ which corroborates that at these flow conditions inertial effects are significant. Thus, F_T is dominated by F_C at low viscosity and high flow rates. Throughout the thesis inertia-dominant flow measurements are taken for flow rates $\geq 50 \mu\text{l}/\text{min}$ in a low viscosity buffer (PBS or DMEM media $\sim 1 \text{ cP}$). Figure 2.13b shows the force contributions as a function of flow rate for a suspension viscosity of $\mu = 33 \text{ cP}$. F_C increases with density whereas F_S increases with viscosity. Methyl cellulose (MC) was used to increase the viscosity of PBS from $\sim 1 \text{ cP}$ to $\sim 33 \text{ cP}$, comparatively changes to density were small (0.5% methyl cellulose). This results in F_T being dominated by F_S up to flow rates of $200 \mu\text{l}/\text{min}$, $Re < 11$ for the entire range shown in Figure 2.13b. Additionally, for flow rates $< 18 \mu\text{l}/\text{min}$ the Reynolds number is < 1 . F_T is dominated by F_S in a low flow rate and high viscosity regime.

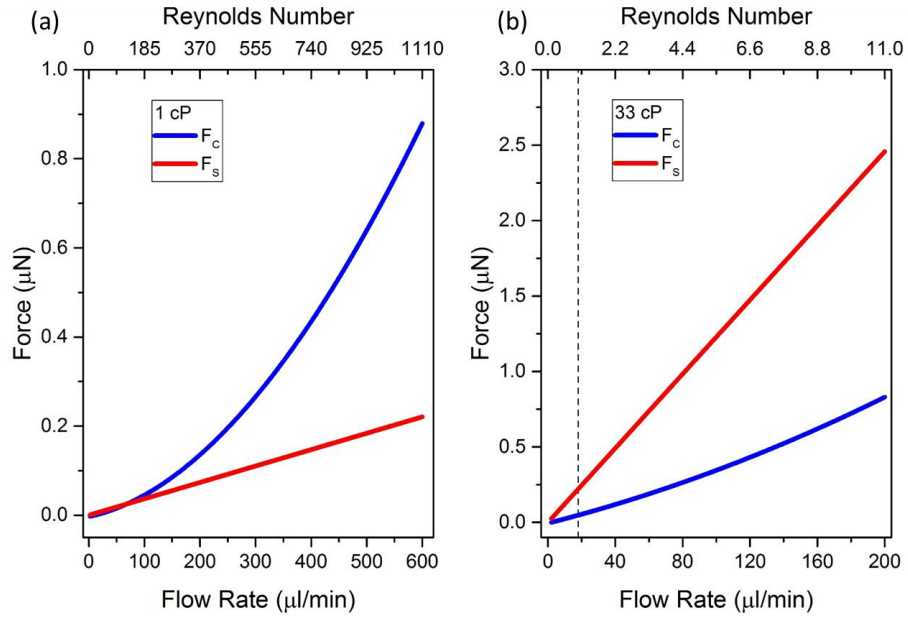


Figure 2.13: Plots of equations 2.23 and 2.24 as a function of flow rate. Changing the viscosity μ of the fluid determines whether the system is inertia or shear dominant. (a) For $\mu=1$ cP, at flow rates above ~ 40 $\mu\text{l}/\text{min}$ the compressive force contribution F_c begins to surpass the shear contribution F_s . (b) For $\mu=33$ cP the shear force has a larger contribution than the compressive force F_c for the entire range of flow rates described. The dashed line is at a $Re=1$.

3 Experimental Methods

3.1 Microfluidic Device Fabrication

Fabrication of microfluidic devices involves three steps: designing the device geometry using the software AutoCAD, creating a master of the device, and using soft lithography to create devices from the master. The methods below detail the protocol of master fabrication and micro-device fabrication. The master fabrication process is summarised in Figure 3.1 and PDMS microdevice fabrication summarised in Figure 3.2. Specific device designs are discussed in Section 3.2.

3.1.1 Master Fabrication

Device masters were fabricated using 3-inch Silicon wafers and the negative photoresist SU-8 2025 (Microchem, Warickshire, UK). Wafers were cleaned using piranha wet etch (using H_2SO_4 & H_2O_2) at >80 °C for 30 mins and then rinsed and stored in deionised water (Figure 3.1 a). Before use, wafers were dried using a nitrogen gun and placed in an oven at 180 °C for ~20 mins. Room temperature wafers were placed on a spin coater (EMS 6000) and coated with SU-8, and then the acceleration, speed and spin times were set to achieve the desired photoresist thickness (Figure 3.1 b).

A soft bake then solidified the SU-8 layer by evaporating the solvent in the SU-8. Wafers were placed on a room temperature hot plate (EMS 1000-1, Salisbury, UK) which was then set to 55 °C (it took ~5 min for the hot plate to heat to 55 °C). Wafers were left at 55 °C for 30 mins before turning the hot plate off and waiting for them to cool to room temperature (Figure 3.1 c), which took ~1 hr 30 min. Direct-write laser lithography was used to etch the microdevice designs into the SU-8 using a 2 μm laser of wavelength 375 nm (MicroWriter ML™, Durham Magneto Optics) (Figure 3.1 d). SU-8 2025 is a negative photoresist, the areas of the wafers exposed to the UV laser became crosslinked whereas the rest of the SU-8 remained soluble. The dose was optimised for device design, lower doses can achieve better resolution for small features but lead to adhesion problems between the SU-8 and wafer. High doses can cause overexposure, reducing resolution and creating “bell-shaped” channels wider than desired. A dose of 400 mJ/cm^2 was optimal for designs in this thesis (smallest channels of ~35 μm width).

A post-exposure bake then completed the polymerisation step, the same temperature ramping procedure as the soft bake was used (Figure 3.1e). Wafers were developed in ethyl lactate ($\text{C}_5\text{H}_{10}\text{O}_3$) solvent (EC solvent) for ~2 mins to remove the uncrosslinked SU-8, then washed in isopropanol ($\text{CH}_3\text{CHOHCH}_3$) for ~1 min (Figure 3.1 f). The previous baking steps can cause stress on the SU-8 layer and cause cracking. A hard bake at 180 °C, slightly below SU-8 glass transition temperature of 210 °C, for 15 mins was sufficient to remove any cracks in the SU-

8 (Figure 3.1 g). The completed master was then usable for PDMS microdevice fabrication (Figure 3.1 h).

The height of the SU-8 channels was confirmed using a Stylus Profiler (Bruker Dektak). Stylus profilers use a mechanical probe to acquire surface topography, the probe scans across a surface whilst a feedback loop monitors the force from the sample. The probe performs a line scan across an SU-8 channel to provide a height profile and give the step-height of the channel.

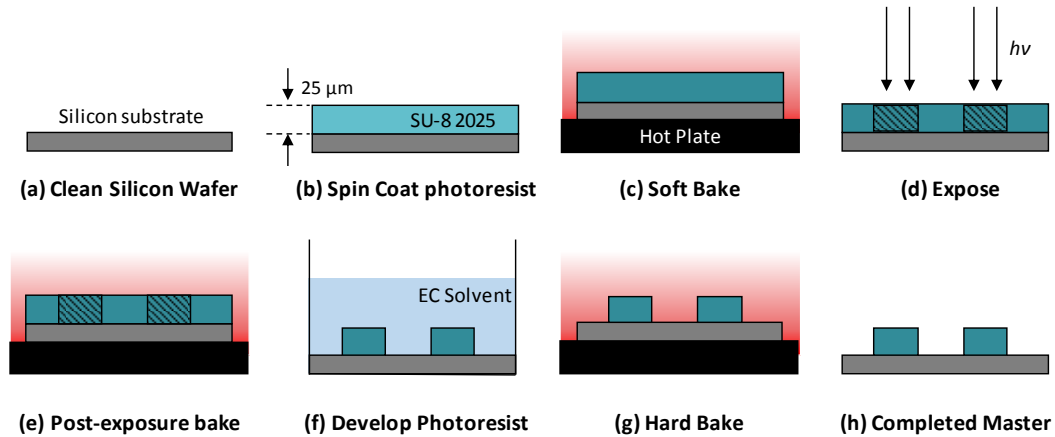


Figure 3.1. Schematic summarising the production steps for fabrication of an SU-8-silicon master, the main steps of the protocol are shown in order (a-h).

3.1.2 PDMS Device Fabrication

Microfluidic device channels were formed in the polymer PDMS (polydimethylsiloxane), using the master as a mould to create a negative replica of the SU-8 structures in the PDMS. A mixture of liquid PDMS and a cross-linking agent (SYLGARD 184) at a ratio of 1:10 was prepared and centrifuged at 14,000 rpm for 4 mins to remove bubbles. The mix was then poured over the master in a petri dish (Figure 3.2 a) and left under soft vacuum for ~1 hr to remove any remaining gas dissolved in the PDMS. The PDMS was then cured in an oven at 75 °C for ~1hr, becoming a hydrophobic elastomer. The now solid PDMS layer was then peeled away from the master (Figure 3.2 b), and the fluid inlet and outlet access holes were punched using a 1 mm diameter Biopsy Puncher (Figure 3.2 c). PDMS moulding creates 3 out of the 4 walls required for an enclosed channel.

The PDMS was sealed to either a glass slide or cover slip by oxygen plasma treatment, creating the fourth wall. The PDMS and glass were placed inside a plasma-cleaning chamber (Zepto, Diener electronics, Germany), and were plasma treated for 1 min, at 0.8-1 mbar of O₂ (Figure 3.2 d). Plasma treatment involves oxidation of the PDMS and glass substrates. Treatment with the reactive gases replaces hydrocarbon groups present in both PDMS and glass, increasing the number of surface hydroxyl groups (-Si-O-H-). The PDMS and glass were then brought into contact and gentle pressure applied to secure the bonding. Strong covalent (-Si-O-Si-)

bonds form between the substrates [178]. Finally, the bonded microfluidic devices were baked at 75 °C for 30 min (Figure 3.2 e).

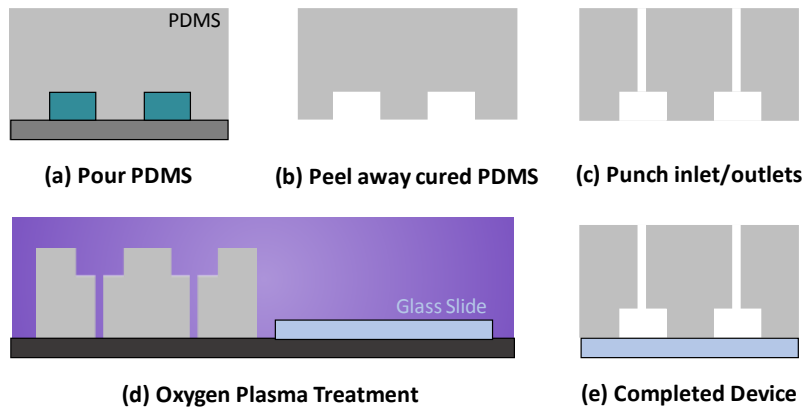


Figure 3.2. Schematic summarising the production steps for fabrication of microdevices using PDMS, the main steps of the protocol are shown in order (a-e).

3.2 Device designs

3.2.1 Cross-slot

Cross-slot microfluidic devices are commonly used to generate an extensional flow, which is used throughout this thesis to deform single cells over a range of flow conditions. Figure 3.3a shows the cross-slot device used in the thesis, designed using AutoCAD, which was used to fabricate devices for deformation cytometry.

A single-cell suspension was flowed through the inlet port (Figure 3.3a). Samples were first passed through an on-chip filter (Figure 3.3ai). This is shown in further detail by Figure 3.3b, an array of filtering pillars with minimum spacing of 50 μm were used to prevent blockages occurring down-stream due to cell debris and cell clumps. The filtered sample was then separated on-chip into two equally sized channels. These channels were redirected to a junction of two opposite inflowing channels and two orthogonal outflowing channels (Figure 3.3aii). This area will be referred to as the *extensional-flow junction* and is shown in further detail by the schematic in Figure 3.3c. This is where the cross-slot design generates the extensional flow, causing cell deformation at the stagnation point at the centre of the junction. Unless stated otherwise, the channels at the extensional-flow junction had a width of 35 μm and a height of 25 μm . The sample then leaves the device through either of the outlet ports.

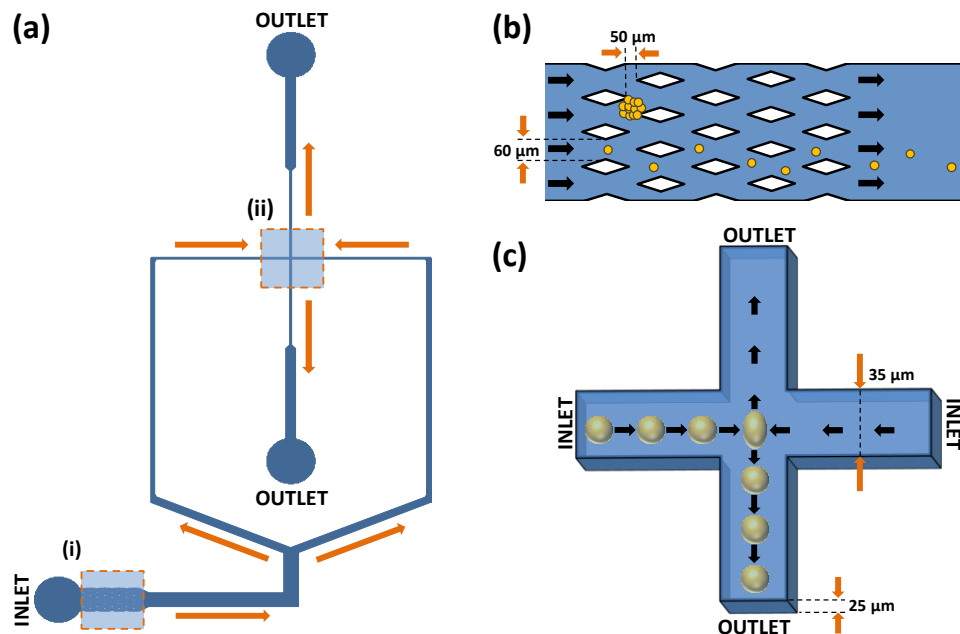


Figure 3.3. (a) Cross-slot device designed using AutoCAD, with inlets and outlets labelled and arrows used to show the direction of flow. Highlighted areas include (i) an on-chip filter and (ii) the extensional-flow junction. (b) A schematic of the on-chip filter placed after the inlet in order to prevent larger particles causing blockages down-stream. (c) A of the extensional-flow junction, the feature of the cross-slot device where cell deformation occurs.

3.2.2 Serpentine

Another application of deformation cytometry is that it can induce transient membrane pores which allows increased uptake of nanoparticles into cells, discussed in section 1.4.3. Other microfluidic geometries have been used to increase uptake of nanoparticles into cells [54], [65], [67], [179].

In the cross-slot devices in the shear-dominant regime the cells undergo small deformations due to confinement in the channel (discussed in section 4.1.4). Therefore, a control was needed to ensure that the QD uptake was improved using a cross-slot device compared to just shearing effects due to channel confinement. A serpentine device, shown in the schematic in Figure 3.4, was used to do this. The serpentine region has the same width and height as the inlet and outlet channels of the cross-slot ($35 \times 25 \mu\text{m}$), the length of the serpentine equates to the length of the inlet and outlets in the cross flow. Therefore, passing a cell through the serpentine at the same flow rate is equivalent to the shear confinement forces in the cross-slot but removes the extensional flow deformation. Results in section 7.1.3 discusses QD uptake in serpentine and cross-slot devices.

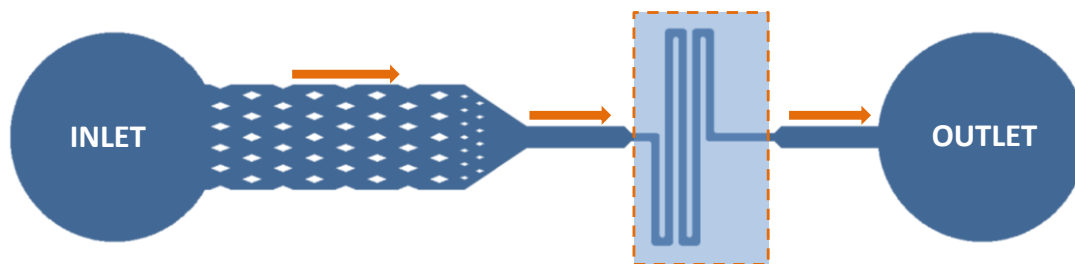


Figure 3.4. Serpentine device designed using AutoCAD, with inlets and outlets labelled and arrows used to show the direction of flow. Highlighted area shows a serpentine channel with a width of $35\ \mu\text{m}$, devices were fabricated to a height of $25\ \mu\text{m}$, and the channel length matched the length a cell would travel down the inlet and outlet of a cross-slot device (Figure 3.3) at these confined dimensions.

3.3 Deformation Cytometry Procedure

The apparatus for deformation cytometry is summarised in Figure 3.5a, using the microfluidic device previously described in Section 3.2.1. A 1ml glass syringe was cleaned with ethanol and deionised water before being loaded with a cell sample. Fine Bore Polythene tubing (Smiths MedicalTM, Kent, UK), 0.36mm ID and 1.09 mm OD, was connected from the syringe to a microdevice. The tubing was fitted directly into 1 mm diameter punctured PDMS inlets and outlets. The syringe was then loaded into a syringe driver (WPI, Hertfordshire, UK), which was used to set a volumetric flow rate ($\mu\text{l}/\text{min}$) to flow samples through the devices. Tubing was also connected from the device outlets into a glass vial or microcentrifuge tube to collect the sample. Microdevices were mounted above an inverted bright field microscope (Figure 3.5b), a 10x objective was used to capture cell deformation events with an additional 1.5x magnification for flow rates $Q < 200\ \mu\text{l}/\text{min}$.

High speed microscopy was used to capture cell deformation events, the high speed camera (Photron, Fastcam SA-X) was operated at frame rates of (7000-260,000) fps and exposure times of (0.37-6.67) μs . An external light source was mounted over the set-up (Figure 3.5c), this additional light allowed image capture at higher frame rates and reduced exposure times to prevent motion blurring.

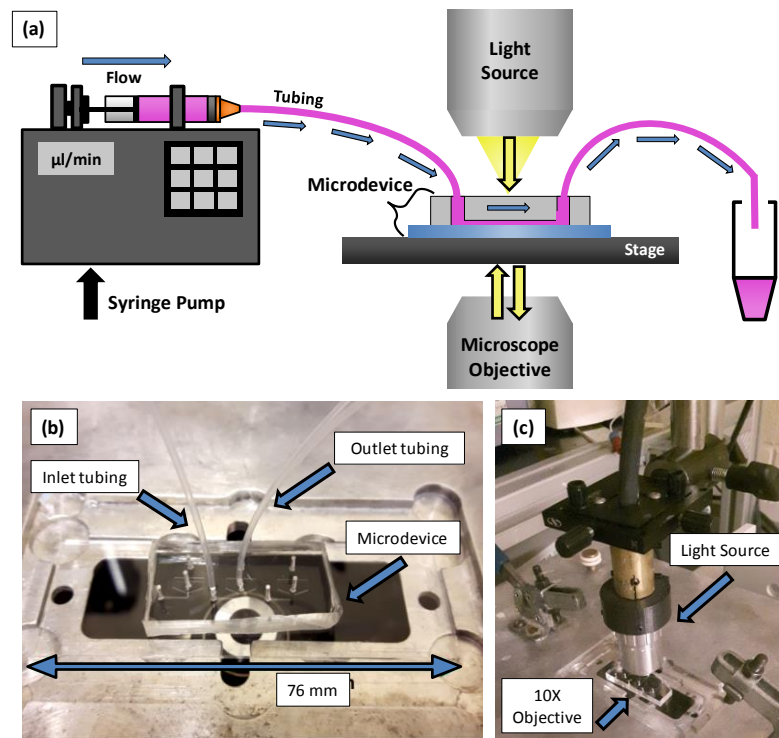


Figure 3.5. (a) Schematic of the microfluidic apparatus used for deformation cytometry. (b) Image of a PDMS device mounted into a holder for high-speed microscopy of cell deformation, with inlet and outlet tubing inserted. (c) Image showing how the device is held between a standard inverted bright field microscope and an additional light source which enhances image intensity.

3.4 Microscopy Techniques

3.4.1 Bright Field Microscopy

The microscope used for deformation cytometry was an inverted microscope (Eclipse Ti-U, Nikon, Japan) utilising reflection bright-field microscopy, which shines white light onto a sample and collects the reflected light. Contrast is achieved by absorbance of the light by the sample. This form of microscopy typically has low contrast when viewing biological samples. Mammalian cells are usually optically transparent and colourless, and bright field images show low definition and little structural detail. High contrast bright field images of cells can only be achieved on samples which are stained, which often requires fixing the sample (i.e. not applicable for imaging of live cells in suspension).

3.4.2 High Speed Microscopy

A camera is high speed if the frame rate exceeds 250 frames per second (fps) with an exposure time less than 1 ms. In this body of work cells were deformed microfluidically, and these deformations and recoveries can occur in less than a millisecond. Therefore, high speed microscopy was required for imaging these events.

The determining properties of a high speed camera are; the image resolution, the frame rate, the exposure time and the data rate. The resolution needs to be high enough so that the field-of-view can capture the cell before, during and after it deforms. Frame rates should be high enough to ensure that the maximum cell deformation will be captured, if the frame rate is too low this information could be missed. The exposure time should be short enough that images do not have motion blur. Here, high speed microscopy was performed using the FASTCAM SA-X camera (Photron). Each acquired pixel has an image sensor, this system uses a CMOS (metal-oxide-semiconductor) sensor. This camera has a maximum resolution of 1024 X 1024 pixels which can be maintained for frame rates $\leq 12,500$ fps. At higher frame rates the resolution is limited by the data rate, thus as frame rate increases the field of view decreases. An ISO value is used to measure a cameras ability to capture the light which falls onto the image sensor, a higher ISO allows for lower exposure times. The SA-X camera has an ISO value of 25,000, allowing for a minimum exposure time of 293 ns.

In this body of work, frame rates of $\leq 230,000$ frames per second and exposure times ≤ 293 ns were achieved. At the highest frame rate the maximum resolution was 128x128 pixels.

3.4.3 Phase Contrast Microscopy

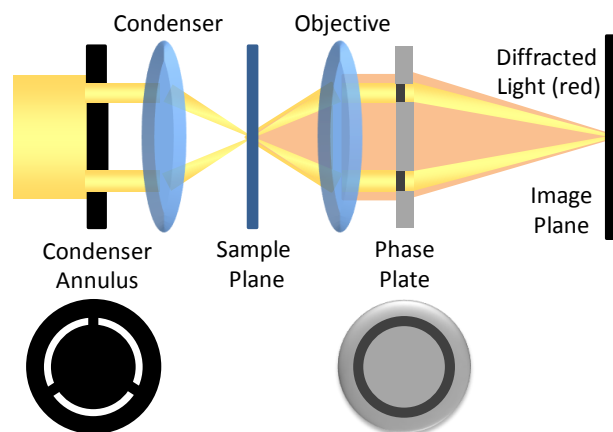


Figure 3.6 Simplified schematic of the optical set-up of a phase contrast microscope. The condenser annulus and $1/4$ wavelength phase plate are used to convert phase shifts into amplitude.

Bright field microscopy relies on absorption of light to see contrast in samples, however absorption is not the only way that light interacts with a sample. Other forms of microscopy utilise polarization or phase shift to see better contrast in sample. The eye is only sensitive to changes in amplitude or colour, however phase contrast microscopy converts differences in phase into amplitude, allowing improved contrast in biological samples.

Different cellular components have different refractive indices. When light is shone on a sample the different optical path length cause a change in phase but not in amplitude. The phase difference of light diffracted by the sample is usually retarded by $1/4$ wavelength

compared to the background (direct) light. Objects will show excellent contrast when the phase difference between the diffracted and direct light is a $\frac{1}{2}$ wavelength, due to destructive interference. Therefore, phase contrast microscopy works to advance the direct light by a $\frac{1}{4}$ wavelength.

Figure 3.6 shows a schematic of a phase contrast microscope. Two components are required to transform a bright field microscope to a phase contrast microscope. The condenser annulus is a mainly opaque ring with a clear ring, whose purpose is to produce a circle of light onto the front of the condenser. The condenser subsequently focuses a hollow cone of light onto the sample plane. The phase plate is a circular shaped clear plate with a ring in it, with equal dimensions to the circular annulus. Most commonly, the ring is made of an optically thinner material to the rest of the plate. When the ring of light hits the sample, some of the light is diffracted and some is not (direct light). The direct light passes through the optically thinner ring of the phase plate, which advances the phase of the direct light by $\frac{1}{4}$ relative to the diffracted light. As the phase of the diffracted light was retarded by $\frac{1}{4}$ wavelength by the sample, the phase difference between direct and diffracted light is now $\frac{1}{2}$ wavelength. This causes destructive interference, leading to the sample appearing dark compared to a light background, this is known as dark/positive phase contrast. A phase plate can also be used to achieve constructive interference, where the sample appears bright compared to the background (bright/negative phase contrast).

3.4.4 Confocal Fluorescence Microscopy

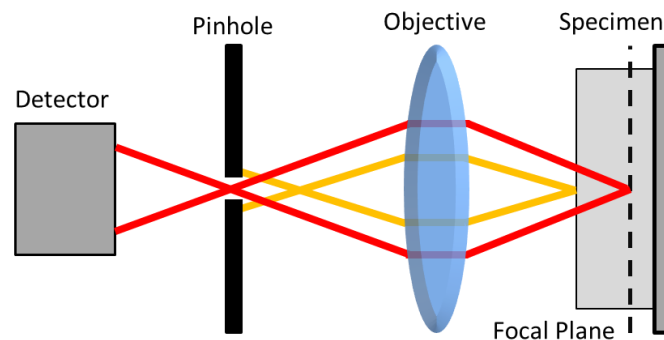


Figure 3.7 Simplified schematic of a confocal microscope. Light from the focal plane (red) is focussed through the pinhole whereas light from other depths within the specimen (orange) is blocked. This results in acquiring fluorescence from a defined depth, reducing background fluorescence.

Fluorescence microscopy uses the detection of light emitted from fluorophores to generate an image and can be performed together with bright field microscopy. In this work, fluorescent stains were used to visualise the substructure of cells and quantify uptake of NPs into cells.

Confocal microscopy is a fluorescence imaging technique with improved resolution over traditional epifluorescence microscopy. In epifluorescence microscopy, light emitted throughout the depth of the sample is detected. Therefore, some of the detected light will be out of focus (more prominent for high magnification objectives) which limits resolution. In confocal microscopy a pin-hole is used to block out light emitted from regions other than the focal plane, this results in a small depth of field and reduced background fluorescence (Figure 3.7). High resolution in x and y is achieved by raster scanning the excitation laser spot over a sample. Samples can also be mapped in 3D, known as a z-stack, where a series of 2D images are collected at varying depths and then stacked.

Confocal microscopy was performed on samples of cells using a Leica DMi8, which allows simultaneous capture of bright field images and fluorescent images using either 488 nm, 552 nm and 638 nm excitation lasers. The microscope was equipped with 2.5×, 10×, 40× objectives, and also 60×, 100× oil immersion objectives. Cytoskeletal imaging was done using a live cell fluorogenic labelling probe based on Silicon-Rhodamine (SiR) (Spirochrome, Cytoskeleton Inc.) to stain F-actin or tubulin, using a 638 nm excitation laser. Adjustable emission filters were used to accommodate the spectra of these dyes. Hoechst 33342 (Thermo Fisher Scientific) was used to stain cell DNA, using laser excitation at 488 nm, imaged simultaneously with either SiR actin or tubulin staining. Confocal fluorescence was also performed on cells incubated with Quantum Dots (QDs), using laser excitation at 488 nm. The confocality was used to collect Z-stacks of the incubated cells to visualise whether quantum dot uptake was endocytic or non-endocytic.

Samples were imaged in transparent chambers (Lab-Tek II), where each chamber held 0.2-0.5 ml of sample. Each chamber had 8 identical wells, which allowed multiple samples to be prepared and imaged with ease. The thickness of the bottom was the same as glass coverslips. The wells were pre-treated with poly-L-lysine, which facilitated cell attachment to the surface of the well before imaging.

3.5 Automated Image Analysis

Automated image analysis was performed offline using ImageJ and MatLab, the position and the shape of each cell event was tracked and parameters such as initial size, velocity, circularity and maximum deformation index ($DI = H/W$) were extracted.

3.5.1 ImageJ particle tracking

The scientific image analysis software *ImageJ* was used to track the size, shape and velocity of cells deforming in microfluidic devices. Figure 3.8 outlines the series of steps performed on a raw image (a) of a deformed cell, to convert the image to binary in order to perform the image analysis. A “subtract background” command was first used to reduce noise (b). This

removes smooth continuous backgrounds based on the “rolling ball” algorithm [180]. Next, the brightness and contrast of the subtracted image is adjusted, to increase the contrast between the dark outline of the cell and the light background (c). From this, the “Make Binary” command is used (d), where image pixels are converted to either black or white. This procedure divides an image into objects (i.e. a cell or channel wall) and background by taking a threshold, above which the pixel is converted to black and below which the pixel is converted to white. ImageJ thresholding uses an iterative algorithm to convert images to binary [181]. The subsequent image shows a black cell outline and black device walls with a white background. The “Fill Holes” command then fills the cell which is shown as an ellipse shape (e). This set of commands was applied to image stacks containing multiple cell deformation events.

The ImageJ “DropletTracker” plugin (created by Travis Geis in 2013) was then used to analyse and track cell shape and movement [182]. A minimum and maximum particle size was defined, only objects within this range were detected and tracked. This was chosen to encapsulate the range of cell sizes for each particular cell line. The channel walls were excluded from tracking as these objects exceeded the maximum size. Additionally, any clumps of multiple cells passing through the device were discarded as they tended to exceed the maximum size. A nearest-neighbour approach was used to track objects across stacked frames. A user-specified maximum “velocity” in pixels/frame was used. If an object in two successive frames moved a distance less than that specified by this “velocity” it was considered the same object, objects above the “velocity” were considered separate. As one frame could contain multiple single cells, the frame rates used were chosen so that the space between cells was large compared to the distance travelled by a cell between two subsequent frames. A minimum track length was also defined and events were only included in the outputted data if they were tracked for at least this number of subsequent frames (between 6 and 30 frames dependent on field of view). This helped to remove noise from the data, for instance if a frame contained noise within the particle size range but only for one frame it would be discarded.

DropletTracker could be run on stacks of up to 30,000 images depending on image resolution. It outputs a spreadsheet which contains the position, shape and size of each cell event as a function of time. Each detected object is assigned a “particle number” as each event spans multiple rows of the spreadsheet corresponding to each frame in which the object appears, a corresponding “frame number” tells you which objects appeared in a specific frame. For each object in each frame, the centroid position (x, y), area, perimeter and various deformation parameters are found (using object width and height, section 3.5.3). Additionally, velocity (pixels/frame) is found for each tracked object. This was later converted to linear velocity

(m/s) via the frame rate (fps) used during high speed imaging and knowing the pixel conversion to meters.

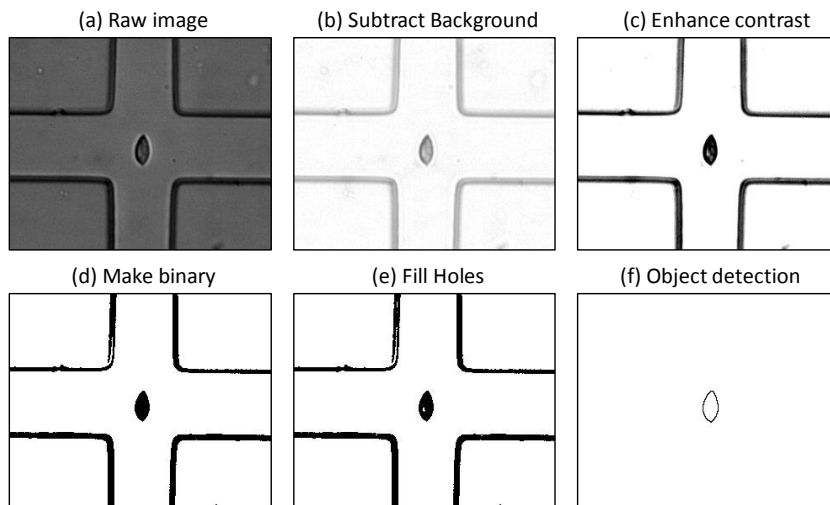


Figure 3.8. An example image of a cell deforming at the stagnation point of a microfluidic device. Steps (a-f) show the process of converting the raw image to a binary image which was then analysed to find the cell size and shape.

The data was processed using Matlab and code was written to extract the parameters of interest and compile each individual event. Various plots were generated to check the ImageJ analysis was robust. Figure 3.9 shows example plots for $N=387$ HL60 cells deformed at $40 \mu\text{l}/\text{min}$ in a cross-slot device (Figure 3.9 d) in a shear-dominant regime ($\mu=33 \text{ cP}$), each individual event is colour coded with adjoining lines to help guide the eye. Figure 3.9a shows the X and Y centroid position of each cell event, tracking the position of the particles across each frame they are present. This clearly shows cells following the expected path through the cross-slot geometry, and that different cells entered from either inlet and exited from either outlet which validates the system symmetry. The velocity profiles are plotted in Figure 3.9 b, which shows the cell events have similar incoming velocities which decrease to near 0 corresponding to being at/near the stagnation point. Figure 3.9 c is a plot of the ratio of cell height to width ($DI=H/W$) as a function of frame number, showing that cells have initial deformation of ~ 1 (undeformed/circular), which increases as they pass through the stagnation point before decreasing as the cells enter the outlet channel. Finally, a scatter plot of the maximum deformation DI of the cells as a function of initial diameter A is shown (Figure 3.9 e). This verified that an appropriate particle size detection range was chosen.

This analysis method was used throughout the thesis for bulk analysis measurements of the maximum cell deformation and initial cell diameter (A). The velocity profiles were also used to threshold the data, discarding any cell events which did not pass through or close to the stagnation point. This thresholding is discussed in section 4.1.3.

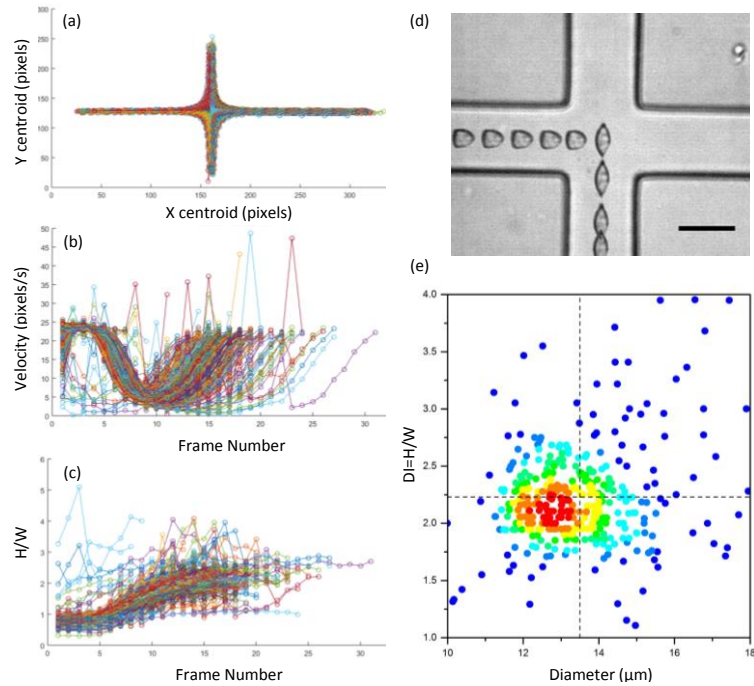


Figure 3.9. An example of particle tracking used to analyse the deformation of a HL60 cell deformation in a cross-slot device ($Q=40 \mu\text{l}/\text{min}$, $\mu=33 \text{ cP}$). (a) The X and Y centroid position of each cell event. (b) The cell velocity (pixels/s) as a function of frame number. (c) The deformation ratio H/W as a function of frame number. (d) An overlaid image of a cell deforming at the SP of a cross-slot device. (e) A density scatter plot of the maximum $DI=H/W$ of each cell at/near to the SP as a function of initial cell diameter (μm), the dashed lines represent the mean values.

3.5.2 Matlab particle tracking

The previously described image analysis method was used mainly for bulk measurements of the DI of 100 s-1000 s of cells at a range of flow conditions. However, some of the work in the thesis required tracking the deformation and recovery of cells deforming in a cross-slot, allowing for multiparameter analysis (i.e. not just the maximum DI at the SP). For more precise tracking and visualisation of each event a mathematical image processing algorithm, written by Dr. Hermes Gadêlha (University of York), adapted from flagellar image tracking was used [38].

Each frame of a video, containing multiple cell events, is loaded and read individually. Firstly, 2D adaptive noise removal filtering is used to improve image quality (matlab function `weiner2`). This type of filtering works best for images where noise is constant (Gaussian noise), looks at the statistical variance of pixel intensity compared to local neighbourhood. A large variance leads to little smoothing and a small variance leads to more smoothing. Thresholding is then used to convert the grayscale video into a binary video and create a mask, with a white background and a black foreground (which should only include any cells present in the image). A set level approach was used, which replaces all pixels above the *set level* to

the value of 1 (white) and below the *set level* to a value of 0 (black). The range is relative to the signals in the loaded image, i.e. a set level of 0.5 corresponds to the half level intensity between the minimum and maximum in that image. After achieving a successful binarized image, a minimum and maximum object size (black pixel area) is set to encapsulate the size range of cells to be detected. Figure 3.10a shows a display screen which is used to check that the filtering and tracking is adequate for image analysis of single cells. This includes filtering the original image, binarizing to create a mask, and filtering by size to leave only objects of interest.

For object tracking, two parameters are defined. The “maximum distance” between objects in subsequent frames is defined. If the distance between two objects is below this, the code recognises this as a single cell event and tracks its movement. If the distance between two objects in subsequent frames is above the “maximum distance” the code recognises these as two separate cell events. The “minimum track length” is also measured and this can be used to filter out cell events which do not pass through or near to the SP (their track length will be shorter). Images of successful tracking are shown by Figure 3.10b and c, where the red line outlines the detected cell contour, the blue dot tracks the cells centroid position, and the black line represents the path of the cell.

Finally, colour contour plots of each detected cell in the video are displayed (Figure 3.10 d). These show superimposed traces of the cell shape as a function of time, starting with dark blue as the cell approaches the SP to red as the cell recovers in the outlet channel. The display of individual objects is a useful check to see if any unwanted objects were detected, which can easily be filtered out from subsequent analysis. The information gathered from these videos is used for multiparameter analysis of cell deformation and recovery of different cell types, and is used throughout the thesis.

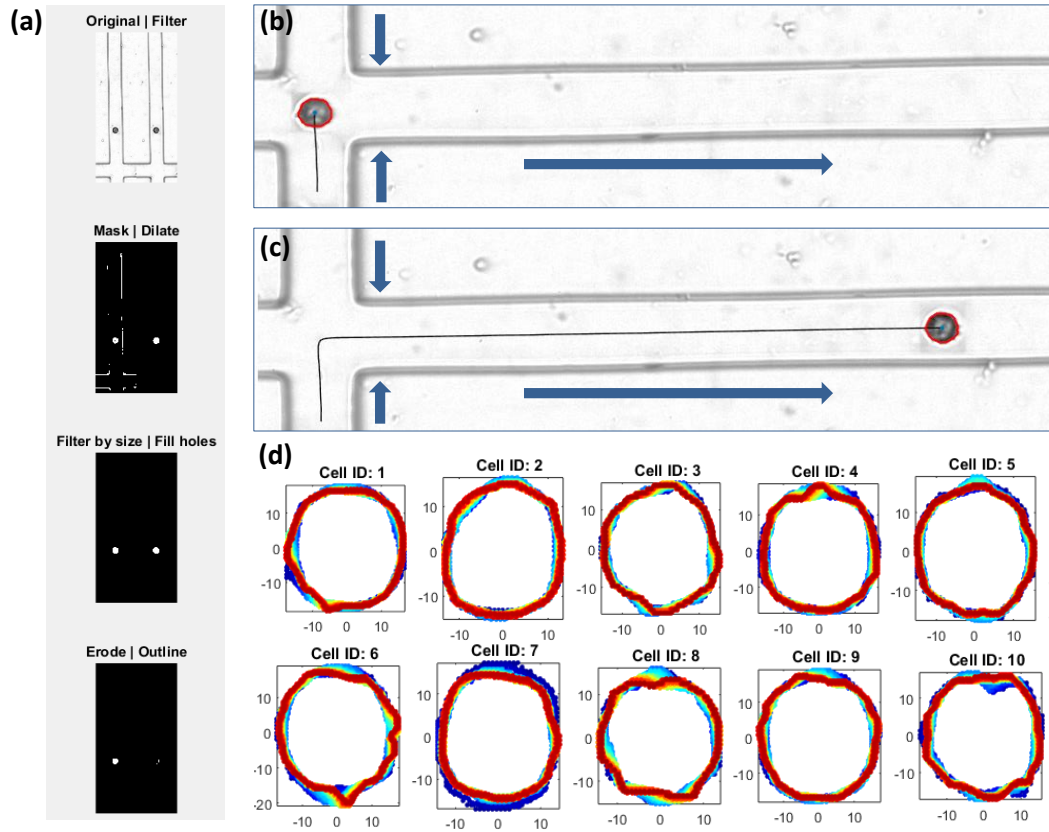


Figure 3.10. Example of precision particle tracking using Matlab. The code is used to track the position and shape of a cell passing through an extensional flow junction. (a) A cell deforming at the SP, the blue dot shows the detected centroid position, the red line shows the detected contour and the black line tracks the path of the object. (b) The same cell as it has traversed further into the outlet. (c) Superimposed colour contour plots that show how the cell shape changes as a function of time, ranging from dark blue where the cell approaches the cross-flow junction to red when the cell reaches the end of the outlet channel.

3.5.3 Parameter definitions

Several parameters were used to measure cell shape and define the deviation in shape due to deformation. Firstly, the deformation index DI is defined by equation (3.1), where H is the height of the cell and W is the width of the cell. Another definition is the Taylor strain parameter, which will be referred to as the cells' strain ε and is defined in equation (3.2). Finally, the circularity c can be used to describe how much the shape deviates from a perfect circle. This is calculated using equation (3.3), where S is the 2D projected surface area and P is the perimeter. A perfect circle has $c = 1$ and for a deformation $c < 1$. The deformation is defined as $D_c = 1 - c$, for ease D_c will be referred to as circularity throughout the thesis, because this quantity increases as a shape deviates from a perfect circle.

$$DI = \frac{H}{W} \quad (3.1)$$

$$\varepsilon = \frac{H - W}{H + W} \quad (3.2)$$

$$D_c = 1 - c = 1 - \frac{2\sqrt{\pi S}}{P} \quad (3.3)$$

Throughout the thesis these three parameters are used to define cell shape and the usefulness of the parameters for different assays can be described by the schematic in Figure 3.11. Shape A in Figure 3.11 shows a circle, where $W=H$ and circularity is 1. Shape B shows an irregular shape which deviates from a perfect circle. If a bounding rectangle is applied the width and height are still equal to each other. Therefore, DI and ε have the same values compared to shape A whereas D_c has increased because the shape perimeter and surface area have changed compared to a circle. Shape C is closer to an ellipsoid, here the width, height, perimeter and surface area have all changed compared to shape A and therefore DI , ε and D_c would all increase.

An undeformed cell under flow has a $DI \sim 1$ and a circular morphology. This parameter is intuitive for characterising the change in cell shape from circular to ellipsoidal due to on-chip deformation at the stagnation point ($DI > 1$). Similarly, the strain ε also uses the height and width to characterise deformation. This parameter can be used in the Kelvin-Voigt model to calculate cell elastic modulus (section 2.3.4). These parameters are directional, i.e. dependent on the orientation of the cell, whereas D_c is independent of orientation. When measuring cell morphology off-chip an image may contain 10 s to 100 s of cells all at different orientations, here D_c is a more suitable measure of cell shape compared to DI or ε .

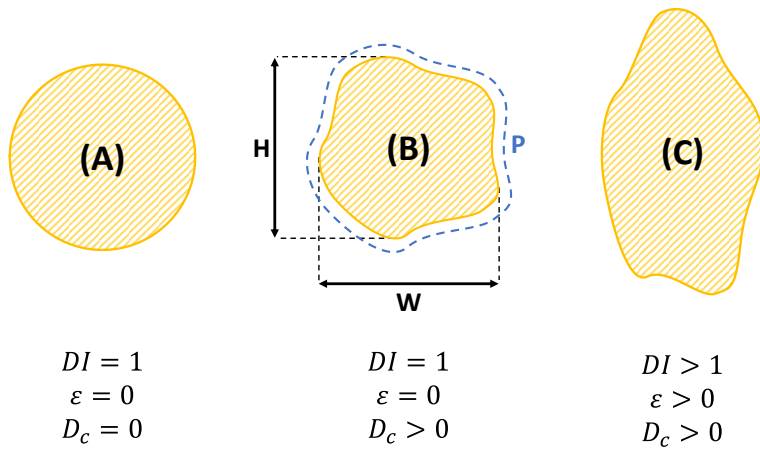


Figure 3.11. Schematic describing how the deformation parameters DI , ε and D_c change when a cell begins to deviate from a perfect circle (Shape A).

3.6 Cell Culture

This section describes the culturing procedure for the different cell lines used within this project. Cells were stored in a moisture-controlled incubator at 37 °C with a 5% CO₂ atmosphere and cultured in either 25 cm² flasks or 75 cm² flasks. Culturing was performed inside a Class II A1 Biosafety Cabinet.

3.6.1 HL60

The HL-60 (Human promyelocytic leukemia) cell line is a non-adherent cell line with a usual doubling time of 36-48 hrs [183], [184]. HL60 are often used in microfluidics as they naturally reside in single cell suspension, without need for trypsinisation or resuspension in an EDTA (Ethylenediaminetetraacetic acid) based anti-clumping buffer.

HL-60 were purchased as a frozen stock European Collection of Authenticated Cell Cultures (ECACC 98070106) and kept in liquid nitrogen in the presence of the cryoprotectant Dimethyl sulfoxide (DMSO) (typically 10% DMSO and 90% Fetal Bovine Serum). The cells were revived by quickly thawing them in a water bath at 37 °C and immediately adding them to 4 ml of RPMI media with 20% Fetal Bovine Serum (FBS), 2 mM Glutamine (Gln) and Penicillin 100 units/ml Streptomycin 100 µg/ml (Sigma). Penicillin and streptomycin are added to prevent bacterial infections, the combination acts against both gram-positive and gram-negative bacteria. Centrifuging at 100 g for 4 mins was sufficient to visibly pellet the cells, they were then resuspended in 10 ml fresh media in a culture flask. Resuspension is necessary to remove DMSO, which is damaging to cells at high concentration and can cause differentiation. Aseptic technique was used for all cell culturing to prevent contamination.

The cells were then split every 2-3 days to ensure the cell concentration did not exceed $1 \cdot 10^6$ cells/ml. After 2 passages after revival, RPMI media with 10% FBS, 2 mM Gln and Penicillin 100 units/ml Streptomycin 100 µg/ml (Sigma) was used for continued culturing. Once cell passage number exceeded 50 the cells were disposed of and replaced with a frozen vial of lower passage.

3.6.2 Colorectal Cancer Cell Lines

The SW480, SW620 and HT29 colorectal cancer cell lines were provided by St James's University Hospital and cultured in Dulbecco's Modified Eagle Medium (DMEM F-12, Glibco) supplemented with 10% Fetal Bovine Serum (Sigma), 2 mM Glutamax (Thermo Fisher Scientific) and Penicillin 100 units/ml Streptomycin 100 µg/ml (Sigma). All three are adherent cell lines and were subcultured when reaching 70-80 % confluency, which occurred every 3-4 days. This was achieved by washing with Dulbecco's phosphate buffered saline (DPBS), before detachment by applying TrypLE dissociation reagent (Thermo Fisher

Scientific) and incubating for 5 mins. One fifth of the resulting suspension was then diluted in growth media, and transferred to a new flask.

3.6.3 MCF-7

MCF-7 are an adherent breast cancer cell line, they were obtained from ECACC (European Collection of Authenticated Cell Cultures) as frozen stock, and subsequently cultured in DMEM (Sigma) with 10% FBS (Sigma), 20 mM GlutaMAX (Sigma) and Penicillin 100 units/ml Streptomycin 100 µg/ml (Sigma). The cells were subcultured every 3-4 days. This was achieved by washing with Dulbecco's phosphate buffered saline (DPBS), before being detached by applying TrypLE dissociation reagent. One fifth of the resulting cell suspension was then diluted in growth media, then transferred to a new flask.

3.6.4 HEK-293 T-REx and Piezo1 T-REx

Ion channels are cell membrane proteins which under certain stimuli form pores which allow ions to pass through the channel. One such stimuli is mechanical deformation. Mechanosensitive ion channels (MSCs) will activate when the membrane deforms under stress, due to changes in membrane tension or curvature. An example of a MSCs protein is Piezo1. Results section 7.2 discusses whether Piezo1 can be activated in HEK292 cells using shear-dominant deformation in a cross-slot microfluidic device. Here, we cover the culturing of HEK293 with and without Piezo1 expression, how Piezo1 can be activated, and how fluorescence measurements can be used to detect Piezo1 activation.

Culturing HEK293 T-REx and Piezo1 T-REx Cells

To test the activation of the MSC Piezo1, two cell lines were used; control HEK293 T-REx and Piezo1 T-REx. HEK293 is an adherent human embryonic kidney cell and T-REx cell lines stably express the tetracycline repressor protein (TetR). Here, expression of Piezo1 can be turned on or off by using the antibiotic tetracycline [185].

HEK293 T-REx and Piezo1 T-REx were provided by the Faculty of Biological Sciences at the University of Leeds as frozen stocks, and subsequently cultured in DMEM (Sigma) with 10% FBS (Sigma), 20 mM GlutaMAX (Sigma) and Penicillin 100 units/ml Streptomycin 100 µg/ml (Sigma). The cells were subcultured every 3-4 days, once cells had reach 70-80% confluency. This was achieved by washing with Dulbecco's phosphate buffered saline (DPBS), before being detached by applying TrypLE dissociation reagent. HEK293 T-REx required a 1:9 dilution and Piezo1 T-REx required a 1:5 dilution. Passage numbers for both cells lines were kept below 20, as Piezo1 response is known to decrease for higher passage numbers.

The antibiotic blasticidin was added to both cell lines whilst in culture (5 µg/ml). As both cell lines contain a plasmid (pc/DNA6/TR©) which encodes TetR, they should have blasticidin resistance. Adding blasticidin ensures any cells that are not resistant to TetR will die. The antibiotic zeocin is also added to the Piezo1 T-REx cell line (400 µg/ml). Only cells resistant to zeocin should express Piezo1. These cells express two tet operator (TetO₂) sequences which serve as binding sites for two TetR proteins. These repress Piezo1 transcription, addition of tetracycline induces transcription (activation) of Piezo1 by binding to the TetR proteins instead and preventing the TetO₂ from binding [186].

Activating Piezo1

Before cells were deformed microfluidically, both cell lines were incubated with tetracycline for 24 hr at a final concentration of 0.1 µg/ml. This should activate Piezo1 expression only in the Piezo1 T-Rex cell line. Next, the cells were loaded with the fluorescent dye Fura-2-acetoxymethyl ester (Fura-2AM). Fura-2AM is used to measure cellular calcium concentrations using fluorescence intensity. It can initially cross the cell membrane, once inside removal of the acetoxymethyl groups occurs by cellular esterases generating “Fura-2” which can no longer cross back out through the cell membrane. Cells were resuspended in a mix of the buffer SBS (Standard Barths Solution) with 1:10 of 10% pluronic acid in DMSO (acting as a dispersing agent) and 2 µM of Fura2-AM. Cells were incubated at 37°C in this mix for 1 hr. The mix was then removed and replaced with SBS buffer for 30 minutes at room temperature in a dark room, this allowed time for esterase’s to cleave AM.

Cells were then detached into a single cell suspension (as previously described), and resuspended in either SBS or SBS with 0.5% methyl cellulose at a final cell concentration of $5 \cdot 10^5$ cells/ml. SBS contains calcium, if Piezo1 is activated calcium can pass through the ion channels into the cell. Fura-2 emits at two wavelengths, unbound Fura-1 emits at 380 nm and Fura-2 bound to calcium emits at 340 nm. Both excitation wavelengths have an emission of 510 nm. When Piezo1 is activated and calcium enters the cell the emission at 340 nm increases and the emission at 380 nm decreases. Therefore, the fluorescence ratio can be used to study Piezo1 activation.

Microfluidic Deformation and Fluorescence Measurements

HEK293 T-REx and Piezo1 T-REx which had been successfully incubated with tetracycline for 24hr and loaded with the calcium indicator Fura-2, were then deformed microfluidically to study Piezo1 activation by mechanical stress. Cells were deformed at the SP of a cross-slot microfluidic device at a range of flow rates. After deformation, samples were collected and the fluorescence intensity was measured using a plate reader (SpectraMax® M2), 3 wells of

each flow condition were measured in a 96 well plate (Costar 96 clear U bottom) with 100 μ l of sample in each well (~ 50,000 cells per well). Fluorescence was measured at $\text{Lm1}=340/520$ nm (excitation/emission) and $\text{Lm2}= 380/520$ nm. The ratio Lm1/Lm2 was used to quantify if deformation lead to an increase in Fura-2 binding to calcium, which is indicative of Piezo1 activation.

3.6.5 Concentration and Viability Measurements

The concentration of single cell suspensions was counted using a haemocytometer. This is a specialised counting chamber of known volume. An engraved grid on the surface of the counting chamber allows the number of cells in a defined volume to be counted. Deformation Cytometry experiments were performed using concentrations of $1 - 2 \cdot 10^6$ cells/ml (Section 3.3).

Cell viability was measured using Trypan blue (Thermo Fisher Scientific). In a viable cell, the dye is unable to pass through the membrane and is not absorbed. However, in a dead cell where the membrane is compromised the dye is absorbed into the cell. Therefore, dead cells appear blue under a microscope and alive cells do not. Live cells are excluded from staining and this is known as a dye exclusion method. Viability is quantified using equation (3.4). All samples used throughout the thesis had viability $\geq 95\%$.

$$\% \text{ viable cells} = \frac{\text{Number of alive cells}}{\text{Number of total cells}} \cdot 100 \quad (3.4)$$

An Alamar Blue assay was also used for cell viability measurements. Healthy living cells maintain a reducing state within their cytosol. The “reducing potential” of cells converts alamarBlue® reagent (BIO-RAD) into a detectable fluorescent (or absorbent) product. The blue indicator dye Resazurin, is irreversibly reduced to the pink coloured and highly red fluorescent resorufin. Metabolic reduction is indicative of cell death, thus fluorescence is proportional to the number of living cells.

For the assay, cells were seeded at a density of 1×10^5 cells/ml in phenol red free media and then seeded in a 96 well plate with 100 μ l per well, 10 μ l of alamarBlue reagent was added and incubated for 1 hr. Fluorescence measurements were taken using a plate reader (SpectraMax® M2) with excitation at 560 nm and emission at 590 nm.

3.7 QD uptake in Cells

3.7.1 Quantum Dots

Quantum dots had a Cadmium telluride (CdTe) core and a Cadmium Sulfide (CdS) shell, these were provided by Abiral Tamang (University of Leeds) and were ~5 nm in size.

3.7.2 Microfluidic Uptake Protocol

Cells were detached into a single cell suspension, their suspension buffer was either DMEM media or PBS with 0.5% methyl cellulose. Quantum dots were added to the cells to achieve a final QD concentration of 100 nM. The sample was separated into two, the first half was set aside as a control to observe QD uptake in cells purely from incubation and via endocytosis. The second half of the sample was loaded into a 1 ml glass syringe to perform deformation cytometry, as described in section 3.3.

Cells were deformed at a range of flow rates and collected in Eppendorfs. After cell deformation, all samples were incubated for ~20 mins. Deformation caused pores to form in the cell membrane, this incubation time allowed time for the QDs to get inside the cells via a non-endocytic route. Cells were then centrifuged at 100 G for 5 mins, the supernatant was removed and replaced with PBS. This process was repeated once more with PBS and a final time to re-suspend cells in DMEM. The washing steps were to ensure any free QDs in the solution were removed, only QDs inside the cells should remain afterwards. Samples were then imaged using confocal fluorescence microscopy as described in section 3.4.4.

3.7.3 Analysis of QD uptake

Matlab was used to analyse confocal fluorescence images of cells containing QDs. Images were taken using a 10 x objective, and each fluorescent image was accompanied by a bright field image. The matlab function “imfindcircles” was used on the BF image, this function automatically detects circular objects in an image. The circles detected from the BF image were then overlaid onto the FL image. This allowed single cell measurement of the fluorescence intensity of each single cell in the image. For each flow condition, images of $N > 1000$ cells were used to quantify the fluorescence due to QD uptake. Average fluorescent intensity of different cell samples were then compared to each other.

4 Cell deformation in shear and inertial flows

This chapter contains the optimisation of cross-slot devices for measuring cell deformation at the stagnation point (SP) of an extensional flow junction, and the characterisation of the deformability of HL60 cells under different flow conditions. Cell deformability was measured as a function of flow rate using two distinct flow regimes, a shear-dominant regime and an inertia-dominant regime. Additionally, cell deformation and recovery were tracked as a function of time in order to extract multiple distinguishing parameters including an elastic modulus. This also allowed further investigation into the use of bulk averaging compared to single cell analysis (SCA) for measuring the mechanical properties of heterogeneous samples.

The deformability assays described in this chapter were subsequently used to probe cells treated with drugs to alter their cytoskeletal structure (chapter 5), and to investigate mechanical changes during colorectal cancer progression (chapter 6).

4.1 Cross-slot optimisation

4.1.1 Tracking particles in flow

The cross-slot microfluidic devices were first tested using suspensions containing 15 μm polystyrene microspheres (Thermo Fisher), the beads were suspended in PBS with 0.5% methyl cellulose resulting in a shear-dominant flow regime (with a viscosity of $\mu \cong 33 \text{ cP}$). Figure 4.1a shows a superimposed bright field image of a bead passing through the device at a flow rate of 50 $\mu\text{l}/\text{min}$, a frame rate of 42,000 fps was used with an exposure time of $\sim 6.8 \mu\text{s}$. The bead showed no deformation and was used as a control to compare to deformable objects (i.e. cells). HL60 (human leukaemia) cells were next deformed under the same flow conditions, Figure 4.1 is a superimposed bright field image of a cell passing through the device. The image shows that the cells undergo a maximum deformation at the SP of the extensional flow.

The deformation index DI ($DI=H/W$, equation (3.1)) was used to characterise deformability of the beads and HL60 cells at the SP. Figure 4.1c shows histograms of the DI of 205 beads and 2653 cells. Results showed a sharp peak at $DI=1$ for the beads (shown in blue), with the average being $DI \cong 1.04$. This confirmed the monodispersity of the sample and that they are an undeformable solid, this also confirmed that the high speed camera settings were satisfactory and no motion blur distorted the images which would lead to a skewed measurement of DI . The DI of HL60 cells showed a normal distribution (shown in red), which was fitted with a Log-normal function with a peak value of $b = 2.16 \pm 0.01$ and a FWHM of $w = 0.80 \pm 0.03$. This demonstrates that the majority of cells deform under these flow

conditions and also shows the heterogeneity of cells resulting in a range of deformability (from $DI=1 - 4.5$).

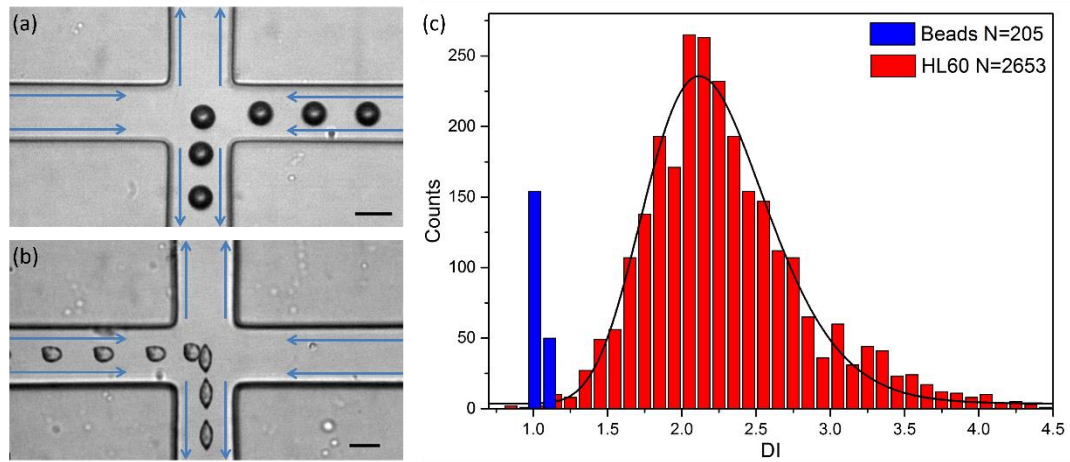


Figure 4.1 Comparison of the trajectory of a cell in a cross-slot microfluidic device compared to a polystyrene bead. (a) Bright field superimposed image of a $\sim 15 \mu\text{m}$ diameter bead passing through the extensional flow junction. The flow rate was $50 \mu\text{l}/\text{min}$ and the beads were suspended in PBS with 0.5% (w/v) methyl cellulose ($\mu \approx 33 \text{ cP}$). (b) A bright-field image of a HL60 cell passing through a device with identical geometry and flow conditions. (c) A histogram of the DI of $N=2653$ HL60 cells deformed at $Q = 50 \mu\text{l}/\text{min}$ (shown in red), the data is fitted with a Lognormal function. As a comparison a histogram of $N=205$ beads is overlaid (shown in blue), with the same bin size as the cell data.

The applied stress leading to deformation at the SP was proportional to the linear velocity of particles under flow (equation 2.24). The volumetric flow rate in m^3/s can be converted to linear velocity in m/s by dividing by the device channel dimensions, where the linear velocity will be a constant value in the inlet and outlet channels (where $v_{inlet} = v_{outlet}$) with the velocity dropping to ~ 0 at the SP. The linear velocity of the beads and cells was measured and compared to the theoretical values.

COMSOL Multiphysics was used to model flow in the inlet channel at a range of flow rates ($5 \mu\text{l}/\text{min}$ to $80 \mu\text{l}/\text{min}$), details of the model can be found in the appendix. Figure 4.2a shows the velocity magnitude through the channel cross-section in the y-z plane, for a volumetric flow rate of $5 \mu\text{l}/\text{min}$ where red is the highest velocity and blue the lowest velocity. This shows that flow is fastest at the channel centre and 0 at the channel walls. Figure 4.2b shows the velocity profile in the x-y plane of the extensional flow junction, including the stagnation point where the velocity is 0. The velocity profile across the mid-section of the channel is plotted in Figure 4.2c for a range of volumetric flow rates, showing a characteristic parabolic profile. From this, the maximum velocity v_{max} at the channel centre and the average velocity v_{avg} in the channel were plotted as a function of volumetric flow rate ($\mu\text{l}/\text{min}$) (Figure 4.3). The linear velocity was found for beads and HL60 over the same range of flow rates, using particle

tracking of high-speed videos (described in section 3.4). Figure 4.3, compares the linear velocity of beads and HL60 to theoretical values as a function of flow rate, with each dataset showing the expected linear relationship (all have $R^2 = 0.99$). Results show that the velocity of HL60 cells as a function of flow rate is the same as the average flow velocity found using simulations. This shows that not all cells pass through the centre of the channel, hence why $v_{HL60} < v_{max}$. For $Q > 20 \mu\text{l}/\text{min}$, the polystyrene beads travelled faster than HL60 and v_{avg} . This may be because the beads are much stiffer (non-deformable) and will be more focused toward the channel centre, increasing their average velocity.

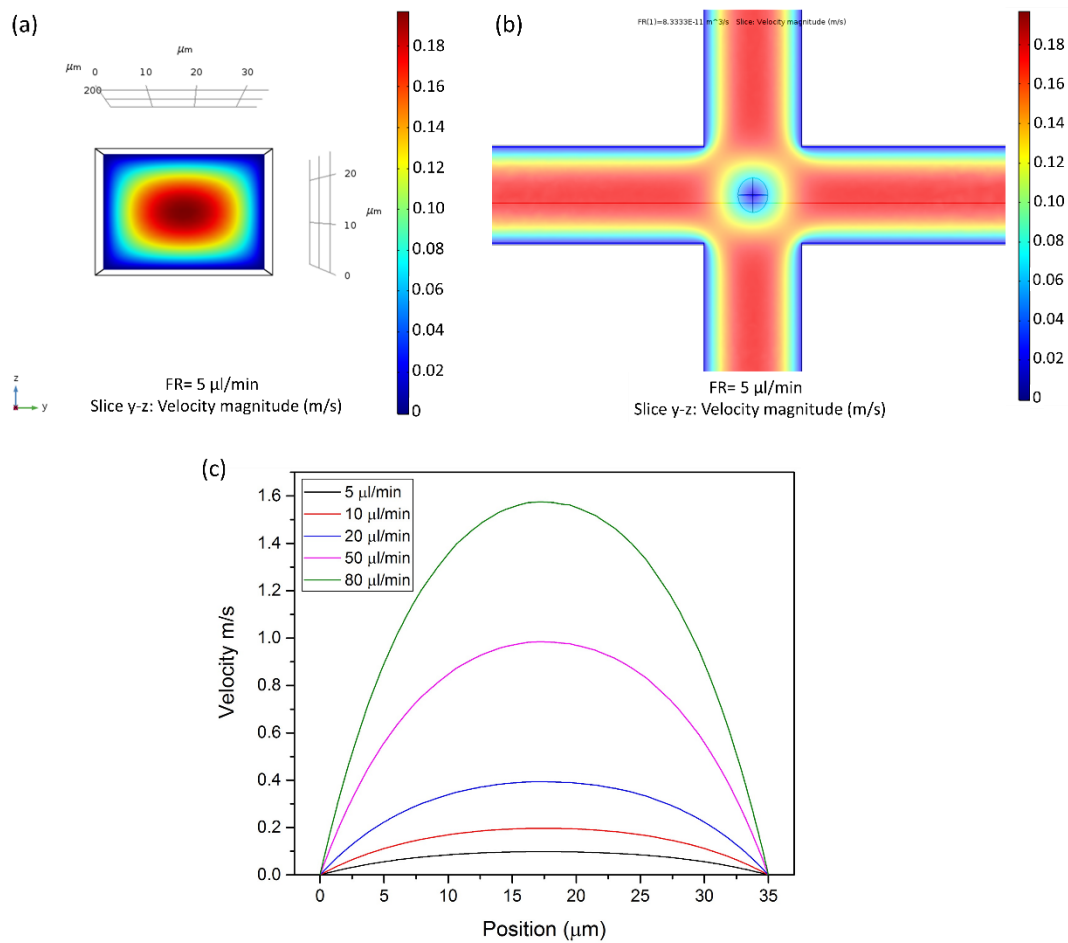


Figure 4.2 COMSOL simulations of flow in a cross-slot microfluidic device. (a) A y-z cross-section of a microfluidic channel of width 35 μm and height 25 μm showing the velocity magnitude when flow through the channel is at a rate of 5 μl/min. (b) An x-y cross-section of the extensional flow junction showing the velocity magnitude when flow through the inlet and outlet channels and around the stagnation point. (c) The parabolic velocity profile through the middle of the channel in the y direction. Showing maximum velocity at the centre which decreases to 0 at the channel walls.

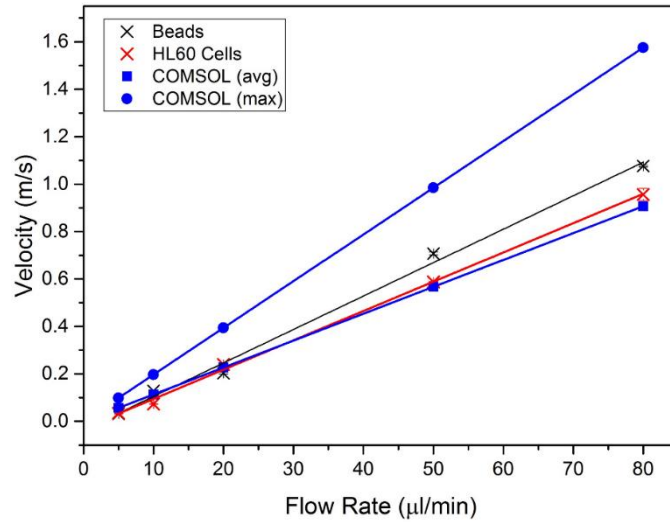


Figure 4.3 The velocity (m/s) as a function of flow rate ($\mu\text{l}/\text{min}$) of polystyrene beads and HL60 cells travelling through a rectangular channel. This is compared to simulations used to calculate the fluid velocity in the channel, including the maximum velocity down the centre and the average velocity across the channel in the y -direction.

4.1.2 Varying Flow Rate

Deformability as a function of flow rate was investigated using HL60 cells and $15\ \mu\text{m}$ polystyrene beads. Both were suspended in PBS with 0.5% methyl cellulose (shear-dominant $\mu \cong 33\ \text{cP}$) and the flow rate range was $5 \leq Q \leq 80\ \mu\text{l}/\text{min}$. Figure 4.4 shows density scatter plots of DI as a function of initial diameter of $1279 < n < 2653$ HL60 cells deformed at different flow rates, where red represents the highest density area and dark blue the lowest density area. The plots also include the DI of $55 < n < 507$ beads as a function of initial diameter, shown in magenta. The mean average DI of cells and beads are marked by dashed lines. Results show that the DI of cells increases with flow rate whereas the DI of the rigid beads does not.

Figure 4.5 shows a graph of average $DI \pm SE$ of cells and beads as a function of flow rate. This shows that HL60 deformation increases with flow rate with the trend showing logarithmic growth. Do due their inverse relation, this trend can be fitted with an exponential decay function ($y = Ae^{-\tau x} + y_0$) shown in red with $R^2 = 0.99$. The DI of beads does not increase with flow rates and is ~ 1 for all flow rates, this dataset is fitted with a linear fit with a fixed gradient of 0 resulting in $R^2 = 0.91$.

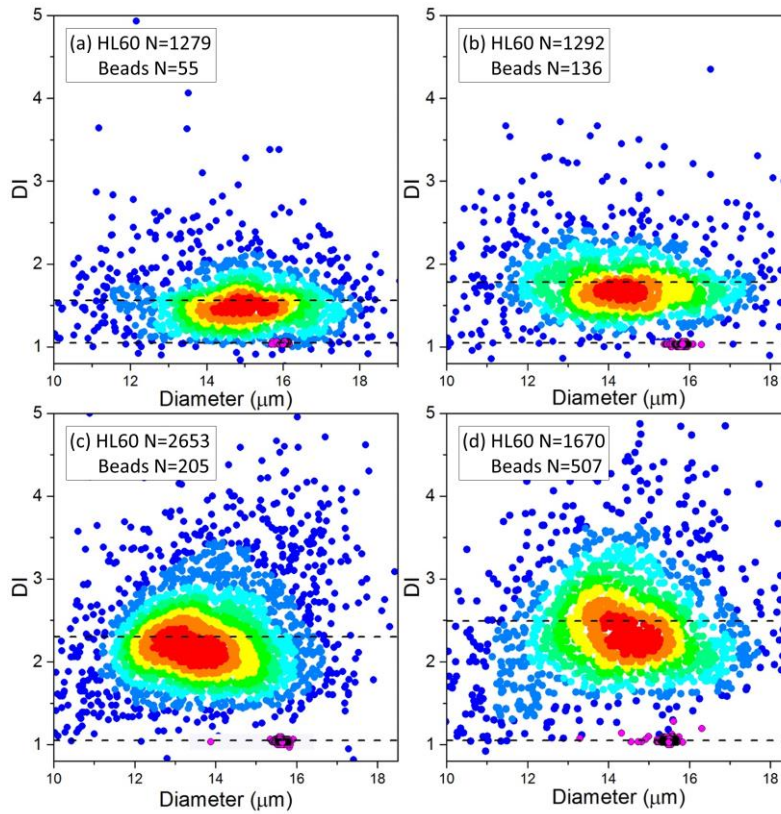


Figure 4.4 Density scatter plots of DI as a function of initial diameter of HL60 cells deformed at various flow rates whilst suspended in PBS with 0.5% (w/v) methyl cellulose. Where red shows the most densely populated areas and dark blue the least populated, a dashed line is used to show the average DI. As a comparison the DI as a function of initial diameter of $\sim 15.5 \mu\text{m}$ beads is shown in magenta. The beads were passed through the device under the same flow condition, the average DI of the beads is also shown with a dashed line. For (a) $Q=5 \mu\text{l/min}$, (b) $Q=20 \mu\text{l/min}$, (c) $Q=50 \mu\text{l/min}$ and (d) $Q=80 \mu\text{l/min}$.

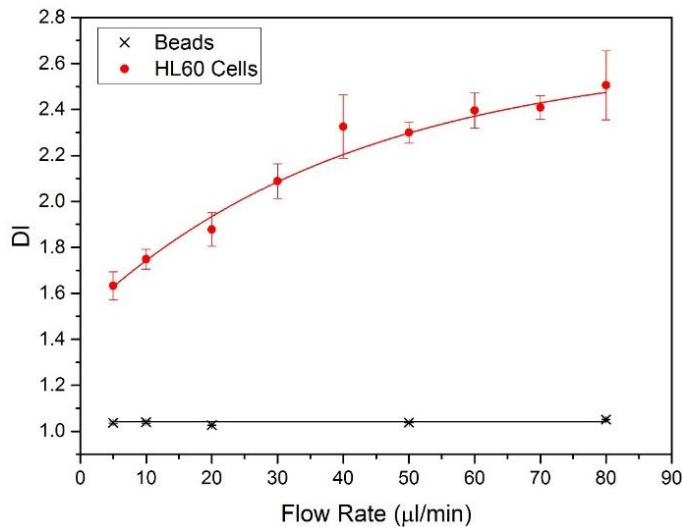


Figure 4.5: A plot of the average $DI \pm SE$ of HL60 cells deformed over a range of flow rates in a shear-dominant flow regime ($\mu \cong 33 \text{ cP}$). This is fitted with an exponential decay function, shown in red. As a comparison the average $DI \pm SE$ of polystyrene beads is shown, this has a linear fit (shown in black).

4.1.3 Varying Velocity Threshold

Cells passing through a cross-slot microfluidic device experience a different applied stress dependant on their initial position as they traverse the inlet before entering the extensional flow junction. An ideal cell would travel at a velocity (v_{inlet}) centrally through the inlet before entering the junction and decelerating to a velocity of 0 at the SP, before accelerating into the outlet channel and returning to its initial velocity ($v_{inlet}=v_{outlet}$). However, many cells are not central in the channel when entering the extensional flow junction and therefore do not pass through the SP. Here, the closer their proximity to the SP the bigger the velocity drop and the larger the applied stress on the cell. Cells must be selected which undergo the same applied stress, in order to compare measurements made between samples. This can be achieved by looking at the velocity profile of each cell traversing the extensional flow junction.

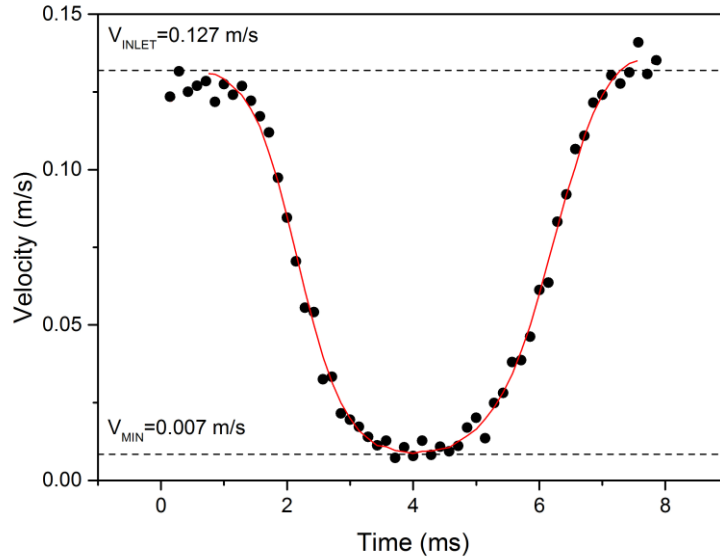


Figure 4.6 The velocity profile of a HL60 cell as it passes through the extensional flow junction of a cross-slot microfluidic device, where the volumetric flow rate was $5 \mu\text{l}/\text{min}$. The cells inlet velocity, before it reaches the extensional flow junction, is marked with a dashed line where $v_{inlet}=0.127 \text{ m/s}$. The cells minimum velocity where it is closest to the SP is marked with a dashed line where $v_{min}=0.007 \text{ m/s}$.

Figure 4.6 shows an example velocity profile of a cell travelling through the extensional flow junction at $5 \mu\text{l}/\text{min}$, a sine function is fitted (shown in red). The initial velocity of the cell is $v_{inlet} = 0.127 \text{ m/s}$, which drops to a minimum velocity of $v_{min} = 0.007 \text{ m/s}$ when the cell is closest to the SP. The velocity threshold Δv is defined by equation 4.1, where $\Delta v = 1$ represents cells which decelerate to a velocity of 0 at the SP and $\Delta v = 0$ represents a cell which undergoes no deceleration ($v_{min} = v_{inlet}$).

$$\Delta v = \frac{v_{inlet} - v_{min}}{v_{inlet}} \quad 4.1$$

As Δv is proportional to applied stress, cells deformed at higher Δv deform more and DI increases. Figure 4.7 shows an example dataset of the average $DI \pm SE$ as a function of Δv , where only cells deformed with Δv greater than this threshold were used for each average. The dataset is fitted with a dose-response function (shown in red). For a threshold of $\Delta v = 0.50$ the average is $DI = 1.33 \pm 0.02$. As Δv is increased further there is a step increase in DI which plateaus at a value ~ 1.41 (found from the fit), which is significantly larger than thresholds of $\Delta v < 0.60$ and outside the range of error. For thresholds $\Delta v > 0.8$ the error begins to significantly increase due to the reduction of cell deformation events included towards the average, without a significant change to the average DI . A threshold of $\Delta v = 0.75$ was found to be sufficient for distinguishing cells deformed at or near to the SP which undergo the same applied stress. Even though Figure 4.7 shows the plateau region was reached at $\Delta v = 0.65$, adding a 10% increase to $\Delta v = 0.75$ ensured measured DI was within the plateau region across multiple datasets. Figure 4.7b shows a scatter graph of DI as a function of Δv for the same dataset, which also demonstrates the general increase in DI as a function of Δv . In this example, the total number of cells was $N=433$, with a velocity threshold of $\Delta v = 0.75$ the sample size was reduced to $N=77$ cells ($\sim 20\%$). Only 11 cells had $\Delta v > 0.9$, which would only leave $\sim 2.5\%$ of the total number of events.

Throughout the thesis the DI index of different cell samples was measured across flow conditions, unless stated otherwise a velocity threshold of $\Delta v = 0.75$ was used to find the average DI to ensure measurement of the average deformability of cells undergoing the same applied stress.

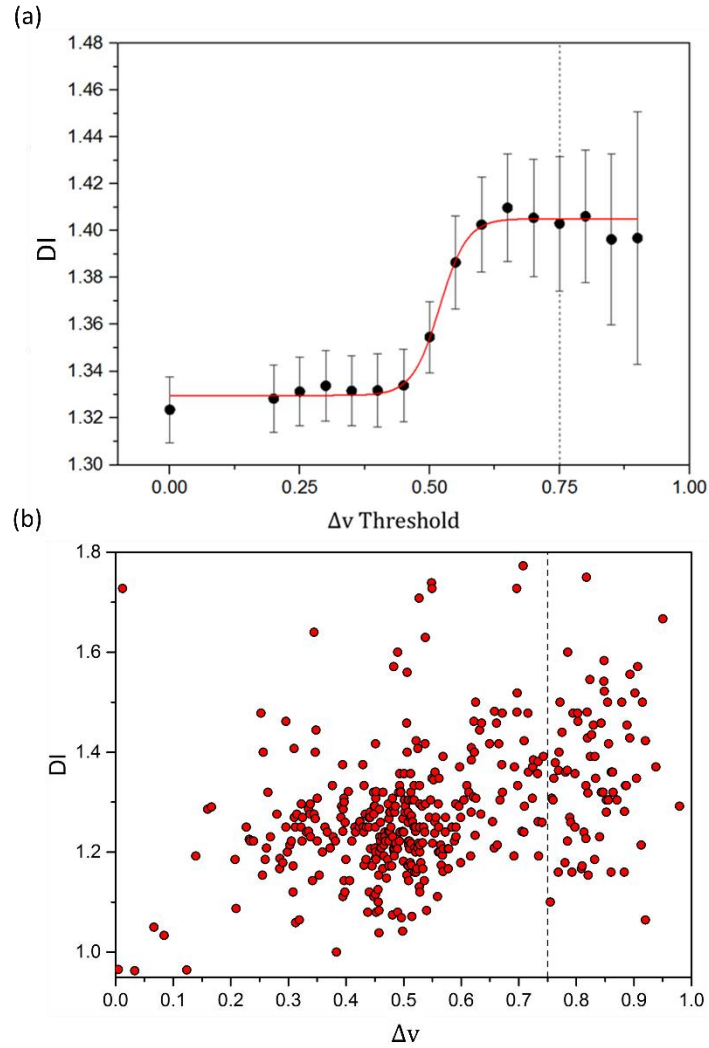


Figure 4.7 (a) The average $DI \pm SE$ of HL60 deformed at $40 \mu\text{l}/\text{min}$ in 0.24% methyl cellulose buffer, as a function of Δv threshold. When no threshold is applied the average DI was taken of the entire dataset $N=433$, when using a velocity threshold of Δv the average DI was taken of the remaining cells. (b) A scatter graph the DI of the HL60 cells as a function of Δv . The shows a general step increase in DI as Δv increases. The threshold chosen as $\Delta v > 0.75$, which is marked by the dashed line.

4.1.4 Varying Channel Dimensions

The channel dimensions of the microfluidic device were varied in order to investigate the effect on cell deformation. This was done by changing the height H of the channels and the width W of the inlet and outlet channels. Figure 4.8 shows the four device geometries tested and includes bright field images of a cell before deformation (in the inlet) and deforming at the SP. The device shown by Figure 4.8a has the smallest channel dimensions, where $H=25 \mu\text{m}$ and $W=35 \mu\text{m}$. The three other devices have $H=35 \mu\text{m}$ and increasingly wider channel widths, the widest being $W=65 \mu\text{m}$ (Figure 4.8d).

Images for each geometry were taken at flow rate corresponding to deformations occurring at $DI \cong DI_{max}$ and a shear-dominant flow regime was used ($\mu \cong 33 \text{ cP}$). The images show that

as the channel dimensions become more comparable to the size of the cell, there is some deformation seen in the inlet channel and cells appear more “bullet-shaped” instead of circular. This is the same deformation described by Otto *et al.* (2015) and is due to shear viscous forces acting due to proximity to the channel wall [96]. Previous works have shown that deforming cells multiple times can lead to a change in cell deformability [187]. Varying channel dimensions allowed investigation into whether any shear-stresses due to confinement may change the measured deformability at the SP.

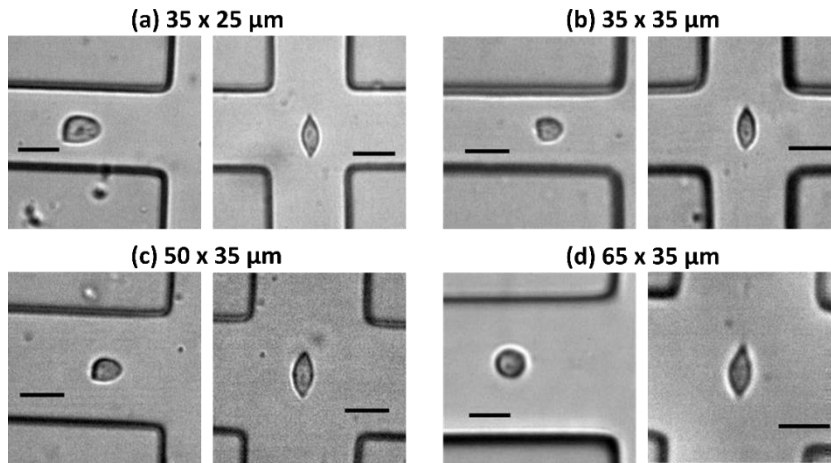


Figure 4.8 Bright field images of HL60 cells deforming at $DI \cong DI_{max}$ in a shear-dominant flow regime ($\mu \cong 33$ cP). Cells were deformed in different channel geometries with a given width W and height H , where (a) had $W=35$ μm and $H=25$ μm , (b) had $W=35$ μm and $H=35$ μm , (c) had $W=50$ μm and $H=35$ μm and (d) had $W=65$ μm and $H=35$ μm . Scale bars are 20 μm .

HL60 cells were deformed over a range of flow rates in a shear-dominant flow regime ($\mu = 33$ cP), this was repeated using the four device dimensions described by Figure 4.8. Figure 4.9a shows a plot of the average DI of HL60 as a function of flow rate for the different datasets, which are fitted with an exponential function. To more accurately compare deformability, the data was plotted as a function of flow velocity as opposed to flow rate (Figure 4.9b). In the shear-regime linear velocity is proportional to applied stress (equation 2.24), so this allowed comparison of cell deformability when applying the same stress in different channel dimensions. Results show mostly no significant changes in measured deformability due to device dimensions. No discernible change or trend could be seen for these geometries; (35 x 25) μm , (35 x 35) μm and (50 x 35) μm . The largest channel width used ($W=65$ μm) showed some increase in DI for $v < 0.6$ m/s.

The exponential decay function fitted to each dataset in Figure 4.9 was used to find the extrapolated value DI_{max} . Where the trend tends asymptotically towards a maximum value DI_{max} . Figure 4.10 shows the values of DI_{max} found for each channel geometry, the averaged value is shown by a dashed line with the SE highlighted in grey. This shows that all values of

DI_{max} are within error of each other, and that channel geometry had no effect on the maximum cell deformation. Overall, results show that no trend can be seen between increasing channel dimensions and changes in measured DI at a set applied stress. This suggests that any initial viscous stresses due to channel confinement do not alter the mechanical properties in a way that measured DI at the SP is affected.

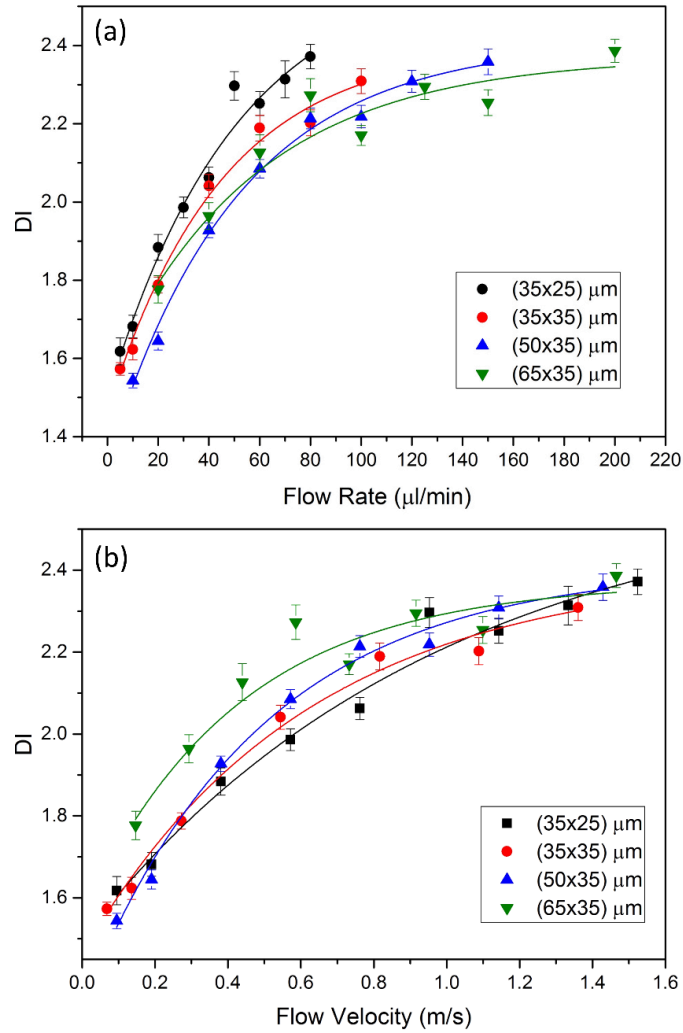


Figure 4.9 HL60 cells were deformed in microfluidic cross-slot devices at a range of flow rate. The flow regime was shear-dominant ($\mu \approx 33$ cP) and device dimensions are labels channel width W by channel height H ($W \times H \mu\text{m}$). (a) A plot of the average $DI \pm SE$ of HL60 cells as a function of flow rate in different device geometries. (b) A plot of the average $DI \pm SE$ of HL60 cells as a function of flow velocity in different device geometries.

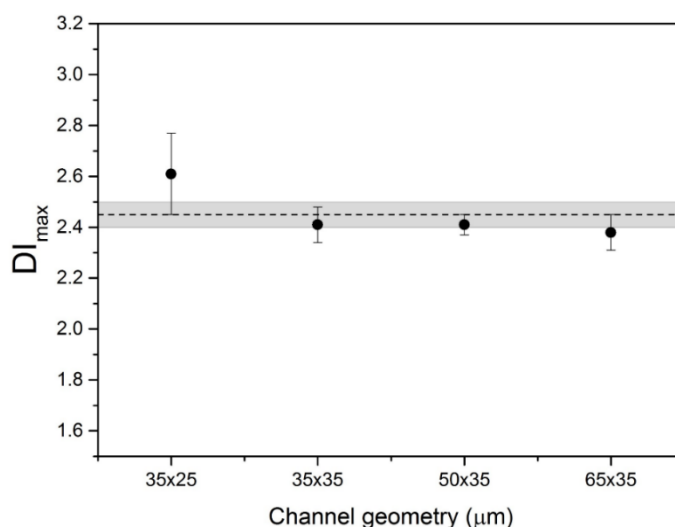


Figure 4.10 A plot of $DI_{max} \pm SE$ of HL60 cells deformed in microfluidic cross-slot devices with different channel dimensions. The dashed line shows the average of the four values, with the SE of the average highlighted in grey. This shows all values of DI_{max} are within error of each other.

Section 4.1.3 described the use of a velocity threshold of $\Delta v > 0.75$ to discard events which do not deform at or near the SP. This thresholding was used for determining the values of DI in Figure 4.9 as a function of flow rate. Figure 4.11 shows bar graphs of the percentage of events collected which had $\Delta v > 0.75$ as a function of flow rate for the four geometries. Figure 4.11a shows that using the smallest channel dimensions (35 x 25) μm , resulting in 40-70% of the collected events being included in the calculated of DI . For $Q > 40 \mu\text{l}/\text{min}$, $>60\%$ of events were above the velocity threshold. Figure 4.11b shows that increased channel height from 25 μm to 35 μm resulting in $<50\%$ of events being above the velocity threshold for all flow rates. Here, 30-50% of collected events were included in the calculation of DI . Subsequent increases in channel width also led to a general reduction in the % of cells included in calculation of DI . Figure 4.11 shows that for the largest channel dimensions (65 x 25) μm , $<50\%$ of events were above the velocity threshold for all flow rates. Particularly, for $Q < 60 \mu\text{l}/\text{min}$ less than 20% of values were above the velocity threshold.

In summary, results showed that even if cells experience an increased viscous-shear force due to channel confinement, there is no change to measured deformability at the SP when the same stress is applied. Figure 4.11 showed that by reducing the channel height and width a higher percentage of cells passing through the device are above the velocity threshold ($\Delta v > 0.75$). This is expected as increased channel confinement will increase wall effects on the cells. Therefore, by using the geometry (35 x 25) μm an increased measurement throughput can be achieved. Unless stated otherwise, this is the geometry used for subsequent deformation cytometry experiments in this thesis.

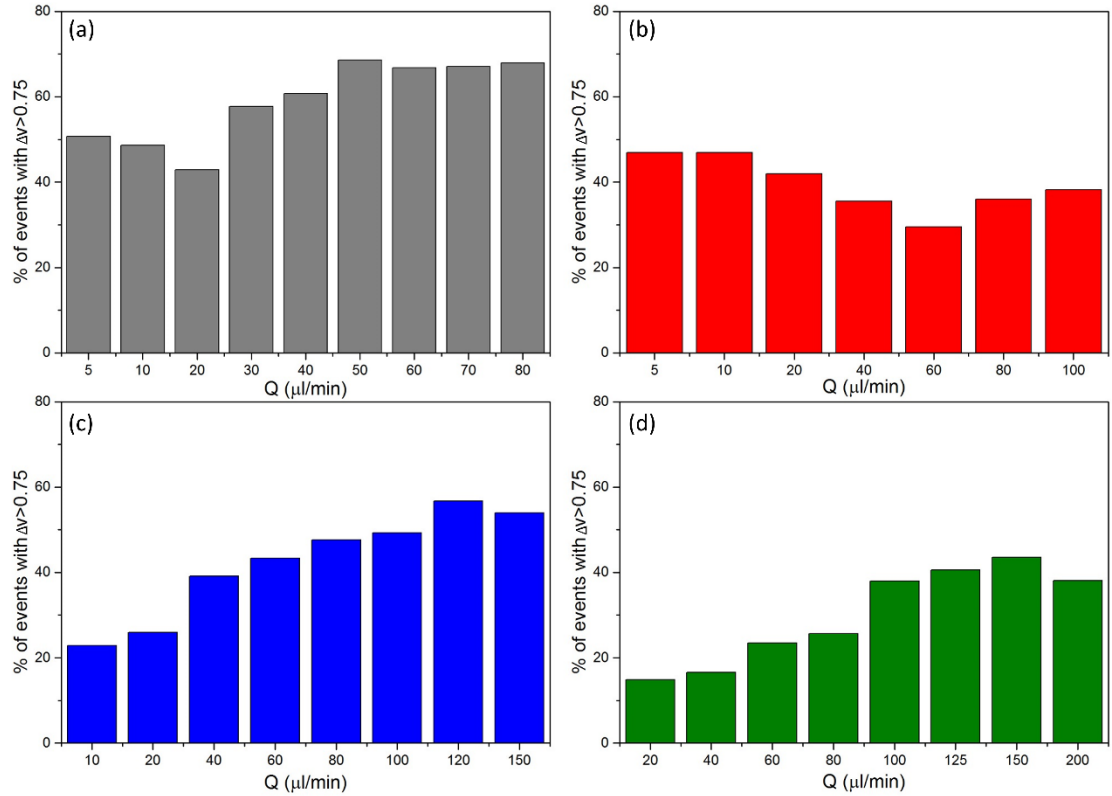


Figure 4.11 Bar graphs showing the percentage number of cell events with $\Delta v > 0.75$ when HL60 cells were deformed microfluidically at a range of flow rates, for different channel dimensions. Cell events with $\Delta v < 0.75$ were discarded and not used for calculating DI . This was calculated for channels of (a) $(35 \times 25) \mu\text{m}$, (b) $(35 \times 35) \mu\text{m}$, (c) $(50 \times 25) \mu\text{m}$ and (d) $(65 \times 25) \mu\text{m}$.

4.2 Cell deformation across flow regimes

4.2.1 Varying suspension buffer viscosity

HL60 cells were deformed in a cross-slot microfluidic device as the SP of an extensional flow junction. Their deformability was measured using the deformation index DI when the cell is at or near the SP. A range of stresses were applied to the cells by changing the cell velocity and the viscosity of the buffer the cells were suspended in.

Figure 4.12a shows DI as a function of flow rate Q for four viscosities of suspension buffer which were; PBS (1 cP), PBS with 0.24% methyl cellulose (11.1 ± 0.1 cP), PBS with 0.35% methyl cellulose (23.8 ± 0.1 cP) and PBS with 0.5% methyl cellulose (33.4 ± 0.3 cP). A rheometer was used to measure the viscosities, this data can be found in the appendix (Figure S1). Here, the range of Q was 0-400 $\mu\text{l}/\text{min}$ for the lowest viscosity suspension buffer. At higher viscosities the maximum Q was limited, the back pressure in the channels increased with viscosity which lead to device failure (leakages or device delamination) at higher flow rates. For each dataset, DI increases asymptotically toward a maximal deformation value DI_{max} . This value was found by fitting an exponential decay function to each dataset, each

fitting had an $R^2 \geq 0.98$. Figure 4.12b shows an image of cell deforming at $\sim DI_{max}$ for each dataset, accompanied by a superimposed colour contour plot. This shows how deformation varies as a function of time, going from blue where the cell approaches the extensional flow junction to red where deformation occurs at the SP.

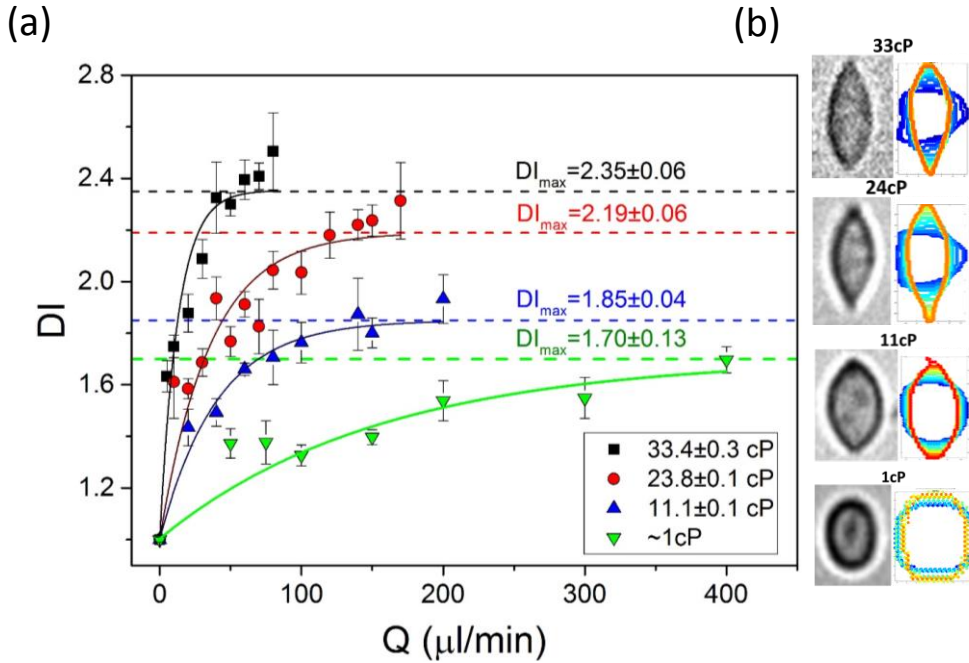


Figure 4.12 DI as a function of Q for HL60 cells in four different suspension buffers with viscosity ranging from 1 to 33 cP. $DI \pm SE$ was averaged from multiple cell events combined from $N=3$ repeats; each data point includes $30 > n > 500$ cell events. Each data set is fitted with an exponential decay function. (b) Images of a cell deformation for each flow condition where $DI \cong DI_{max}$. They are accompanied by superimposed color contour plots that show how the cell shape changes as a function of time.

Section 2.5.3 discussed how two distinct flow regimes, shear and inertial, can be defined. Where $Re > 40$ defines the beginning of the inertial regime. This shows that the low viscosity dataset (1 cP) occurs in the inertial regime, whereas the other three datasets move increasingly into the shear regime as viscosity is increased. In the inertia-dominant regime ($\mu = 1 \text{ cP}$), the Reynolds number is $Re > 40$ for $Q > 11 \mu\text{l}/\text{min}$. In the most shear-dominant regime ($\mu = 33.4 \text{ cP}$), the Reynolds number is $Re < 6$ for the entire range of flow rates. Supporting video 1 shows examples of HL60 deforming in this regime at $Q=80 \mu\text{l}/\text{min}$. Figure 4.13 shows that DI_{max} increased linearly as a function of suspension buffer viscosity. This indicates that as the flow regime becomes more shear dominant, higher cell deformations can be achieved for lower flow rates. Additionally, Figure 4.12b shows that as flow regime becomes more shear dominant the cell shape at maximal deformation changes from elliptical at low viscosity to tear-shaped at higher viscosities, the perimeter of the cell changes from convex to concave.

The low Reynolds number and increasingly shear-dominant regime is indicative of the observed change in shape.

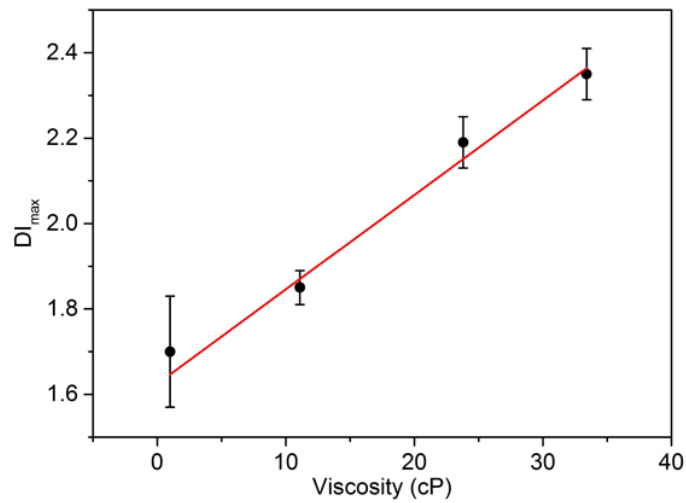


Figure 4.13 A graph of the extrapolated value DI_{max} associated with the deformability of HL60 cells as a function of flow rate for four different viscosities of suspension buffer. DI_{max} varies linearly as a function of viscosity.

4.2.2 Inertial Regime

Measurements of DI in the inertial regime ($\mu = 1$ cP) were extended to $Q = 600$ $\mu\text{l}/\text{min}$, shown by Figure 4.14. As discussed in the previous section, for $Q \leq 400$ $\mu\text{l}/\text{min}$ the DI tended towards a plateau value DI_{max} . For $Q \geq 400$ $\mu\text{l}/\text{min}$, DI increased nonlinearly until $Q = 600$ $\mu\text{l}/\text{min}$. For $Q > 600$ $\mu\text{l}/\text{min}$ the cells begin to rupture and visibly break apart at the extensional flow junction, and DI could no longer be measured. Figure 4.14 includes example images of cells deforming at the SP at different flow rates. The deformations at 50 $\mu\text{l}/\text{min}$ and 300 $\mu\text{l}/\text{min}$ are both relatively low and show an ellipsoidal shape which is characteristic of an inertia-dominant regime. Comparatively, the cell is highly strained at 600 $\mu\text{l}/\text{min}$ and shows sharply pointed ends. This is further indication of the change in trend seen for flow rates above and below $Q = 400$ $\mu\text{l}/\text{min}$.

The stress corresponding to a flow rate of 400 $\mu\text{l}/\text{min}$ was thus defined as the *yield stress* of the cell. The *yield stress* is thought to be associated with the breakdown of the cells internal structure (such as actin depolymerisation), leading to the sudden nonlinear increase in deformation at higher applied stresses. Supporting videos 2-4 show examples of HL60 deforming at flow rates below the *yield stress* ($Q = 200$ $\mu\text{l}/\text{min}$), at the *yield stress* ($Q = 400$ $\mu\text{l}/\text{min}$) and above the *yield stress* ($Q = 600$ $\mu\text{l}/\text{min}$). The flow rate $Q = 600$ $\mu\text{l}/\text{min}$ was defined as the cell's *failure point* which has an associated maximum strain of the cell before rupture, called the critical deformation where $DI_{crit} = 2.84 \pm 0.27$. The associated *yield stress* and *failure*

point are suggestive of the ability of cells to recovery post deformation, and their subsequent viability. These values may also be useful parameters for distinguishing between cell types.

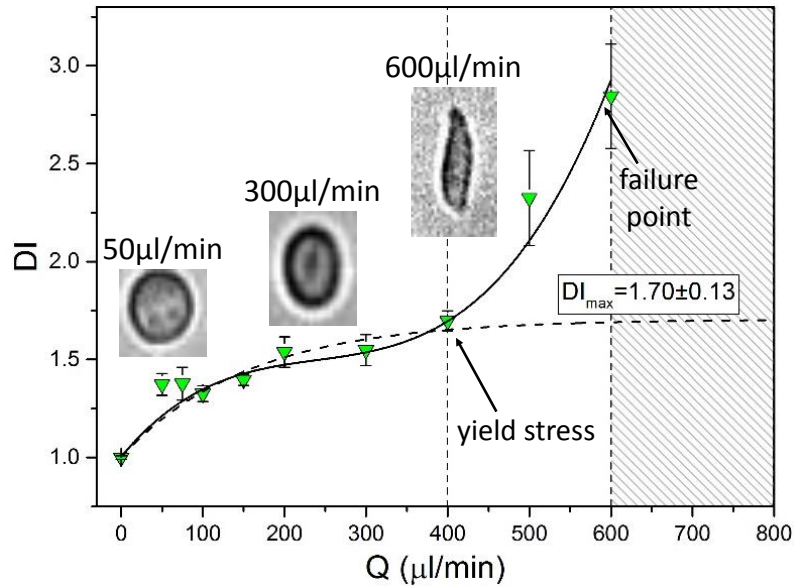


Figure 4.14 The average $DI \pm SE$ of HL60 cells versus Q , in an inertial-dominant flow regime ($\mu = 1 \text{ cP}$). DI was averaged from multiple cell events combined from $N=3$ repeats; each data point includes $30 > n > 500$ cell events. For $Q \leq 400 \mu\text{l}/\text{min}$ the dataset was fitted with an exponential decay function, to extrapolate the value DI_{max} , shown by the dashed line. The entire dataset is fitted with a third order polynomial function, shown by the black line.

4.2.3 Deformation as a function of force

Figure 4.12 and Figure 4.13 introduced four datasets of HL60 cells deformed over a range of flow rates suspending in four different viscosities of suspension buffer. These results showed that lower flow rates can be used to achieve higher strains when the regime is more shear-dominant (i.e. high viscosity and low Re). However, an inertia-dominant regime showed a unique behaviour where high-strain deformations can be achieved above an associated *yield stress* of the cell.

The different mechanical responses of cells dependent on flow regime was further investigated by plotting DI as a function of force instead of flow rate (Figure 4.15). The total force on the cell (F_T) was calculated using equations 2.23 and 2.24 which sums the shear and inertial contributions of force. Figure 4.15 shows that for the same total force, F_T , the cells were generally more deformable in a shear-dominant regime. As the regime becomes more shear-dominant the same force can be applied at lower flow rates, thus the magnitude of the force is the same but the time over which the stress is applied increases (lower strain rate). Therefore, the cells show a stiffening behaviour which means that if the same force is applied more quickly the subsequent strain is lower. Cells are inherently viscoelastic and are known to exhibit strain-stiffening behaviour under certain conditions [147].

However, this strain-stiffening is only observed for forces below the previously defined *yield stress* behaviour seen in the inertia-dominant regime. The *yield stress* is equivalent to $F_T = 0.58 \mu\text{N}$, below this DI is greater in the shear-regime at the same applied force. For $F_T > 0.58 \mu\text{N}$, the DI begins to surpass that of the shear regime. This coincides with the sub-structural breakdown, leading to softening of the cells.

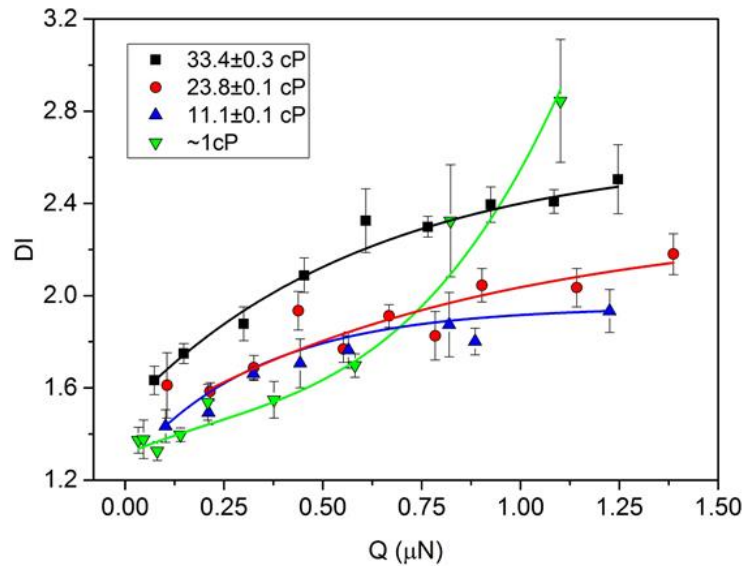


Figure 4.15 The DI of HL60 cells as a function of applied force (μN), where F_T is the sum of the shear force (F_S) and inertial force (F_C). The four datasets vary the viscosity of the cell suspension buffer, ranging from 1 cP (where the inertial force dominates (F_T)) to 33 cP (where the shear force dominates F_T). DI was averaged from multiple cell events combined from $N=3$ repeats, each data point includes $30 > n > 500$ cell events.

4.3 Cell viability after deformation

4.3.1 Shear Regime

The viability of cells was measured post-deformation at the SP of a cross-slot microfluidic device. HL60 cells were deformed in a shear-dominant flow regime (using PBS with 0.5% w/v of methyl cellulose ($\mu = 33 \text{ cP}$) over a range of flow rates Q .

Samples were collected off-chip and a trypan blue viability assay was performed (described in section 3.6.5). Before performing the assay, cells were centrifuged to a pellet at 100 g for 5 mins and resuspended in PBS. Each deformed sample was accompanied by a control sample, which derived from the same initial sample but did not undergo any microfluidic deformation. Controls were outside of the incubator for the same time period as deformed samples and went through the same centrifugation and resuspension steps. This was to ensure that any observed viability drop was due only to microfluidic deformations, and not due to stresses associated with resuspending cells in a buffer of higher viscosity. Results are summarised by Figure 4.16, which shows that there was no significant drop in viability associated with cell deformation

in this regime over the entire range of flow conditions. The viability remained >95% for the range of flow rates, which encompass the flow rates used for measuring *DI* in the shear-dominant regime throughout the thesis.

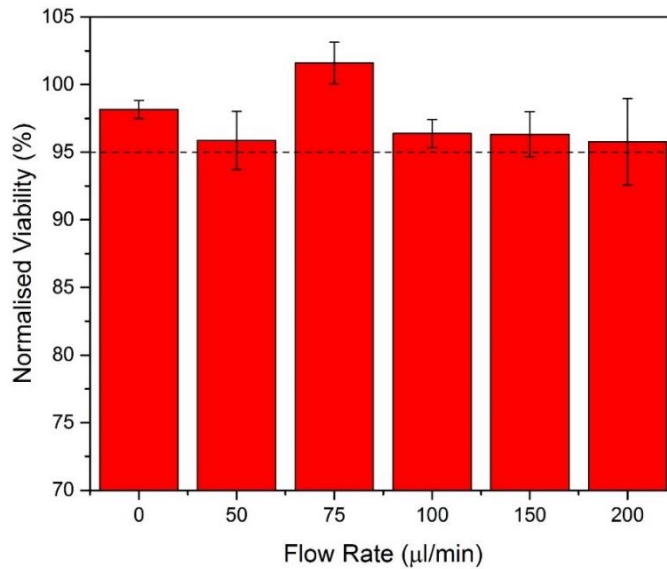


Figure 4.16 The viability of HL60 cells after being deformed on-chip over a range of flow rates, where the flow regime was shear dominant ($\mu \cong 33$ cP). Here, the viability of the deformed sample is normalised to a control sample which was not deformed to ensure any changes were only due to microfluidic deformation. Results show that the viability did not drop significantly and was >95% for the entire range of flow rates.

4.3.2 Inertial Regime

Cell viability was measured post-deformation at the SP of a cross-slot microfluidic device, where HL60 cells were deformed in an inertia-dominant flow regime (suspended in PBS, $\mu = 1$ cP) over a range of flow rates Q . Trypan blue viability assays were performed on samples collected off-chip. A control sample accompanied each deformed sample, the control sample derived from the same initial sample and was out of the incubator for the same time period but was not deformed on-chip. Figure 4.17 shows that there was no significant change in viability for $Q \leq 600$ $\mu\text{l}/\text{min}$, where viability remained >90% for this range of flow rates. For $Q > 600$ $\mu\text{l}/\text{min}$, the viability dropped to <50%. This substantial viability drop occurs for flow rates above the *failure point* where cell rupture was observed during microfluidic deformation.

Figure 4.18a shows phase contrast images of HL60 cells collected after deformation at 600 $\mu\text{l}/\text{min}$ and 800 $\mu\text{l}/\text{min}$ and a sample which was not deformed. The control and 600 $\mu\text{l}/\text{min}$ sample show a similar rounded morphology, whereas the 800 $\mu\text{l}/\text{min}$ sample shows a significant reduction in rounded cells and an increase in cell debris, potentially from internal components being released from ruptured cells. Further, any permanent shape change in cells

post-deformation was measured from these images by calculation of the circularity D_C (using equation (3.3 shown by Figure 4.18b). A perfect circle has $D_C = 0$, and shapes which deviate from a perfect circle have $D_C > 0$. The control and 600 $\mu\text{l}/\text{min}$ samples have relatively low values of D_C with average values of $D_C = 0.18 \pm 0.08$ and $D_C = 0.17 \pm 0.09$. The 800 $\mu\text{l}/\text{min}$ sample shows a general increase in scatter of D_C with a population remaining similar to the control and a second population with $D_C > 0.2$ corresponding to the increase in cell debris. These results validate that for $Q > 600 \mu\text{l}/\text{min}$ a drop in viability is associated with on-chip cell destruction leading to some cells not recovering their original shape.

The *failure point* of HL60 cells ($Q = 600 \mu\text{l}/\text{min}$) represents a limit below which live cells could be mechanically phenotyped by on-chip deformation and then collected for potential further studies, such as chemical phenotyping via Raman spectroscopy [2] or gene sequencing.

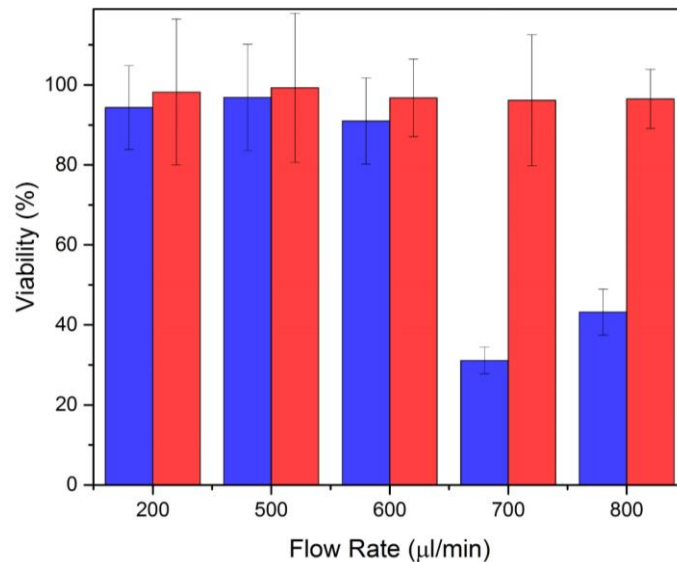


Figure 4.17 The viability of HL60 cells after microfluidic deformation at a range of flow rates Q (blue) in the inertial regime ($\mu=1 \text{ cP}$), compared to a control which was not deformed (red). The viability assay was performed using Trypan blue dye exclusion method.

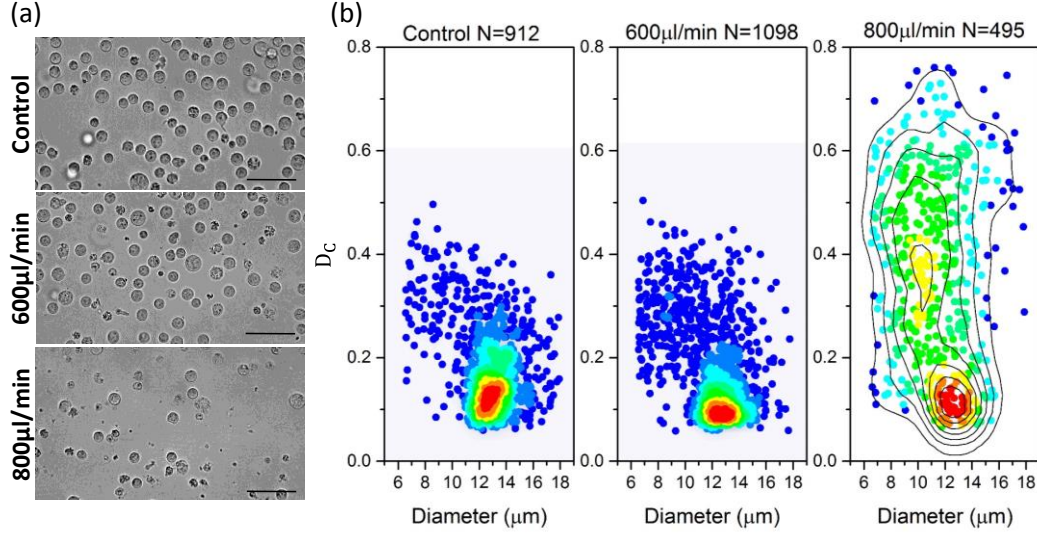


Figure 4.18 Shape analysis of HL60 post-deformation. (a) Phase contrast images of HL60 cells post-deformation in the inertial regime ($\mu = 1$ cP). Scale bar $40 \mu\text{m}$. (b) Density scatter plots of HL60 cell shape, using D_c as a function of diameter, comparing cells which were not deformed to those which were deformed at $600 \mu\text{l/min}$ and $800 \mu\text{l/min}$.

4.4 Tracking cell deformation and recovery

4.4.1 Single cell tracking in the shear regime

The on-chip deformation and recovery of HL60 cells was tracked as cells passed through the SP of an extensional flow junction. Here, cell shape was measured using strain $\varepsilon = (H - W)/(H + W)$, where H is the height of the cell and W is the width of the cell, introduced in section 3.4 by equation (3.2).

Figure 4.19a shows the average ε of $N=50$ cells as a function of time, deformed at a flow rate of $5 \mu\text{l/min}$ in a shear dominant regime ($\mu=33$ cP). A low-velocity and shear-dominant regime was chosen for tracking deformation and recovery, as this allowed a reduced frame rate (7000 fps) and a maximized field of view for operation of the high-speed camera (discussed in section 3.4.2). Supporting video 5 shows examples of HL60 deforming under these conditions. The sign of the strain value describes the cell direction, which changes as the cell moves from the inlet to the outlet as they are perpendicular to each other, whereas magnitude describes the amount the cell is strained.

Figure 4.19b shows a superimposed bright field image of a cell as it moves through the inlet channel, deforms at the SP, and then recovers to its original shape in the outlet channel. The strain trace in Figure 4.19a shows that as cells traversed from the inlet to the SP there was an increase in ε ; this was fitted with an exponential decay function with an associated deformation time τ_d . The strain ε continued to increase as the cell moved from the SP to the outlet, reaching a maximum $\varepsilon_{max} = 0.18 \pm 0.04$. As the cells travelled through the outlet, the strain ε

decreased exponentially with a relaxation time τ_r . The initial strain (before the cell entered the extensional flow junction) ε_0 was also found and compared to the final strain ε_∞ , found by extrapolation of the exponential function fitted to the relaxation.

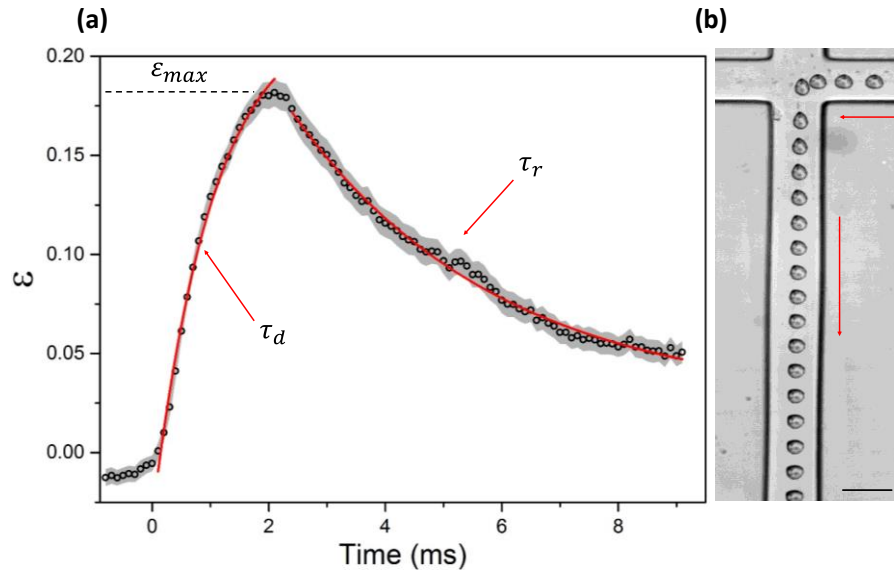


Figure 4.19 (a) Strain, ε , as a function of time, averaged over 50 HL60 cells, with the standard error shown in gray. Q was fixed at $5 \mu\text{l}/\text{min}$, and the suspension medium viscosity was 33 cP . The exponential fits shown in red were used to quantify the deformation and relaxation of the cells. (b) A superimposed brightfield image of a cell as it deforms and relaxes at $5 \mu\text{l}/\text{min}$ ($\mu \approx 33 \text{ cP}$) is shown. Scale bars, $30 \mu\text{m}$. The arrows indicate the direction of cell motion.

Figure 4.20 compares the average strain profile to the velocity profile of the cells. The velocity profile can be approximated as a single period of a sine wave, as discussed in section 4.1.3, which is fitted in red to Figure 4.20a with $R^2 = 0.99$. A cell is closest to the SP when the velocity profile is at a minimum, occurring here at $\Delta v \cong 0.025 \text{ m/s}$. Figure 4.20b shows that the sine-oscillating Kelvin-Voigt model (equation 2.13) can be fitted to the strain trace, this shown in red and $R^2 = 0.98$. The sine-oscillating Kelvin-Voigt model (discussed in section 2.3.4) was equated to find the elastic modulus of HL60 to be $E = (0.30 \pm 0.03) \text{ kPa}$.

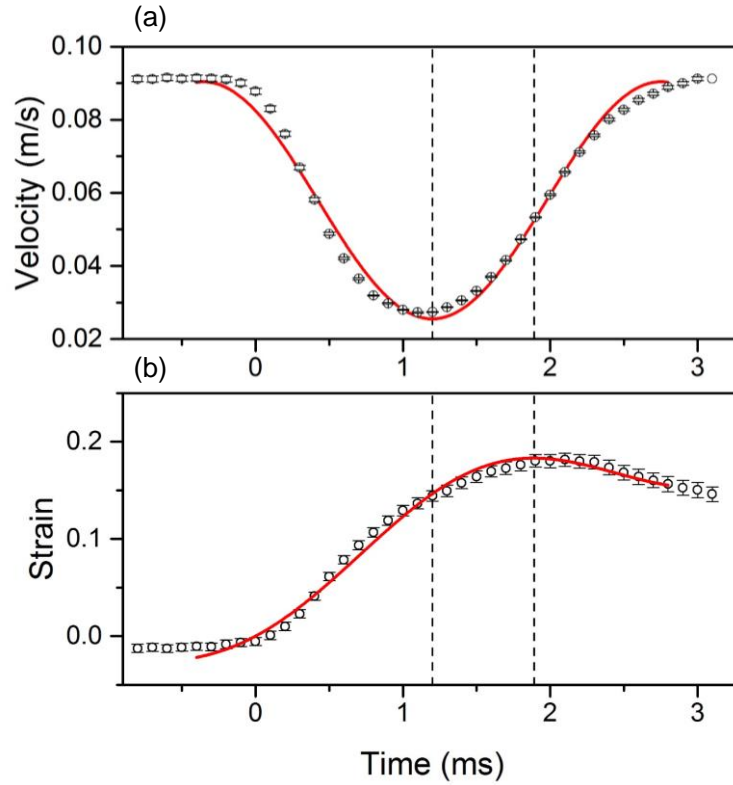


Figure 4.20 (a) The average velocity profile of $N=50$ HL60 cells as they pass through the SP of the cross flow. A sine function is fitted, shown in red. (b) The strain profile of the same 50 cells, the Kelvin-Voigt model was fitted, both shown in red. Q was $5 \mu\text{l}/\text{min}$ and viscosity was $\mu=33 \text{ cP}$.

Multiple parameters were extracted from the average strain trace shown by Figure 4.19, these are summarised in Table 4.1. However, cells are known to be heterogeneous and their mechanical properties may change depending on their stage in the cell cycle. Bulk measurements, using averaging, on heterogeneous samples often miss any subpopulations within a large sample. Also, bulk measurements cannot make correlations between specific parameters (e.g. whether larger cells have a larger maximum strain). Therefore, single cell analysis (SCA) was also performed on the $N=50$ HL60 strain traces to elucidate any advantages of SCA compared to bulk averaging. Appendix Figure S2 shows the raw data of the $N=50$ HL60 strain traces.

Figure 4.21 shows example of four individual strain traces of HL60 cells, these were used to perform single cell analysis. A Savitsky-Golay filter was applied to each strain trace, shown by the black line of the traces, this was used to remove noise from the signal and to find a more accurate value of ϵ_{max} . An exponential decay function was fitted to the trace, from 5 data points after ϵ_{max} occurred until the last datapoint. The fit was used to extract τ_r and ϵ_{∞} for each cell. The initial strain ϵ_0 of each cell was found by averaging the first 5 datapoints, before the cell entered the extensional flow junction and strain began to increase. The initial

diameter A of each cell was also found, by averaging the cell diameter for the first 5 datapoints of each trace (before any deformation occurred).

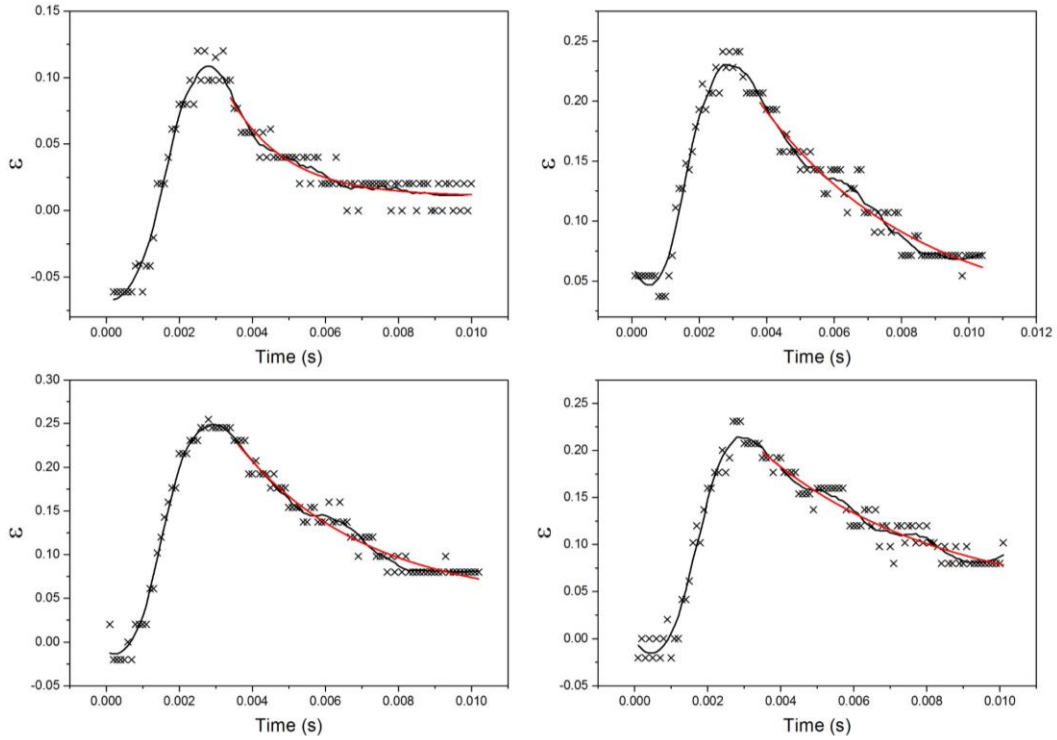


Figure 4.21 Examples of 4 strain traces of HL60 cells deforming in the extensional flow junction of a microfluidic cross-slot device. Savitsky-Golay filtering was applied to the datasets (shown by the black line) and used to find the maximum strain ϵ_{max} . An exponential function was fitted to the strain recovery and used to find the relaxation time τ_r and final strain ϵ_∞ .

Table 4.1 Multiple characteristic parameters extracted from the strain traces of $N=50$ cells. Including the initial cell diameter A , the initial strain ϵ_0 , the final strain ϵ_∞ , the maximum strain ϵ_{max} , the deformation time τ_d , the relaxation time τ_r and the elastic modulus E . Two analysis methods were used and the resulting values were compared: 1. the $N=50$ strain traces were averaged and values were extracted, ‘‘Averaged Strain Trace’’ and 2. values were separately found from individual traces and then averaged with $\pm SE$, ‘‘Single Cell Analysis’’.

	Averaged Strain Trace	Single Cell Analysis
A (μm)	n/a	12.3 ± 0.2
ϵ_0	-0.012 ± 0.004	-0.012 ± 0.005
ϵ_∞	0.030 ± 0.009	0.030 ± 0.004
ϵ_{max}	0.18 ± 0.01	0.18 ± 0.01
τ_r (ms)	3.52 ± 0.14	3.04 ± 0.15
τ_d (ms)	1.04 ± 0.05	n/a
E (Pa)	301 ± 29	n/a

The values for ϵ_{max} , ϵ_0 , ϵ_∞ and τ_r using SCA were compared to those found from the averaged strain trace, summarised in Table 4.1. This shows that the extracted values from both methods are all within error of each other, apart from τ_r which was 1.16 times larger when

calculated from the averaged strain trace compared to SCA. Four of the individual traces could not be fitted sufficiently with an exponential, which may account for the small difference seen in τ_r .

Figure 4.22 shows histograms of the values found for 5 single cell parameters extracted from the individual strain traces of HL60 cells. A normal distribution is seen for: A , ε_{max} , ε_0 and τ_r , and these were fitted with a Gaussian function (shown in black) with $0.85 > R^2 > 0.94$. The average ε_0 using SCA has a magnitude of 0.012, likely due to some shear confinement between the cell and the channel walls, this relatively small compared to ε_{max} which is ~ 15 times smaller than ε_0 . An elastic material would recover fully after stress is removed and have $\varepsilon_\infty = \varepsilon_0$, however HL60 are shown to have a final strain of 0.030 which is more than double the initial strain. The fact the cells do not fully recover suggests either a viscoelastic effect where subsequent relaxations occur over timescales not within our field of view, or that the applied stress results in a permanent strain due to cell plasticity. Additionally, the histogram shown by Figure 4.22e may offer more insight into shape recovery. Unlike the other parameters, ε_∞ does not show a normal distribution and cannot be fitted with a Gaussian. Here, the majority of values fall in the 0-0.02 range, which is the same for the ε_0 histogram (Figure 4.22b). Figure 4.22e suggests smaller populations of cells do not recover and undergo some permanent strain.

These results show the potential advantages of using SCA analysis for elucidating the mechanical response of cells to applied force. Histograms of the single cell properties allow visualisation of the sample heterogeneity and whether the parameters follow a normal distribution, information not provided by bulk analysis. For example, (a) to (d) follow a normal distribution which would allow extraction of the Gaussian peak value, standard deviation and coefficient of variation ($CV = SD/mean$). Further, increased sample sizes may allow identification of smaller sub-populations with differing mechanical properties, inferring even more information.

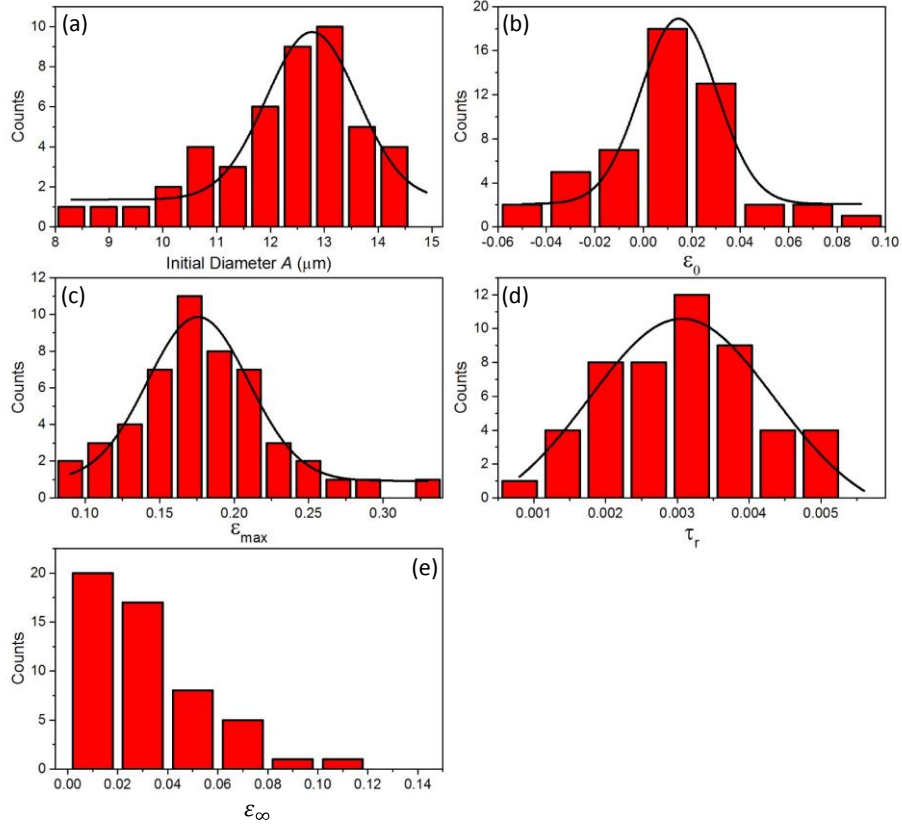


Figure 4.22 Histograms of the single cell parameters extracted from strain traces of $N=50$ HL60 cells deformed in the shear-dominant regime ($\mu = 33$ cP) at a flow rate of $5 \mu\text{l}/\text{min}$. Fitted Gaussian functions are shown in black. Where (a) shows the initial diameter A , (b) the initial strains ϵ_0 , (c) the maximum strain ϵ_{max} , (d) the relaxation time τ_r and (e) the final strain ϵ_∞ .

4.4.2 High strain recovery in the shear regime

The previous section discussed the deformation and recovery of HL60 in a cross-slot microfluidic device, in a low-velocity ($5 \mu\text{l}/\text{min}$) and high viscosity (33 cP) flow regime. This resulted in generally low maximum strains being applied to the cells ($\epsilon_{max} \cong 0.18$ and $DI \cong 1.61$). Figure 4.12 and Figure 4.14 showed that the trend in mechanical response can change between a low-strain and high-strain regime. To elucidate this, the recovery of HL60 cells deformed in a high-strain regime was also studied. Here, a higher flow rate of $150 \mu\text{l}/\text{min}$ was used in a suspension buffer viscosity of $\mu \cong 33$ cP. This required capturing videos at a frame rate of $150,000$ fps at a resolution of 320×192 pixels. This field of view was not enough for capturing both deformation and recovery. Therefore, instead of acquiring single cell strain traces, bulk measurements of deformation index were measured at different positions in the cross-slot device.

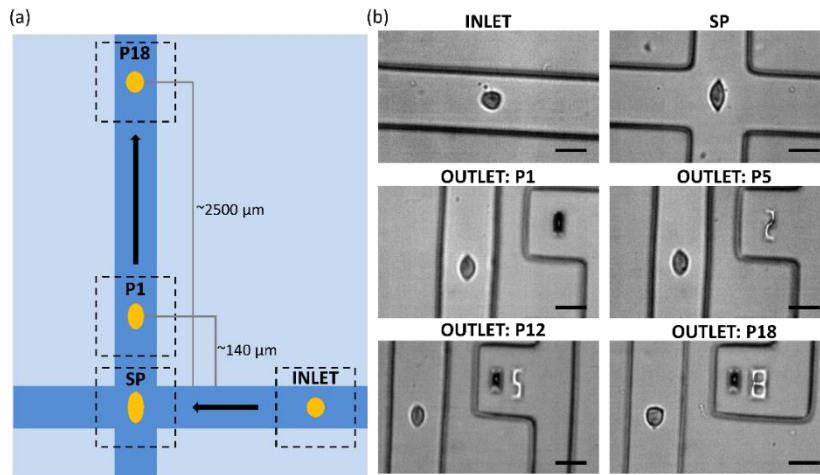


Figure 4.23 Schematic and bright field images of cell recovery after deformation at the SP of a cross-slot device. (a) A schematic showing the different positions at which the DI of cells was measured. This includes the inlet (before deformation), the stagnation point SP (where maximum stress is applied due to extensional flow), and various positions along the outlet (to track recovery) which were labelled positions 1-18. The maximum distance down the outlet where the cells DI was measured ($P18$) was $\sim 2500 \mu\text{m}$ from the SP . (b) Example bright field images of cells at the different positions, where the flow rate was $150 \mu\text{l}/\text{min}$ and the flow regime was shear-dominant ($\mu \approx 33 \text{ cP}$). Scale bars $20 \mu\text{m}$.

Figure 4.23a shows a schematic which highlights the various positions that deformation was measured on-chip, including the inlet (before deformation), at the SP , and various positions down the outlet. The outlet had equally spaced positions labelled number 1-18, which were a design feature to allow capture of DI at known distances from the SP . Figure 4.23b shows example images of cells captured at the different positions. At the inlet cells underwent a relatively small bullet-like deformation due to confinement, at the SP the cells experienced a high-strain and became tear-drop shaped, and through the outlet the amount of strain decreases with distance from the SP . The DI of 100s-1000s of cells was measured at each of these positions, the averaged value of DI as a function of position are shown in Figure 4.24. Here, no velocity thresholding was applied and all cells which passed through the device were included in the final averages. This was because thresholding could not be applied to bulk DI measurements collected after the SP , as this requires single-cell velocity profiles in the extensional flow junction.

Results show that the initial deformation in the inlet (before the cell enters the extensional flow junction) was $DI_0 = 1.34 \pm 0.02$ and the maximum deformation at the SP was $DI = 2.14 \pm 0.08$. The recovery of the cell as it moves through the outlet (positions 1-18) was fitted with an exponential function (shown in red), the full distance which was tracked was $\sim 2556 \mu\text{m}$. From the fit, the final deformation index was extracted $DI_\infty = 1.63 \pm 0.02$. If the cell

shape recovered fully then $DI_{\infty} = DI_0$. Here, $DI_{\infty} > DI_0$ suggesting some permanent strain due to the applied stress at the SP.

Low-strain and high-strain recovery both showed a permanent strain due to the applied stress (Figure 4.20 and Figure 4.24). This allowed comparison of the change in initial and final strains after low-strain recovery and high-strain recovery. The strain change was defined by normalising the change between final and initial strain by the maximum strain $\Delta\varepsilon = (|\varepsilon_{\infty}| - |\varepsilon_0|)/\varepsilon_{max}$. After low-strain recovery the strain change was $\Delta\varepsilon = 0.10 \pm 0.05$, and after high-strain recovery it was $\Delta\varepsilon = 0.14 \pm 0.01$. These values are within error of each other suggesting that applying both low and high-strains to cells in the shear-dominant regime results in a characteristic strain change representative of plasticity after deformation. The histogram of ε_{∞} values after low-strain recovery (Figure 4.22e) showed that most cells recover back to their initial strain ε_0 with a smaller population not recovering, resulting in an average value with $\varepsilon_{\infty} > \varepsilon_0$. This highlights the importance of single-cell analysis vs bulk averaging, as averaging suggests all cells do not recover. This was investigated after high-strain recovery by plotting histograms of DI at various positions to see if recovery followed a normal distribution.

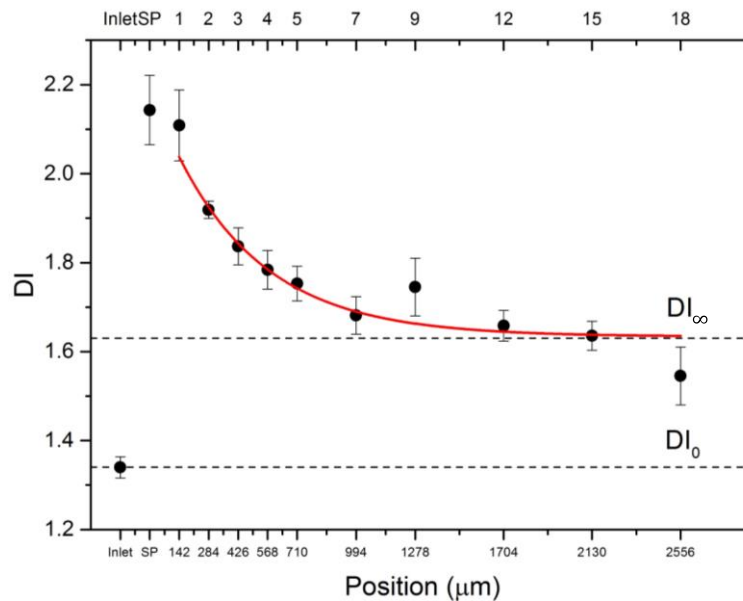


Figure 4.24 The $DI \pm SE$ of HL60 cells as a function of position in a cross-slot device ($\mu \cong 33$ cP), averaged from multiple cell events combined from $N=3$ repeats; Where the flow rate was $150 \mu\text{l}/\text{min}$ and flow was shear-dominant.

Figure 4.25 shows histograms of the DI of HL60 cells deformed at different positions in the device. Each dataset was expected to show a normal distribution and was fitted with a Gaussian function, which allowed calculation of the position at the centre of the peak b and the full width at half maximum (FWHM) w . Figure 4.25 (a) shows the DI at the inlet position,

(b) the SP, (c) position 1 and (d) at position 18. For each position, the experiment was repeated three times and each dataset is shown. The FWHM of the curves fitted to the inlet datasets (Figure 4.25a) is $w = 0.23 \pm 0.01$. Comparatively, at the SP $w = 0.80 \pm 0.03$ which is a ~ 3.5 fold increase. This is expected as cells are inherently heterogeneous, and have different deformability's depending on their initial size and stage in the cell cycle. At P18 ($\sim 2500\mu\text{m}$) from the SP into the inlet channel, $w = 0.31 \pm 0.05$ suggesting the cells are near to full recovery.

Figure 4.25b shows that for two of the repeats there was a smaller peak at $DI \sim 1$ as well as the larger peak at $DI > 1.5$. This could be due to the fact that no velocity threshold was used here, and this peak could represent cells which did not pass near to the SP and thus did not deform. It could also suggest a small population of cells were less deformable. For example, apoptotic cells are known to be less deformable and therefore these could be cells in early stages of apoptosis [188], [189]. Finally, all the values of the peak centres b shown in Figure 4.25 are less than the averaged DI values shown in Figure 4.24. The reason for this is apparent in the histograms. Even though a Gaussian function is fitted, many of the datasets show a log normal distribution. Thus, even though the majority of cell DI 's occur at b , the skew to the right of b shows more than 50% of cells deform with $DI > b$, which leads to an increase in the mean average.

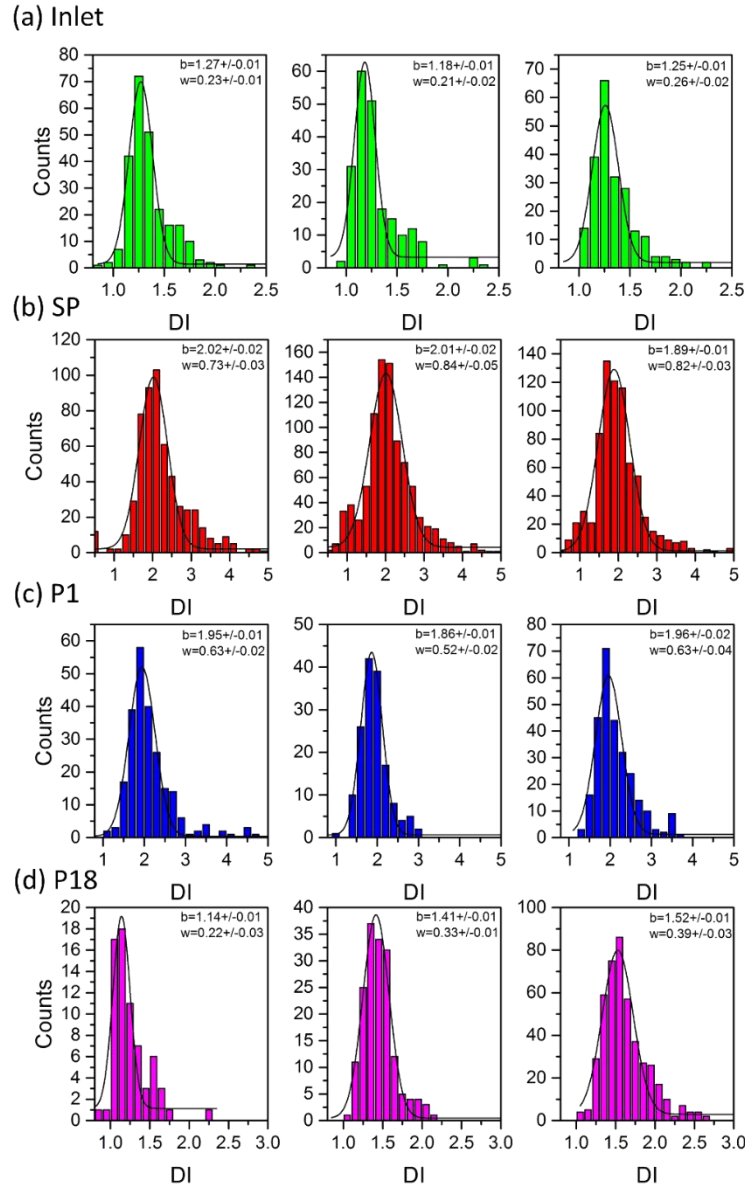


Figure 4.25 Histograms of the DI of HL60 cells at various positions in a cross-slot microfluidic device which were deformed in a shear-dominant regime ($\mu \cong 33$ cP) at $150 \mu\text{l}/\text{min}$, each dataset shows a normal distribution and is fitted with a Gaussian function, where b is the position at the centre of the Gaussian peak and w is the full width at half maximum. For each position, the experiment was repeated three times, where (a) is the DI at the inlet position, (b) the SP, (c) at position 1 which was $\sim 140 \mu\text{m}$ into the outlet channel and (d) at position 18 which was $\sim 2500 \mu\text{m}$ into the outlet channel.

4.4.3 High strain recovery in the inertial regime

The recovery of HL60 cells has been discussed after low-strain and high-strain deformations in a shear-dominant regime. Figure 4.15 showed that high-strains can also be achieved in an inertia-dominant regime, and that this regime seems to show *yield stress* behaviour (not seen in the shear-regime). This may indicate that cells deformed to high-strains in an inertia-dominant regime are less likely to recover their original shape compared to a shear-dominant regime.

To investigate high-strain recovery in the inertia-dominant regime, cells were deformed at 600 $\mu\text{l}/\text{min}$ whilst suspended in PBS buffer ($\mu \cong 1 \text{ cP}$). The average DI of 100s-1000s of cell was measured at different positions, including the inlet, SP and outlet (as described in section 4.4.2). Figure 4.26 shows example images of cells deforming at the inlet (before the applied stress), at the SP (where maximum applied stress occurs) and at various positions through the outlet (after the applied stress is removed). Images show that the cell is relatively undeformed in the inlet, incurs a high-strain at the SP and P1, then the strain begins to decrease at positions further from the SP.

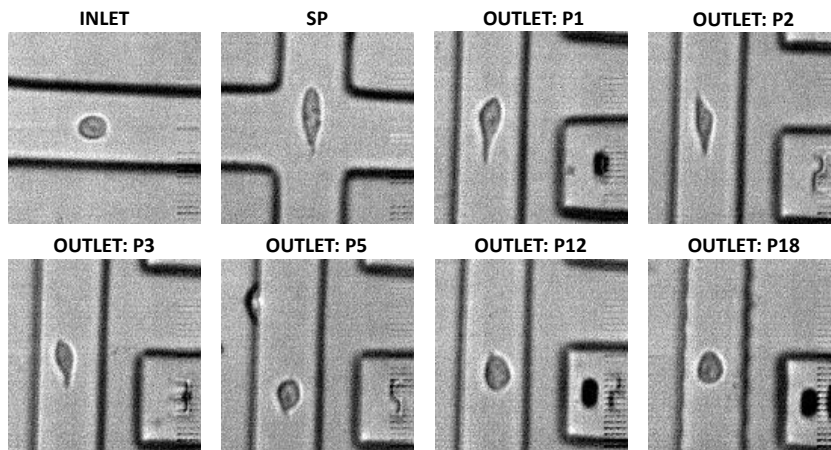


Figure 4.26 Example bright field images of cells in the cross-slot device at the different positions, where the flow rate was 600 $\mu\text{l}/\text{min}$ and the flow regime was inertia-dominant ($\mu \approx 1 \text{ cP}$).

Figure 4.27 shows the DI as a function of these positions. The cell recovery at different positions through the outlet was fitted with an exponential decay function (shown in red), which is similar to the results for the shear-dominant regime (Figure 4.24). Here, the initial deformation was $DI_0 = 1.17 \pm 0.02$, the final deformation was $DI_\infty = 1.46 \pm 0.04$ and the deformation at the SP was $DI_{SP} = 1.81 \pm 0.07$. As with the low-strain and high-strain shear-dominant regimes, this also showed some permanent strain ($DI_\infty > DI_0$). Interestingly, in this regime the maximum deformation occurred after the SP and at position 1 ($DI_{P1} = 2.15 \pm 0.30$) and also showed a ~ 4 fold increase in the standard error compared to the DI_{SP} . This behaviour may be indicative of this deformation occurring above the yield stress. Cells are known to be viscoelastic, and if destruction of the subcellular structure has occurred the cell may begin to behave more like a viscoelastic liquid resulting in the material “flowing” even after the applied stress is reduced.

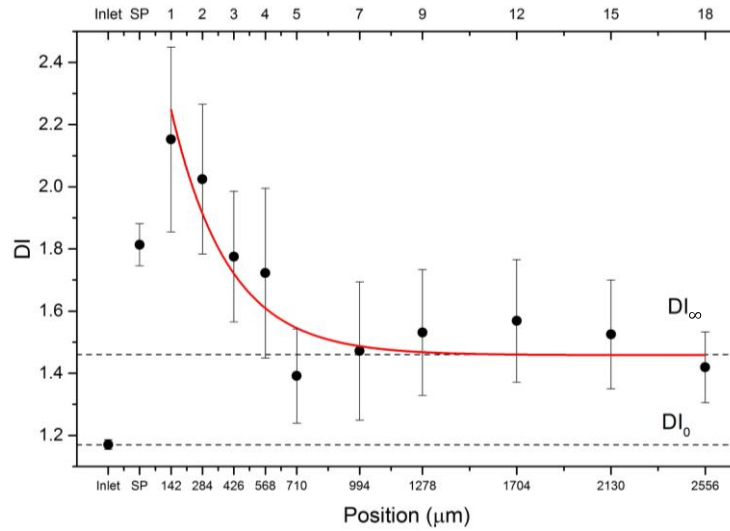


Figure 4.27 The $DI \pm SE$ of HL60 cells as a function of position in a cross-slot device ($\mu \cong 1cP$), averaged from multiple cell events combined from $N=3$ repeats; Where the flow rate was $600 \mu\text{l}/\text{min}$ and flow was inertia-dominant.

Figure 4.28 shows histograms of the DI of HL60 cells deformed at $600 \mu\text{l}/\text{min}$ in the inertia-dominant regime as different positions in the device. Each dataset was fitted with a Gaussian function which was used to find the position of the peak centre b and the FWHM w . The experiment was repeated three times and all datasets are shown for each position, where: (a) is the inlet position, (b) the SP, (c) position 1 and (d) position 18 which was $\sim 2500 \mu\text{m}$ from the SP into the outlet. The average FWHM of the curves for the inlet datasets (Figure 4.28a) was $w = 0.14 \pm 0.02$, which increase ~ 5 fold at the SP (Figure 4.28b) where $w = 0.75 \pm 0.22$. The spread of data at position 1 was similar to the SP $w = 0.78 \pm 0.23$, and at position 18 $w = 0.23 \pm 0.04$ showing that cells were near to recovery.

Similar to behaviour in high-strain recovery in the shear-dominant regime (Figure 4.25), some of the average values of the peak centre b were less than the mean averaged DI shown in Figure 4.27. For the inlet, $b = \pm 1.17 \pm 0.01$ which is within error of the average DI at this position $DI_0 = 1.17 \pm 0.02$. At the SP the average $b = \pm 1.52 \pm 0.01$ is significantly less than the average $DI_{SP} = 1.81 \pm 0.07$. Once again, Figure 4.28b shows a skewed distribution which may be better represented by log normal than a Gaussian function. This shows that even though the majority of cells deform with $DI=b$, more than 50% of cells have $DI > b$ resulting in the mean average being $DI_{SP} > b$. Figure 4.28d shows that at position 18 $b = 1.25 \pm 0.04$ which is also significantly different to the mean average $DI_{\infty} = 1.46 \pm 0.04$. The histograms show that the majority of cells recover to their initial shape ($DI \sim 1.17$), however, some cells remain deformed 2-3 times as much as this. This suggests that a small population of cells undergo a permanent strain after applied stress. As measurements are done by bulk averaging at different positions, it is unclear whether the permanently strained cells are those which

underwent the highest deformations at the SP. This regime occurs above the *yield stress* and before the *failure point* which suggests that even though these cells show permanent strains, they are able to recover over longer time periods and no viability drop was detected using a trypan blue viability assay (Figure 4.17).

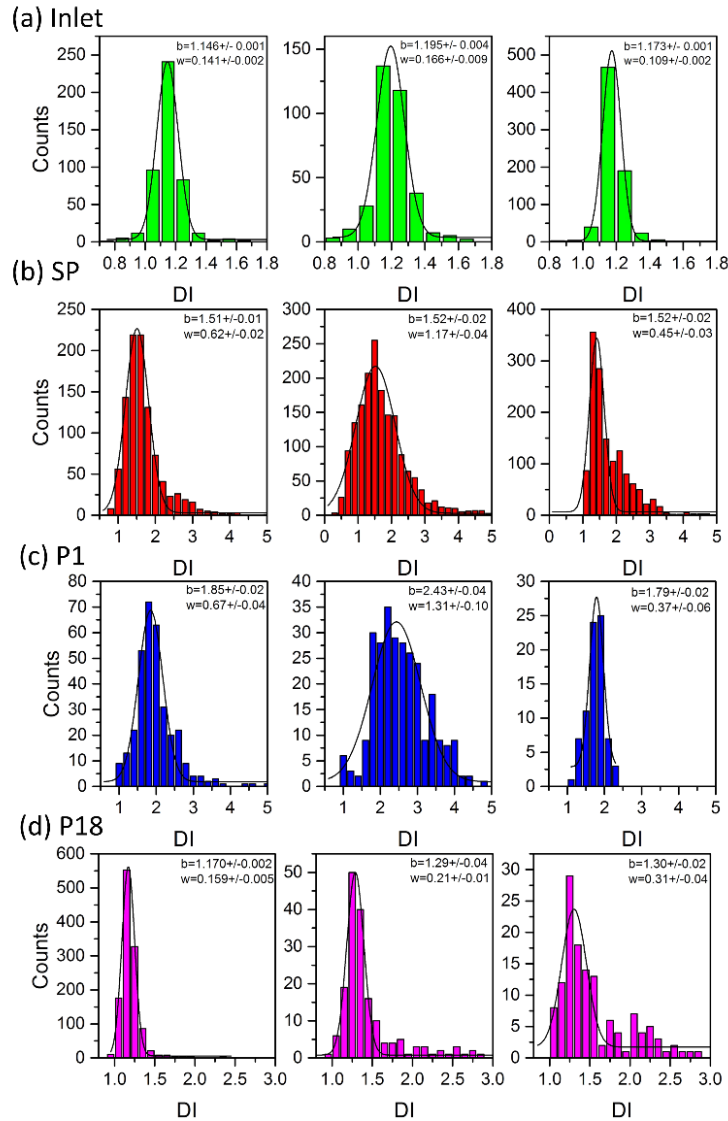


Figure 4.28 Histograms of the DI of HL60 cells at various positions in a cross-slot microfluidic device which were deformed in a inertia-dominant regime ($\mu \cong 1$ cP) at $600 \mu\text{l}/\text{min}$, each dataset shows a normal distribution and is fitted with a Gaussian function, where b is the position at the centre of the Gaussian peak and w is the full width at half maximum. For each position, the experiment was repeated three times, where (a) is the DI at the inlet position, (b) the SP, (c) at position 1 which was $\sim 140 \mu\text{m}$ into the outlet channel and (d) at position 18 which was $\sim 2500 \mu\text{m}$ into the outlet channel.

4.4.4 Summary of section 4.4

Figure 4.29 shows the summarised data from Figure 4.24 and Figure 4.27, showing the DI of the cells replotted as a function of time as they recover whilst travelling down the outlet. Here, in both shear and inertia-dominant flow regimes the maximum DI are within error of each

other. The graph shows that the cells in the shear regime relax at a slower rate than the inertial regime, and their final deformation DI_{∞} is larger than the inertial regime.

As the flow rate in the inertial-regime was 4 times faster than the shear regime, the strain-rate and relaxation times should reflect this. Table 4.2 confirms that the strain-rate in the inertial regime was ~ 4 times that of the shear regime. However, the relaxation time in the inertial regime was ~ 6 times quicker than that of the shear regime. The slower relative relaxation time in the shear-regime may be indicative of the viscous element of cells (known to be viscoelastic) which may also explain why the cells do not recover their original shape as much as in the inertial regime. Quicker strain-rates are likely probing the cell elasticity whereas slower strain-rates may lead to some viscous flow.

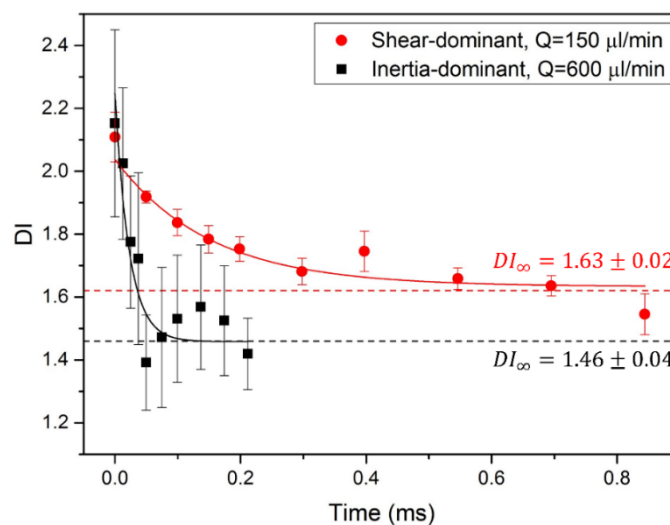


Figure 4.29 The $DI \pm SE$ of HL60 cells as a function of time in a cross-slot device as cells recover through the outlet after deformation at the SP, averaged from multiple cell events combined from $N=3$ repeats. Comparing deformation in an inertia-dominant regime ($Q= 600 \mu\text{l}/\text{min}$ and $\mu \cong 1 \text{ cP}$) to a shear-dominant regime ($Q= 150 \mu\text{l}/\text{min}$ and $\mu \cong 33 \text{ cP}$).

Table 4.2 A summary of the strain rate and relaxation time of HL60 cells after deformation at the SP of an extensional flow, in the shear-dominant regime ($Q= 150 \mu\text{l}/\text{min}$ and $\mu \cong 33 \text{ cP}$) and the inertia-dominant regime ($Q= 600 \mu\text{l}/\text{min}$ and $\mu \cong 1 \text{ cP}$).

Regime	Strain Rate $\times 10^5 \text{ (s}^{-1}\text{)}$	$\tau_r \times 10^{-4} \text{ (s)}$
Shear	1.63	1.51 ± 0.35
Inertial	6.53	0.25 ± 0.08

4.5 Discussion

The aim of this chapter was to show that a microfluidic cross-slot device could be used to measure the deformation properties of HL60 cells over a wide-range of flow conditions in two flow regimes, showing the method has potential for the mechanical phenotyping of cells and that it is rich in information regarding cell response to an applied force.

Cells were deformed in two distinct flow regimes: a *shear-dominant* regime working at low Re , low Q , and increased suspension buffer viscosity μ , and an *inertia-dominant* regime working at $Re > 40$, high Q and low μ . Results showed that using a shear-dominant regime could achieve higher cell deformations for the same applied force (showing cell viscoelastic stiffening behaviour). The inertia-dominant regime also showed a non-linear increase in deformation at $Q > 400 \mu\text{l}/\text{min}$, which was defined as the cell *yield stress* and is associated to sub-structural breakdown. Further, the *failure point* of HL60 cells was found to be $600 \mu\text{l}/\text{min}$ as it resulted in on-chip cell destruction and a drop in subsequent viability. Comparatively, in both flow regimes cells remained viable after deformation (even above the *yield stress* but before the *failure point*).

A low-strain shear-dominant regime was used to capture “strain traces” of HL60 cells, which showed the variation in cell shape from steady-state in the inlet to passing through the SP and relaxation through the outlet channel. Figure 4.19 showed strain as a function of time which was used to find multiple characteristic mechanical cell parameters. Particularly, the elastic modulus of HL60 was found to be $E = 0.30 \pm 0.03 \text{ kPa}$ using an adapted Kelvin-Voigt model. Table 4.3 shows a summary of other values of E reported for HL60 using a variety of techniques utilising different applied stresses and strain rates [1], [34], [190]–[192].

Mietke *et al.* 2015 measured the modulus of HL60 using both AFM and microfluidics by shear-confinement, their value using microfluidics was ~ 8 times larger than for AFM [34]. They attributed this to the shorter timescales used to apply strain in microfluidics ($\sim 1 \text{ ms}$), compared to AFM, inducing a stiffening response in the cells. However, our result found using extensional flow microfluidics is closer to the reported AFM value even though the strain-rate was closer to that of shear-confinement ($\sim 2 \text{ ms}$). This suggests that strain-rate is not the only factor responsible for differences in measured elastic modulus. Additionally, Rosenbluth *et al.* (2006) also used AFM to measure elastic modulus and this value is ~ 5 times greater than the value reported by Mietke *et al.* (2015) using the same technique [190]. Overall, the difference between the stiffest and softest reported values is ~ 16 . This showed that the applied stress, strain, technique and applied model had a huge effect on measured elastic modulus.

The values in Table 4.3 show a range of sample sizes used to find the average elastic modulus of HL60, the highest was $N=281$, using microfluidics, and the lowest was 12, using optical tweezers [34], [192]. The value we found using microfluidic extensional flow, was averaged from a sample size of 50. This is relatively low compared to the other microfluidic values reported. However, the throughput of the experiment was still higher than using AFM or optical tweezers ($\sim 1 \text{ cell}/\text{min}$). Here, the cell deformation rate was $\sim 800 \text{ cells}/\text{s}$ which is 2 orders of magnitude higher throughput compared to these techniques. The current limiting

factor resulting in the lower sample size is the processing times of saving large files containing the high-speed videos. In conclusion, microfluidic extensional flow was used to measure the elastic modulus of HL60 using an adapted Kelvin-Voigt model and resulting in a value comparable to previous reported results. This method increases measurement throughput and shows proof of concept, performing real-time analysis of deformation would be necessary to utilise this throughput and achieve higher sample sizes (100s-1000s of cells).

Table 4.3 A table summarising the different values of elastic modulus reported for HL60 cells using a range of techniques.

Elastic Modulus (kPa)	Technique	Sample Size	Reference
0.30±0.03	Microfluidics: Extensional Flow	50	(Armistead et al. 2019)
1.48±0.03	Microfluidics: Shear- confinement	281	(Mietke et al. 2015)
0.53±0.04	Microfluidics: Constriction	>200	(Nyberg et al. 2017)
0.90±0.08	AFM	60	(Rosenbluth et al. 2006)
0.17±0.01	AFM	169	(Mietke et al. 2015)
~0.09	Optical Trap	12	(Zhou et al. 2014)

The strain traces of n=50 HL60 cells was also used to find multiple characteristic parameters; the initial diameter A , relaxation time τ_r , initial strain ε_0 , maximum strain ε_{max} and the final strain ε_∞ . These were found from both the averaged strain trace and single cell analysis (SCA) of individual cell traces. This showed that the two sets of analysis were comparable to each other, however SCA offered more insight into the distribution of parameters. Particularly showing that most cells recover their original strain ($|\varepsilon_0| = |\varepsilon_\infty|$) and a smaller population do not recover ($|\varepsilon_0| < |\varepsilon_\infty|$). Permanent deformations have been seen after applied stress is removed, particularly using cyclic loading, and attributed to a plastic element due to subcellular disruption [86], [155], [156]. These deformations are known to depend on loading frequency, applied stress, technique used and potentially an inherent property of specific cell phenotypes. Thus, the final strain ε_∞ acquired from strain traces may be a measure of plasticity and useful for distinguishing phenotypes or identifying sub-populations.

Overall, a microfluidic cross-slot device was successfully used to measure the deformation properties of HL60 cells in two distinct flow regimes. The shear and inertia-dominant flow regimes revealed different behaviours allowing more mechanical information to be obtained. The shear-dominant regime can achieve higher strains for lower applied stresses, and the inertia-dominant regime shows *yield stress* behaviour and an apparent *failure point* where cell viability drops. This yield stress may be associated with subcellular disruptions such as actin

fluidisation [83]. This was corroborated by high-strain deformations occurring above the *yield-stress* showing subpopulations of cells not recovering initial shape which is indicative of a plastic (i.e. permanent) deformation. Strain traces allowed multiparameter single cell measurements to be collected for HL60 including initial shape and strain, maximum strain and relaxation properties. An elastic modulus value was also found which is within the range of values reported in the literature. The method shows promise for improving the sensitivity of microfluidic mechanophenotyping by probing a range of forces and strains and extracting multiple parameters on a single-cell level.

5 The sensitivity of DC to subcellular alterations

This chapter covers the use of DC to probe the mechanical properties of cells treated with various drugs to alter subcellular components. Latrunculin A (LatA) was used to prevent polymerisation of F-actin, Combretastatin (CA4) was used to disassemble microtubules and Trichostatin A (TSA) was used to decondense chromatin. Deformation Cytometry was used in the shear-dominant and inertia-dominant flow regimes to deform cells at low and high strains. This was to investigate whether certain strains and strain-rates are more sensitive to specific subcellular structural changes induced by the drugs. Multiparameter single cell analysis was also used to track the deformation and recovery as a function of time. This allowed further insight into whether subcellular changes also affect the relaxation process, and if the response to drug was heterogeneous across the sample.

5.1 Treating cells with Latrunculin A

Latrunculins are a family of products known to affect the polymerisation of actin filaments. They do this by binding to actin monomers and preventing further polymerisation [193]. Latrunculin A (LatA) binds to G-actin monomers near the nucleotide binding cleft with a 1:1 molar complex [194]. This sequesters the monomers from polymerisation, thus growth from the barbed end of microfilaments ceases but dissociation from the pointed end continues resulting in eventual depolymerisation. As discussed in section 2.1.3, actin is a major component of the cell cytoskeleton responsible for giving cells structure and rigidity. Here, cells are treated with LatA and deformed microfluidically, using DC, in both shear and inertia-dominant flow regimes.

Different cell types may respond differently to treatment with LatA and may require different concentrations to inhibit polymerisation. Mouse neuroblastoma clone NII-115 cells required 90 nM of LatA, whereas Swiss 3T3 mouse fibroblasts required 900 nM to show the same effects. Additionally, LatA was shown to disrupt actin organisation after 1 hr of incubation and the effects were fully reversible within 1 hr of removing the drug [194].

In this study, the deformability of two cell lines treated with LatA was measured. Continuing from the results in chapter 4, HL60 cells were used to study the effects of LatA on non-adherent leukaemia cells. The colorectal cancer cell line SW480 was also studied to allow comparison of cells derived from a primary tumour and represent an adherent cell line. The differing functions and initial morphology of these states means that HL60 are known to be more deformable than SW480, suggesting their cytoskeletons differ significantly. Therefore, probing the effect of both cell types to LatA could offer further insight into the sensitivity and scope of DC.

5.1.1 Drug treatment and observations

Both cell lines were treated with LatA and imaged using phase contrast and confocal fluorescence microscopy. This was to show whether the drug altered cell morphology and also to visualise the actin disruption.

HL60 and SW480 were first incubated with $1 \mu\text{M}$ of LatA (Cayman Chemical) for 2 hr, before imaging on a phase contrast microscope (VWR IT404 - 630-1575) using a 40x objective. Figure 5.1a shows an image of HL60 cells after treatment with LatA compared to untreated cells. The images show a change in morphology of the treated cells, they are generally less rounded and have more protrusions. This shape change was quantified by measuring the circularity D_c (introduced in section 3.5.3). Figure 5.1b shows histograms of the D_c of treated and untreated cells which show a log normal distribution, density scatter plots of D_c as a function of cell diameter are also included. These show that treatment with LatA led to an increase in D_c which indicates they are less round. The average diameter and D_c for treated and untreated cells are shown in Figure 5.1c, which shows no significant change in cell diameter but a ~ 1.3 times increase in D_c of treated cells.

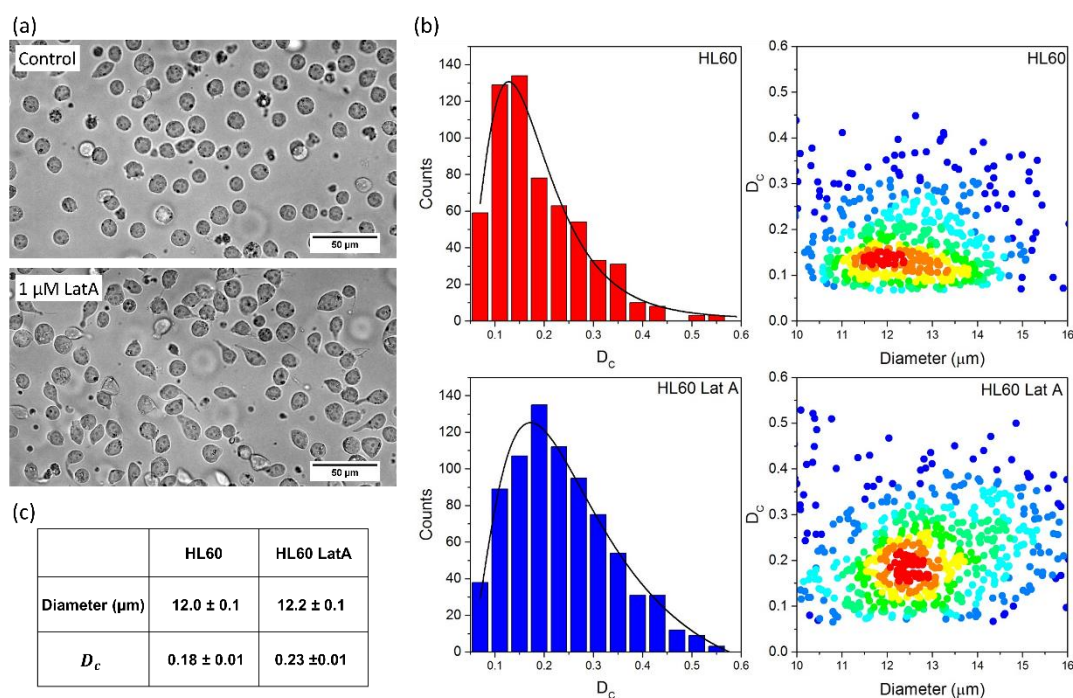


Figure 5.1 Measurement of the size and shape of HL60 cells compared to those treated with $1 \mu\text{M}$ of LatA: (a) Phase contrast images of HL60 and HL60 LatA cells taken with a 40x objective. (b) Histograms of the circularity D_c of HL60 and HL60 LatA, and density scatter plots of D_c as a function of diameter of HL60 and HL60 LatA. (c) A table summarising the average diameter and D_c of HL60 and HL60 LatA.

Comparatively, Figure 5.2a shows images of SW480 cells treated LatA and untreated cells. Here, the images show no immediate change in morphology. This was then quantified by measuring D_c of treated and untreated SW480 (Figure 5.2b). The histograms of D_c show a log normal distribution and show an increased shift in the peak of D_c of treated cells. The increase can also be seen in the density scatter plots. Finally, the averaged cell diameter and D_c of treated and untreated SW480 (Figure 5.2c) show no significant change in diameter and a ~ 1.2 x increase in D_c .

Both HL60 and SW480 show no change in diameter due to incubation with 1 μM of LatA, and both show similar increases in D_c . However, the phase contrast images clearly show a more obvious change in morphology in HL60 than SW480. This suggests that our image analysis and use of the circularity D_c may not be sensitive enough to discern the protrusions seen in Figure 5.1a. The protrusions in HL60 could be related to the fact the cells are initially non-adherent, whereas SW480 were detached from a surface.

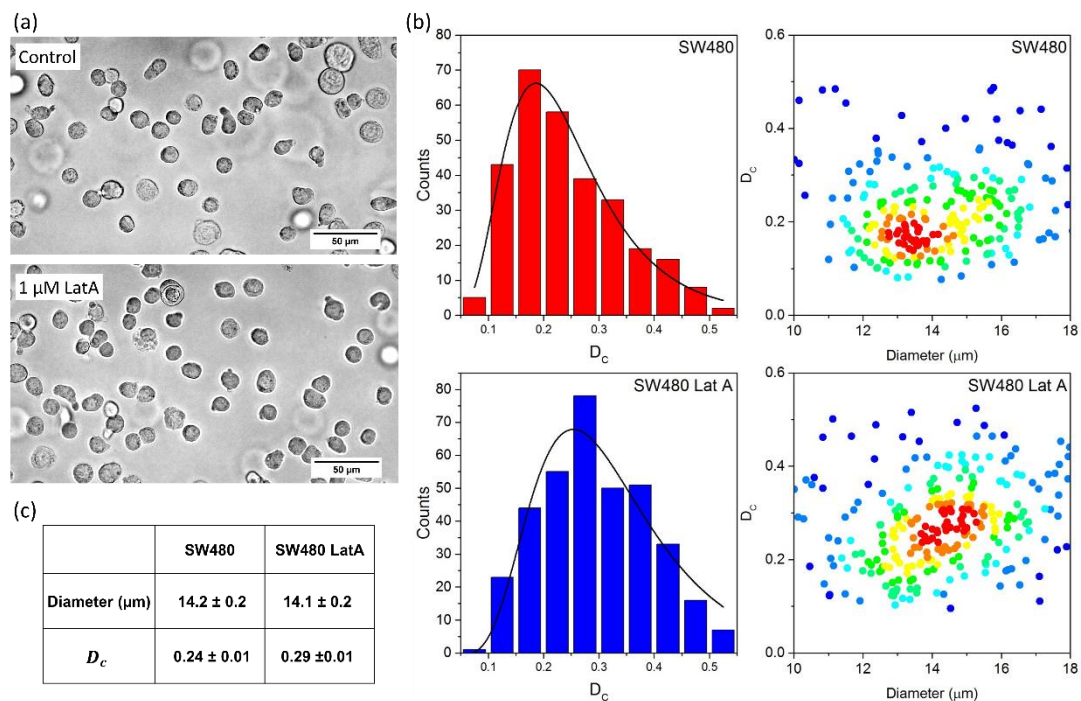


Figure 5.2 Measurement of the size and shape of SW480 cells compared to those treated with 1 μM of LatA: (a) Phase contrast images of SW480 and SW480 LatA cells taken with a 40x objective. (b) Histograms of the circularity D_c of SW480 and SW480 LatA, and density scatter plots of D_c as a function of diameter of SW480 and SW480 LatA. (c) A table summarising the average diameter and D_c of SW480 and SW480 LatA.

Confocal fluorescence of live cells was used to visualise the actin structure of HL60 and SW480 cells treated with varying concentrations of LatA. Concentrations of 0.01 μM , 0.1 μM and 1 μM were compared to a control sample. Cells were incubated with the drug and

fluorescent stains for 2 hours before imaging. F-Actin was stained using a live cell fluorogenic labelling probe based on Silicon-Rhodamine (Sir) (Spirochrome, Cytoskeleton Inc.), using a final concentration of 1 μM . DNA was stained using the dye Hoechst 3342 (Thermo Fisher Scientific) at a final concentration of 0.5 $\mu\text{g/ml}$.

Figure 5.3 shows fluorescent images of HL60 at different concentrations of LatA, with actin shown in red and DNA shown in blue. The images do not show obvious changes in the actin structure, the 0.1 μM and 1 μM samples show a less uniform actin structure compared to the 0.01 μM and control sample. Comparatively, Figure 5.4 shows SW480 treated with different concentrations of LatA whilst adhered to a surface and Figure 5.5 shows detached SW480 treated with different concentrations of LatA. Both adhered and attached samples show a clear disruption of actin filaments as a function of concentration. Untreated SW480 show a defined actin cortex, especially compared to untreated HL60 (Figure 5.3) which is an expected result as these cells are more deformable. As LatA concentration increases the cortex begins to break down and the structure is more dotted.

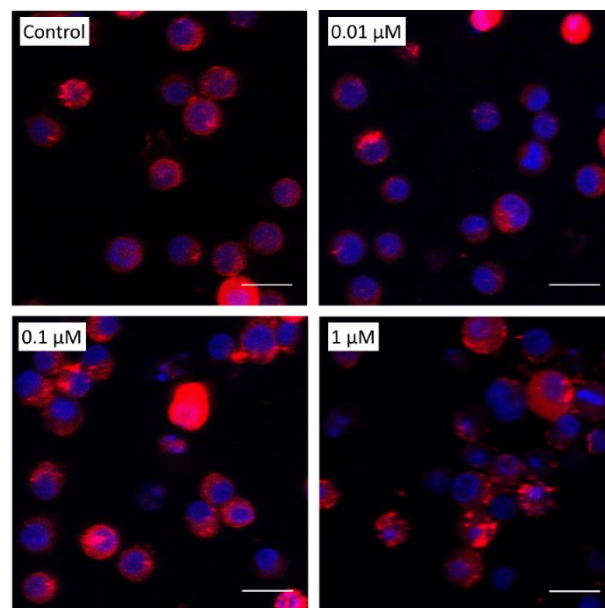


Figure 5.3 Confocal fluorescence images of control HL60 cells and HL60 treated with 0.01 μM , 0.1 μM and 1 μM of LatA, stained for actin (red) and DNA (blue). Images were taken using a 40 x objective, scale bar 20 μm .

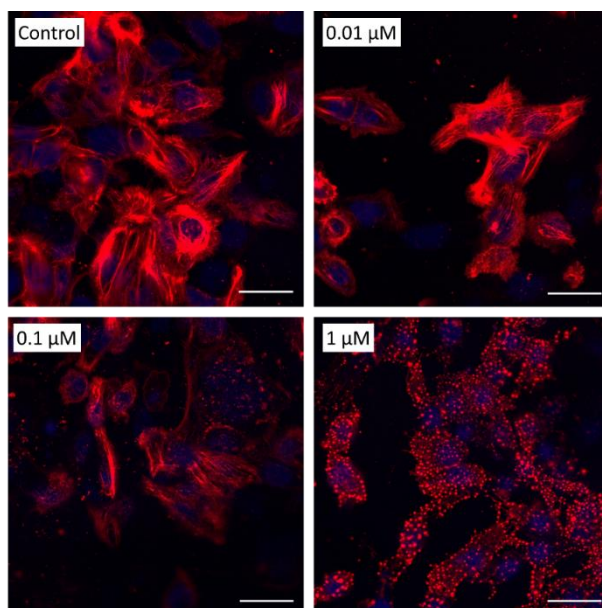


Figure 5.4 Confocal fluorescence images of control SW480 cells and SW480 treated with 0.01 μM , 0.1 μM and 1 μM of LatA. Cells were adhered to a surface and stained for actin (red) and DNA (blue). Images show that with increased LatA concentration the actin cortex is less pronounced due to the drug inhibiting actin polymerisation. Scale bar 20 μm .

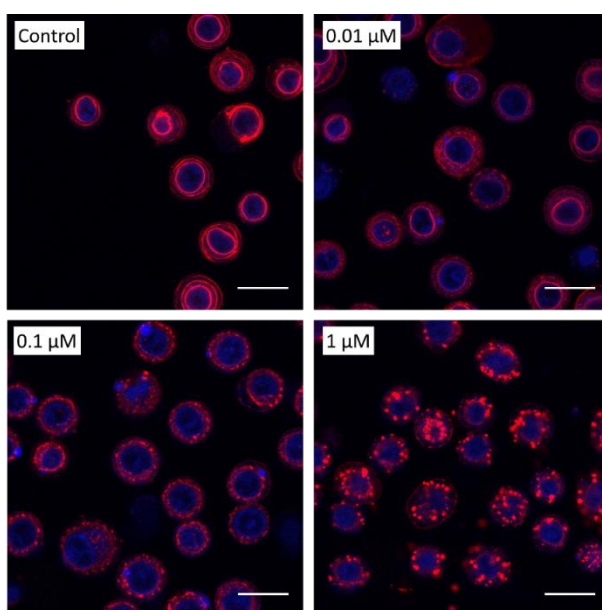


Figure 5.5 Confocal fluorescence images of control SW480 cells and SW480 treated with 0.01 μM , 0.1 μM and 1 μM of LatA. Cells were detached and have a rounded morphology, and were stained for actin (red) and DNA (blue). Images show that with increased LatA concentration the actin cortex is less pronounced due to the drug inhibiting actin polymerisation. Scale bar 20 μm .

The fluorescent images were also used to measure the diameter of the nuclei ($A_{nucleus}$) of HL60 and SW480 treated with LatA compared to untreated cells. Figure 5.6 shows histograms of $A_{nucleus}$ of HL60 and SW480 treated with 1 μM of LatA compared to control samples. Each histogram shows a normal distribution and is fitted with a single Gaussian peak. Results

show no significant change in nuclear diameter due to the effects of LatA, and that SW480 had a significantly bigger nucleus than HL60 (~1.2 x bigger).

Overall, results confirm that a 2 hr incubation of 1 μM of LatA leads to changes in cell morphology and actin structure of HL60 and SW480 cells, without affecting the whole cell or nucleus diameter.

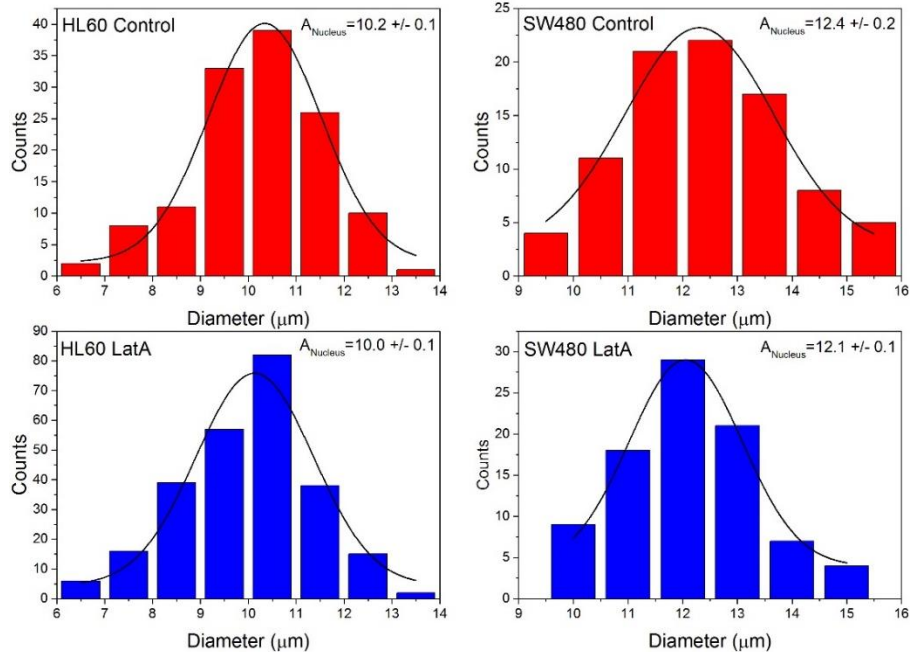


Figure 5.6 The nuclear diameter of HL60 and SW480 cells was measured using confocal fluorescence images with DNA staining. Histograms were plotted of the nuclear diameters A_{nucleus} of HL60 and SW480 treated with LatA and compared to control samples. Plots are fitted with a Gaussian function.

5.1.2 Deformation Cytometry in the shear regime

DC experiments on LatA treated cells were done at a concentration of 1 μM and an incubation time of 2 hr. Cells were microfluidically deformed over a range of flow rates whilst suspended 0.5% PBS-MC buffer ($\mu \sim 33$ cP), whilst maintaining a constant concentration of LatA throughout the measurement period. Measurements were taken over a range of flow rates, collecting 10s-100s of cell events for each condition. Experiments were repeated $N=3$ to calculate an average and standard error for the deformation index DI .

Figure 5.7a shows the DI of HL60 cells treated with LatA as a function of flow rate in the shear regime, compared to a control sample. For $Q < 20 \mu\text{l}/\text{min}$, the treated cells showed increased deformability compared to the control cells. For $Q > 20 \mu\text{l}/\text{min}$, the treated and untreated cells show no significant change in DI . Both datasets are fitted with an exponential function, used to extrapolate the maximum deformation index DI_{max} . For the treated cells $DI_{\text{max}} = 2.25 \pm 0.05$ and for the untreated cells $DI_{\text{max}} = 2.35 \pm 0.05$, showing that the maximum deformation values are within error of each other.

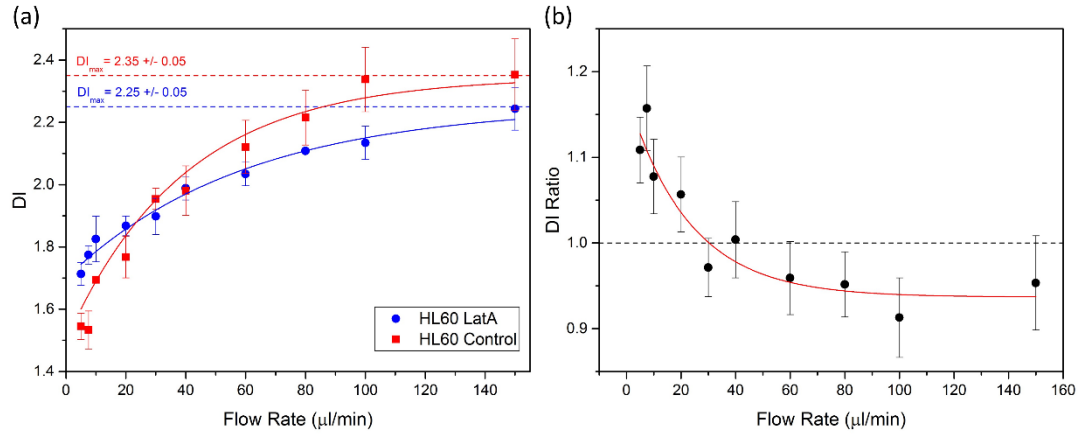


Figure 5.7 (a) The deformation index DI of HL60 cells treated with $1 \mu\text{M}$ of LatA as a function of flow rate, compared to a control sample. Cells were deformed in a shear-dominant regime where $\mu \cong 33 \text{ cP}$. Both datasets are fitted with an exponential function. (b) The DI ratio of HL60 cells treated with LatA compared to untreated cells ($DI_{\text{HL60LatA}}/DI_{\text{HL60}}$), which is fitted with an exponential function.

The change in DI due to LatA can be quantified using the DI_{ratio} , which equates to $DI_{\text{LatA}}/DI_{\text{control}}$. Where $DI_{ratio} = 1$ indicates no change due to treatment with LatA, and $DI_{ratio} > 1$ indicates increased deformability due to LatA. Figure 5.7b shows the DI_{ratio} of HL60 as a function of flow rate, the trend shows an exponential decay which is fitted in red. Results show $DI_{ratio} > 1$ for $Q < 30 \mu\text{l}/\text{min}$, for $Q > 30 \mu\text{l}/\text{min}$ values of the $DI_{ratio} \sim 1$. Results show that DC can be used in the shear regime to detect increased deformability of HL60 cells, and that a low-strain regime (i.e. low flow rates) is most sensitive to these changes. On the other hand, higher strains (using higher flow rates) were not sensitive to any changes due to treatment with LatA.

Figure 5.8a shows the DI of SW480 cells treated with $1 \mu\text{M}$ of LatA as a function of flow rate, compared to an untreated control sample. Both datasets are fitted with an exponential decay function tending to a maximum deformation index DI_{max} . The plot shows a general increase in the DI of treated cells compared to untreated cells, where $DI_{max} = 1.70 \pm 0.02$ for treated cells and $DI_{max} = 1.62 \pm 0.04$ of untreated cells. Further, Figure 5.8b shows the DI_{ratio} as a function of flow rate which shows an exponential decay and is fitted in red. Here, $DI_{ratio} > 1$ for the majority of flow rates apart from the highest flow rate used ($Q = 100 \mu\text{l}/\text{min}$) which was within error of $DI_{ratio} = 1$.

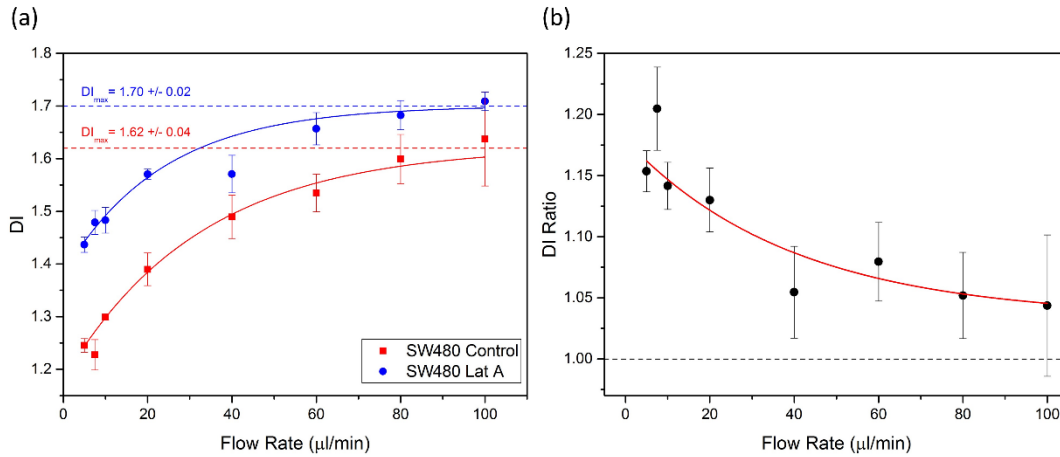


Figure 5.8 (a) The deformation index DI of SW480 cells treated with $1 \mu\text{M}$ of LatA as a function of flow rate, compared to an untreated sample. Cells were deformed in a shear-dominant regime where $\mu \cong 33 \text{ cP}$. Both datasets are fitted with an exponential decay function. (b) The DI ratio of SW480 cells treated with Lat A compared to a control sample ($DI_{SW480LatA}/DI_{SW480}$), which is fitted with an exponential decay function.

Overall, both HL60 and SW480 showed increased deformability when treated with LatA. This is the expected result as LatA prevents actin polymerisation and the actin cortex is known to provide the cell with mechanical rigidity. In the shear-regime, lower flow rates (which impart smaller strains) were most sensitive to changes due to LatA. At higher flow rates, treated HL60 could no longer be distinguished from untreated HL60, and the DI_{ratio} of SW480 was also reduced and tended to ~ 1 . Treated SW480 could still be distinguished from untreated SW480 for $Q < 100 \mu\text{l}/\text{min}$ whereas HL60 could only be distinguished for $Q < 30 \mu\text{l}/\text{min}$. This could be due to the fact HL60 are more deformable than SW480, the DI_{max} of HL60 is ~ 1.5 times larger than SW480. At $Q = 30 \mu\text{l}/\text{min}$ HL60 have $DI = 1.90 \pm 0.06$, and at $Q = 100 \mu\text{l}/\text{min}$ SW480 have $DI = 1.64 \pm 0.09$. This corroborates that a low-strain regime is more sensitive to changes due to LatA prohibiting actin polymerisation.

So far only the average DI values of treated and untreated cells have been investigated. However, as cells are heterogeneous due to the process of the cell cycle different cells may respond differently to treatment with LatA. This was investigated by looking at histograms of DI of treated and untreated cells. Figure 5.7 and Figure 5.8 showed that SW480 showed the biggest change in deformability due to LatA at the lowest flow rate $Q = 10 \mu\text{l}/\text{min}$. Whereas, at the highest flow rate $Q = 100 \mu\text{l}/\text{min}$, showed a smaller relative difference. Figure 5.9 shows histograms of the DI of untreated and treated SW480 deformed at $Q = 10 \mu\text{l}/\text{min}$ and $Q = 100 \mu\text{l}/\text{min}$.

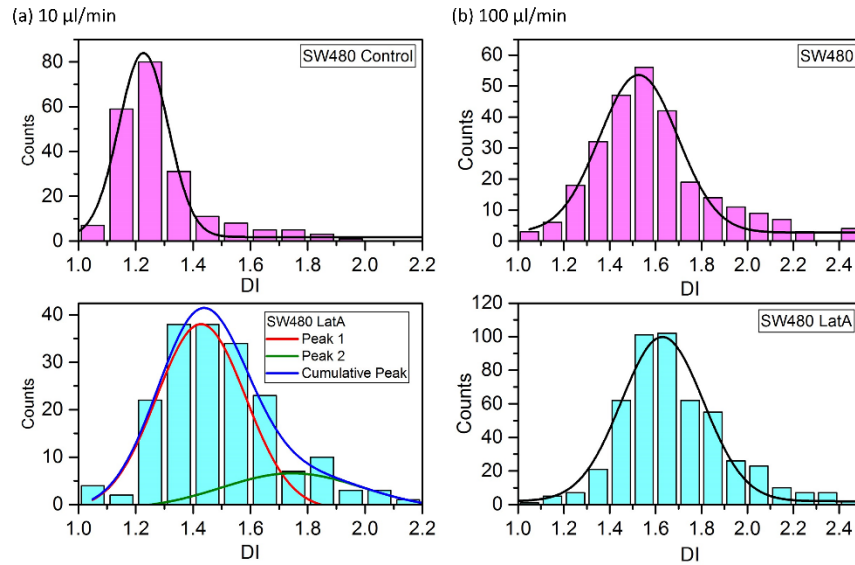


Figure 5.9 Histograms of the DI of SW480 treated with $1 \mu\text{M}$ of LatA compared to an untreated sample. (a) Cells were deformed at $Q = 10 \mu\text{l}/\text{min}$ in the shear-dominant regime ($\mu \cong 33 \text{ cP}$). The control cells are fitted with a single Gaussian peak. The LatA treated cells are fitted with two Gaussian peaks and the cumulative peak is also shown. (b) Cells deformed at $100 \mu\text{l}/\text{min}$ in the same flow regime, both graphs are fitted with a single Gaussian peak.

Figure 5.9a shows that untreated SW480 deformed at $10 \mu\text{l}/\text{min}$ show a normal distribution of DI which is fitted with a Gaussian function. The peak value is at $DI = 1.23 \pm 0.01$ and the FWHM is $w = 0.17 \pm 0.01$. The treated SW480 show a distribution of DI with a large peak at $DI = 1.43 \pm 0.06$ and a smaller peak with $DI = 1.75 \pm 1.29$. The cumulative peak is also shown which has a peak value of $DI = 1.45 \pm 0.01$, showing that the larger peak dominates the average of the distribution. The FWHM of the cumulative peak is $w = 0.33 \pm 0.03$, which is ~ 2 x greater than the untreated sample. These results show that treatment with LatA increased the average cell deformability, and also the spread of deformability's increases. This could be due to some cells being more susceptible to the effects of LatA. Additionally, a smaller population of cells had a bigger increase in deformability as shown by the second peak.

Figure 5.9b shows histograms of the DI of treated and untreated SW480 deformed at $100 \mu\text{l}/\text{min}$. Both plots show a normal distribution and are fitted with single Gaussian peaks. The untreated sample has a peak value of $DI = 1.52 \pm 0.01$ and a FWHM of $w = 0.34 \pm 0.01$, the treated sample of $DI = 1.63 \pm 0.01$ and a FWHM of $w = 0.36 \pm 0.02$. The FWHM of untreated SW480 deformed at $100 \mu\text{l}/\text{min}$ is ~ 2 x larger than when deformed at $10 \mu\text{l}/\text{min}$. This shows that imparting high-strains leads to larger spread of responses compared to low strains, therefore high-strains may be more sensitive to initial sample heterogeneity. Results show that the peak value and FWHM of treated and untreated SW480 deformed at $100 \mu\text{l}/\text{min}$ are within

error of each other. Thus, a high-strain regime is much less sensitive to changes in actin structure due to LatA when investigated by averaging and using SCA.

5.1.3 Deformation Cytometry in the inertial regime

Deformation Cytometry experiments on LatA treated cells were also performed in an inertia-dominant flow regime, at a concentration of $1 \mu\text{M}$ and an incubation time of 2 hr. Cells were microfluidically deformed over a range of flow rates whilst suspended in cell media ($\mu \sim 1 \text{ cP}$), whilst maintaining a constant concentration of LatA throughout the measurement period. Measurements were taken for a range of flow rates, collection 10s-100s of events for each condition. Experiments were repeated $N=3$ and used to calculate an average and standard error for the deformation index DI .

Figure 5.10a shows the average DI HL60 cells treated with LatA as a function of flow rate in the inertia-dominant regime, compared to a control sample. As discussed in section 4.2.2, $Q = 400 \mu\text{l}/\text{min}$ is associated with the cells apparent “*yield stress*” with a change in behaviour seen above and below this condition. A linear slope is fitted to data below the *yield stress* with a lower gradient than a linear slope fitted to data points above the *yield stress*. Figure 5.10b shows the DI_{ratio} of treated and untreated HL60 cells, where the majority of datapoints are within error of $DI_{ratio} = 1$ which suggests no changes in deformability due to treatment with LatA. A linear slope is fitted to the data with a fixed slope of 0, resulting in an intercept value of $y_0 = 1.08 \pm 0.02$. Figure 5.10 shows no changes in DI of HL60 cells when treated with LatA for the entire range of flow rates. Comparatively, Figure 5.7 shows that in the shear-regime there was an increase in DI of the treated cells when probed at low strains ($DI < 1.9$) similar to those probed in the inertia-dominant regime but below the *yield stress*.

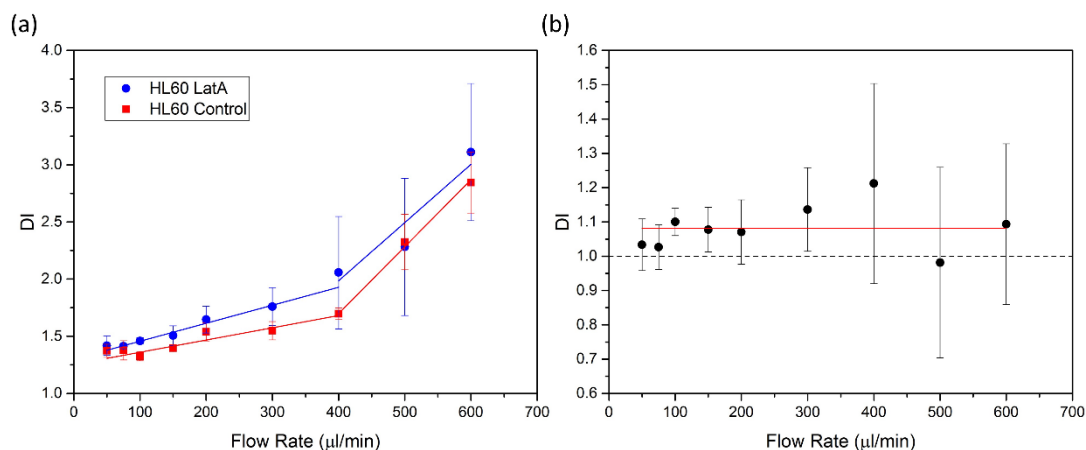


Figure 5.10 (a) The deformation index DI of HL60 cells treated with $1 \mu\text{M}$ of LatA as a function of flow rate, compared to a control sample. Cells were deformed in an inertia-dominant regime where $\mu \cong 1 \text{ cP}$. Both datasets are fitted with linear fits for $Q > 300 \mu\text{l}/\text{min}$ and $Q > 300 \mu\text{l}/\text{min}$. (b) The DI ratio of HL60 cells treated with Lat A compared to untreated cells ($DI_{HL60LatA}/DI_{HL60}$), which is fitted with a linear fit with a set slope of 0.

Figure 5.11a shows a plot of the DI of SW480 cells treated with LatA deformed over a range of flow rates in the inertia-dominant regime, compared to an untreated sample. Here, a change in behaviour is seen at $Q = 300 \mu\text{l}/\text{min}$ corresponding to the associated *yield stress* of the cells. Linear slopes are fitted separately to the datasets above and below the yield stress ($Q = 300 \mu\text{l}/\text{min}$), with the gradients of the slopes increasing above the yield stress. Results show an increase in DI of treated cells for $Q < 300 \mu\text{l}/\text{min}$, whereas for $Q > 300 \mu\text{l}/\text{min}$ there is no significant change in DI due to LatA. Figure 5.11b shows the DI_{ratio} of treated SW480 compared to untreated cells, which shows that $Q > 400 \mu\text{l}/\text{min}$ results in $DI_{ratio} \sim 1$ (this area is shaded in blue).

In the inertia-dominant regime, high-strain deformations cannot be used to distinguish between SW480 treated with LatA and a control. The effects of LatA could not be detected when the deformation index of the control sample was $DI > 1.6$, which occurred at $Q > 300 \mu\text{l}/\text{min}$. Similarly, in the shear-dominant regime any changes due to LatA were not detected for $Q > 100 \mu\text{l}/\text{min}$ where the deformation index was also $DI > 1.6$.

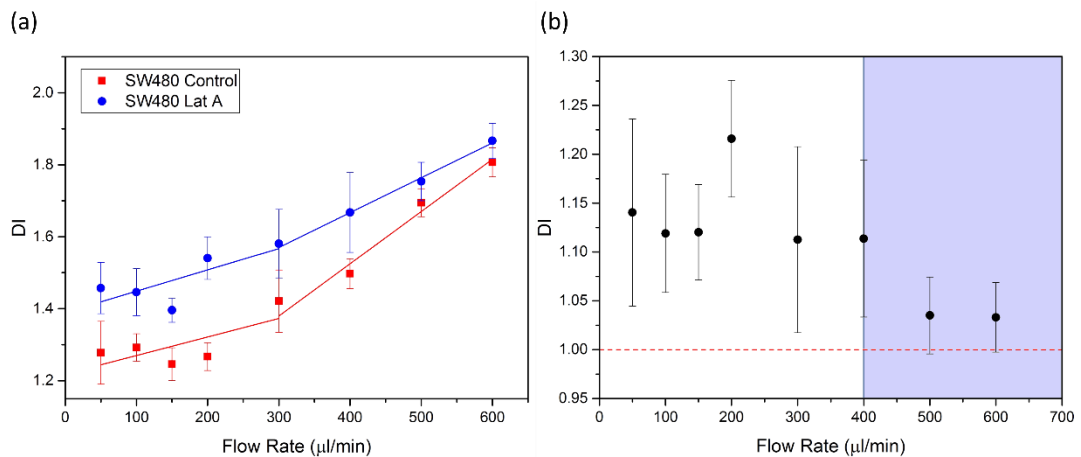


Figure 5.11 (a) The deformation index DI of SW480 cells treated with $1 \mu\text{M}$ of LatA as a function of flow rate, compared to an untreated sample. Cells were deformed in an inertia-dominant regime where $\mu \cong 1 \text{ cP}$. Both datasets are fitted with linear fits for $Q > 300 \mu\text{l}/\text{min}$ and $Q > 300 \mu\text{l}/\text{min}$. (b) The DI ratio of SW480 cells treated with Lat A compared to a control sample ($DI_{SW480LatA}/DI_{SW480}$).

Overall, in the shear-dominant regime both HL60 and SW480 became more deformable due to treatment with LatA (Figure 5.7 and Figure 5.8). The DI_{ratio} also showed that the relative increase in deformability was highest for low-strains, and decreased exponentially for high-strains and tending towards no detectable change ($DI_{ratio} = 0$). In the inertia-dominant regime no changes in the deformability of HL60 due to LatA could be detected at low or high strain deformation (Figure 5.10). For SW480, in the inertial regime, increased deformability due to LatA was detected in the low strain regime (below the *yield stress*) but not at high strains (above the *yield stress*). Therefore, results suggest that a low-strain and shear-dominant

flow regime is the most sensitive to deformability changes induced by disruption of the actin cytoskeleton. SW480 previously showed a more defined actin cortex than HL60 (Figure 5.3 and Figure 5.5), which could explain why they showed a larger change in deformability due to LatA which could be detected in both flow-regimes. Actin destabilisation at high strains could contribute to why a low strain regime shows most sensitivity when measuring deformability changes due to LatA.

5.1.4 Deformation traces and SCA

The strain ε (equation (3.2)) of SW480 treated with LatA was tracked as cells deformed and recovered through the SP of an extensional flow junction and compared to a control sample. Treated cells were incubated with 1 μM of LatA for 2 hr. A shear-dominant flow regime was used ($\mu \cong 33 \text{ cP}$), at a flow rate of 5 $\mu\text{l}/\text{min}$. These conditions were chosen because measurement of DI at low strain in the shear-regime proved to be most sensitive to changes in LatA Figure 5.8.

The averaged strain traces of treated (N=56) and untreated (N=30) SW480 are shown by Figure 5.12, which can be used to extract multiple characteristic parameters. These include; the initial strain ε_0 , the maximum strain ε_{max} , the deformation time τ_d , the relaxation time τ_r and the final strain ε_∞ . The deformation and relaxation times were found by fitting exponential functions to the deformation region of the graph (as the cell moves toward to SP) and the recovery region of the graph (as the cells moves away from the SP). The final strain was found by extrapolation of the exponential fit to the recovery region. Further, the different parameters are summarised in Table 5.1. This confirms that the LatA treated cells are more deformable than the control sample, as they have a larger ε_{max} . The initial strain ε_0 of treated and untreated cells are within error of each other. However, the final strain ε_∞ of the treated cells is ~6 times bigger than of the control cells. The results show that the LatA treated cells have a relaxation time twice as fast as the untreated cells but they recover to a higher strain value than the magnitude of the initial strain ($\varepsilon_\infty > \varepsilon_0$). Whereas, for the control cells the initial and final strains were within error of each other ($\varepsilon_0 = \varepsilon_\infty$).

Figure 5.13 shows the average velocity profiles of treated and untreated SW480 as they pass through the extensional flow junction, which were fitted with *sine* functions (shown in red). This was used to fit the Kelvin-Voigt model (described in section 2.3.4) to the strain traces (shown in red). From this, the elastic modulus of SW480 was found to be $E = 542 \pm 66 \text{ Pa}$ and SW480 treated with LatA was $E = 419 \pm 54 \text{ Pa}$. This corroborates the results shown by measurement of DI and ε_{max} in this flow regime, SW480 treated with LatA become softer.

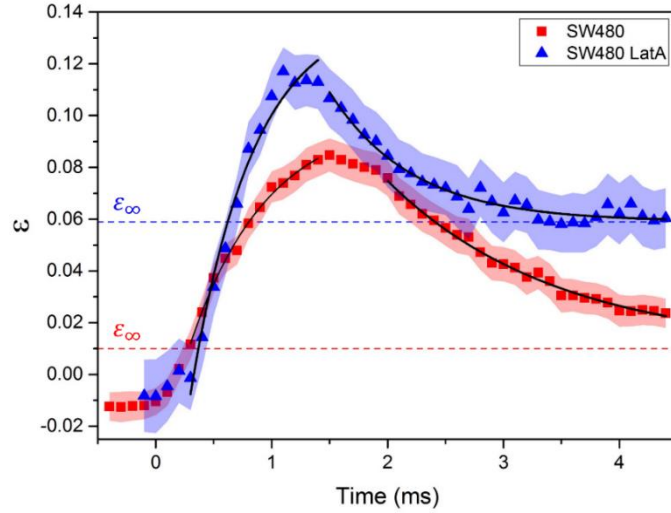


Figure 5.12 The averaged strain trace for SW480 ($N = 56$) and SW480 treated with $1 \mu\text{M}$ LatA ($N = 30$) as a function of time, with the standard error shown by the shaded areas. Q was $5 \mu\text{l}/\text{min}$, and the suspension medium viscosity was 33 cP . The recovery is fitted with an exponential function and the dashed lines represent the extrapolated final strain ϵ_∞ for both samples.

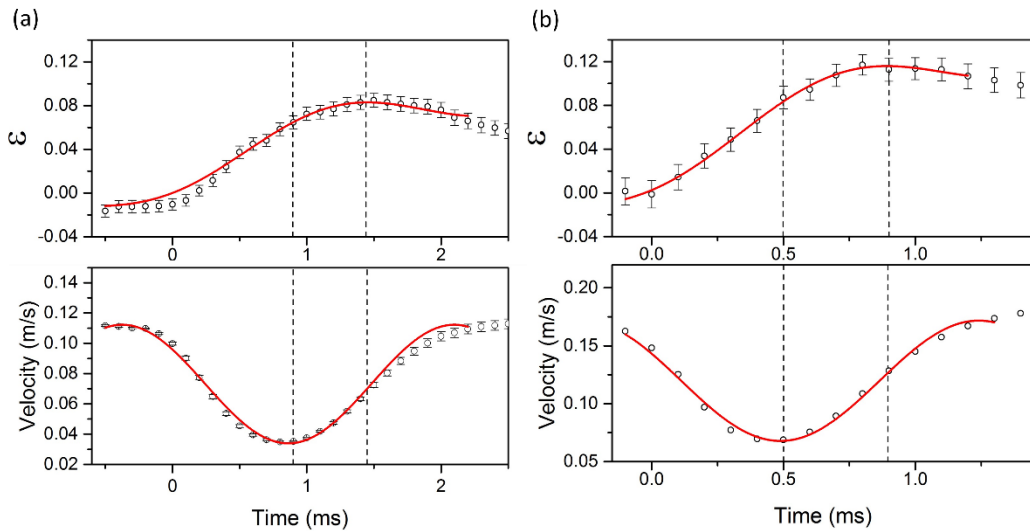


Figure 5.13 Strain traces of SW480 and SW480 treated with LatA fitted with the Kelvin voigt model, accompanied by velocity profiles fitted with a sine function. (a) The average strain trace of $N=56$ SW480 cells, the Kelvin-Voigt model was fitted, shown in red. The average velocity profile of the same 56 cells is shown and fitted with a sine function, shown in red. (b) Strain and velocity profiles for $N=30$ SW480 cells treated with $1 \mu\text{M}$ of LatA. Cells were deformed in a shear-dominant regime where $Q = 5 \mu\text{l}/\text{min}$ and $\mu \cong 33 \text{ cP}$.

Multiple parameters extracted from the averaged strain traces showed that ϵ_{max} , τ_r , ϵ_∞ and E were able to distinguish between the two samples, whereas τ_d and ϵ_0 could not. However, as discussed in section 2.1.5 cell populations are heterogeneous and their mechanical properties depend on their stage in the cell cycle. Bulk measurements can often miss any subpopulations within a large sample. Therefore, single cell analysis (SCA) was also performed on the $N=56$

SW480 cells and the N=30 SW480 cells treated with LatA. SCA analysis was performed in the same manner described in results section 4.4.1.

Table 5.1 compares the different parameters extracted from the “Averaged Strain Trace” and from averaging values found using SCA. Firstly, the values of ϵ_{max} found using both methods are within error of each other. The values of ϵ_0 are also comparable, and show the cells have relatively negligible initial strain compared to the applied strain at the SP (ϵ_{max}). The values of ϵ_{∞} from both methods confirm that the SW480 recover back to their initial strain, whereas the treated cells recover to a higher strain ($\epsilon_{\infty} > \epsilon_0$). The values for relaxation time τ_r for the treated cells are within error of each other, however the τ_r calculated from the averaged strain trace is ~ 1.5 times greater than the SCA value. This suggests some outliers may skew the value from the averaged trace and shows the importance of investigation at the single cell level.

Table 5.1 Multiple characteristic parameters extracted from the strain traces of N=56 SW480 cells and N=30 SW480 cells treated with LatA. Including the initial cell diameter A, the initial strain ϵ_0 , the final strain ϵ_{∞} , the maximum strain ϵ_{max} , the deformation time τ_d , the relaxation time τ_r , and the elastic modulus E. Two analysis methods were used and the resulting values were compared: 1. the strain traces were averaged and values were extracted, “Averaged Strain Trace” and 2. Single cell analysis was used “SCA” then averaged with $\pm SE$.

	Averaged Strain Trace		SCA	
	SW480	SW480-LatA	SW480	SW480-LatA
A (μm)	N/A	N/A	15.1 \pm 0.3	15.0 \pm 0.4
ϵ_{max}	0.08 \pm 0.01	0.11 \pm 0.01	0.09 \pm 0.01	0.12 \pm 0.01
τ_r (ms)	1.36 \pm 0.06	0.67 \pm 0.09	0.89 \pm 0.11	0.79 \pm 0.14
τ_d (ms)	1.19 \pm 0.20	0.78 \pm 0.24	N/A	N/A
E (Pa)	542 \pm 66	419 \pm 54	N/A	N/A
ϵ_0	-0.012 \pm 0.006	-0.007 \pm 0.014	-0.012 \pm 0.003	-0.003 \pm 0.013
ϵ_{∞}	+0.010 \pm 0.003	+0.059 \pm 0.001	+0.018 \pm 0.005	+0.053 \pm 0.001

The statistical significance of the different parameters to classify the treated and untreated cell was investigated further using two sample t-tests. A t-test uses the difference between the mean values from two data sets, the standard deviation of the datasets and the sample size, to measure how significant differences between the datasets are. This is measured by the “p-value” found from the t-test. Smaller p-values indicate a higher significance between differences measured by the t-test. A p-value ≤ 0.05 suggests strong evidence that the two datasets show significant differences, p-values ≥ 0.05 suggest no significant difference.

Figure 5.14 shows bar graphs of the average A, ϵ_{max} , ϵ_{∞} , τ_r and ϵ_0 of the two sample and the level of significance is labelled: where $p > 0.05$ is not significant (ns), $0.01 < p < 0.05$ is significant (*), $0.001 < p < 0.01$ is very significant (**), $0.0001 < p < 0.001$ is extremely significant (***) and $p < 0.0001$. The raw p-values are also included in a table. Results show that there is

no significant difference in A , τ_r and ϵ_0 when SW480 cells are treated with LatA. However, ϵ_{max} and ϵ_∞ show a significant difference between treated and untreated cells and these parameters can potentially be used to classify these cell types.

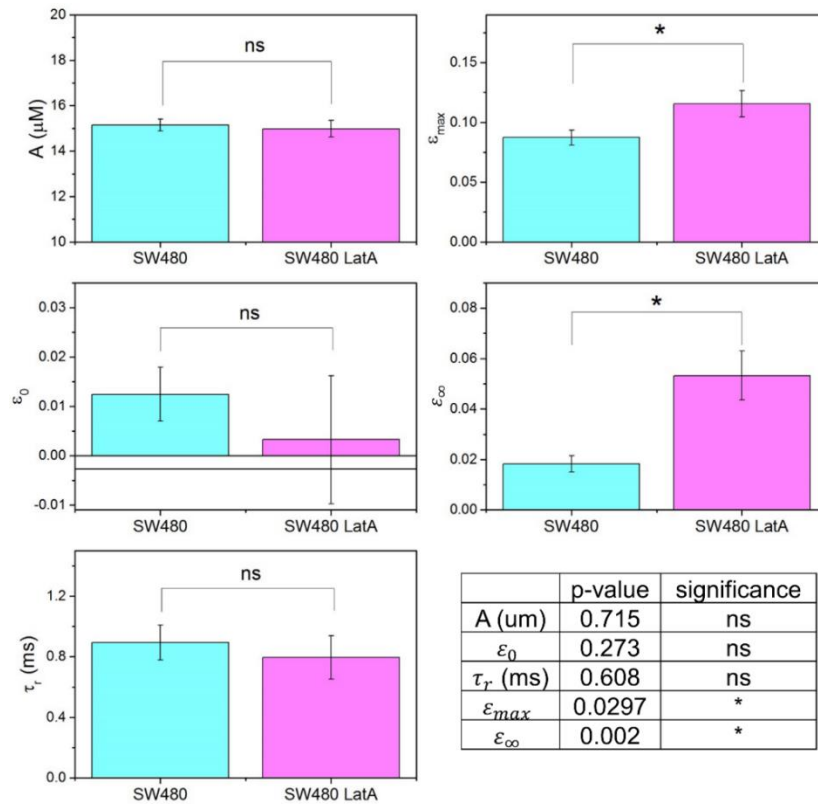


Figure 5.14 SCA was performed on strain traces of SW480 treated with LatA and a control sample to extract multiple parameters. The plots show the average values of the cell diameter A , maximum strain ϵ_{max} , initial strain ϵ_0 , the relaxation time τ_r and the final strain ϵ_∞ . The error bars denote the standard error SE and statistical t -tests were done to determine the level of significance, where ns indicates “no significance”.

The heterogeneity of the two samples was explored by plotting histograms of parameters of interest. Table 5.1 and Figure 5.14 showed that LatA had no effect on the A or ϵ_0 of SW480 cells using bulk averaging and SCA, therefore the histograms were not included. Figure 5.15 shows histograms of ϵ_{max} , ϵ_∞ and τ_r of the treated and untreated samples. The histograms of ϵ_{max} both show a normal distribution, fitted with a Gaussian peak, with a shift in the peak position of the treated cells indicating an increase in deformability. The histogram for ϵ_∞ of the control sample shows that most cells have $\epsilon_\infty=0$, indicating their full recovery after deformation. The treated sample shows a peak of $\epsilon_\infty=0$ and also a significant peak at $\epsilon_\infty\sim 0.06$, resulting in the non-zero average shown in Table 5.1. The histogram gives more information than using averages, suggesting that treatment with LatA leads to two populations with some cells recovering their initial shape and some having a “plastic deformation”. It is worth noting that ϵ_∞ shows a non-normal distribution, and typically t -tests are performed on datasets with normal

distributions (Figure 5.14). However, t-tests can still be performed on large enough sample sizes and thus the p-values are still significant. Finally, the histograms of τ_r both show a normal distribution, fitted with a Gaussian, with similar peak positions ~ 0.3 ms. Both datasets show some outliers with a relaxation time ~ 10 times greater than the peak position, this may explain the differences in τ_r found between the averaged strain trace and SCA Table 5.1.

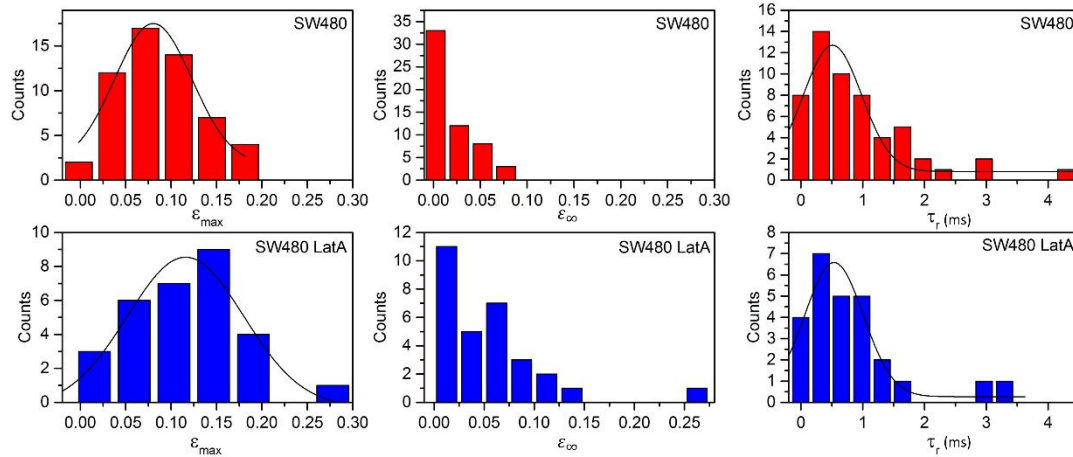


Figure 5.15 Histograms showing the maximum strain ϵ_{max} , final strain ϵ_{∞} and relaxation time τ_r of SW480 treated with LatA ($N=30$), compared to an untreated control sample ($N=56$).

5.1.5 Discussion

The deformability of HL60 and SW480 cells treated with LatA was probed using deformation cytometry. An increase in cell deformability was detected in both cell lines when deforming cells in the shear-dominant regime. For HL60 treated with LatA, an increase in deformability was only detectable at low applied strains ($Q < 30 \mu\text{l}/\text{min}$). Increased deformability was detected at both low and high strains in the treated SW480 cells; however, the relative increase was more apparent at lower strains. The inertia-dominant regime was not sensitive to the effects of LatA in the HL60 cells. An increase in deformability was detected in SW480 but only for low applied strains below the *yield stress* ($Q < 300 \mu\text{l}/\text{min}$).

LatA binds strongly to actin monomers which precludes polymerisation of actin filaments and prevents actin recycling. Many studies have shown that treating cells with LatA leads to a reduction in cell stiffness, measurable over a wide range of techniques including; AFM, micropipette aspiration and optical stretching [8], [195]–[198]. Cytochalasin D is another drug which destabilises actin by capping the plus ends of filaments, leading to similar measurable decreases in cell stiffness [8], [199]–[201]. These techniques are classically high-accuracy and low-throughput and impart relatively small deformations. Therefore, actin filaments contribute greatly to cell elasticity at low applied strains.

Microfluidic assays have also been used to measure deformability of cells treated with LatA and CytoD [22], [50], [174], [202]. Adamo *et al.* 2012 used microfluidic constriction channels to measure the transit time of HeLa cells treated with LatA. They showed that the treated cells had a ~26% faster transit time, which is equivalent to a decrease in cell stiffness allowing them to more easily deform through the channel. Kim *et al.* 2018 also used microfluidic constriction channels to measure the deformability of cells treated with LatA [203]. They compared the deformability of the malignant breast cancer cell line MCF7 to the non-malignant epithelial breast cell line MCF7-10A, when treated with LatA. Both cell lines showed increased deformability due to LatA, however MCF7 were more affected. They theorize that this may be due to initial F-actin content in the two cell lines. Similarly, we tested two cell lines and saw that SW480 were more affected than HL60. Confocal fluorescence images also showed that SW480 had an initially more defined F-actin structure.

Golfier *et al.* 2017 studied deformability changes in HL60 due to disrupting the actin structure using the drug CytoD [50]. This was done using RT-DC where cells experience a fluid-induced deformation due to shear confinement in a channel ($Re < 0.1$). HL60 cells showed increased deformability due to treatment with CytoD, and their maximal relative deformation was ~1.5. Using LatA we showed a maximal deformation ratio ~1.1. This suggests that CytoD reduces the stiffness more than LatA. However, RT-DC imparts much smaller strains than Deformation Cytometry which may also indicate that lower-strains are more sensitive to cytoskeletal changes. Ahmmed *et al.* (2018) used a similar microfluidic deformation method and showed increased deformability of MCF7 cells treated with LatA [44].

Gossett *et al.* 2012 used an inertia-dominant extensional flow in a microfluidic device to deform 3T3 fibroblasts and HeLa cells treated with LatA ($Re \gg 40$) [27]. No significant changes in the deformation index of treated and control cells were seen for both cell lines. This technique deforms at high strains and high strain rates ($\sim 10^5 \text{ s}^{-1}$). They noted that these conditions are likely more sensitive to changes in the cytoplasmic viscosity and cell chromatin structure, whereas actin is known to fluidise at high-strains [83]. Our study showed that HL60 and SW480 deformed in the inertial regime above the *yield stress* showed no significant change in *DI* due to LatA. Notably, the median deformability of T3T cells in Gossett *et al.* 2012 was $DI \cong 1.8$ which is above strains which could not distinguish HL60 ($DI \cong 1.5$) and SW480 ($DI \cong 1.4$) in this flow regime.

Kubitschke *et al.* 2018 used a microfluidic cell stretcher to study the deformability of cells treated with LatA deformed at low and high strains [198]. Small deformations were defined as <5% the initial cell diameter, and large strains as >5% the initial cell diameter, no measurements were taken for strains >20%. They reported a strain-independent softening of

cells treated with LatA. This differs from our results using the shear-dominant regime, where cells deformed at low-strains were more effected by LatA leading to an increased relative deformation. However, the study in [198] showed that for small strains there was up to 75% increased deformability and for high strains there was up to 65% deformability. This result may also be indicative of small-strain deformation being more sensitive to actin changes. Additionally, the “high strains” defined here are relatively small compared to those in Gossett *et al.* 2012 and also in our study above the *yield stress*. Therefore, strains 0-20% may not be a sufficient range to fully study sensitivity to LatA at low and high strain. Strain-rate may also be a factor toward LatA sensitivity as the optical traps deform at a strain rate of seconds compared to inertia-dominant microfluidics which deforms at $10^{-5}s$.

An elastic modulus of SW480 treated with LatA was found from strain traces of cells deforming in the shear-dominant regime, using the Kelvin-Voigt model. Treated cells had an elastic modulus of $E = 419 \pm 54 Pa$ compared to control cells which had $E = 542 \pm 66 Pa$ control cells were ~ 1.3 times stiffer. Abidine *et al.* 2015 used optical trap indentation of 200 nm to find the elastic modulus of T24 human urinary bladder cancer cells to be $E = 100 \pm 10 Pa$ compared to control cells $E = 29 \pm 4 Pa$, a ~ 3.4 times decrease in stiffness [197]. Nawaz *et al.* 2012 used micropipette aspiration to deform MCF7 cells and found the elastic modulus to be $E = 441 \pm 65 Pa$ which reduced to $E = 225 \pm 41 Pa$ when treated with LatA, a ~ 2 times decrease in stiffness [196]. This is further evidence toward low strain and strain rate techniques being most sensitive to F-actin structure.

The strain traces were also used to extract multiple deformation and relaxation parameters, and SCA was used to perform t-tests to quantify the significant of these parameters. Results showed that LatA and control SW480 initially had the same size A and shape ϵ_0 . As expected, there was a significant increase in the maximum deformation ϵ_∞ of the treated cells. Additionally, the final strain of the treated cells did not recover over the time period whereas the control cells did. This suggests that actin disruption leads to some plastic deformation and changes the relaxation process of the cells. Kubitschke *et al.* (2017) tracked the recovery of MCF7 cells after a step force deformation using optical trapping. They found that cells treated with LatA did not recovery their original shape as much as control cells, also indicating that LatA induces more plasticity in cells [198].

5.2 Treating cells with Combretastatin A4

Combretastatins are a group of natural products related to the tubulin-binding agent colchicine [204]. Combretastatin A4 (CA4) belongs to this group and has a strong binding affinity to tubulin, which inhibits microtubule polymerisation and leads to morphological changes of the cell cytoskeleton [205], [206]. Tubulin has a vital role in cell division, making it a potent target

in cancer treatments. CA4 is a drug of interest for treating cancer due to its abilities to disrupt tubulin and prevent cell proliferation, including being able to rapidly shut down established tumour vasculature [207]. The previous section showed that disruption to the actin cytoskeleton leads to changes in cell deformability. Here, CA4 was used to investigate whether changes in microtubule structure could be sensed using DC in shear and inertia-dominant flow regimes.

The effects of CA4 on microtubule structure can be seen within 2-4 hr of incubation with the drug, and different studies report different concentrations being required for complete microtubule destabilisation. Mico *et al.* (2017) incubated SVR mouse pancreatic islet endothelial cells with 40-100 nM of CA4 for 2 hrs and saw complete destabilisation using fluorescence microscopy. Greene *et al.* (2010) incubated K562 and HL60 cells with 50 nM of CA4 for 4 hours. The effects of CA4 can be reversible below a critical concentration if the drug is removed, however above this concentration and long incubation times (>24 hr) induce cell apoptosis [208].

HL60 and SW480 were previously used to study the effects of actin disruption using LatA, these cell lines showed different responses to LatA which may relate to their differing initial morphologies and functionalities. Therefore, the same cell lines were used to study the effects of tubulin disruption using CA4. Probing both cell types in different flow regimes will elucidate more the importance of microtubules to cell deformability.

5.2.1 Drug treatment and observations

HL60 and SW480 cells were treated with CA4 and imaged using phase contrast microscopy and confocal fluorescence microscopy. This was to investigate whether the drug affected cell size and morphology and to visualise changes to the microtubule structure.

HL60 cells were incubated with 100 nM of CA4 for 2 hr and imaged using a phase contrast microscope (VWR IT404 - 630-1575) with a 40x objective (Figure 5.16a). A control sample of HL60 show a rounded morphology and the CA4 treated cells show a less rounded morphology. This was quantified using the circularity deformation parameter D_C , where $D_C = 0$ represents a perfect circle and $D_C > 0$ deviates from a perfect circle. Figure 5.16b shows histograms of D_C of treated and untreated HL60 cells, both datasets are fitted with a Lognormal distribution. The peak position of the untreated sample was $D_C = 0.075 \pm 0.001$ and for the treated sample was $D_C = 0.121 \pm 0.005$. The standard deviation of the lognormal curves was $w = 0.152 \pm 0.017$ for the control cells and $D_C = 0.334 \pm 0.042$ for the treated cells.

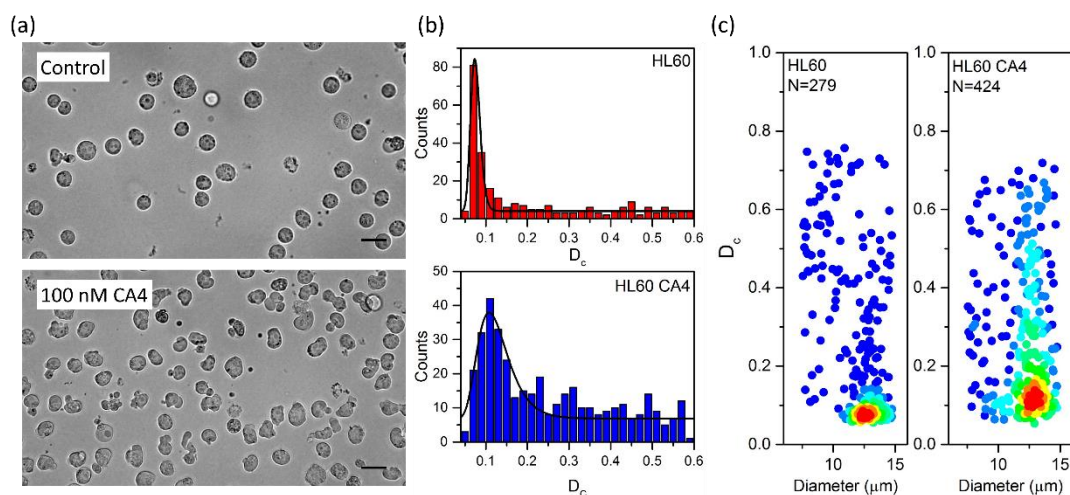


Figure 5.16 Measurement of the size and morphology of HL60 treated with 100 nM of CA4, compared to a control sample: (a) Phase contrast images of HL60 and HL60 CA4 cells taken with a 40x objective. (b) Histograms of the circularity D_C of HL60 and HL60 CA4, fitted with Lognormal functions. (c) Density scatter plots of D_C as a function of diameter of HL60 and HL60 CA4.

These results show that cells treated with CA4 change their cell morphology, the average D_C increased ~ 1.6 times compared to the control sample. The standard deviation of the results increased ~ 2.2 times for the treated cells, which could suggest that cells have a range of susceptibilities to the drug leading to a wide range in morphological changes. Figure 5.16c shows density scatter plots of D_C as a function of diameter for treated and untreated cells. It corroborates that treatment with CA4 leads to a change in circularity of HL60 cells. It also shows that the cell diameter does not change, the average diameter of untreated cells was $A_{control} = 12.04 \pm 0.09 \mu\text{m}$ and of treated cells was $A_{CA4} = 12.24 \pm 0.09 \mu\text{m}$.

The same treatment protocol was repeated using SW480 cells, which were first detached into a single cell suspension. Figure 5.17a shows phase contrast images of CA4 treated cells compared to a control sample, showing no obvious changes in morphology. Figure 5.17b shows histograms of D_C of both samples, which are fitted with Gaussian functions. The peak position for the control sample was $D_C = 0.323 \pm 0.013$ and for the treated sample was $D_C = 0.322 \pm 0.010$, which confirms no change in SW480 morphology due to CA4. Figure 5.17c shows density scattered plots of D_C as a function of cell diameter, this shows a larger spread of D_C of SW480 compared to HL60 cells (Figure 5.16c) which may relate to the fact SW480 were detached from a surface whereas HL60 are naturally non-adherent. It also shows the size of SW480 is not changed by treatment with LatA, the control sample had an average diameter of $15.64 \pm 0.13 \mu\text{m}$ and the treated sample had an average diameter of $A_{CA4} = 15.21 \pm 0.09 \mu\text{m}$.

Overall, analysis of phase contrast images show that treatment with 100 nM of CA4 for 2 hr lead to no changes in the diameter of HL60 and SW480 cells. Changes to morphology were measured using D_c which showed that HL60 cells become less rounded when treated with CA4, whereas SW480 do not change shape. This could indicate that HL60 were more effected by treatment with CA4.

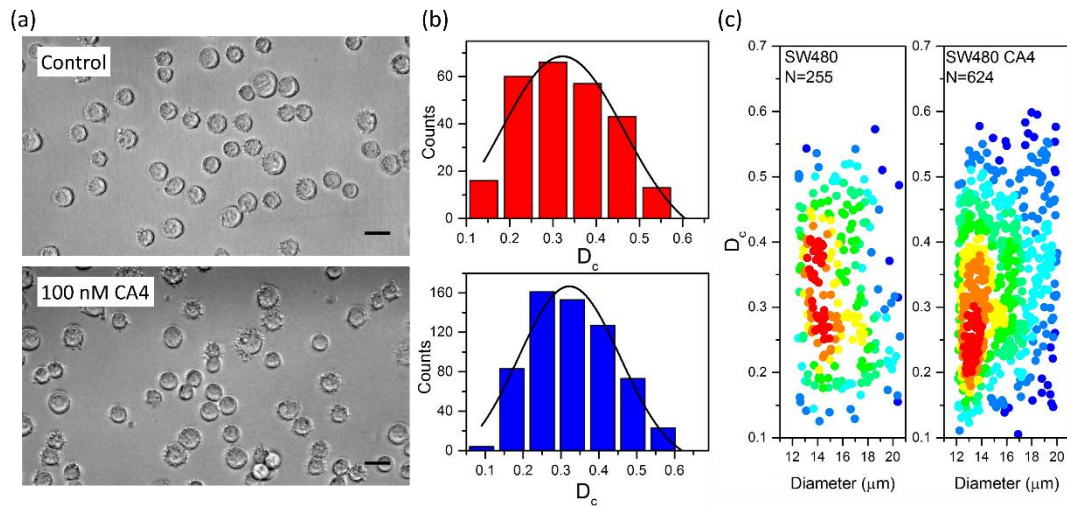


Figure 5.17 Measurement of the size and morphology of SW480 cells treated with 100 nM of CA4, compared to a control sample: (a) Phase contrast images of SW480 and SW480 CA4 cells using a 40x objective. (b) Histograms of the circularity D_c of SW480 and SW480 CA4, fitted with Gaussian functions. (c) Density scatter plots of D_c as a function of diameter of SW480 and SW480 CA4.

Live cell confocal fluorescence images were taken to visualise the microtubule structure of HL60 and SW480 cells treated with CA4. Concentrations of 10 nM, 50 nM and 100 nM were compared to a control sample. Cells were incubated with CA4 and the fluorescence stains for 2 hr before imaging occurred. Tubulin was stained using a live cell fluorogenic labelling probe based on Silicon-Rhodamine (Sir) (Spirochrome, Cytoskeleton Inc.) at a final concentration of 1 μM . The dye Hoechst 3342 (Thermo Fisher Scientific) was used to stain the DNA, at a final concentration of 0.5 $\mu\text{g/ml}$.

Figure 5.18 shows fluorescent images of HL60 treated with the different concentrations of CA4. In the image of the control sample there is a defined microtubule structure, with microtubules protruding radially from centrosomes (the main organelle of the microtubule organising centre). Cells treated with 10 nM of CA4 also show clear microtubule filaments, however there are notably less of them and they appear generally shorter in length. By a concentration of 100 nM of CA4 there are no defined microtubules, instead there is a diffuse background of tubulin and stronger fluorescence of what remains at the centrosome. Figure 5.19 show fluorescent images of SW480 cells treated with CA4. The results are similar to

HL60, the control sample shows a defined microtubule structure which is highly disrupted for concentrations of CA4 >50 nM.

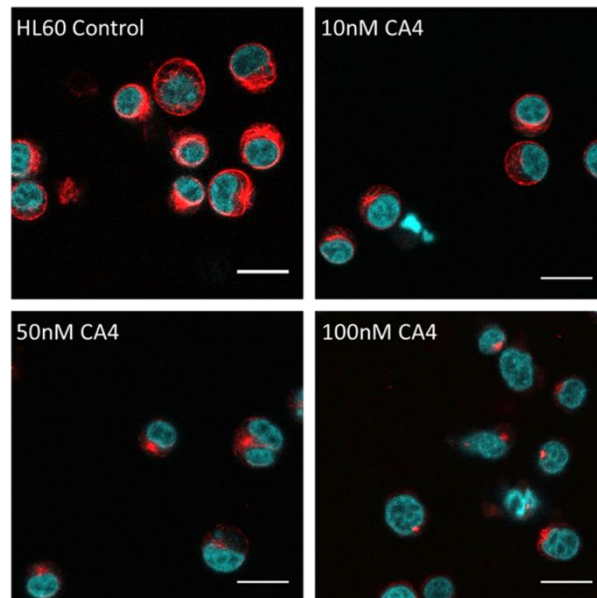


Figure 5.18 Confocal fluorescence images of control HL60 cells and HL60 treated with 10 nM, 50 nM and 100 nM of CA4, stained for tubulin (red) and DNA (blue). Images were taken using a 40 x objective, scale bar 20 μ m.

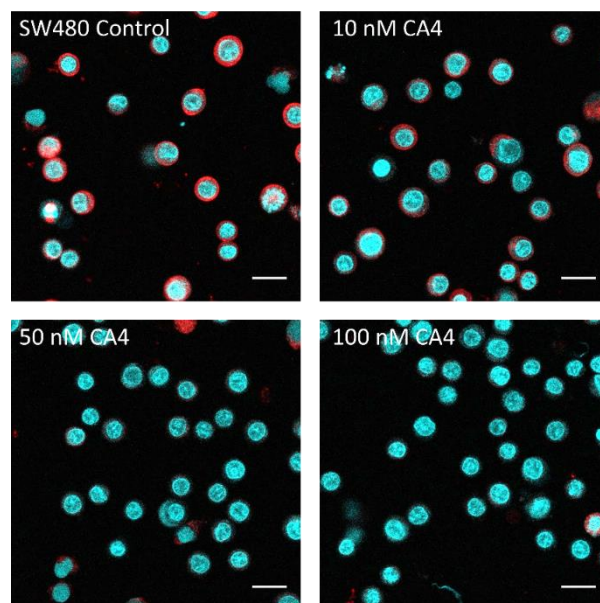


Figure 5.19 Confocal fluorescence images of control SW480 cells and SW480 treated with 10 nM, 50 nM and 100 nM of CA4, stained for tubulin (red) and DNA (blue). Images were taken with a 40x objective, scale bar 20 μ m.

The microtubules of HL60 cells looked more defined than for the SW480 cells (Figure 5.18 and Figure 5.19). This may be because SW480 have a bigger nucleus compared to HL60, therefore the microtubules in HL60 have more room to pervade the cytosol. The confocal

fluorescence images were also used to measure the nuclear diameter of HL60 and SW480 treated with 100 nM of CA4.

Figure 5.20 shows histograms of the nuclear diameter of HL60 and SW480 treated with CA4, compared to control samples. The nuclear diameter of HL60 was $A_{nucleus} = 8.98 \pm 0.04$ which is within error of HL60 treated with CA4, $A_{nucleus} = 8.43 \pm 0.13$. The nuclear diameter of SW480 was $A_{nucleus} = 10.66 \pm 0.13$, which was also within error of the treated sample $A_{nucleus} = 10.59 \pm 0.11$. These results show that CA4 has no effect on the nucleus size of HL60 and SW480.

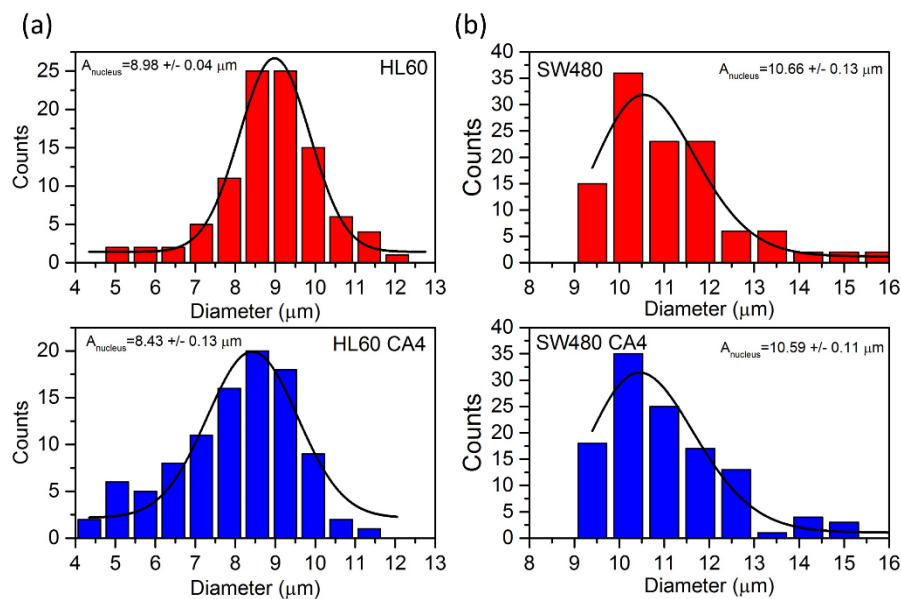


Figure 5.20 DNA stained images were used to measure the nuclear diameter of HL60 and SW480 treated with CA4. Histograms were plotted of the nuclear diameters $A_{nucleus}$ of HL60 (a) and SW480 (b) treated with CA4 and compared to control samples. Plots are fitted with a Gaussian function.

5.2.2 Deformation Cytometry in the shear regime

Deformation Cytometry was performed on HL60 and SW480 cells which were incubated with 100 nM of CA4 for 2 hr. Cells were deformed microfluidically over a range of flow rates whilst suspended in 0.5% PBS-MC buffer ($\mu \cong 33$ cP). A constant concentration of CA4 was maintained throughout the measurement period. For each flow rate, the DI of 10s-100s of cell events were measured. Experiments were repeated $N=3$ and the averaged DI and standard error in DI were calculated from this.

Figure 5.21a is a plot of the DI of HL60 cells treated with CA4 as a function of flow rate in the shear-dominant regime, compared to a control sample. Results show a decrease in DI for the cells treated with CA4 for the entire range of flow rates. An exponential function was fitted to both datasets and used to extrapolate the maximum deformation index DI_{max} . For the control

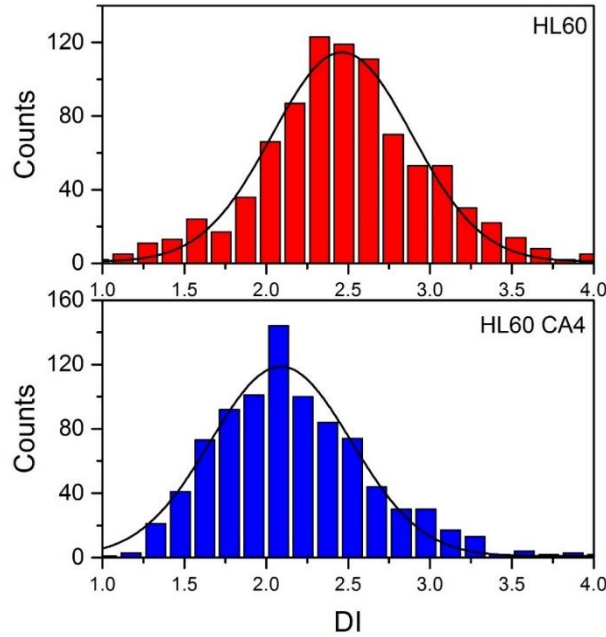


Figure 5.22 Histograms of the DI of HL60 treated with 100nM of CA4 ($N=890$) and a control sample ($N=853$), cells were deformed at 60 $\mu\text{l}/\text{min}$ in a shear dominant regime ($\mu \cong 33 \text{ cP}$). Both datasets are fitted with a Gaussian function.

Figure 5.23a shows a plot of DI as a function of flow rate for SW480 cells treated with CA4 and deformed in the shear regime, compared to a control sample. Results show no significant change in DI between the treated and untreated cells for the entire range of flow rates. The maximum deformation DI_{max} of the treated sample was $DI_{max} = 1.74 \pm 0.06$ and for the control sample was $DI_{max} = 1.66 \pm 0.04$, which are within error of each other. Further, Figure 5.23 shows the deformation ratio where $DI_{ratio} = DI_{CA4}/DI_{control}$. This shows that $DI_{ratio} \cong 1$ for all flow rates, corroborating that the shear regime is not sensitive to any mechanical changes induced by CA4 in SW480 cells.

Figure 5.18 and Figure 5.19 showed that CA4 inhibits polymerisation of microtubules in both SW480 and HL60 cells, and a concentration of 100 nM leads to complete destabilisation of microtubules. Deformation cytometry in the shear regime was used to measure deformability changes of the cells due to microtubule disruption. Interestingly, HL60 become less deformable whereas no changes were measured in SW480. Confocal fluorescence imaging also showed that HL60 have a smaller nucleus and nuclear ratio compared to SW480, making their microtubule filaments able to pervade more of the cytoplasm. This could mean that the mechanical rigidity of HL60 is more affected by microtubule filaments than SW480, where the mechanical properties of the nucleus may dominate instead. Additionally, untreated HL60 are naturally much softer than SW480 (DI_{max} of HL60 is ~ 1.5 times that of SW480). This means SW480 may also become stiffer due to CA4 but deformation cytometry in this regime may not be sensitive enough to detect these changes.

HL60 becoming stiffer due to treatment with CA4 is counter-intuitive. Destabilising microtubules, part of the cell cytoskeleton, would suggest an increase in deformability. CA4 is also known to be cytotoxic and can induce apoptosis after ~24 hr of incubation. Cells in the early stages of apoptosis become stiffer [48], therefore is it important to separate whether the decrease in stiffness is due to microtubule changes, apoptosis, or other subcellular changes. This is investigated in subsequent sections.

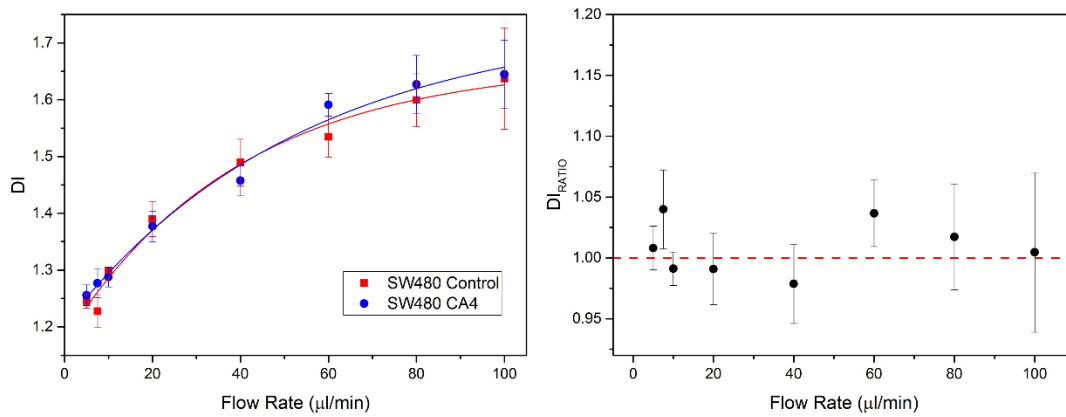


Figure 5.23 (a) The deformation index DI of SW480 cells treated with 100 nM of CA4 as a function of flow rate, compared to a control sample. Cells were deformed in a shear-dominant regime where $\mu \cong 33$ cP. Both datasets are fitted with an exponential decay function. (b) The DI ratio of SW480 cells treated with CA4 compared to untreated cells ($DI_{SW480CA4}/DI_{SW480}$).

5.2.3 Deformation Cytometry in the inertial regime

Deformation cytometry was also performed on HL60 and SW480 cells treated with CA4 in the inertia-dominant flow regime. Cells were incubated with 100 nM of CA4 for 2 hr and then deformed microfluidically whilst suspended in cell media ($\mu \sim 1$ cP). A constant concentration of CA4 was maintained throughout the measurement period. Cells were deformed over a range of flow rates ($Q \leq 600$ μl/min), 10s-100s of events were collected for each flow conditions. Experiments were repeated $N=3$ and the average DI and standard error were found.

Figure 5.24a shows DI as a function of flow rate for HL60 cells treated with CA4 and deformed in the inertia-dominant flow regime. Both datasets are fitted with an exponential decay function and follow similar trends. Both datasets shows the previously discussed *yield stress* behaviour at $Q \cong 400$ μl/min corresponding to a larger increase in DI . Figure 5.24b shows the $DI_{ratio} = DI_{CA4}/DI_{control}$ as a function of flow rate, with $DI_{ratio} = 1$ equivalent to no deformability change induced by CA4. This shows that for the majority of flow rates $DI_{ratio} \cong 1$. Results show that no deformability changes could be detected in HL60 in the inertial-dominant regime at low or high applied strains (above and below the *yield stress*).

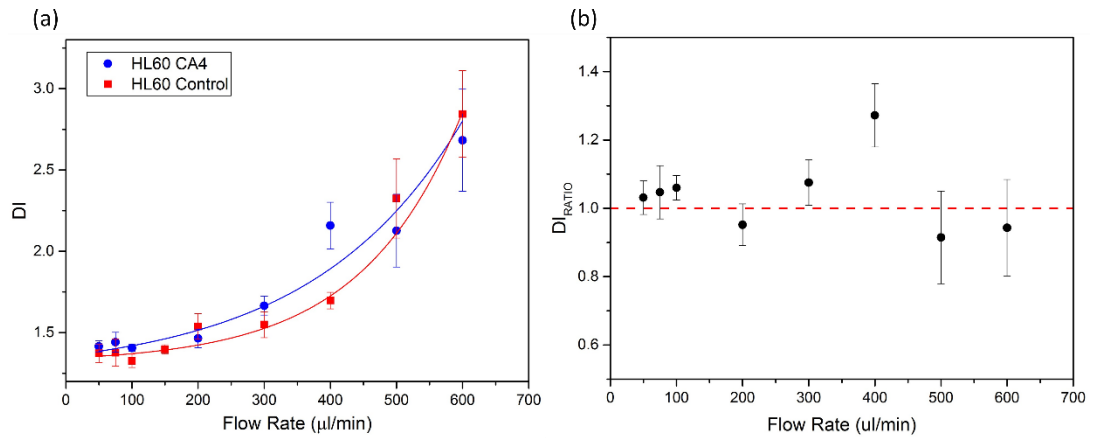


Figure 5.24 (a) The deformation index DI of HL60 cells treated with 100 nM of CA4 as a function of flow rate, compared to untreated cells. Cells were deformed in an inertia-dominant regime where $\mu \cong 1$ cP. Both datasets are fitted with an exponential decay function. (b) The DI ratio of HL60 cells treated with CA4 compared to untreated cells ($DI_{HL60CA4}/DI_{HL60}$).

Figure 5.25a is a plot of DI as a function of flow rate for SW480 cells treated with CA4 and deformed in the inertia-dominant flow regime, compared to a control sample. Results show that DI of the treated sample and the control sample are within error of each other across the range of flow rates. The datasets exhibit *yield stress* behaviour at $Q \cong 300 \mu\text{l}/\text{min}$, and are fitted with linear functions above and below this value. The gradient of the fits increases significantly for $Q > 300 \mu\text{l}/\text{min}$. Figure 5.25b shows the $DI_{ratio} = DI_{CA4}/DI_{control}$ as a function of flow rate. For the majority of flow rates $DI_{ratio} = 1$, showing that there was no change in the deformability of SW480 due to CA4.

These results show that no significant change in deformability could be detected in HL60 or SW480 treated with CA4 when using deformation cytometry in the inertia-dominant flow regime. No changes were observed at low strains (below the *yield stress*) or at high strains (above the *yield stress*).

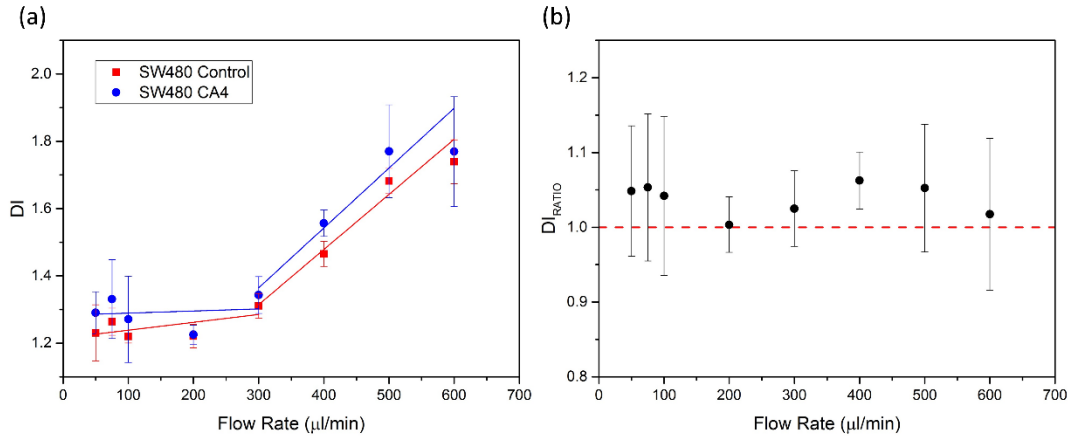


Figure 5.25(a) The deformation index DI of SW480 cells treated with 100 nM of CA4 as a function of flow rate, compared to untreated cells. Cells were deformed in a inertia-dominant regime where $\mu \cong 1$ cP. (b) The DI ratio of SW480 cells treated with CA4 compared to untreated cells ($DI_{\text{SW480CA4}}/DI_{\text{SW480}}$).

5.2.4 Viability Assays

Apoptosis had been shown to increase cell stiffness [188]. Lam *et al.* 2007 used AFM to show that the chemotherapy drug daunorubicin caused cell death leading to an increase in cell stiffness [200]. The stiffness increase was detected in early (~ 1 hr) and late stage apoptosis (>2 hr incubation). CA4 has shown cytotoxic effects and is being researched as a chemotherapy drug due to its ability to cause cell death, apoptosis is generally induced after 24–48 hr of incubation [208]. Figure 5.21 and Figure 5.30 showed that HL60 cells treated with CA4 became stiffer. This suggests that the mechanical changes could be due to early stage apoptosis as opposed to inhibited microtubule organisation, even though incubation times were kept low to avoid this (2 hr). This was investigated by performing viability assays on both HL60 and SW480, particularly over the incubation and measurement time (>4 hr) and the expected time to induce late stage apoptosis (~ 48 hr).

Trypan blue exclusion assays were first performed (described in section 3.6.5) on HL60 cells. The cells were treated with 10 nM, 50 nM and 100 nM of CA4 and incubated for a period of 48 hr. The viability was measured after 2 hr, 24 hr and 48 hr and compared to a control sample which was not exposed to CA4. Additionally, the effects of CA4 are known to be reversible below a critical concentration. Therefore, samples were compared that were incubated with CA4 for 2 hr and then the drug was removed and replaced with fresh media. These samples are referred to as “washed” samples. Figure 5.26 shows bar graphs of the viability of HL60 treated with CA4 over a 48 hr period for samples washed after 2 hr incubation compared to unwashed samples (incubated with CA4 for the 48 hr period).

Figure 5.26a shows that HL60 cells treated with 10 nM of CA4 remained viable ($>95\%$) over an incubation period of 24 hr. Cells incubated with 10 nM of CA4 for 48 hr had a significant

drop in viability (~10% viability), showing apoptosis was induced. Cells incubated with 10 nM for 2 hr and then washed also remained viable, showing that the effects of CA4 are reversible at this concentration. Figure 5.26b shows cells treated with 50 nM of CA4 also remained viable for 24 hr (>90%). Cells incubated with 50 nM for 48 hr had a significant drop in viability (~10% viable), cells washed after 2 hr also had a significant viability drop (~25% viable). This shows that 50 nM induces apoptosis after 48 hr and the effects are non-reversible after a 2 hr incubation period. Figure 5.26c shows cells treated with 100 nM of CA4 behaved the same as those treated with 50 nM. Cells had viability >95% after 2 hr incubation, which dropped to ~90% after 24 hr. After 48 hr the viability dropped to ~10% viability and treatment with CA4 was non-reversible.

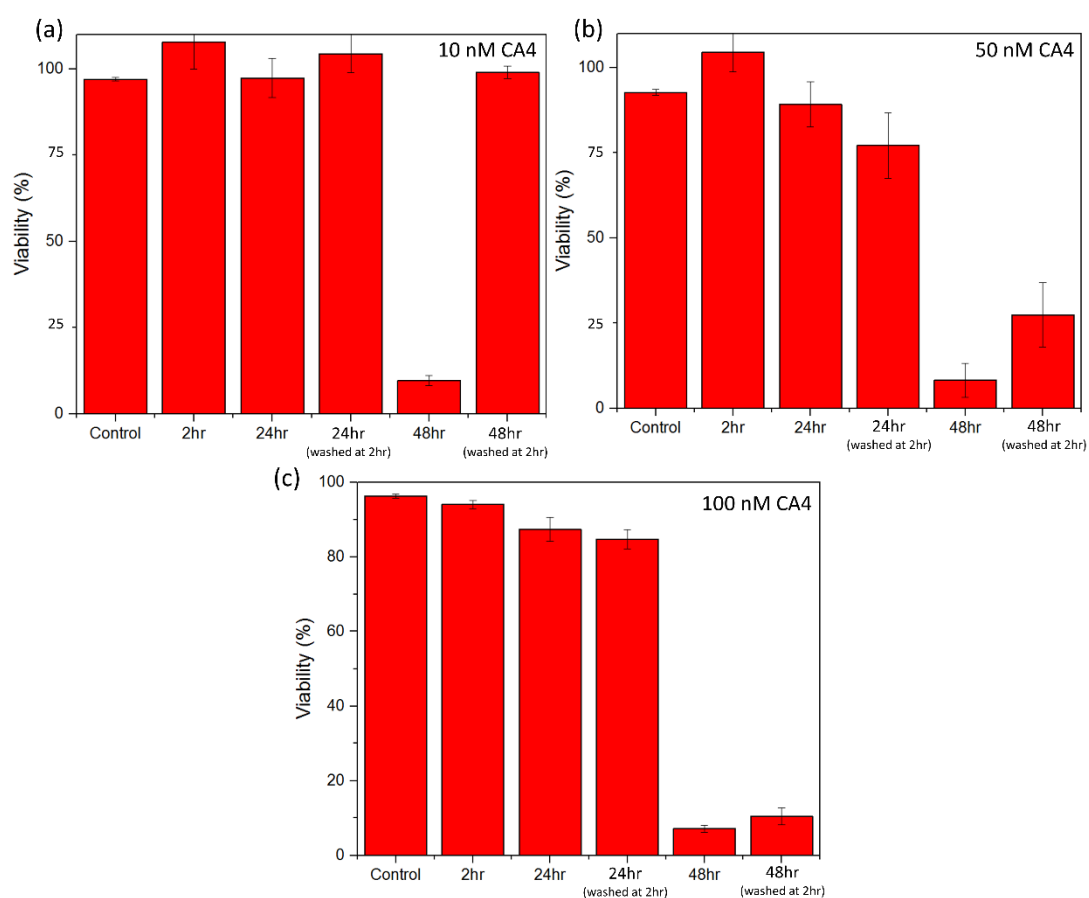


Figure 5.26 The viability of HL60 cells treated with CA4 was tested up to 48 hr of incubation with the drug. The reversibility of the drug was tested by also incubating samples with CA4 for 2 hr before removing the drug and replacing with fresh media, described as “washing” the cells. This was done for three concentrations of CA4: (a) 10 nM, (b) 50 nM and (c) 100 nM.

Phase contrast images of HL60 were also taken after different incubation times with 10 nM and 100 nM CA4, these images were used to measure the circularity of the cells using D_c . Figure 5.27a shows density scatter graphs of HL60 treated with 10 nM of CA4 over 48 hr, where the cells were washed after 2 hr incubation with the drug. Results show an increase in

D_c after the 2 hr incubation period from $D_c = 0.13 \pm 0.02$ to $D_c = 0.25 \pm 0.01$, cells were previously shown to become less rounded after incubation with CA4 (Figure 5.16). After 48 hr, D_c decreased again to $D_c = 0.15 \pm 0.02$ which is within error of the control sample. Figure 5.27b shows density scatter graphs of cells treated with 100 nM of CA4 over 48 hr, where cells were washed of the drug after 2 hr. Results show the cells become less rounded after the 2 hr incubation and increase in D_c increased from $D_c = 0.13 \pm 0.01$ to $D_c = 0.23 \pm 0.01$. D_c continued to increase to a value of $D_c = 0.44 \pm 0.01$ over 48 hr, showing the cells do not recover after the drug is removed. Figure 5.27c shows a phase contrast image of cells treated with 100 nM of CA4 for 48 hr compared to a control sample and cells incubated for 2 hr. After 48 hr the cells show signs of deterioration, are more polydisperse in size and shape and have less contrast.

DC was performed on HL60 incubated with 100 nM of CA4 for 2 hr. Results show that cells remained viable at this concentration for 24 hr, significantly later than the measurement period of 4 hr. The effects of CA4 were also non-reversible and significant apoptosis was induced after 48 hr leading to a viability of ~10%. These results initially suggested that the decrease in deformability of HL60 treated with CA4 was not due to apoptotic effects. However, trypan blue may not detect early stage apoptosis which may already effect the mechanical phenotype.

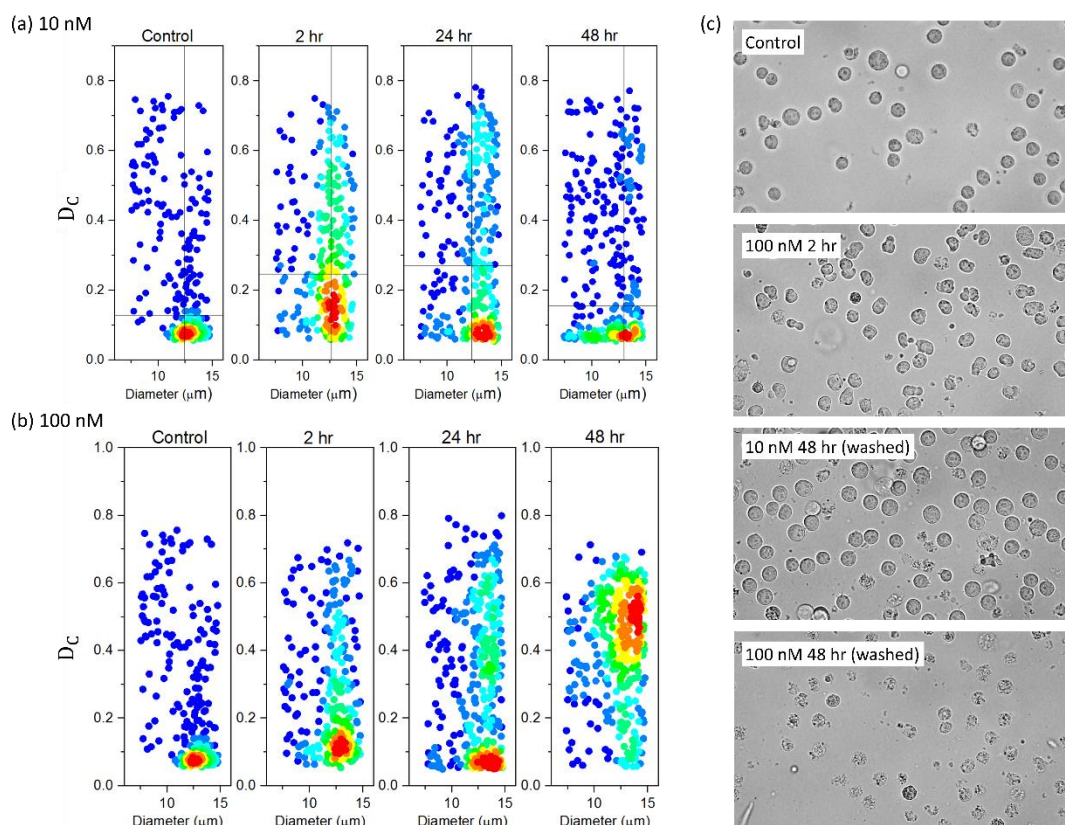


Figure 5.27 The circularity of HL60 cells treated with CA4 was measured using D_c up to 48 hr of incubation with the drug. Samples were incubated with CA4 for 2 hr before removing the drug and replacing with fresh media, described as “washing” the cells. Density scatter plots of D_c as a function of cell diameter, for two concentrations of CA4: (a) 10 nM and (b) 100 nM. (c) Phase contrast images of HL60 cells after incubation with CA4 for 2 hr, which was then removed and images were also taken after 48 hr.

The viability of SW480 treated with CA4 was also tested using the trypan blue assay. Cells were incubated with 100 nM of CA4 for a 48 hr period. Figure 5.29a shows that cell viability was >95% even after 48 hr incubation, whereas HL60 cells had a significant viability drop after 48 hr. The concentration of cells was also monitored over 48 hr, and treated and untreated SW480 cells were compared (Figure 5.28b). The control sample showed an increase in cell concentration after 48 hr, indicating proliferation. The CA4 treated cells showed a decrease in concentration. This shows that CA4 stops proliferation (due to inhibiting microtubule function) and the drop indicates some cells have died during this time. As SW480 are adherent cells they were detached for viability and concentration measurements. The washing steps may have washed away any late stage apoptotic cells which would already have detached, leaving only the viable cells and resulting in a high viability measurement. Phase contrast images of adhered cells treated with CA4 for 48 hr showed no morphological changes compared to a control sample seeded on the same day, however the control samples are clearly more confluent (images found in the appendix Figure S2).

These results indicate that CA4 inhibits proliferation in SW480 cells, however after 48 hr the initial cells were still viable using a trypan blue assay. SW480 also did not show any mechanical changes due to CA4 (Figure 5.23). This could suggest that CA4 takes longer to induce apoptosis in SW480 compared to HL60, where increased cell stiffness was detected after 2-4 hr.

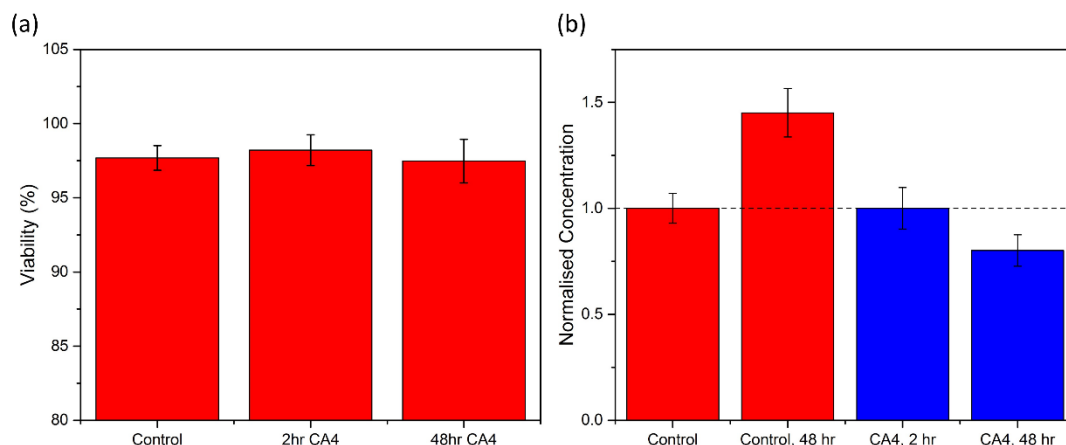


Figure 5.28 (a) The viability of SW480 cells after incubation with 100 nM of CA4 for 2 hr and 48 hr was measured using a Trypan blue assay. (b) The concentration of SW480 cells after 2 hr and 48 hr incubation with 100 nM of CA4 is compared to a control sample of SW480, results are normalised to the initial measurement.

Another assay was also used to measure the viability of HL60 and SW480 incubated with CA4 over a period of 4 hr, which encompasses the 2 hr initial incubation and additional time where deformation measurements were taken (<1 hr). The Alamar Blue Assay (protocol described in section 3.6.5) measures the reducing potential of cells. Initially non-fluorescent, the reagent is reduced in living cells and becomes highly fluorescence. This fluorescence intensity was measured using a well plate reader and used to quantify viability. Alamar Blue may be able to detect early stages of apoptosis whereas Trypan blue may not, the metabolic activity of living cells is likely altered before the cell membrane is significantly compromised for measurement using the trypan blue exclusion method.

Figure 5.29a shows the normalised fluorescence intensity of HL60 cells incubated with different concentrations of CA4 for 4 hr, using Alamar Blue. The average fluorescence intensity was averaged from n=5 wells, and normalised to a control sample which was not treated with CA4. Results show that the viability was >95% for concentrations ≤ 10 nM. For a concentration of 100 nM the viability was still ~93%. Figure 5.29b shows the normalised fluorescence intensity of SW480 cells treated with CA4 at different concentrations for 4 hr. Results show that for all concentrations the viability was >90%, and at 100 nM the viability remained within error of 95%.

These results suggest that treatment with CA4 over 4 hr did not induce a significant viability drop in HL60 or SW480 cells. Which is in accordance with results using the Trypan blue assay.

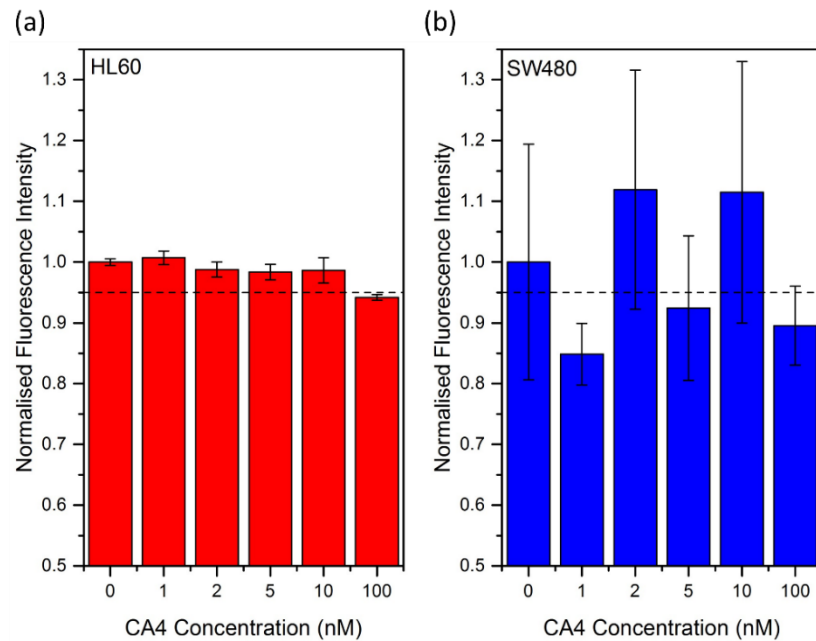


Figure 5.29 The normalised fluorescence intensity of SW480 and HL60 using an AlamarBlue assay after 4 hr incubation with different concentrations of CA4. For each condition, the average fluorescence was found from $n=5$ wells and a standard error was calculated (scale bars). Values were normalised using the control sample, where no CA4 was added.

5.2.5 Deformation traces and SCA

Deformation cytometry was also used to track the strain ϵ of HL60 cells treated with CA4 and was compared to a control sample. Cells were treated with 100 nM of CA4 for 2 hr and deformed in the shear-dominant regime ($\mu \cong 33$ cP) at 5 μ l/min. These conditions were chosen as HL60 cells treated with CA4 and deformed in the shear-regime previously showed decreased deformability (Figure 5.21) whereas the inertial regime showed no changes in deformability due to CA4 (Figure 5.23 and Figure 5.24).

Figure 5.30 shows the averaged strain traces of $N=56$ HL60 cells, and $N=38$ HL60 cells treated with CA4. These traces were used to extract multiple deformation and relaxation parameters, summarised in Table 5.2. The deformation time τ_d and relaxation time τ_r were found by fitting exponential functions to the deformation and recovery regions of the strain traces (shown in black in Figure 5.30). The exponential fit of the relaxation was also used to extrapolate the final strain ϵ_∞ . The results in Table 5.2 confirm that CA4 decreases the deformability of HL60 as the ϵ_{max} of the control cells is ~ 1.4 x larger than the CA4 treated cells. The initial strains ϵ_0 of both samples are within error of each other, whereas the final strain of the treated cells is ~ 2.5 x greater than the control cells. This also shows that the control sample recovers its

initial shape ($\varepsilon_0 = \varepsilon_\infty$) whereas the treated sample does not ($\varepsilon_0 < \varepsilon_\infty$). The τ_d of both samples are within error of each other, however the τ_r shows that the treated cells relax $\sim 4x$ quicker than the control cells. Therefore, the CA4 treated cells relax more quickly after deformation but have an apparent permanent strain because $\varepsilon_0 < \varepsilon_\infty$.

Figure 5.31 shows the average velocity profile of N=38 HL60 cells treated with CA4 (the average velocity profile of untreated HL60 was shown in section 4.1.3), which is fitted with a *sine* function (shown in red). This allowed the Kelvin-Voigt model (described in section 2.3.4) to be fitted to the averaged strain trace (shown in red in Figure 5.31). The elastic modulus of HL60 treated with CA4 was found to be $E = 598 \pm 66 Pa$, the elastic modulus of HL60 was previously found to be $E = 301 \pm 29 Pa$ (section 4.4.1). This shows that HL60 become approximately twice as stiff when treated with CA4.

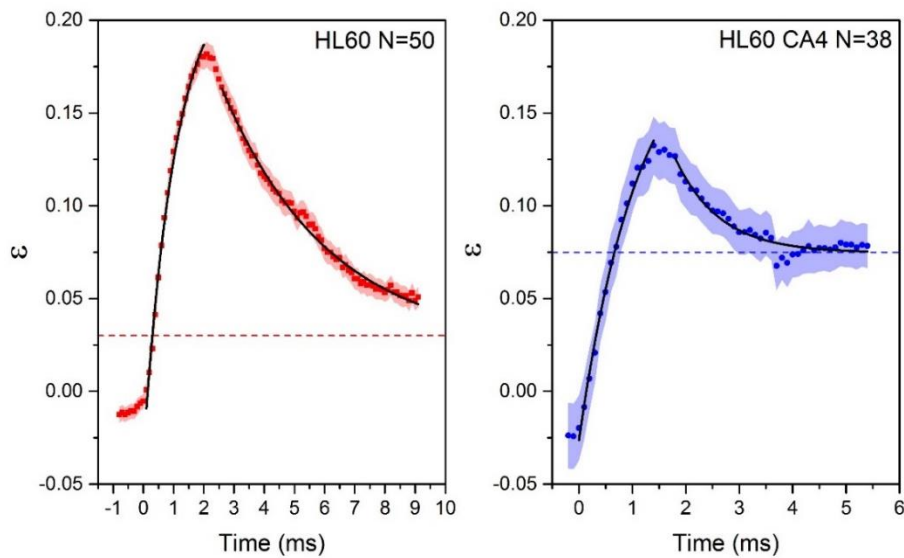


Figure 5.30 The averaged strain trace for HL60 ($N = 50$) and HL60 treated with 100 nM LatA ($N = 30$) as a function of time, with the standard error shown by the shaded areas. Flow rate was $5 \mu\text{l}/\text{min}$, and the suspension medium viscosity was 33 cP. The deformation and recovery are fitted with an exponential function and the dashed lines represent the extrapolated final strain ε_∞ for both samples.

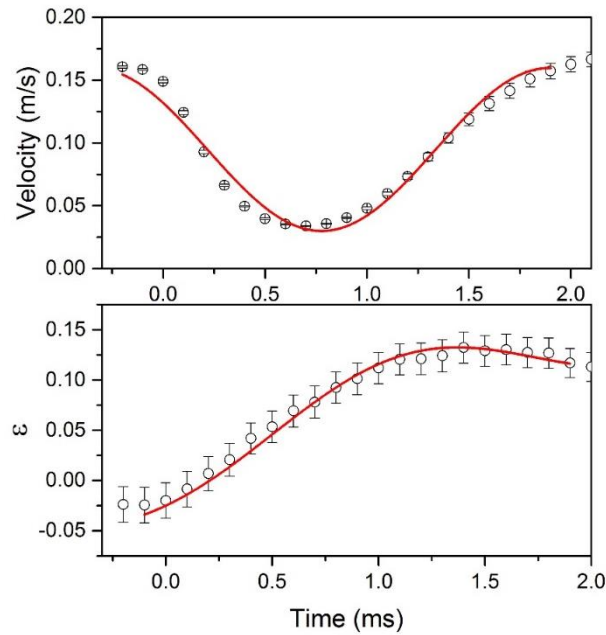


Figure 5.31 The averaged strain trace of $N=38$ HL60 cells treated with CA4, the Kelvin-Voigt model was fitted, shown in red. The average velocity profile of the same 38 cells is shown and fitted with a sine function, shown in red. Cells were deformed in a shear-dominant regime where $Q = 5 \mu\text{l}/\text{min}$ and $\mu \cong 33 \text{ cP}$.

As previously discussed, bulk averaging can miss subpopulations within a sample and offers less information than single cell analysis. SCA was also performed on the individual traces of HL60 treated with CA4 ($N=38$). This was performed using the method previously described in section 4.4.1. Table 5.2 shows the parameters found from the “Averaged Strain Trace” and compares them to values averaged from SCA. The values found of ϵ_{max} and ϵ_0 are within error of each other. The relaxation time τ_r of both samples is ~ 1.25 times bigger using the averaged strain trace compared to SCA. This suggests outliers may skew the averaged trace and indicates the importance of investigation at the single cell level. Both methods show that HL60 recover their initial strain ($\epsilon_\infty = \epsilon_0$), whereas the treated cells show an apparent “permanent strain” ($\epsilon_\infty > \epsilon_0$). However, the ϵ_∞ calculated for treated HL60 was ~ 1.3 times greater using the averaged strain trace compared to SCA. This difference is likely carried through from the differences in τ_r as these values are extrapolated from the same fit.

Statistical t-tests were used to classify the level of significance between the parameters measured using SCA on control and treated HL60 populations. Figure 5.32 shows bar graphs of the average A , ϵ_{max} , ϵ_∞ , τ_r and ϵ_0 of both samples found by SCA, where the level of significance was measured by calculation of the p-value. The raw p-values are also included in a table shown in Figure 5.32. Results show no significant difference in A and ϵ_0 due to treatment of HL60 with CA4. Significant differences (*) were shown using ϵ_{max} and ϵ_∞ , and extremely significant differences were shown using the relaxation time τ_r . Overall, the initial

size and strain could not be used to distinguish the two samples but deformation and relaxation parameters could. This demonstrates the ability of mechano-phenotyping on the single cell level to accurately classify changes in cells due to treatment with a drug.

Table 5.2 Multiple characteristic parameters extracted from the strain traces of $N=50$ HL60 cells and $N=38$ HL60 cells treated with CA4. This includes the initial cell diameter A , the initial strain ϵ_0 , the final strain ϵ_∞ , the maximum strain ϵ_{max} , the deformation time τ_d , the relaxation time τ_r and the elastic modulus E . Values were found from the “Averaged Strain Trace” and also using single cell analysis “SCA” of individual traces which were then averaged with $\pm SE$.

	Averaged Strain Trace		SCA	
	HL60	HL60-CA4	HL60	HL60-CA4
A (μm)	N/A	N/A	12.3 ± 0.2	12.9 ± 0.2
ϵ_{max}	0.18 ± 0.01	0.13 ± 0.02	0.18 ± 0.01	0.13 ± 0.02
τ_r (ms)	3.52 ± 0.14	0.83 ± 0.1	3.04 ± 0.15	0.70 ± 0.08
τ_d (ms)	1.04 ± 0.05	1.10 ± 0.10	N/A	N/A
E (Pa)	301 ± 29	598 ± 66	N/A	N/A
ϵ_0	-0.012 ± 0.005	-0.02 ± 0.02	-0.012 ± 0.005	-0.01 ± 0.02
ϵ_∞	$+0.030\pm 0.004$	$+0.075\pm 0.01$	$+0.030\pm 0.004$	$+0.06\pm 0.01$

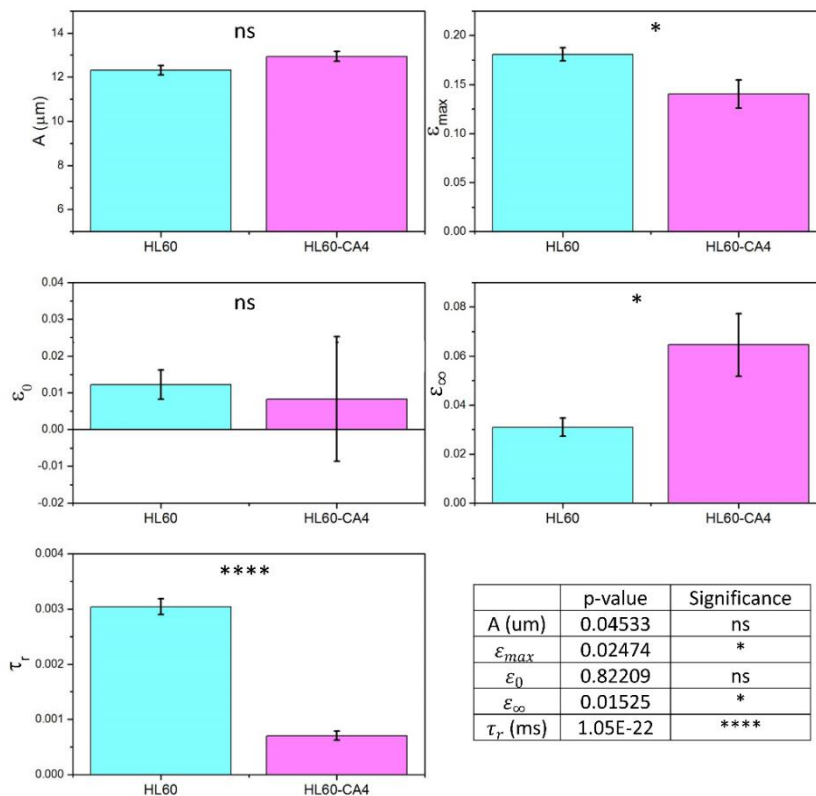


Figure 5.32 SCA performed on strain traces of HL60 treated with CA4 and a control sample. The plots show the average values of the cell diameter A , maximum strain ϵ_{max} , initial strain ϵ_0 , the relaxation time τ_r and the final strain ϵ_∞ . The error bars denote the standard error SE. Statistical t -tests were done to determine the level of significance, where $p > 0.05$ is not significant (ns), $0.01 < p < 0.05$ is significant (*), $0.001 < p < 0.01$ is very significant (**), $0.0001 < p < 0.001$ is extremely significant (***) and $p < 0.0001$ (****).

Mechanical changes on the single cell level were further explored by plotting histograms of parameters which showed significant changes. Figure 5.33 shows histograms of ε_{max} , τ_r and ε_{∞} of both datasets. For ε_{max} , both histograms show a normal distribution fitted with a single Gaussian peak. There is a shift in the peak position of the treated cells, showing the decrease in average deformability. The histograms of τ_r also show a normal distribution, fitted with a Gaussian. The peak position for the treated cells is shifted which shows that the treated cells relax quicker after being deformed. For the control sample, the histogram of ε_{∞} shows the majority of cells have $\varepsilon_{\infty}=0.025$ which is within error of the initial strain ε_0 shown in Table 5.2. The treated sample shows a peak at $\varepsilon_{\infty}=-0.01$, showing that some of the treated cells recover their original strain ($\varepsilon_0 = \varepsilon_{\infty}$). There is also a second significant peak at $\varepsilon_{\infty}=0.06$, resulting in the non-zero average in ε_{∞} in Table 5.2. The histograms offer more information than the reported averages. Figure 5.33 indicates that treatment with CA4 affects some cells differently resulting in two populations, with some cells recovering their initial shape and some showing signs of a “plastic deformation”.

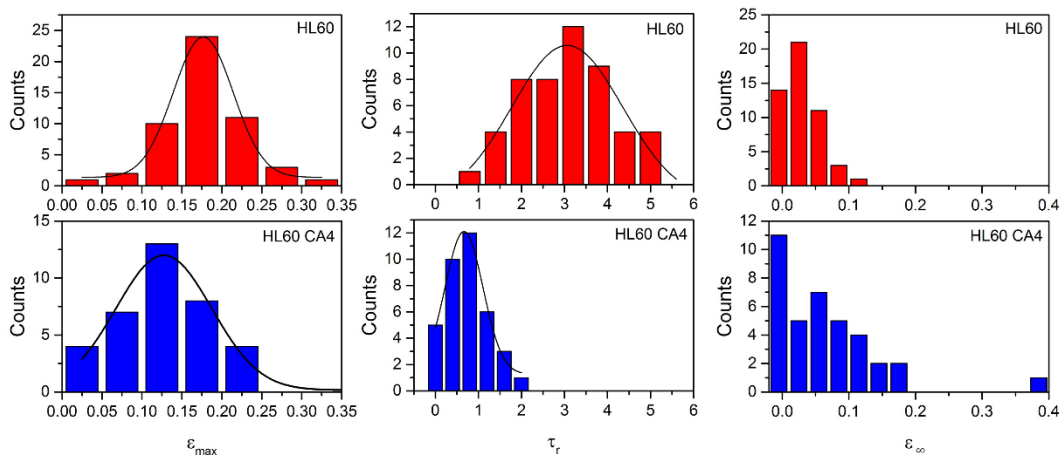


Figure 5.33 Histograms showing the maximum strain ε_{max} , relaxation time τ_r and final strain ε_{∞} of HL60 treated with CA4 ($N=38$), compared to an untreated control sample ($N=50$).

5.2.6 Discussion

HL60 and SW480 cells were treated with CA4 to investigate changes in cell stiffness due to microtubule destabilisation. DC was used in both shear-dominant and inertia-dominant flow regimes, confocal fluorescence confirmed that CA4 fully destabilised microtubules at 100 nM. No changes in deformability were detected for SW480 in either flow regime. No deformability changes were detected in HL60 in the inertia-dominant regime, a decrease in deformability was seen across the entire range of flow rates in the shear dominant regime ($1.4 < DI < 2.5$). This result is unexpected as disrupting the cytoskeletal intuitively suggests the cells becoming softer.

Martinez Vazquez *et al.* 2015 measured the pressure gradient required to deform cells through a constriction channel [209]. The pressure required to squeeze single cells through the constriction was measured, higher pressures were correlated to increased deformability due to deformable cells having higher contact area and adhesion to channel walls. Cells were treated with various cytoskeletal altering drugs; CA4 and nocodazole which disrupt microtubules, and paclitaxel which enhances microtubules. They found that CA4 and nocodazole made the cells softer and required an increased pressure to pass through the constriction, paclitaxel made the cells stiffer and required a decreased pressure. Their CA4 results show the opposite result to those by deformation cytometry.

CA4 has been shown to cause shutdown of tumour vasculature and eventual tumour death [210]. Severe destabilisation of tubulin causes a time-dependent cytotoxic and antiproliferation effect [211]. Cells become stuck in the G₁/S phase of the cell cycle due to failure to complete mitosis, and thus cell death can occur due to mitotic catastrophe as well as apoptotic pathways [212]. Trypan blue and Alamar Blue assays showed that CA4 induced apoptosis in HL60 over a 48-hr incubation period. The viability did not decrease in SW480 however proliferation stopped over this time-period (indicating mitotic catastrophe). Green *et al.* 2010 studied an analogue of CA4, CA423, which displayed similar antiproliferation and cytotoxic effects [208]. HL60 cells treated with CA423 showed no increase in apoptosis over an 8 hr incubation period, after 48 hr >75% of cells were apoptotic. This agrees with the trypan blue and alamar assay results (section 5.2.4). HL60 treated with 100 nM of CA4 for 16 hr also showed that 75% of cells were in the G₂M phase. Cells in this phase are known to be stiffer [96], [213]. However, after 4 hr there was a <5% increase in cells in the G₂M which is the maximum measurement period used in our deformation cytometry study. These results suggest the increased stiffness of HL60-CA4 found using shear-dominant deformation cytometry is not due to apoptosis or mitotic catastrophe.

Kubitschke *et al.* 2017 investigated how microtubule structure influences cell elasticity and recovery under small (<5%) and large strains (5-20%), using optical stretching. The drug nocodazole was used to disassemble microtubules. This led to no changes in cell deformability at small strains and an increase in deformability at large strains. They theorise that the actin scaffold dominates cell elasticity at small strains, also shown in our results using the actin depolymerising drug LatA. However, individually microtubules are mechanically stiffer than microfilaments and actin fluidises under high strains, therefore high strains may be required to probe microtubules [198].

Comparatively, our results on HL60 treated with CA4 showed that at high strains in the inertial-regime no changes were found, and in the shear-regime a counter-intuitive stiffening

affect was found. Kubitschke *et al.* 2017 also found some counter-intuitive changes to cell deformability using the microtubule enhancing drug paclitaxel. No changes were seen at small strains, however concentration dependent changes were seen at high strains. For high-concentrations (>200 nM) the cell stiffened which is the intuitive result. For low concentrations (<200 nM) the cells softened, which suggests that the microtubule enhancement leads to secondary mechanisms activating in the cell. Danowski *et al.* 1989 showed that stabilising microtubules inhibits acto-myosin contractions which leads to softening [214].

Golfier *et al.* 2017 used RT-DC to deform HL60 cells treated with various drugs to perturb the cytoskeletal structure [50]. They also showed counter-intuitive results, cells treated with Nocodazole became stiffer and those treated with Paclitaxel became softer over a range of concentrations. They argued that F-actin assembly occurs to compensate the loss of microtubules. Verin *et al.* 2001 found that disrupting microtubules initiates specific signalling pathways with microfilaments leading to myosin light chain phosphorylation which enables cell contraction [215]. Tsai *et al.* 1998 treated neutrophils with colchicine (a microtubule disruptor) and paclitaxel and measured deformability using micropipette aspiration. High concentrations of colchicine lead to increased actin polymerisation and cell rigidity, low concentrations had no effect on either and Paclitaxel did not influence actin and mechanical changes were not detected [216]. Paclitaxel is a chemotherapy drug which arrests cells in the mitosis stage of the cell cycle and stops proliferation. Similarly to CA4, it eventually induces apoptosis in cells.

Our results confirmed that over the measurement period cells were not yet apoptotic, indicating that the stiffening was not due to apoptosis and likely a secondary mechanism due to microtubule destabilisation. Confocal fluorescence images of HL60 treated with CA4 with an actin stain are shown by Figure 5.34, and are compared to a control. The treated cells show signs of a more defined actin cortex and additional protrusions containing actin filaments. This may indicate that destabilisation of HL60 microtubules by CA4 leads to enhancement of microfilaments, resulting in cell stiffening.

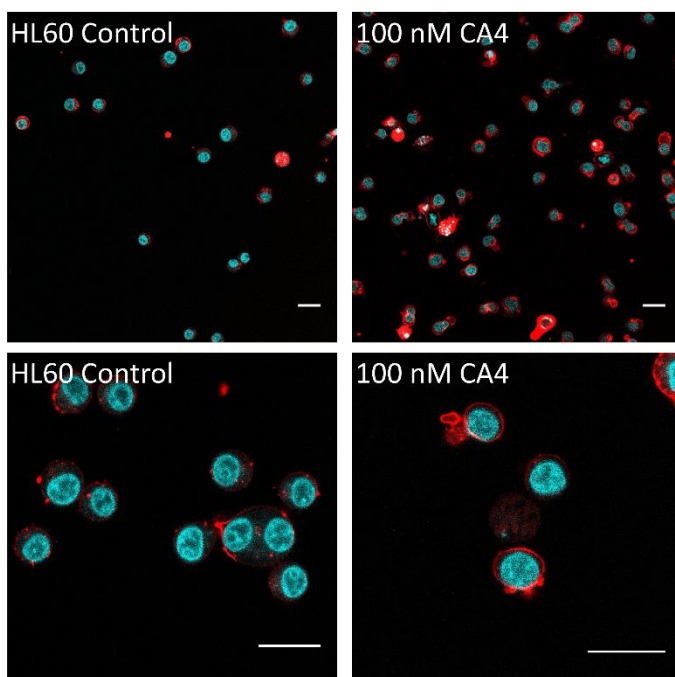


Figure 5.34 Confocal fluorescence images of control HL60 cells and HL60 treated with 100 nM of CA4, stained for actin (red) and DNA (blue). Images were taken using a 10x (above) or a 40 x (below) objective, scale bar 20 μm .

Gossett *et al.* 2012 used inertia-dominant deformability cytometry to deform HeLA and fibroblast cells treated with nocodazole. They showed no significant changes in deformability due to nocodazole, which contradicts the work by Kubitschke *et al.* 2017 who suggested high-strain deformations were more sensitive to microtubule disruption [27], [198]. However, the strains in this work were still relatively low compared to deformability cytometry. Additionally, the strain rates used in optical stretching are on the second timescale whereas deformation cytometry works at 10^5s^{-1} . Gossett argues that the high strains and strain-rates in deformability cytometry are not sensitive to cytoskeletal changes and measurements are dominated by cytoplasmic properties and nuclear structure. This corroborates our work as both SW480 and HL60 treated with CA4 showed no deformability changes in the inertia-dominant regime at high strains.

Kubitschke *et al.* 2017 also measured cell recovery after deformation and treatments with both nocodazole and paclitaxel [198]. Nocodazole lead to a lack of relaxation indicating increased plasticity. Similarly, we found that HL60 treated with CA4 did not recover their original shape also indicating a plastic deformation. Paclitaxel also showed an increased plasticity even though it enhances microtubules. This is further evidence that microtubule alterations lead to further changes in the cell which effects both cell elasticity and recovery.

Overall, previous works suggest that actin is the dominant cytoskeletal component of cell elasticity at low strains compared to microtubules. However, it is clear that multiple drugs

used to disrupt or enhance microtubules trigger changes in actin and myosin within the cell which can lead to surprising changes in cell deformability. CA4 leads to cell stiffening using a shear-dominant deformation cytometry assay, suggesting secondary mechanisms may alter the substructure. Additionally, CA4 treated cells also did not recovery after deformation suggesting some plasticity is induced due to removal of prestressed microtubules.

5.3 Treating cells with Trichostatin A

The cell nucleus is the largest and stiffest organelle, its mechanical properties influence whole cell deformability. The nucleus rigidity is defined by nuclear lamina and chromatin structure. Chromatin structure is regulated by proteins including histones, which organise chromatin into a condensed structure. TSA is a drug which induces hyper-acetylation of histone tails leading to increased negative charges, thus electrostatic forces drive chromatin decondensation [217].

HL60 cells were used to study the effects of chromatin decondensation using TSA, these cells were previously used to study the effects of actin disruption using LatA and microtubule disruption using CA4. Cells were probed using deformation cytometry in shear-dominant and inertia-dominant flow regimes to compare how whole cell deformability is affected by nuclear changes compared to cytoskeletal perturbations.

5.3.1 Drug treatment and observations

HL60 cells were treated with the drug Trichostatin A (TSA), to test the sensitivity of DC to nuclear structural changes. Firstly, treated cells were imaged using phase contrast and confocal fluorescence microscopy to visualise TSA induced changes to cell morphology and substructure.

Figure 5.35a shows phase contrast images of HL60 incubated with 1 μ M of TSA for 2 hr and compared to a control sample. The treated sample shows a generally less rounded morphology compared to the control sample, with some cells showing blebbing and protrusions. The morphological changes were quantified by measuring the circularity D_C . Figure 5.35b shows histograms of D_C for the treated sample compared to the control sample. The control sample is fitted with a lognormal distribution with a single peak, the centre of the peak was $D_C = 0.07 \pm 0.01$ and the curve had a standard deviation of $w = 0.02 \pm 0.01$. The treated sample shows a large peak at $D_C = 0.07 \pm 0.01$ with a standard deviation of $w = 0.04 \pm 0.01$, this is within error of the peak position of the control sample. There is a second peak at position $D_C = 0.38 \pm 0.01$ with a ~ 6 times larger standard deviation of $w = 0.25 \pm 0.03$. This is likely the cells which experience blebbing and may indicate that a subpopulation of the cells are more effected by TSA than others. Figure 5.35c shows density scatter plots of D_C as a function of cell diameter for both samples. This highlights that treatment with TSA leads to a subpopulation with a less rounded morphology as D_C increases. From this, the average

diameter of control cells was found to be $A_{control} = 13.6 \pm 0.1 \mu\text{m}$ and of treated cells was $A_{TA} = 14.6 \pm 0.1 \mu\text{m}$. This shows that the treated cells had a small increase in size (~ 1.1 times).

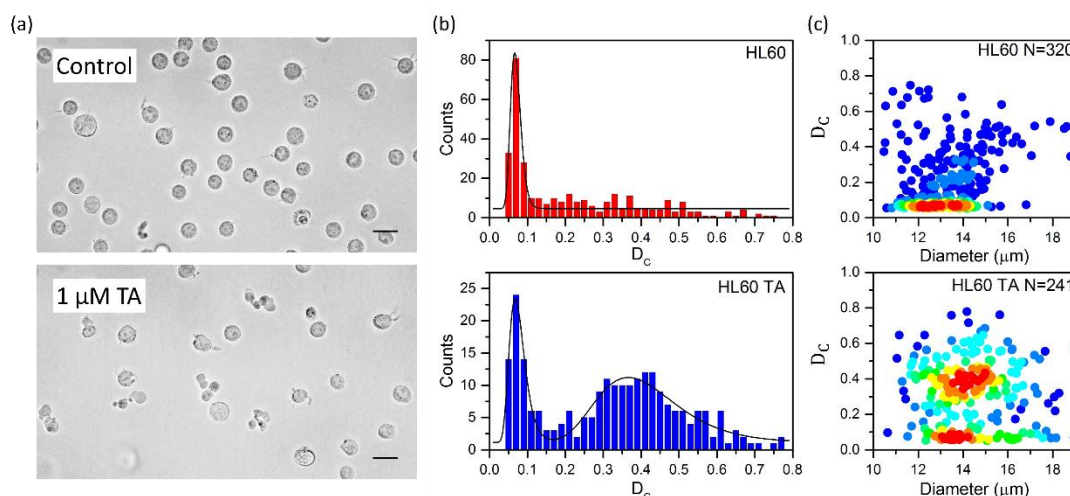


Figure 5.35 Measurement of the size and shape of HL60 cells compared to those treated with 1 μM of TSA: (a) Phase contrast images of HL60 and HL60 TSA cells taken with a 40x objective. Scale bars are 20 μm . (b) Histograms of the circularity D_c of HL60 and HL60 TSA, with peak fitting. (c) Density scatter plots of D_c as a function of diameter of HL60 and HL60 TSA.

Confocal fluorescence images were taken of HL60 cells treated with TSA for concentrations of 0.1 μM , 1 μM and a control sample, which encompasses ranges previously used to destabilise chromatin [49], [87], [88]. Cells were incubated with the drug and fluorescent stains for 3 hr before imaging occurred. DNA staining was done using the dye Hoechst 3342 (Thermo Fisher Scientific) at a concentration of 0.5 $\mu\text{g/ml}$. Tubulin was stained using a live fluorogenic labelling probe (Sir) (Spirochrome, Cytoskeleton Inc.) at a final concentration of 1 μM .

Figure 5.36 shows fluorescent images of HL60 control cell and those treated with TSA, DNA staining is shown in blue and tubulin staining is shown in red. The control cells and those treated with 0.1 μM TSA show a defined microtubule structure, with filaments arranged radially originating at centrosomes. Cells treated with 1 μM show disrupted microtubule, instead showing a diffuse background with a fluorescent spot remaining at the centrosome. The DNA staining of the control sample shows a defined nucleus in each cell with similar size and a rounded morphology, this can also be seen in the 0.1 μM TSA sample. Treatment with 1 μM of TSA shows obvious differences in the morphology of the nucleus of HL60. The nucleus appears less uniform and shows a larger diffuse background with bright spots of DNA, indicating changes in the chromatin structure.

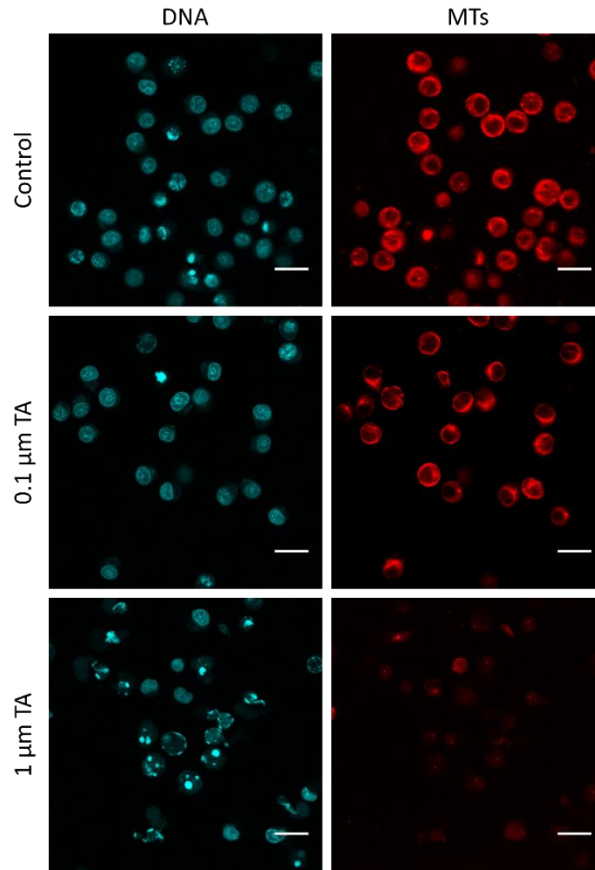


Figure 5.36 Confocal fluorescence images of control HL60 cells and HL60 cells treated with 0.1 μM and 1 μM of TSA, stained for DNA (blue) and tubulin (red). Images were taken using a 40 x objective, scale bar 20 μm .

5.3.2 Deformation Cytometry in the shear regime

Deformation Cytometry was performed on HL60 cells treated with 1 μM of TSA for 2 hr. Cells were deformed on-chip over a range of flow rates whilst suspended in 0.5% PBS-MC buffer ($\mu \cong 33 \text{ cP}$). The concentration of TSA was maintained over the measurement period. The DI of 10s-100s of cells was measured for each flow rate, experiments were repeated $N=3$ to acquire an average and standard error of DI .

Figure 5.37a shows a plot of DI as a function of flow rate for cells treated with TSA in the shear-dominant flow regime and compared to a control sample. Results show no change in deformability due to treatment with TSA for any of the flow rates. Both data sets are fitted with an exponential decay function which was used to extrapolate DI_{max} . The control sample had $DI_{max} = 2.64 \pm 0.11$ and the treated sample had $DI_{max} = 2.79 \pm 0.38$, also indicating no changes in deformability. The DI_{ratio} was also used to quantify if any changes in DI occurred due to treatment with TSA, where $DI_{ratio} = DI_{TA}/DI_{control}$ and $DI_{ratio} = 1$ indicates no change. Figure 5.37b is a plot of DI_{ratio} as a function of flow rate, where $DI_{ratio} = 1$ is marked with a dashed red line. This shows that the majority of datapoints are

within error of $DI_{ratio} \cong 1$. This confirms no deformability changes, due to TSA, are observed using deformation cytometry in the shear-dominant regime.

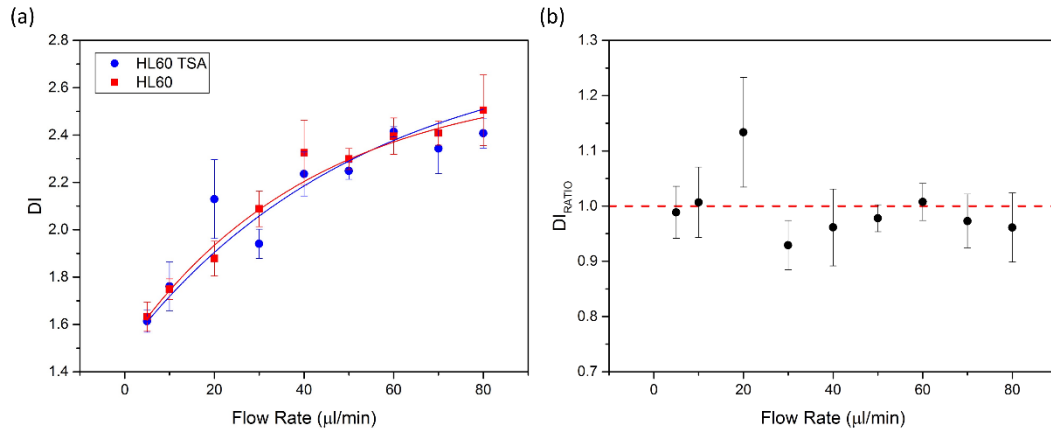


Figure 5.37(a) The deformation index DI of HL60 cells treated with $1 \mu M$ of TSA as a function of flow rate, compared to a control sample. Cells were deformed in a shear-dominant regime where $\mu \cong 33 \text{ cP}$. Both datasets are fitted with an exponential function. (b) The DI_{RATIO} of HL60 cells treated with TSA compared to untreated cells ($DI_{HL60TSA}/DI_{HL60}$) in the shear regime.

5.3.3 Deformation Cytometry in the inertial regime

Deformation Cytometry was also performed on HL60 treated with TSA in the inertia-dominant flow regime, where cells were incubated with $1 \mu M$ of TSA for 2 hr. Cells were deformed whilst suspended in cell media ($\mu \sim 1 \text{ cP}$) and a constant concentration of TSA was maintained throughout the measurement period. For a range of flow rates, 10s-100s of deformation events were collected. This was repeated $N=3$ to acquire an average and standard error in DI .

Figure 5.38a shows DI as a function of flow rate for HL60 cells treated with TSA, compared to a control sample. Both datasets are fitted with an exponential and show the previously discussed *yield stress* behaviour occurring at $\cong 400 \mu l/min$, and a general increase in deformability of cells treated with TSA. The DI_{ratio} was used to quantify the increase in DI due to the effects of TSA, where $DI_{ratio} > 1$ indicated increased deformability. Figure 5.38b is a plot of DI_{ratio} as a function of flow rate. This shows that below the *yield stress* there is a small increase in deformability due to TSA ($DI_{ratio} \cong 1.1$). At the *yield stress* the increase in deformability is more apparent $DI_{ratio} = 1.34 \pm 0.10$. At $Q = 600 \mu l/min$ the DI_{ratio} is within error of 1 indicating that no deformability changes can be distinguished here. Flow rates $Q > 600 \mu l/min$ lead to a on-chip cell destruction and this was previously labelled the *failure point* (discussed in section 4.2.2). Therefore, this indicates the maximum strain of HL60 before cell destruction which may explain why the effects of TSA can no longer be detected.

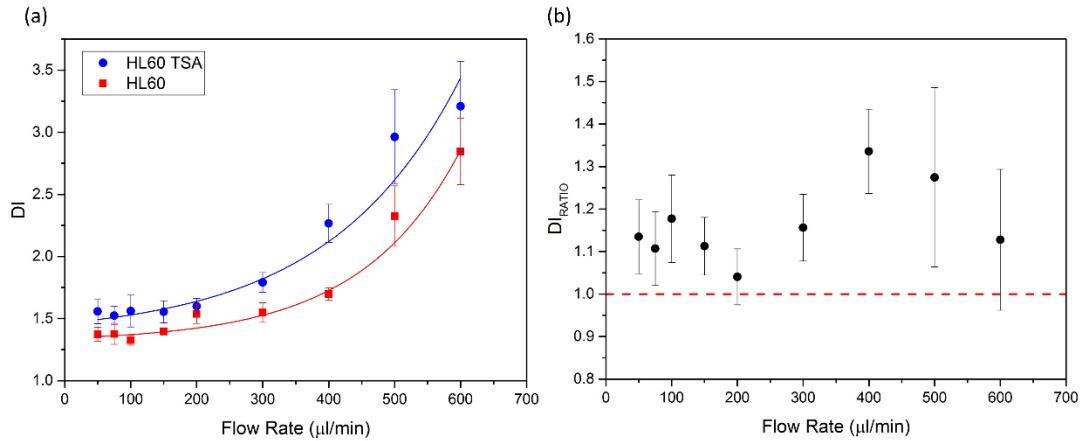


Figure 5.38 (a) The deformation index DI of HL60 cells treated with $1 \mu\text{M}$ of TSA as a function of flow rate, compared to untreated cells. Cells were deformed in an inertia-dominant regime where $\mu \cong 1 \text{ cP}$. Both datasets are fitted with an exponential function. (b) The DI ratio of HL60 cells treated with TSA compared to untreated cells ($DI_{HL60TSA}/DI_{HL60}$).

The heterogeneity in the response of HL60 to TSA was investigated by plotting histograms of DI . Figure 5.39a shows histograms of DI of treated and control cells deformed at $300 \mu\text{l}/\text{min}$ (below the yield stress), $400 \mu\text{l}/\text{min}$ (at the yield stress) and $600 \mu\text{l}/\text{min}$ (at the failure point). Histograms are fitted with log-normal functions and the peak values DI_{peak} and standard deviation w are summarised in Table 5.3.

Figure 5.39a shows that at $300 \mu\text{l}/\text{min}$, both datasets have a single peak which is fitted with a log-normal function. The control dataset has a peak at $DI_{peak} = 1.38 \pm 0.01$ and the standard deviation of the curve is $w = 0.09 \pm 0.01$. The TSA treated dataset has a peak at $DI = 1.59 \pm 0.01$ and a standard deviation of $w = 0.16 \pm 0.01$. This shows that there was an increase in average deformability due to TSA, with the peak DI increasing ~ 1.2 fold. Also, the spread of the data increased as the standard deviation was ~ 1.8 times greater for the treated cells. The datasets for $400 \mu\text{l}/\text{min}$ show similar results (Figure 5.39b) and are both fitted with a lognormal function. The peak position of the control is $DI_{peak} = 1.75 \pm 0.01$ and the standard deviation $w = 0.22 \pm 0.01$, for the treated sample $DI_{peak} = 2.06 \pm 0.02$ and $w = 0.34 \pm 0.01$. The peak DI increased ~ 1.2 fold and the standard deviation ~ 1.5 fold.

Figure 5.39c shows histograms of cells deformed at $600 \mu\text{l}/\text{min}$. The control dataset is fitted with a lognormal function, with a peak at $DI_{peak} = 2.32 \pm 0.01$ and a standard deviation of $w = 0.23 \pm 0.01$. The dataset of the treated cells has a main peak fitted with a lognormal function, where $DI_{peak} = 2.71 \pm 0.13$ and $w = 0.60 \pm 0.04$. There is a second smaller peak fitted with a Gaussian function, with peak position at $DI_{peak} = 7.35 \pm 0.29$ and a FWHM of $w = 0.29 \pm 0.09$. The main peak of the treated cells ~ 1.2 fold bigger than the control, and the standard deviation is ~ 2.6 fold bigger. The second peak is likely due to $600 \mu\text{l}/\text{min}$ being the

failure point. These smaller second peak occurs at strains ~ 3 times bigger than the main peak. This may represent a population of cells which rupture on-chip and lose all mechanical structure-acting more like a liquid. In the control sample, a small quantity of cells also have these high strains (>8). TSA makes cells more deformable hence more “ruptures” occur at this flow rate compared to the control.

The histograms show an increase in average DI of the treated cells for all the flow rates. The spread of the data also increased which is indicative of heterogeneous effects of TSA. Additionally, a sub-population was seen in the TSA treated cells at the *failure point* where cells achieved much higher strains ($\sim DI=7$). This suggests there is a critical strain of HL60 cells, after which cell rupture occurs.

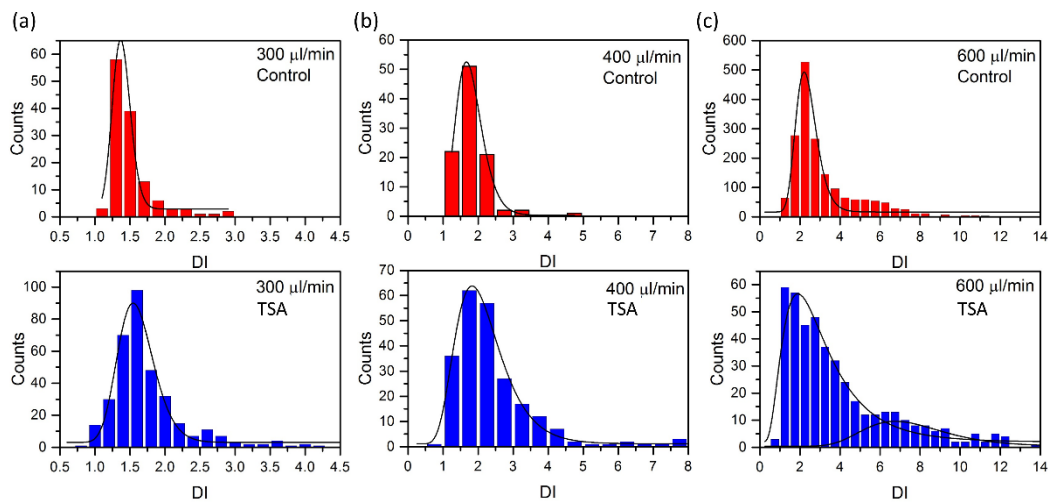


Figure 5.39 Histograms of DI of HL60 at various flow rates, comparing cells treated with $1 \mu M$ of TSA to a control sample. Flow rates used include (a) $300 \mu l/min$, (b) $400 \mu l/min$ (c) $600 \mu l/min$. Samples were deformed in the inertia-dominant regime ($\mu \cong 1 cP$).

Table 5.3 Summary of DI results w between untreated HL60 cells and those treated with TSA. Including the peak values (DI_{peak}) and standard deviations (w) of log-normal fits to histograms of SW480 cells deformed at different flow rates in the inertia-dominant regime.

	300 $\mu l/min$		400 $\mu l/min$		600 $\mu l/min$	
	w	DI_{peak}	w	DI_{peak}	w	DI_{peak}
Control	0.09 ± 0.01	1.38 ± 0.01	0.22 ± 0.01	1.75 ± 0.01	0.23 ± 0.01	2.32 ± 0.01
LatA	0.16 ± 0.01	1.59 ± 0.01	0.34 ± 0.02	2.06 ± 0.02	0.60 ± 0.04	2.71 ± 0.13

5.3.4 Discussion

HL60 cells were treated with TSA to investigate changes in cell deformability due to chromatin decondensation. Phase contrast and confocal fluorescence microscopy confirmed a small increase in cell size and changes in nuclear morphology due to treatment with TSA. DC in the shear-regime showed no changes in deformability across the entire range of flow rates.

The inertial-regime showed increased deformability in treated cells, which was more apparent above the cell *yield stress*.

Decondensation of chromatin has been shown to reduce nuclear stiffness [49], [87], [88]. Chalut *et al.* 2000 combined optical stretching and fluorescence recovery after photobleaching (FRAP) to study the differentiation of embryonic stem cells. Embryonic cell states associated with a more condensed chromatin structure, were also found to have softer nuclei, treatment with TSA was also shown to soften cells. Krause *et al.* 2013 combined AFM and confocal Z-stacks to visualise nuclear deformations of cells treated with TSA [88]. AFM measurements were specifically chosen over the cell nucleus and stiffness was measured to be 0.2-2.5 kPa. TSA induced nuclear softening up to 50%. For a contact force of 2 nN the control cells had maximal compression of 80% compared to 95% for treated cells.

Masaeli *et al.* 2016 used inertia-dominant deformability cytometry to study the deformation of cells treated with TSA over a 3 day period [48]. After 1 day, two subpopulations emerged with the dominant group having increased size and deformability and a smaller group with decreased size and deformability. After 3 days all cells merged into the smaller group having decreased size and deformability compared to a control. TSA is commonly researched as a cancer therapy drug as it induces apoptosis. The time-dependent study shows that initial decondensation of chromatin leads to increased deformability, however after a day apoptosis was induced which decreased deformability. Hodgson *et al.* 2017 measured the nuclear deformability of fluorescently labelled cells deformed through constriction channels and treated with TSA [49]. They found that treatment with TSA decreased the stiffness of the nucleus.

Golifer *et al.* 2017 used real-time deformability cytometry to deform HL60 cells treated with TSA [50]. They saw no change in deformability due to TSA for all concentrations tested (<10 μM). This indicates that the small shear-dominant strains used in RT-DC are not sensitive to the effects of chromatin decondensation. Under these flow conditions, changes in nuclear structure may be masked by the cytoskeleton [218]. These results are in agreement with our deformation cytometry results. No changes were detected in shear-dominant and low-strain regimes, and this regime was shown to be sensitive to actin cytoskeletal changes (section 5.1). Cell softening was most apparent in the high-strain inertia-dominant regime, also used by Masaeli *et al.* 2017.

Confocal fluorescence images showed that HL60 treated with 1 μM of TSA lead to destabilised microtubules as well as changes in chromatin structure. Ninios *et al.* 2010 found that HL60 showed decreased α tubulin as a function of incubation time with TSA [219], and Davis *et al.* 2004 also found decreased expression of α and β tubulin in cells [220]. Zhang *et*

al. 2015 used fluorescent microscopy to image the actin and microtubule structure of HeLa cells treated with TSA [221]. After 48 hr incubation they showed disruption of microfilaments and microtubules, which is indicative of cell cycle arrest. The deformability cytometry results indicate that changes in deformability due to TSA derive from the decondensation of chromatin and not secondary cytoskeletal changes. Section 5.1 showed that DC is most sensitive to actin disruption at a low-strain and high-shear regime, whereas changes in TSA was most apparent in a high-strain and inertia-dominant regime. Section 5.2 indicated that microtubule disruption alone did not lead to cell stiffening and this is likely a secondary mechanism.

5.4 Chapter Overview

Changes in cell deformability due to cytoskeletal perturbations were studied using deformation cytometry in shear-dominant and inertia-dominant regimes. Results found that deformation cytometry is sensitive to cytoskeletal and nuclear changes, dependent on flow regime.

Actin filaments were disrupted using Latrunculin A, which increased the deformability of HL60 and SW480 cells. A low-strain and shear-regime showed the largest relative increase in deformability. Additionally, high-strains above the *yield stress* in the inertial-regime showed no significant changes in deformability which may indicate breakdown of the actin network under these conditions. Nuclear chromatin was decondensed using Trichostatin A, this showed increased deformability of HL60 cells only in the inertia-dominant regime with the largest increase above the *yield stress*. These results indicate that the cytoskeleton dominates cell response at shear-dominant and low-strains and may shield any nuclear changes, whereas high-strains may disrupt the cytoskeleton and nuclear changes dominate here.

Microtubules were destabilised using Combretastatin A4, this showed a counter-intuitive response as HL60 cells became stiffer when probed in the shear-dominant regime. These results suggest that microtubule disruption may trigger secondary mechanisms in the cells resulting in a stiffening affect. Previous works show that microtubule disruption can cause enhancement of microfilaments, which may explain why stiffening was observed only in the shear-dominant regime.

Strain traces of cells showed that both deformation and recovery parameters are affected by changes in the cytoskeleton, and can be used to distinguish treated and untreated samples. Treatment with both LatA and CA4 showed that cells did not recover their original shape after deformation, suggesting that disruption of microfilaments and microtubules leads to increased cell plasticity. SCA also showed significant changes in multiple measured parameters and potential for identifying subpopulations. Ideally sample sizes would be larger (>100 cells)

however processing times limited the number of events. Even so, deformation cytometry shows promise for mechanical phenotyping single cells and identifying that subcellular perturbation leads to changes in whole cell deformability.

6 Changes to mechanical phenotype with colorectal cancer progression

6.1 Colorectal cancer cell lines

This chapter discusses the use of DC to examine the mechanical properties of different colorectal cancer (CRC) cell lines. Which includes: the primary tumour cell line SW480, the more advanced primary tumour cell line HT29 and the lymph node secondary tumour cell line SW620. These three cell lines offer a model system of CRC cancer progression (introduced in greater detail in section 2.2.3). Results were also compared to the mechanical phenotype of the leukaemia cell line HL60, presented in chapters 4 and 5, as their mechanical properties were expected to differ. DC was performed in the shear-dominant and inertia-dominant flow regime, inducing low to high strain deformations. Cell deformation and recovery were also tracked as a function of time in order to perform multiparameter single cell analysis. This allowed investigation into how well the cell types could be classified based on deformation and relaxation parameters, and how the mechanical phenotype changes with disease progression.

6.1 Colorectal cancer cell lines

6.1.1 Initial morphology

Cell size and morphology varies between cell lines. The three CRC cell lines are naturally adherent, phase contrast images of their morphology are shown by Figure 6.1. This is also compared to the non-adherent leukaemia cell line HL60. HT29 have an epithelial-like morphology, their shape is more polygonal. SW480 have two morphologies in their adherent state, the majority have an epithelial-like morphology however some cells have a rounded morphology [222]. SW620 have a fibroblast-like morphology, these are more elongated compared to SW480 and HT29.

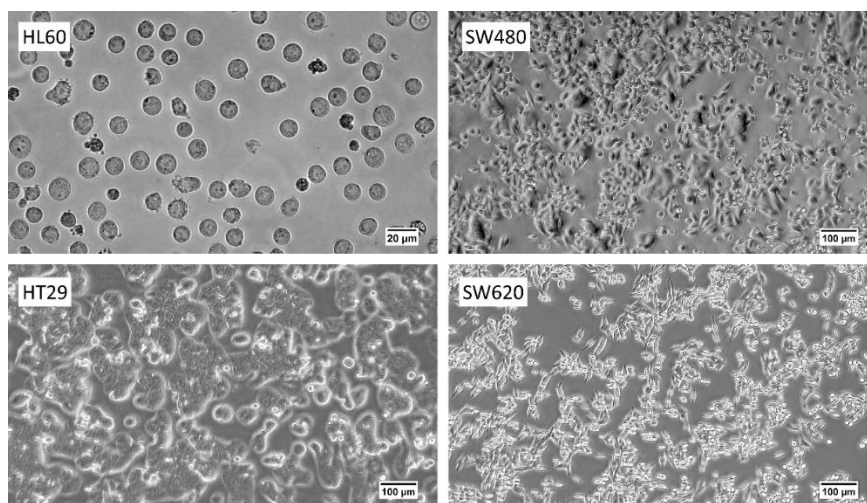


Figure 6.1 Phase contrast images of HL60, SW480, HT29 and SW620 in cell culture flasks to show their characteristic morphology.

6.1.2 Nucleus size

Confocal fluorescence imaging was used to visualise the actin and nuclear structure of live detached SW480, HT29 and SW620 cells. Cells were detached by incubation with TrypleE (procedure described in section 3.6.2) and incubated with fluorescent dyes for ~30 mins. Actin was stained using the fluorogenic labelling probe based on Silicon Rhodamine (Sir) (Spirochrome, Cytoskeleton Inc.), using a final concentration of 1 μM , DNA staining used the dye Hoechst 3342 (Thermo Fisher Scientific) at a final concentration of 0.5 $\mu\text{g/ml}$.

Figure 6.2 shows example fluorescent images of SW480, HT29 and SW620 with actin (red) and DNA (blue) stained. Fluorescence and corresponding bright field images were used to measure the whole cell diameter and apparent nuclear diameter of the three cell lines. Histograms are plotted of the whole cell diameter, using both a bright field image and using the actin cortex, and the nuclear diameter (Figure 6.2). Results show that bright field and actin cortex size measurements resulted in the same value for the cell diameter for SW480 and HT29. SW620 show a slight decrease in diameter using actin cortex compared to bright field. This may suggest a less structured actin cortex, a more diffuse fluorescence can also be seen in the accompanying fluorescent image. The distributions of the nuclear diameter of SW480 and HT29 show a normal distribution and are fitted with Gaussian function. The distribution of SW620 nuclear diameter is unclear and suggests a higher population is needed to accurately characterise the size. These differences may be related to the fact SW480 and HT29 adhere in an epithelial morphology whereas SW620 have a fibroblast morphology.

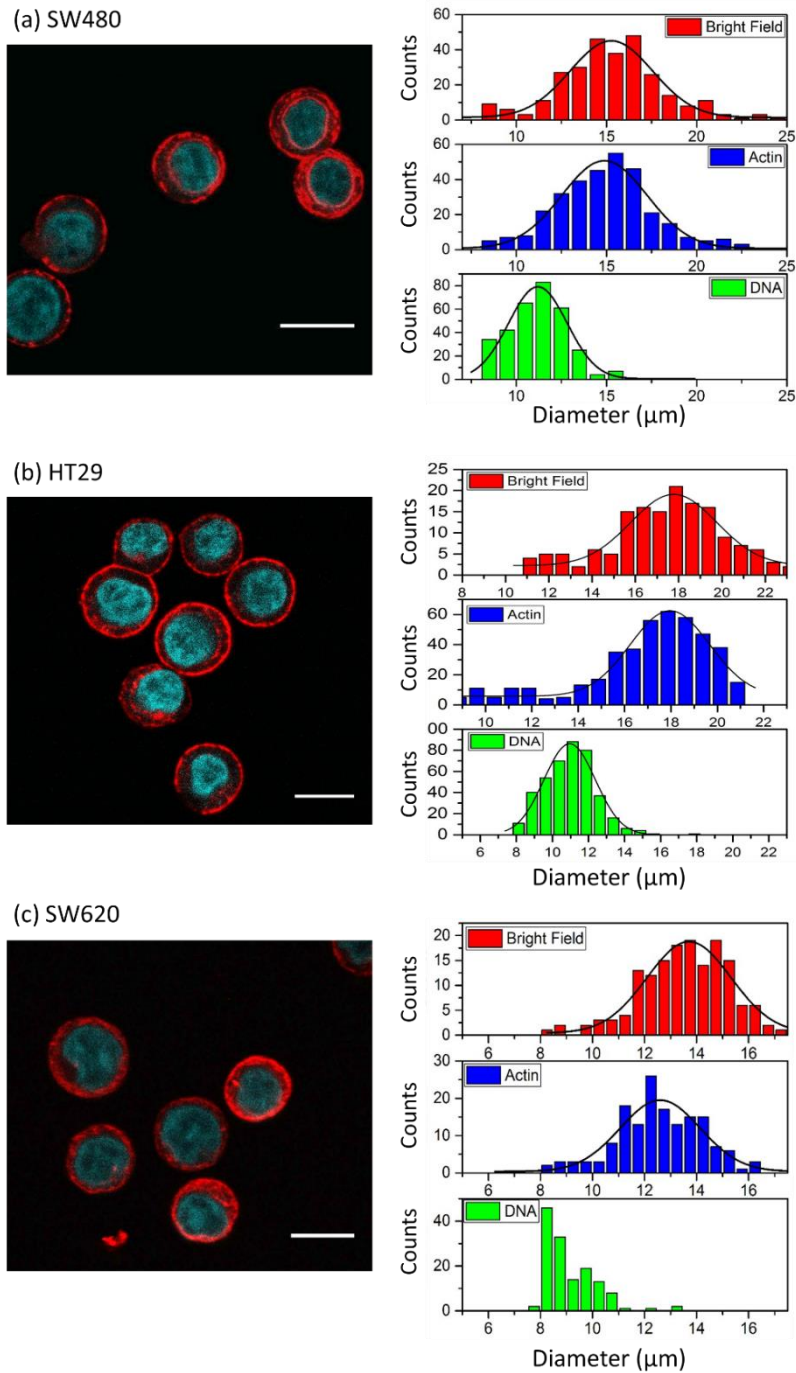


Figure 6.2 Confocal fluorescence images of detached (a) SW480, (b) HT29 and (c) SW620 cells, stained for DNA (blue) and actin (red). Also included are corresponding histograms of the cell diameter found from bright field images (red graph) and the actin cortex diameter (blue graph), also the nuclear diameter using the DNA stain (green). Scale bars are 20 μm .

From the datasets shown in Figure 6.2, the average nuclear diameter was found for the three CRC cell lines. These are shown in Table 6.1 and also compared to the nuclear diameter of HL60 cells (first presented in section 5.1.1). From this, the nuclear ratio $A_{nucleus}/A_{cell}$ of the four cell lines was found which quantifies the relative space the nucleus occupies within the

cell. The nuclear ratio is also presented as a bar graph for the four cell lines (Figure 6.3). This shows that HL60 has a low nuclear ratio compared to the three CRC cell lines, SW480 has the largest nuclear diameter and HT29 and SW620 have comparable nuclear diameters.

Table 6.1 The average nuclear diameter of HL60, SW480, HT29 and SW620 cells (measured using confocal images), and the nuclear ratio of each cell line ($A_{nucleus}/A_{cell}$).

	Nuclear Diameter (μm)	Nuclear Ratio
HL60	8.9 ± 0.1	0.55 ± 0.02
SW480	11.2 ± 0.1	0.72 ± 0.01
HT29	11.0 ± 0.1	0.63 ± 0.01
SW620	9.2 ± 0.1	0.67 ± 0.06

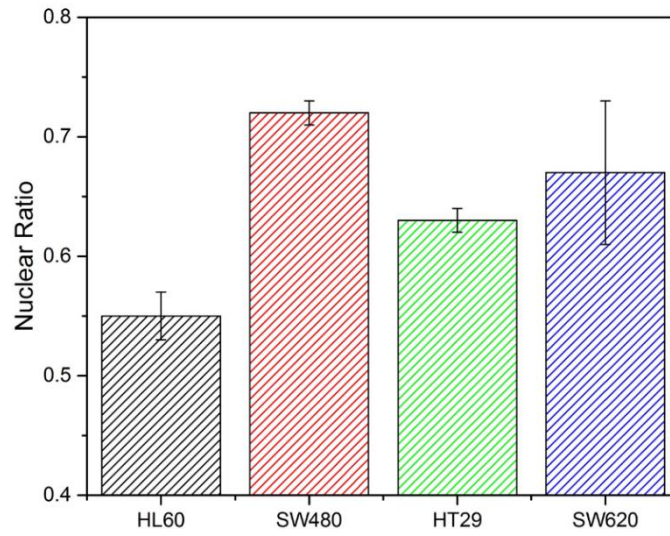


Figure 6.3 Bar graph showing the Nuclear Ratio of HL60, SW480 and SW620 cells ($A_{nucleus}/A_{cell}$). Bright field images were used to measure A_{cell} and fluorescent images were used to measure $A_{nucleus}$.

6.2 Deformation Cytometry

6.2.1 Shear-dominant regime

The three colorectal cancer cell lines were deformed in a cross-slot microfluidic device at the SP of an extensional flow junction. The cells were deformed over a range of flow rates Q in a shear-dominant flow regime (suspension buffer viscosity was $\mu \approx 33$ cP and $\text{Re} < 6$). Deformability was characterised using the deformation index DI. For each condition, 10s-100s of cell events were collected and experiments were then repeated $N=3$. An average value and standard error of the DI was found.

Figure 6.4 shows DI as a function of Q for SW480, HT29 and SW620 cells. The three datasets increase asymptotically as a function of Q toward a maximum value DI_{max} . The plot shows that SW480 and SW620 cannot be distinguished by DI over the entire range of flow rates. For $Q < 20 \mu\text{l}/\text{min}$, HT29 cells had increased DI compared to SW480 and SW620 cells. The

values of DI_{max} were all within error of each other; $DI_{max}(SW480) = 1.71 \pm 0.02$, $DI_{max}(HT29) = 1.68 \pm 0.06$, $DI_{max}(SW620) = 1.72 \pm 0.10$.

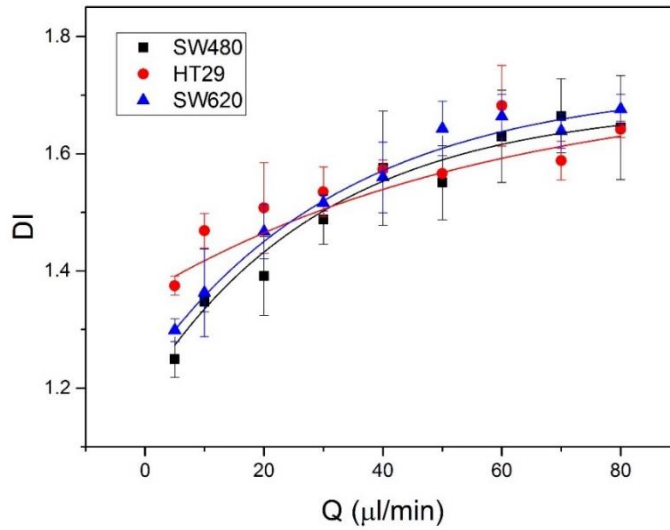


Figure 6.4 DI of SW480, HT29 and SW620 cell lines over a range of flow rates Q ($\mu\text{l}/\text{min}$). The flow regime was shear dominant ($\mu \approx 33$ cP). $DI \pm SE$ was averaged from multiple cell events combined from $N=3$ repeats. The total number of events measured was: $93 < n < 931$ for SW480, $160 < n < 596$ for HT29 and $280 < n < 734$ for SW620.

To further investigate the heterogeneity of CRC cell deformation, histograms of DI were plotted. This was first done for low strain deformation at $Q = 5 \mu\text{l}/\text{min}$, shown by Figure 6.5 a-c. Each histogram shows a normal distribution and is fitted with a Gaussian function, the central peak value is also shown b . Results show that b of SW480 and SW620 are within error of each other, whereas b of HT29 shows a small increase (~ 1.1 fold).

A two sample t-test was also used to measure the level of significance between these datasets (introduced in section 4.4.1). Figure 6.5d shows a bar graph of the average DI of SW480, HT29 and SW620 with the levels of significance denoted using the p -value. Results confirm that the DI of HT29 compared to SW480 and SW620 shows a significant difference ($p < 0.0001$), whereas SW480 and SW620 cannot be distinguished by DI alone ($p > 0.5$, not significant).

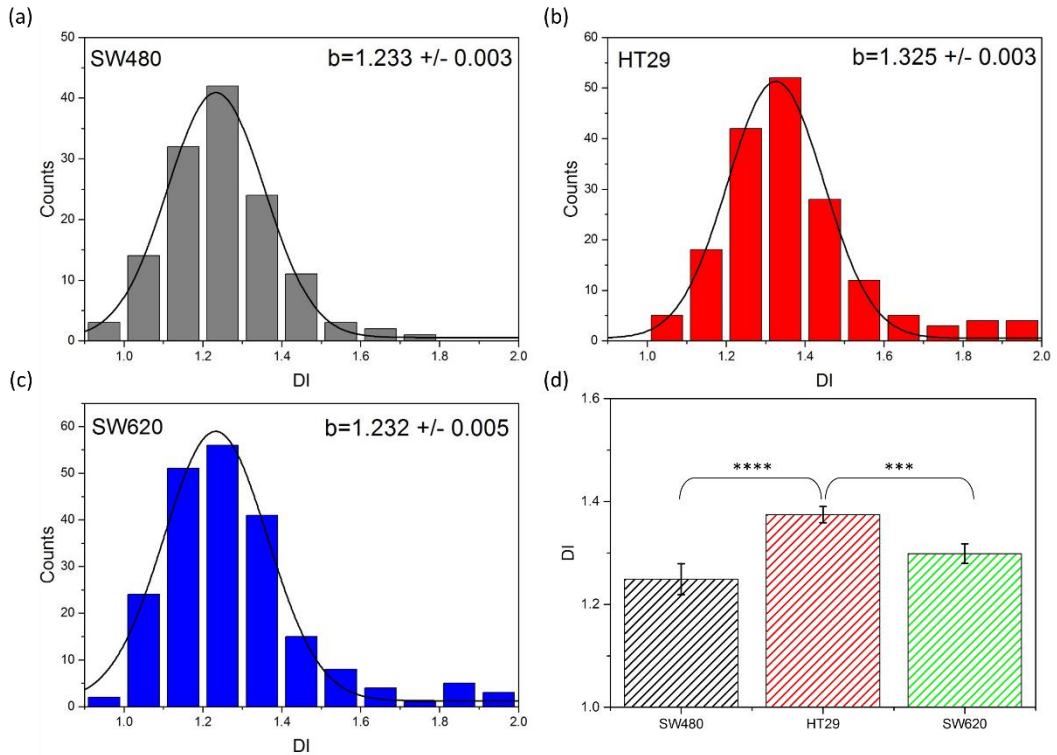


Figure 6.5 Histograms of the DI of the CRC cells lines deformed at $5 \mu\text{l}/\text{min}$ in a shear-dominant regime ($\mu \approx 33 \text{ cP}$). Where (a) is SW480, (b) is HT29 and (c) is SW620. Each dataset is fitted with a Gaussian function. (d) Shows a bar graph of the average DI of the CRC cell lines. The error bars denote the standard error SE and statistical t-tests were done to determine the level of significance. HT29 shows extremely significant difference to SW480 ($p = 7.5 \cdot 10^{-6}$) and SW620 ($p = 5.5 \cdot 10^{-4}$), whereas SW480 and SW620 showed no significant difference ($p=0.058$).

Histograms of DI were also plotted for high strain deformation at $Q = 80 \mu\text{l}/\text{min}$, shown by Figure 6.6 a-c. Each histogram shows a normal distribution and is fitted with a Gaussian function. Results show that b of HT29 and SW620 are similar, whereas b of SW80 shows a slight decrease (~ 1.1 fold). However, Figure 6.6d shows a bar graph of the average DI of the three cell lines. Consequently, this shows the average DI of SW480 to be within error of the DI of SW620 and HT29. Two sample t-tests confirm no significance between SW480 with SW620 and HT29. SW620 and HT29 however do show a significant difference ($p < 0.05$).

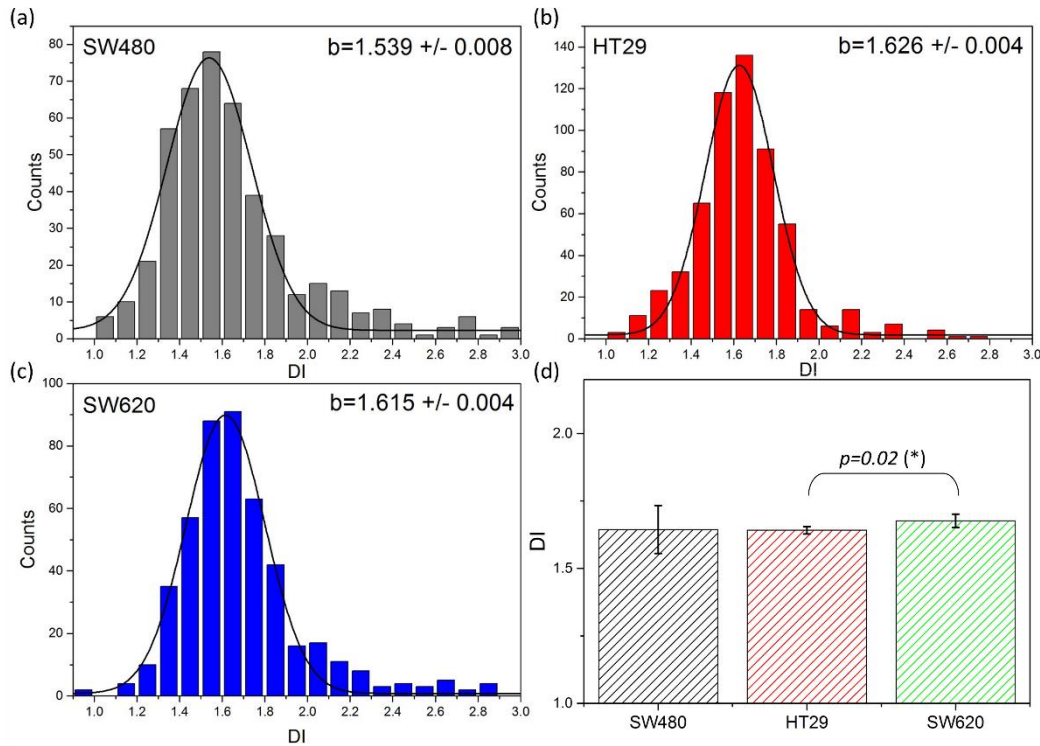


Figure 6.6 Histograms of the DI of the CRC cells lines deformed at $80 \mu\text{l}/\text{min}$ in a shear-dominant regime ($\mu \approx 33 \text{ cP}$). Where (a) is SW480, (b) is HT29 and (c) is SW620. Each dataset is fitted with a Gaussian function. (d) Shows a bar graph of the average DI of the CRC cell lines. The error bars denote the standard error SE and statistical t-tests were done to determine the level of significance. HT29 shows a significant difference to SW620 ($p = 0.02$). Whereas SW480 and SW620 showed no significant difference ($p=0.09$), as did SW480 and HT29 ($p=0.72$).

Overall, Figure 6.4 shows that the DI of SW480, HT29 and SW620 are largely indistinguishable from each other. This suggests that DI alone is not sensitive enough to characterize and separate the three CRC cell lines. Additional analysis was done at the lowest and highest strains, as we've previously shown that a low-strain and shear-dominant regime is more sensitive to cytoskeletal changes (section 5.1). These results showed that the low-strain datasets could significantly distinguish HT29 from SW480 and SW620, however neither low nor high strain could distinguish between SW480 and SW620 using DI.

Section 6.1.1 showed that the initial diameter of the three cell lines are different. Therefore, the values of DI were next normalized by initial size A (DI/A). This is a better representation of relative change in stiffness with metastatic progression, it better accounts for size-dependent difference in applied stress [48], [174]. Figure 6.7 is a plot of DI/A as a function of Q for the three CRC cell lines, with each dataset fitted with an exponential function. Here, SW620 shows a systematic increase in DI/A compared to SW480 which indicates that SW620 are in fact more deformable. At low flow rates, HT29 display properties similar to those of SW620 ($Q < 30 \mu\text{l}/\text{min}$), but at increasingly higher flow rates end up displaying properties

closer to those of SW480 ($Q \geq 40 \mu\text{l}/\text{min}$). DI/A increased asymptotically toward a maximum deformation value $(DI/A)_{max}$. For SW480 $(DI/A)_{max} = 0.101 \pm 0.004$ which is within error of HT29 where $(DI/A)_{max} = 0.106 \pm 0.007$. SW620 had $(DI/A)_{max} = 0.119 \pm 0.002$ which is significantly higher than SW480 and HT29.

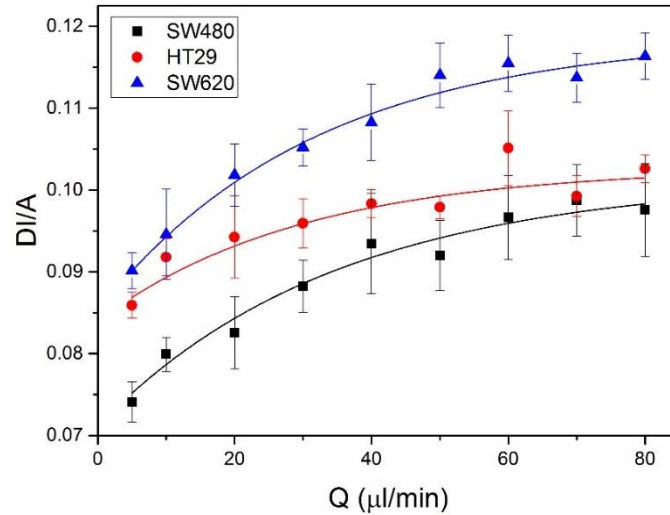


Figure 6.7 The initial size normalised deformation index DI/A of three colorectal cancer cell lines over a range of flow rates Q ($\mu\text{l}/\text{min}$), $DI/A \pm SE$ was averaged from multiple cell events combined from $N=3$ repeats. The flow regime was shear dominant ($\mu \approx 33$ cP).

6.2.2 Inertia-dominant regime

The three colorectal cancer cell lines were also deformed over a range of flow rates Q in an inertia-dominant flow regime (suspension buffer viscosity was $\mu \approx 1$ cP and $Re < 40$). For each condition, 10s-100s of cell events were collected and experiments were then repeated $N=3$. An average value of the deformation index DI was found with standard error.

Figure 6.8 shows DI as a function of Q for SW480, HT29 and SW620. An abrupt change in behaviour can be seen at $Q = 400 \mu\text{l}/\text{min}$, which is equivalent to the previous described *yield stress* and is associated with the disruption of the cytoskeleton (section 4.2.2). For each dataset there is a linear relationship between DI/A and Q for $Q < 300 \mu\text{l}/\text{min}$. A linear trend is also seen for $Q \geq 400 \mu\text{l}/\text{min}$, with an associated gradient increase for both SW480 and SW620. Below the *yield stress*, DI is unable to distinguish between any of the cell lines. Above the *yield stress*, HT29 and SW620 remain indistinguishable whereas SW480 has a relative increase in DI .

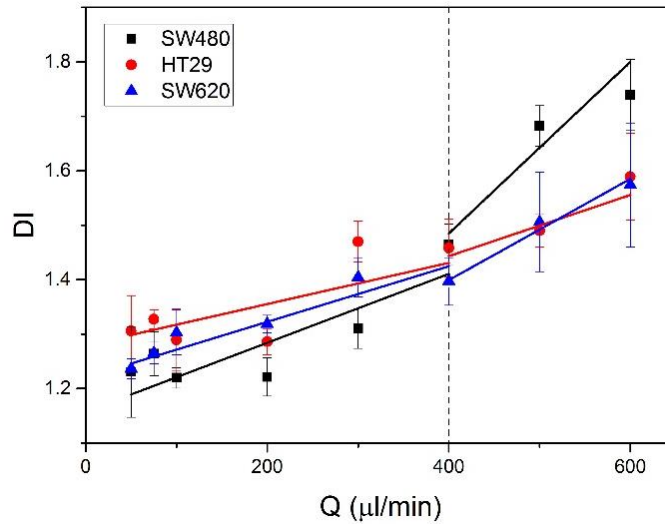


Figure 6.8 DI of SW480, HT29 and SW620 cell lines over a range of flow rates Q ($\mu\text{l}/\text{min}$). The flow regime was inertia dominant ($\mu \approx 1$ cP). $DI \pm SE$ was averaged from multiple cell events combined from $N=3$ repeats. The dashed line represents the “yield stress” behaviour, the datasets are fitted with separate linear fits before and after this value.

Histograms of DI were also plotted for inertial regime deformations of SW480, HT29 and SW620. This was first done for a low strain, below the *yield stress*, at $Q = 300 \mu\text{l}/\text{min}$. The plots are shown by Figure 6.9a-c and each histogram shows a log-normal distribution function, the central peak value is denoted on the plots as b . Figure 6.9d shows a bar graph of the average DI of the three cell lines. Results show that HT29 and SW620 have DI within standard error, whereas SW480 has a lower DI . However, two sample t-tests confirm that all three datasets show a significant difference ($p < 0.05$). Particularly SW480 and HT29 are shown to have an extremely low p -value ($p < 0.0001$).

Histograms of DI were also plotted for high strain deformations, above the *yield stress*, at $Q=600 \mu\text{l}/\text{min}$, shown by Figure 6.10 a-c. Each histogram is fitted with a log-normal function. Results show that b of HT29 and SW620 are within error of each other, whereas b of SW80 shows a ~ 1.2 fold increase. Figure 6.10d shows a bar graph of the average DI of the three cell lines, which shows the DI of HT29 to be within error of the DI of SW620. Here, SW480 has decreased DI which is the opposite result to below the *yield stress* (Figure 6.9d). Two sample t-tests confirm no significance between HT29 with SW620 ($p > 0.05$). SW480 shows an extremely significant difference to both cell lines ($p < 0.0001$).

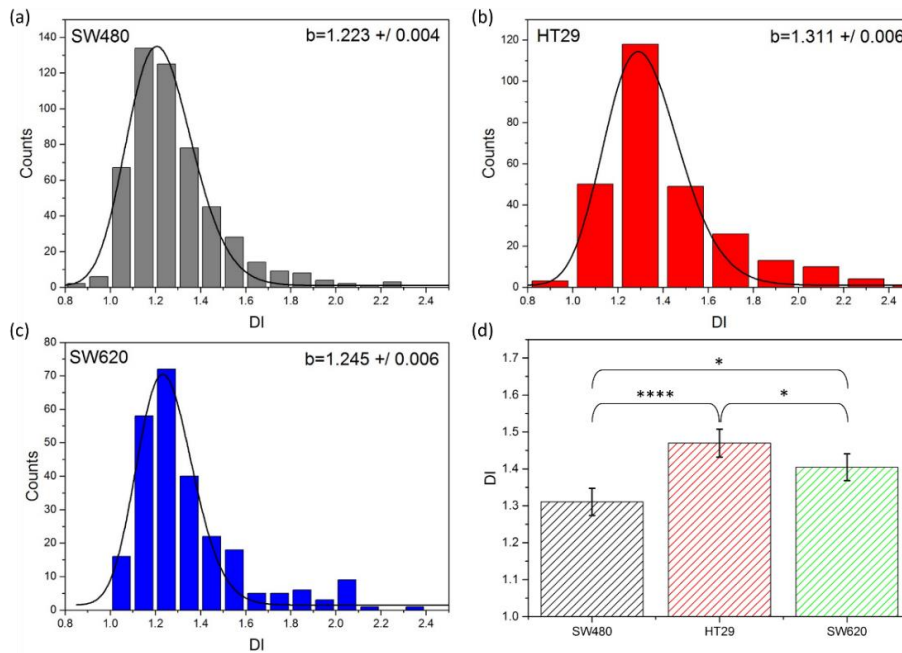


Figure 6.9 Histograms of the DI of the CRC cells lines deformed at $300 \mu\text{l}/\text{min}$ in the inertia-dominant regime ($\mu \approx 1 \text{ cP}$). Where (a) is SW480, (b) is HT29 and (c) is SW620. Each dataset is fitted with a Lognormal function. (d) Shows a bar graph of the average DI of the CRC cell lines. The error bars denote the SE and statistical t -tests determined the level of significance. HT29 shows extremely significant difference to SW480 ($p = 2.26 \cdot 10^{-5}$) and a significant different to SW620 ($p = 0.03$), SW480 and SW620 also showed a significant difference ($p=0.008$).

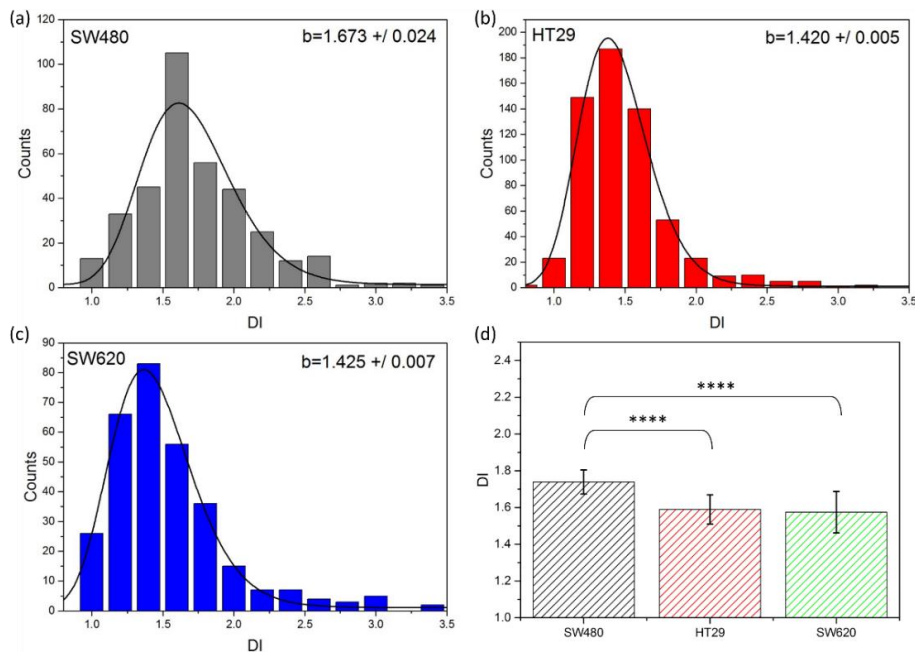


Figure 6.10 Histograms of the DI of the CRC cells lines deformed at $600 \mu\text{l}/\text{min}$ in the inertia-dominant regime ($\mu \approx 1 \text{ cP}$). Where (a) is SW480, (b) is HT29 and (c) is SW620. Each dataset is fitted with a Lognormal function. (d) Shows a bar graph of the average DI of the CRC cell lines. The error bars denote the SE and statistical t -tests determined the level of significance. HT29 showed an extremely significant difference to SW480 ($p = 1.25 \cdot 10^{-6}$) and no significant different to SW620 ($p = 0.592$). SW480 and SW620 also showed an extremely significant difference ($p = 3.60 \cdot 10^{-9}$).

Figure 6.11 shows the DI values normalised by the initial size of the cells (DI/A), to give a better relative representation of stiffness. Here, for $Q < 400 \mu\text{l}/\text{min}$ (below the *yield stress*) the cell lines show systematic changes with SW620 having the highest DI/A followed by HT29 and then SW480 having the lowest. For, $Q \geq 400 \mu\text{l}/\text{min}$ the cell lines are less distinguishable from each other. These results show a distinct behavioural change above and below the apparent *yield stress* of the cells ($Q \approx 300 \mu\text{l}/\text{min}$).

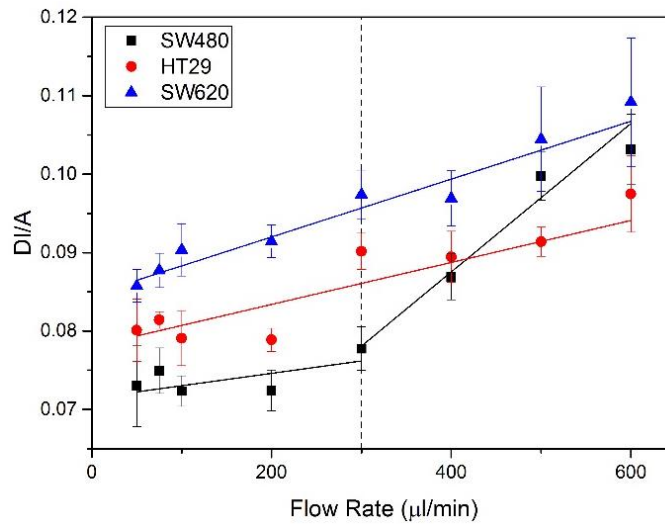


Figure 6.11 DI/A of three colorectal cancer cell lines over a range of flow rates ($\mu\text{l}/\text{min}$), in an inertia dominant regime ($\mu \approx 1 \text{ cP}$). $DI/A \pm SE$ was averaged from multiple cell events combined from $N=3$ repeats. The total number of events measured was: $30 < n < 603$ for SW480, $47 < n < 619$ for HT29 and $30 < n < 450$ for SW620.

6.2.3 Cell width and height

Previously, the deformation index DI was used to characterise the maximum “cell squeezing” which occurs at the SP of the cross-slot devices. During these deformations, the cell width W decreases compared to initial cell diameter A whereas cell height H increases. In the shear-regime (Figure 6.7) we see a maximum cell deformability as DI tends to DI_{max} as a function of flow rate. By looking at W and H separately more information about the cell stretching can be elucidated, such as whether these individual parameters reach a minimum/maximum at the same rate.

Figure 6.12 shows W and H plotted as a function of flow rate for HL60, SW480, HT29 and SW620 cells deformed in the shear-dominant regime. Results show that for the four cell lines W decreases as an exponential decay and is fitted accordingly. The nuclear diameter (Table 6.1) is marked in a dashed line, this shows that the minimum W does not surpass the nuclear diameter. A general increase in H as a function of flow rate is seen for the four cell lines. HL60, SW480 and SW620 are fitted with exponential functions, however HT29 was better

fitted with a linear fit. The initial cell diameter A is also marked with a dashed line. The plots show that cell deformation shows relatively larger change to H than to W .

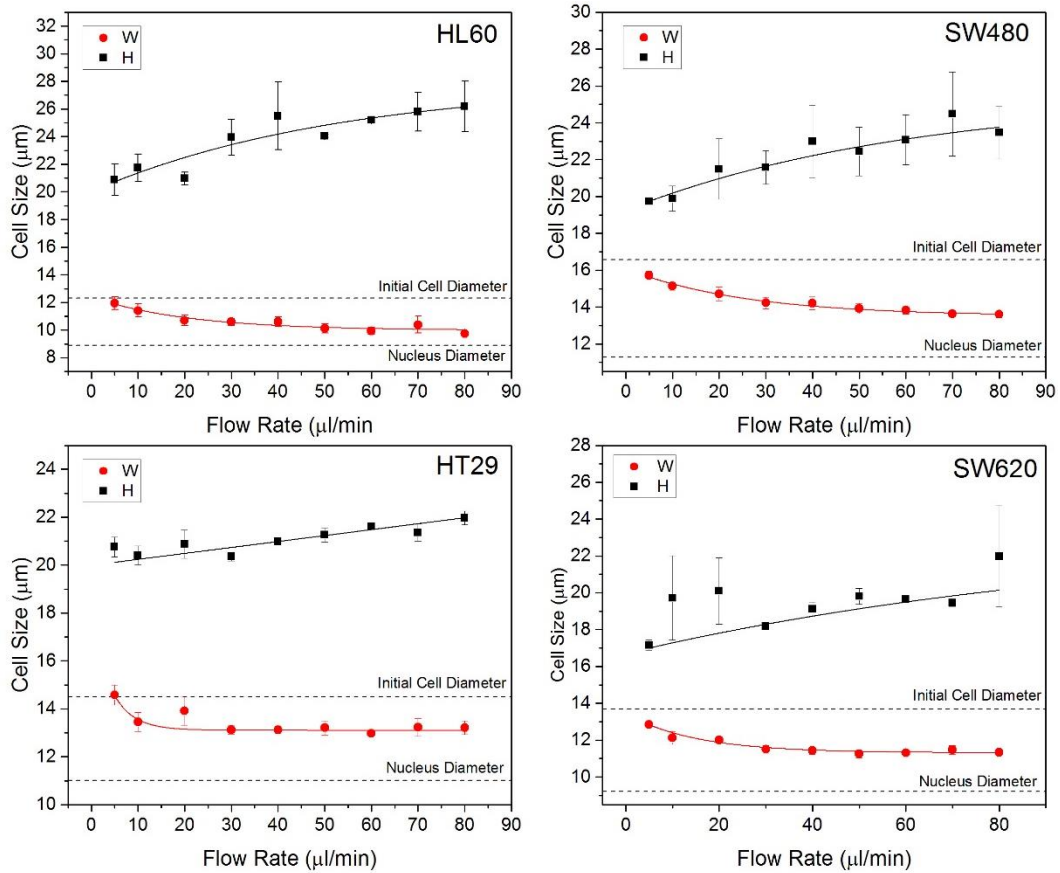


Figure 6.12 Cells were deformed at the SP of a cross-slot device, the width (W) and (height) of the cell were measured at their maximum deformed state at the SP ($\mu \approx 33$ cP). Here, graphs are plotted of W and H of four cell lines under deformation as a function of flow rate. Measurements were taken in the shear-dominant regime. The initial cell diameter (before deformation) and nucleus diameter (from fluorescence imaging) are marked by dashed lines.

Several parameters can be extracted from the exponential fits shown in Figure 6.12. Including the exponential decay constants for W as a function of flow rate (τ_W), and H as a function of flow rate (τ_H). These values are summarised in Table 6.2. Additionally, the exponential fit to W can be extrapolated to find the minimum deformed width of the cell (W_{MIN}). Table 6.2 also shows the difference between W_{MIN} and the diameter of the nucleus ($W_{MIN} - A_{Nucleus}$). The τ_W of HL60 and SW480 are within error of each other, HT29 and SW620 have lower τ_W values which shows they tend to W_{MIN} at a faster rate. The values of τ_H are generally larger than τ_W , however their associated errors are also larger (>50%). HT29 do not have a value for τ_H as a linear fit was more applicable. The three CRC cell lines show similar values for $W_{MIN} - A_{Nucleus}$, HT29 and SW620 are within error of each other and SW480 shows a slight increase (~ 1.1 fold). Comparatively, HL60 show a ~ 2 fold decrease in $W_{MIN} - A_{Nucleus}$ compared to the CRC cell lines. This shows that HL60 can deform to a minimum width closer to their nuclear size

compared to the other cell lines. This may be indicative of HL60 being more deformable than the CRC cell lines, and potentially having a softer nucleus.

Table 6.2 Summary of parameters associated with cell width W and H during deformation at the SP over a range of flow rates.

	τ_W	τ_H	$W_{MIN} - A_{Nucleus}$
HL60	20.8±7.9	53.3±50.3	1.07±0.02
SW480	25.8±4.4	61.5±34.9	2.30±0.03
HT29	4.3±2.4	N/A	2.10±0.02
SW620	15.0±2.6	109.89±159.3	2.11±0.02

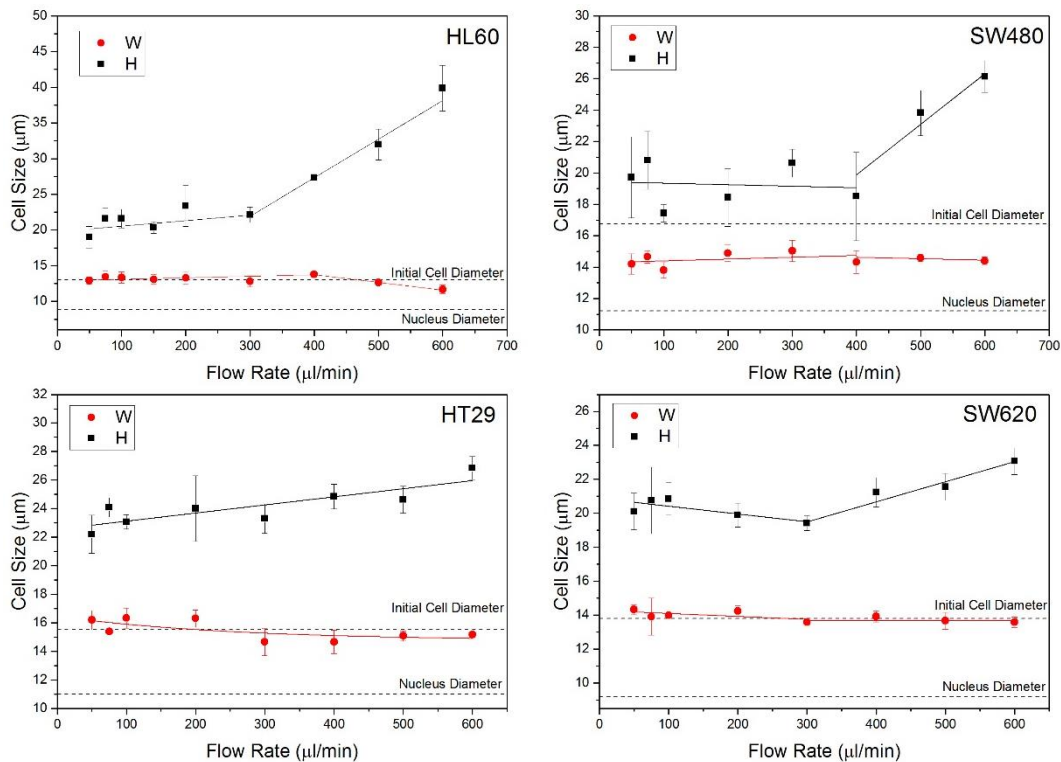


Figure 6.13 Cell were deformed at the SP of a cross-slot device, the width (W) and (height) of the cell were measured at their maximum deformed state at the SP ($\mu \approx 1$ cP). Here, graphs are plotted of W and H of four cell lines under deformation as a function of flow rate. Measurements were taken in the inertia-dominant regime. The initial cell diameter (before deformation) and nucleus diameter (from fluorescence imaging) are marked by dashed lines.

Similarly, Figure 6.13 shows W and H plotted for the four cell lines deformed in the inertia-dominant regime as a function of flow rate. Results show negligible change in W as a function of flow rate for SW480, HT29 and SW620. HL60 shows a small decrease in W for $Q > 500 \mu\text{l}/\text{min}$. HL60 shows linear relationships between H and flow rate, with a distinct increase in gradient at $Q > 300 \mu\text{l}/\text{min}$ which coincides with the previously discussed *yield stress*. For $Q > 300 \mu\text{l}/\text{min}$, the H of SW620 is fitted linearly with a slightly negative

gradient, however the standard error values suggest no significant change in H over this flow range. For $Q > 300 \mu\text{l}/\text{min}$, the H of SW620 increases significantly and has a linear fit (also suggesting *yield stress* behaviour. SW480 shows no significant changes in H for flow rates $Q > 400 \mu\text{l}/\text{min}$, then a linear increase for $Q < 400 \mu\text{l}/\text{min}$ suggesting *yield stress* behaviour. Differently, HT29 show a linear trend encompassing the entire range of flow rates suggesting no *yield stress* behaviour.

For all four cell lines, even at the highest flow rate the minimum W does not surpass the nuclear diameter (marked with a dashed line). The *yield stress* associated behavioural change is dominated by H in the calculation of DI . The lack of change in W of the *yield stress* could indicate that nuclear rupture is yet to occur and this change is likely associated with filament rupture of the cytoskeleton, leading to further extension of the cytosol in H .

6.3 Deformation and Recovery

6.3.1 Strain trace multiparameter analysis

The strain ε of the three CRC cell lines was tracked as cells deformed and recovered through the SP of an extensional flow junction. Measurements were taken in the shear-dominant regime ($\mu \cong 33 \text{ cP}$) at $Q=5 \mu\text{l}/\text{min}$. This high-shear and low-strain regime was previously shown to be most sensitive to changes in the actin cytoskeleton (section 5.1).

Figure 6.14 shows the averaged strain traces of $N=56$ SW480 cells (previously shown in section 5.1), $N=49$ HT29 cells and $N=50$ SW620 cells. The results for the HL60 cell lines (first discussed in chapter 4) are also included as a comparison. The strain traces were used to extract multiple characteristic parameters, including; the initial strain ε_0 , the maximum strain ε_{max} , the deformation time τ_d , the relaxation time τ_r and the final strain ε_∞ . The associated time constants (τ_d and τ_r) were found by fitting exponential decay functions to the deformation region (cell approach to the SP) and relaxation region (cell moving away from the SP) of the graph. The final strain ε_∞ was also found by extrapolation of the same fit used to find the relaxation time. As the inlet channels are perpendicular to the outlet channels some values of ε_0 are slightly below 0 (this is due to small deformations induced by shear channel confinement, which are relatively small compared to deformation at the SP). Thus, if cells recover their original shape post deformation the magnitude of final strain should match initial strain ($|\varepsilon_0| = |\varepsilon_\infty|$). The areas shaded in pink in Figure 6.14 have a width of $2|\varepsilon_0|$, therefore if the final strain (denoted by a dashed line) falls within this vicinity then the cell recovers its initial shape.

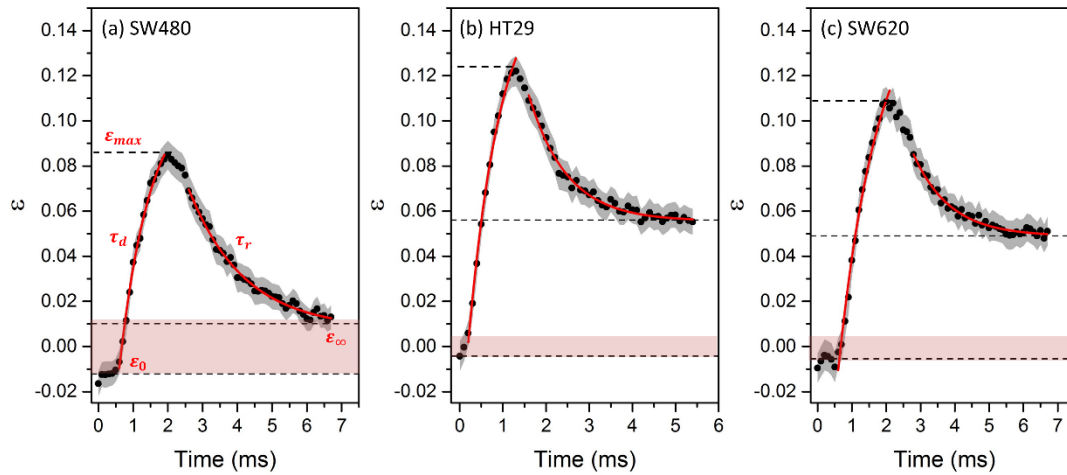


Figure 6.14 Strain ε was tracked for SW480, HT29 and SW620 cells as a function of time, with the SE shown by the shaded areas. The flow rate was $5 \mu\text{l}/\text{min}$ and the suspension medium viscosity was 33 cP . The final strain is marked by dashed lines (ε_∞), found by extrapolation of a exponential fit to the relaxation (red line). (a) The averaged deformation trace of $N=56$ SW480 cells. (b) The averaged deformation trace of $N=49$ HT29 cells. (c) The averaged deformation trace of $N=50$ SW620 cells.

The averages of all the mentioned parameters are summarised in Table 6.3. Results show that the initial strain ε_0 and deformation time τ_d of the four cell lines are within error of each other. The maximum strain of HT29 and SW620 are within error of each other, and SW480 has the lowest maximum strain of all the cell lines. The leukaemia cell lines HL60 is shown to be highly deformable compared to the three tumour originating cell lines, the maximum strain ε_{max} is ~ 2.2 times larger than SW480 cells. HL60 are expected to be more deformable due to their original cellular function as a blood cell, which requires movement through blood vessels, whereas the CRC cell lines derive from a stationary tumour environment. HL60 also have the slowest relaxation time τ_r out of the four cell lines, HT29 relax at a rate 4-fold faster than HL60. Interestingly, even though SW480 deformed to a lower ε_{max} its relaxation time was slower than both HT29 and SW620.

Table 6.3 and Figure 6.14 also show that the final strain ε_∞ of HL60 and SW480 is within error of the initial strain ($|\varepsilon_0| = |\varepsilon_\infty|$), demonstrating that these cell types undergo complete initial shape recovery after deformation. Comparatively, both HT29 and SW260 show incomplete shape recovery as their final strain ε_∞ is significantly larger than the initial strain ($|\varepsilon_0| < |\varepsilon_\infty|$). Both cell lines only recovery to approximately half of the applied ε_{max} .

Table 6.3 Multiple characteristic parameters extracted from the strain traces of $N=56$ SW480 cells, $N=49$ HT29 and $N=50$ SW620 cells. The strain traces were averaged in order to extract the initial strain ε_0 , the final strain ε_∞ , the maximum strain ε_{max} , the deformation time τ_d , the relaxation time τ_r , with $\pm SE$.

	HL60	SW480	HT29	SW620
ε_{max}	0.18 ± 0.01	0.08 ± 0.01	0.12 ± 0.01	0.11 ± 0.01
τ_r (ms)	3.52 ± 0.14	1.36 ± 0.06	0.89 ± 0.05	1.04 ± 0.05
τ_d (ms)	1.04 ± 0.05	0.89 ± 0.10	0.76 ± 0.10	1.15 ± 0.20
E (Pa)	301 ± 29	542 ± 66	309 ± 50	372 ± 98
ε_0	-0.012 ± 0.004	-0.012 ± 0.006	-0.004 ± 0.007	-0.007 ± 0.007
ε_∞	$+0.03 \pm 0.009$	$+0.010 \pm 0.003$	$+0.056 \pm 0.001$	$+0.049 \pm 0.001$

Figure 6.15 a-c show the averaged cell velocity as a function of time through the extensional flow junction for SW480, HT29 and SW620, which were fitted with sine functions (shown in red). Alongside this are the strain traces which could then be fitted with the Kelvin-Voigt model (described in section 2.3.4), also shown in red. From this fit, the Elastic modulus of the three CRC cell lines was found. These values are also included in Table 6.3. Figure 6.16 is a bar graph of the elastic moduli of SW480, HT29, SW620 and also HL60. Results show that HL60 are the softest cell, HT29 and SW620 have similar stiffness within error of each other, and SW480 are the stiffest of the four cell types.

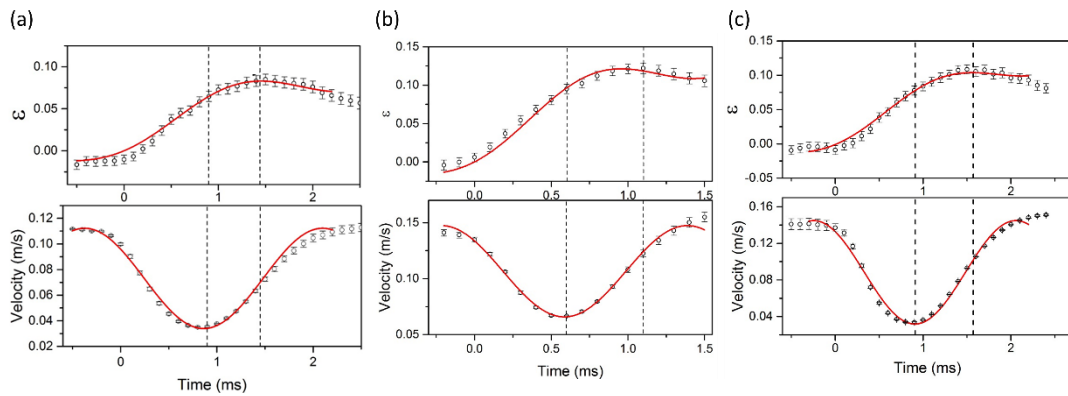


Figure 6.15 The average strain trace of SW480, HT29 and SW620 cells fitted with the Kelvin-Voigt function accompanied by the velocity profile fitted with a sine function (shown in red). (a) $N=56$ SW480 cells, (b) for $N=49$ HT29 cells and (c) $N=50$ SW620 cells. For all datasets Q was $5 \mu\text{l}/\text{min}$ and viscosity was ($\mu=33 \text{ cP}$).

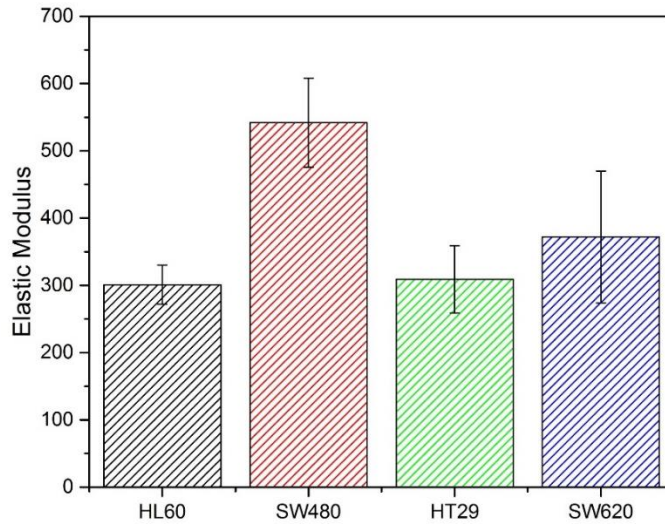


Figure 6.16 A bar graph of the Elastic moduli of HL60, SW480, HT29 and SW620 cells. This was found by fitting the Kelvin-Voigt model to strain traces of single cells deforming in an extensional flow.

6.3.2 Single Cell Analysis

As discussed in the previous results chapters, single cell analysis can offer additional insight into the heterogeneity of mechanical responses of a cell sample. Thus, SCA was also performed on individual strain traces of SW480, HT29 and SW620 in order to extract multiple parameters and perform additional statistical tests. The SCA procedure was identical to that described for HL60 cells in section 4.1.1. SCA was successfully used to extract ε_{max} , ε_0 , ε_∞ , τ_r and also the initial cell diameter A .

Table 6.4 Characteristic parameters of HL60, SW480, HT29 and SW620 cell lines, found using single cell analysis of cells deforming at the stagnation point of an extensional flow at 5 $\mu\text{l}/\text{min}$ in the shear-dominant regime ($\mu \approx 33$ cP). The mean value of each parameter is given with the associated standard error, the coefficient of variation is also given as a percentage where $CV = \text{mean}/SD$.

	HL60		SW480		HT29		SW620	
	Mean \pm SE	CV	Mean \pm SE	CV	Mean \pm SE	CV	Mean \pm SE	CV
A (μm)	12.3 \pm 0.21	12	15.2 \pm 0.25	13	14.5 \pm 0.20	9	11.5 \pm 0.14	9
ε_{max}	0.18 \pm 0.01	27	0.09 \pm 0.01	54	0.12 \pm 0.01	39	0.11 \pm 0.01	42
τ_r (ms)	3.04 \pm 0.15	34	1.11 \pm 0.14	82	1.15 \pm 0.24	141	0.96 \pm 0.10	86
ε_0	-0.012 \pm 0.004	52	-0.012 \pm 0.006	281	-0.005 \pm 0.006	155	-0.005 \pm 0.006	201
ε_∞	+0.03 \pm 0.004	87	+0.018 \pm 0.003	129	+0.047 \pm 0.006	80	+0.047 \pm 0.006	86

The average of these values are shown in Table 6.4 with their standard error, the HL60 dataset first shown in section 4.4.1 is also included as a comparison. Histograms of the 5 parameters for the four cell lines can be found in the appendix (Figure S4-S8), the distributions follow the same trends as described for HL60. Table 6.4 also shows the coefficient of variation CV of the parameters expressed as a percentage. CV is a ratio of the standard deviation to the mean

and offers a measure of dispersion. Thus, CV can be used to compare the heterogeneity of the parameters between the cell lines.

Two sample t-tests were performed on the 5 parameters to quantify their individual use for distinguishing between the four cell types. Figure 6.17 shows a bar graph of the average A , ϵ_{max} , ϵ_{∞} , τ_r for HL60, SW480, HT29 and SW620 cells, with the level of significance labelled using the p -value. Where, $p > 0.05$ is not significant (ns), $0.01 < p < 0.05$ is significant (*), $0.001 < p < 0.01$ is very significant (**), $0.0001 < p < 0.001$ is extremely significant (***) and $p < 0.0001$ is extremely significant (****). The raw p -values are summarised in Table 6.5, we note that the values for initial strain ϵ_0 showed no significant between any cell lines (an expected result as the cells should have near 0 strain).

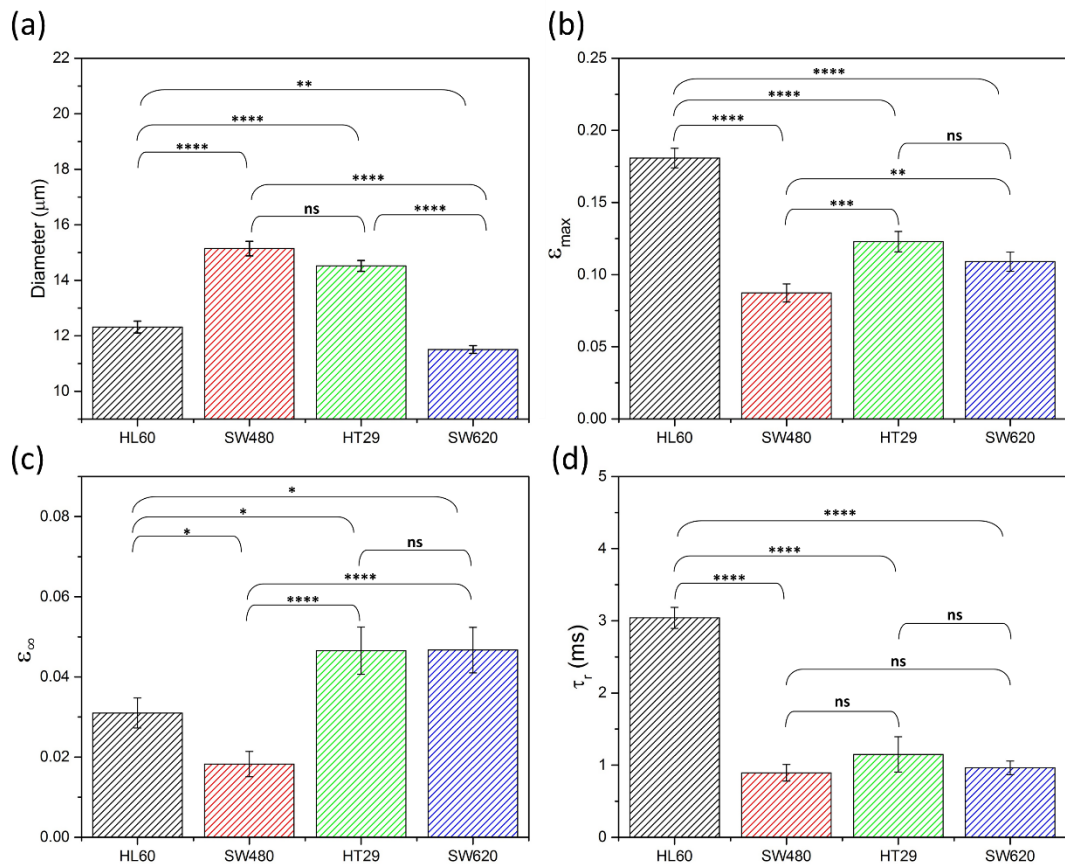


Figure 6.17 Multiparameter analysis of HL60, SW480, SW620 and HT29 cell populations using statistical t-tests were done to determine the level of significance, where the error bars denote the standard error SE, (a) Initial cell diameter, (b) The maximum strain ϵ_{max} , (c) the final strain ϵ_{∞} and (d) the relaxation time τ_r were extracted from deformation traces of single cells deforming at $5 \mu\text{l}/\text{min}$ in a shear dominant regime ($\sim 33 \text{ cP}$).

Figure 6.17a shows that the initial diameter A shows statistical significance in separating all the cell lines, apart from SW480 and HT29 showing a non-significant p -value ($p > 0.05$). Figure 6.17b shows that the ϵ_{max} of SW480 shows significance compared to both HT29 and SW620

($p < 0.05$), whereas HT29 and SW620 show no significance ($p > 0.05$). Interestingly, this shows that even though SW480 and HT29 are non-distinguishable by their initial size, the maximum strain can be used to separate the populations. Results also corroborate that SW620 and HT29 have similar deformability (Figure 6.16).

Figure 6.17c indicates that the final strain ϵ_∞ of SW480 shows an extremely significant p -value compared to the other two CRC cell lines ($p < 0.0001$), whereas SW620 and HT29 show no significance via ϵ_∞ ($p > 0.05$). This corroborates the previously discussed result that SW480 completely recovers its initial shape, whereas HT29 and SW620 do not (Figure 6.14). Additionally, these results continue to show a trend that SW480 are mechanically different to the later stage CRC cell lines which show similar deformation and relaxation behaviour. The HL60 cell line also shows a significant difference to all of the CRC cell lines ($p < 0.05$). Finally, Figure 6.17d compares the relaxation time τ_r of the four cell lines. Results show no significance from the τ_r datasets between any of the CRC cell lines ($p > 0.05$). However, the τ_r of HL60 shows extreme significant compared to each of the CRC cell lines ($p < 0.0001$). HL60 were highly deformable compared to the CRC cell lines and their average relaxation time was ~ 3 fold larger.

Overall, Figure 6.17 shows that no single parameter is statistically significant when comparing the four cell types, and demonstrates the need for multiple parameter analysis for accurate classification of different cell types.

Table 6.5 Summary of p -values comparing properties of HL60, SW480, SW620 and HT29 cell populations using; initial cell diameter A , the initial strain ϵ_0 , the maximum strain ϵ_{max} , the final strain ϵ_∞ and the relaxation time τ_r .

		A (μm)		ϵ_∞		ϵ_{max}		τ_r		ϵ_0	
		p-value	Sig.	p-value	Sig.	p-value	Sig.	p-value	Sig.	p-value	Sig.
HL60	SW480	2.77E-13	****	0.01074	*	4.23E-17	****	7.03E-18	****	9.78E-01	ns
HL60	HT29	5.09E-12	****	1.44E-02	*	3.78E-09	****	2.09E-19	****	0.33807	ns
HL60	SW620	0.0022	**	2.35E-02	*	2.10E-11	****	7.38E-10	****	0.35094	ns
SW480	HT29	0.07687	*	1.44E-05	****	7.03E-04	***	5.93E-01	ns	0.38193	ns
SW480	SW620	1.35E-20	****	3.66E-05	****	1.90E-02	*	8.92E-01	ns	3.94E-01	ns
SW620	HT29	1.43E-22	****	9.05E-01	ns	2.80E-01	ns	5.19E-01	ns	9.84E-01	ns

6.3.3 Linear Discriminant Analysis

Linear Discriminant analysis was next used on the multiparameter datasets of HL60, SW480, HT29 and SW620 to test their abilities to accurately classify the different cell types. LDA is a supervised multivariate method which obtains linear combinations of the parameters able to best separate the different cell lines. This method is trained with a subset of the sample, where the expected outputs are already known. The LDA method used in this system was developed

by Julia Gala De Pablo and used on Raman Spectroscopy data for classifying cell lines, including SW480, HT29 and SW620 [2], [223].

The method was trained on a 4-class dataset (4 cell types), where each linear discriminant (LD) maximises the separation of a pair of classes. Then using all the LD scores to provide a final classification. A k-fold validation test was then applied to the data. This involves a random fraction of the data being first used to train the LDA model. The model is then used on the remaining data which assesses the models ability to correctly classify the cell types from the given parameters. Here, a 5-fold validation test was applied and the loadings and scores of the LDs are presented in Figure 6.18 and the confusion matrix is shown by Table 6.6. Figure 6.18 shows that LD1, LD3 and LD5 result in the best separation of HL60 compared to the CRC cell types, with individual scores shown in Figure 6.18 B1, 3 and 5. The discriminants generally correspond to ε_{max} , ε_0 and τ_r . Between the CRC cell lines, LD2 and LD6 showed the best separation of SW480 from HT29 and SW620. These correspond to the initial diameter A and ε_{∞} . Comparing SW620 to either SW480 or HT29 shows the best separation by LD4 and LD6, mainly classified by their smaller diameter.

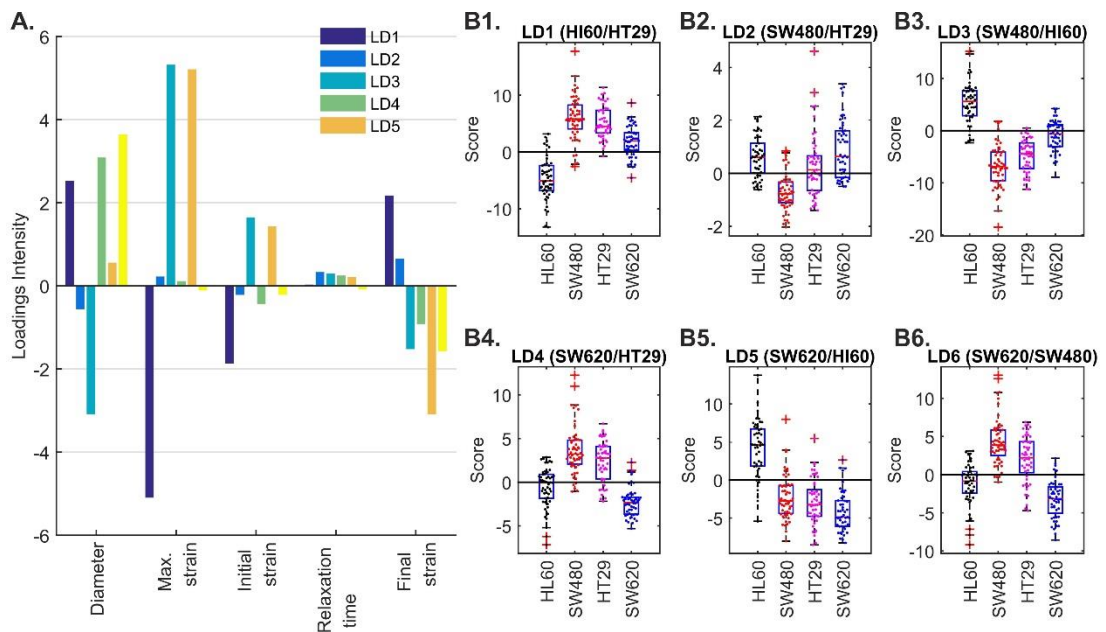


Figure 6.18 Linear discriminant analysis of 5 parameter datasets for HL60, SW480, HT29 and SW620 Where the bar plot (left) indicates the loadings for each of the linear discriminants (LD), and the box-plots/beeswarm plots (right) on the right correspond to the scores on each of the LDs. Analysis was performed by Julia Gala De Pablo.

Using the 5-fold LDA classification, summarised by the confusion matrix Table 6.6, we found that 82% of the HL60, 71% of SW480 and 85% of SW620 cells were correctly classified by the model. Comparatively, only 36% of HT29 were correctly classified with 39% incorrectly classified at SW480 and 20% incorrectly classified as SW620. The average correct

classification rate of the 4-class dataset was ~69%. These results show that >70% classification rate of SW480 and SW620, indicating significant differences detected from deformation and relaxation parameters. However, HT29 (the intermediate step of the CRC model) is generally harder to distinguish from the other CRC cell lines. This may be indicative of it having intermediate properties between the two.

Table 6.6 *k*-fold validation tests to classify the four cell lines (5-fold). Shows that 82% of the HL60 can be classified correctly as HL60, that 71% of SW480 were classified correctly and that 85% of SW620 were classified correctly. HT29 harder to classify (36%), the average classification of the four cell lines was $69 \pm 1\%$. The rows represent the actual cell type and the columns represent the predicted cell type.

	HL60	SW480	HT29	SW620
HL60	82 ± 3	2 ± 1	5 ± 1	10 ± 2
SW480	9 ± 1	71 ± 3	15 ± 2	5 ± 1
HT29	5 ± 2	39 ± 3	36 ± 3	20 ± 3
SW620	8 ± 2	2 ± 1	6 ± 1	85 ± 2

6.4 Discussion and Chapter Overview

Three CRC cell lines were used as a model system to study how mechanical phenotype changes with disease progression. Each cell line represents a different cancer stage: SW480 originate from a primary adenocarcinoma (Dukes stage B), HT29 originate from a more advance primary tumour (Dukes stage C), and SW620 are from a metastasis to the local lymphatic system (Dukes stage C). Cells were deformed in shear-dominant and inertia-dominant flow regimes as a function of flow rate (Figure 6.4 and Figure 6.8). In the *inertial* regime (Figure 6.11), for $Q < 300 \mu\text{l}/\text{min}$ the deformation index normalized by initial size, DI/A , was largest for SW620 cells and lowest for SW480 cells (HT29 was intermediate). For $Q \geq 300 \mu\text{l}/\text{min}$, cell lines could not be distinguished by DI/A . This behavior suggests that $Q \cong 400 \mu\text{l}/\text{min}$ represents the apparent cell *yield stress* (introduced in section 4.2.2). In chapter 5, we showed that disruption of the actin cytoskeleton using LatA lead to cell softening only at flow rates below the *yield stress* of SW480 cells [1]. Therefore, the CRC results suggest that cytoskeletal changes associated with progression, and actin breakdown above the *yield stress* results in no measurable changes to deformability under these flow conditions.

In the shear regime, the DI/A of SW620 was largest for the entire range of flow rates and SW480 was the lowest (Figure 6.7). The DI/A of HT29 was more similar to those of the SW620s for low flow rates, but the values approached those of SW480 cells for higher flow rates ($Q \geq 40 \mu\text{l}/\text{min}$). A larger value of DI/A is indicative of increased cell deformability. The

secondary tumour cells (SW620) being softer than the primary tumour cells (SW480) has been reported in previous works [117], [222]. Several papers report that SW620 cells have up-regulated genes associated with cytoskeletal alterations particularly related to actin structure. Which in turn, accompanies higher proliferation, increased motility, enhances invasive potential and reduced adhesion compared to SW480 [111]–[115].

It should be noted that characterising using deformation index, without adjusting for cell size, generally resulted in no significant differences between the cell types in either flow regime (Figure 6.4 and Figure 6.8). In the shear regime, the mean values of DI were within standard error of each other for all flow rates above 5 $\mu\text{l}/\text{min}$. Statistical t-tests showed a significant difference ($p < 0.0001$) between HT29 and SW480 and SW620 for the DI at 5 $\mu\text{l}/\text{min}$ (Figure 6.5). Whereas SW480 compared to SW620 showed no significance ($p > 0.05$). In the inertial regime, for $Q > 400 \mu\text{l}/\text{min}$ the SW480 cells had increased DI compared to HT29 and SW480. However, SW480 cells have the largest initial diameter which could make them appear more deformable above the *yield stress* where cytoskeletal rupture may occur. These results indicate that other deformation and relaxation parameters may better characterise and separate the different CRC cell lines.

Mechanical changes in the CRC model system were also studied by collecting single cell strain traces to perform multiparameter analysis (Figure 6.14), including fitting the Kelvin-Voigt model to averaged traces to find elastic modulus values (Figure 6.15). Table 6.3 showed that SW480 have a higher elastic modulus and a lower maximum strain ϵ_{max} compared to SW620, indicating that the secondary SW620s are softer. Palmieri *et al.* 2015 used AFM to measure the elastic modulus of SW480 and SW620 [117]. They also noted that SW480 have two appearances in culture, an epithelial-type (E-type) and rounded morphology. They found the elastic modulus of E-type SW480 to be 1060 Pa and R-type to be 580 Pa. The R-type value is within error of the reported value using microfluidic strain traces and the Kelvin-Voigt model. The mechanical properties of adhered cell types compared with detached can differ significantly, due to adhered cells containing stress-fibers and focal adhesions. Thus, the mechanical properties found using detached microfluidic deformation would intuitively be more similar to a cultured rounded morphology compared to epithelial-like. Additionally, they reported SW620 to have a lower elastic modulus, also indicating they are softer, also within error of our reported value. Therefore, SW620 still being softer than SW480 post-detachment suggests additional structural changes, not only stress fibers, occur within the cells with disease progression.

Tsrikitis *et al.* 2015 used AFM to measure the elastic modulus of SW480 and SW620, finding that SW620 are ~ 3 fold softer. However, they do not distinguish between the two

morphologies of SW480. Boccaccio *et al.* 2017 combined nanoindentation results with finite element models to study the hyperelastic behaviour of SW480 and SW620 [224]. They discussed that previously measured differences are purely a result of initial morphology as opposed to intrinsic structural changes. SW380R and SW620 showed comparable hyperelastic parameters whereas SW480E were stiffer. Tomita *et al.* 1992 found that SW480R and SW620 continue growth without anchorage (i.e. without attachment to a surface), whereas SW480E did not, which is indicative of lower stiffness [225].

SW620 cells have a smaller initial diameter compared to SW480 and HT29, however the ϵ_{max} and elastic modulus of SW620 and HT29 are comparable whereas SW480 is different. This suggests that as CRC progresses from Duke stage B (SW480) to stage C (HT29), where cells migrate toward the outer lining of the bowel, the cells undergo sub-structural changes leading to increased deformability. The similar mechanical properties between HT29 and SW620 may indicate that as cells metastasise from the outer lining to a secondary site (lymph node), changes to the cell structure are less essential.

Cell shape recovery after deformation was investigated using the final strain ϵ_{∞} . SW480 and HL60 cells recovered their original shape post-deformation ($\epsilon_0 \cong \epsilon_{\infty}$). Comparatively, HT29 and SW620 only recovered to a final strain of $\epsilon_{\infty} > 0.04$ which is significantly higher than their initial strain ($\epsilon_0 \cong 0$). Incomplete shape recovery may be indicative of a slower relaxation process occurring over a timescale longer than our experiment captures. Additionally, it could be a “permanent” deformation associated to “plastic” deformation (introduced in section 4.4). Cells commonly show a viscoelastic response to applied stress, however permanent plastic deformations have been seen to occur due to rupture of cytoskeletal bonds [86], [155]. SW620 and HT29 also have a shorter relaxation time τ_r compared to SW480, which may reflect a more active cytoskeleton.

Single cell analysis was also performed on individual strain traces of N=56 SW480 cells, N=49 HT29 cells, N=50 SW620 cells and also compared to N=50 HL60 cells. Two sample t-tests were used to measure the level of significance when using different parameters to characterise cell types, these included; A , ϵ_{max} , ϵ_{∞} , τ_r and ϵ_0 . p -values were obtained for each parameter between each cell type and summarised in Table 6.5 and Figure 6.6. The initial strain ϵ_0 of the four cell lines are within error of each other and show no significance ($p > 0.05$), additionally τ_d values were previously shown to be within error of each other (Table 6.3) and thus were not studied using SCA. Figure 6.17a shows statistical significance ($p < 0.05$) for separation of all cell lines using initial diameter A , apart from HT29 and SW480 which showed no significance ($p > 0.05$). Comparatively, using ϵ_{max} results in a significant p -value ($p < 0.05$) compared to both SW620 and HT29 (Figure 6.17b). This shows that even though SW480 and

HT29 cannot be distinguished by initial size, they can be better identified using deformation parameters. These results also verify previous discussions that SW620 and HT29 show similar mechanical responses.

Cell recovery was fitted with an exponential function used to extrapolate the final strain ε_∞ , with averages and p -values summarised in Figure 6.17c. Here, ε_∞ shows an extremely significant difference between SW480 and the other CRC cell lines ($p < 0.0001$), whereas SW620 and HT29 show no significance ($p > 0.05$). This furthers the trend that SW480 are mechanically different compared to later stage CRC cell lines HT29 and SW620. HT29 and SW620 show similar deformation and relaxation characteristics.

Figure 6.17d showed that τ_r is unable to distinguish between any of the CRC cell lines ($p > 0.05$). However, there is an extremely significant difference in τ_r between HL60 and each of the CRC cell lines ($p < 0.0001$). HL60 are a non-adherent leukaemia cell line and are softer than the CRC cell lines, and their relaxation time τ_r is ~ 3 fold longer. However, other deformation and relaxation parameters could distinguish the CRC cell lines (ε_{max} and ε_∞). Mechanical changes between SW480 and SW620 have previously been attributed to changes in actin structure [117], [226]. This could suggest that τ_r is less sensitive to cytoskeletal changes and could be dominated by nuclear mechanics instead. The nuclear diameter and nuclear ratio ($A_{nucleus}/A_{cell}$) of the four cell lines was shown by Table 6.1. The nucleus is the largest organelle and is known to be stiffer than the rest of the cell [84], [90]. Compared to the CRC cell lines HL60 have a smaller nucleus and nuclear diameter, which may factor towards its increased deformability and longer relaxation time. However, coupling between τ_r and ε_∞ makes it likely that response is more complex. HL60 and SW480 recovered their initial shape whereas HT29 and SW620 did not ($|\varepsilon_\infty| \neq |\varepsilon_0|$), suggesting longer relaxation processes may also be in play. Overall, the statistical t-tests showed that no individual parameter can significantly distinguish between all the cell lines. Thus, multiparameter analysis is necessary for accurate classification.

LDA was used to perform a 5-fold validation test on the four datasets (Table 6.6) which showed that HL60, SW480 and SW620 had reasonable classification rates ($< 71\%$). Only 36% of HT29 were correctly classified, 39% were incorrectly classified as SW480 and 20% as SW620. This result is likely due to HT29 and SW480 having a similar initial diameter, shown to be a dominant parameter in their classification (Figure 6.18). Additionally, multiparameter analysis and t-tests showed HT29 and SW620 have similar deformation and relaxation properties hence their difficulty to classify. As HT29 are the intermediate stage of the CRC system, their difficulty to classify against SW480 and SW620 may be indicative of this. The relatively low sample size is likely to have negatively affected classification rates ($49 < N < 56$).

In practice 1000s of cell events can be captured for a sample, however limiting factors due to data processing of collection and analysis of high speed videos prevented this. However, even using relatively small sample size the average classification rate was still ~69% for the four cell types. Therefore, larger datasets combined with multiparameter analysis is ideal for accurately classify different cell types.

Results in this chapter have shown that mechanical parameters can be used to distinguish between three CRC cell lines. Particularly, that cells tend to become softer with disease progression. Primary adenocarcinoma cell line SW480 have a similar cell size to advanced primary HT29 cells, however the deformation and relaxation properties of HT29 are more similar to further advanced cells SW620 (lymph node metastasis). Interestingly, relaxation time of the CRC cells did not significantly distinguish the CRC cell lines even though it showed an extreme difference to HL60 cells (non-adherent leukemia). Additionally, incomplete shape recovery was seen only in HT29 and SW620 suggesting additional relaxation processes of a permanent deformation due to internal filament rupture.

These results are the first example of using a mechanical microfluidic assay to distinguish between non-metastatic and metastatic CRCs, supporting the expectation that further advanced cells are more deformable due to cytoskeletal changes. Further, it was found that multiple physical parameters were required to distinguish between the four tested cell types. Single cell analysis has potential beyond bulk measurements for studying heterogeneity, for instance to identify a diseased population in a mixed sample. Results show that a high-throughput single cell technique combined with multiparameter analysis is necessary to further understanding of cancer progression, and to accurately classify samples of disease states.

7 Other applications of Deformation Cytometry

7.1 Non-Endocytic uptake of Quantum Dots

This chapter discusses the use of microfluidic cell deformations towards increasing non-endocytic uptake of Quantum Dots (QDs) into MCF7 cells. Cell deformation in microfluidic devices has been shown to create transient membrane pores allowing passage of macromolecules and nanoparticles across cell membranes by passive diffusion [61], [68], [227]. This topic was introduced in more detail in section 1.4.3.

The redox state of cells is regulated by redox couples (a reducing species and its corresponding oxidizing form), which are vital for many cellular processes. The ratio of redox couples can be an indicator of disease states, such as cancer. For example, the ratio of the redox pair Nicotinamide Adenine Dinucleotide (reduced, NADH; oxidised NAD⁺) is known to be shifted in breast cancer cell line MCF7 to a high ratio of NADH/NAD⁺. Thus, methods to measure the redox potential of cells have diagnostic applications. Ubiquinone-modified ligands in conjugation with QDs were reported to sense NADH [228]. Where the electron acceptor ubiquinone ligand reduces the NADH, and subsequently the QD emission is quenched. As such, an appealing use of QDs is their redox sensing abilities. A more detailed description of QDs for redox sensing can be found in the thesis of Harvie 2018 [229]. A hurdle in using QDs for redox sensing is that cells typically uptake QDs via endocytosis. QDs trapped inside endosomes are subject to a different chemical environment to the cytosol and thus cannot measure the true cell redox potential. For use as redox sensors a technique is needed to efficiently deliver QDs to the cell cytoplasm.

Here, DC was investigated as a method to achieve non-endocytic uptake of ~5 nm core-shell CdTe/CdS QDs into MCF7 cells. MCF7 were chosen as they display a particularly reduced redox state [230]. Both shear and inertial regimes were tested to investigate if a particular flow regime achieved more efficient delivery. Figure 7.1 is a schematic showing the concept of the method, deformation at the SP of a cross-slot may generate transient membrane pores allowing passive diffusion of QDs into the cell's cytoplasm. This work is in collaboration with the Critchley group in the Molecular and Nanoscale Physics department at the University of Leeds. Abiral Tamang synthesised and provided quantum dots and participated in deformation cytometry experiments, as well as developing and performing confocal fluorescence imaging method to measure QD uptake in cells using relative fluorescence measurements.

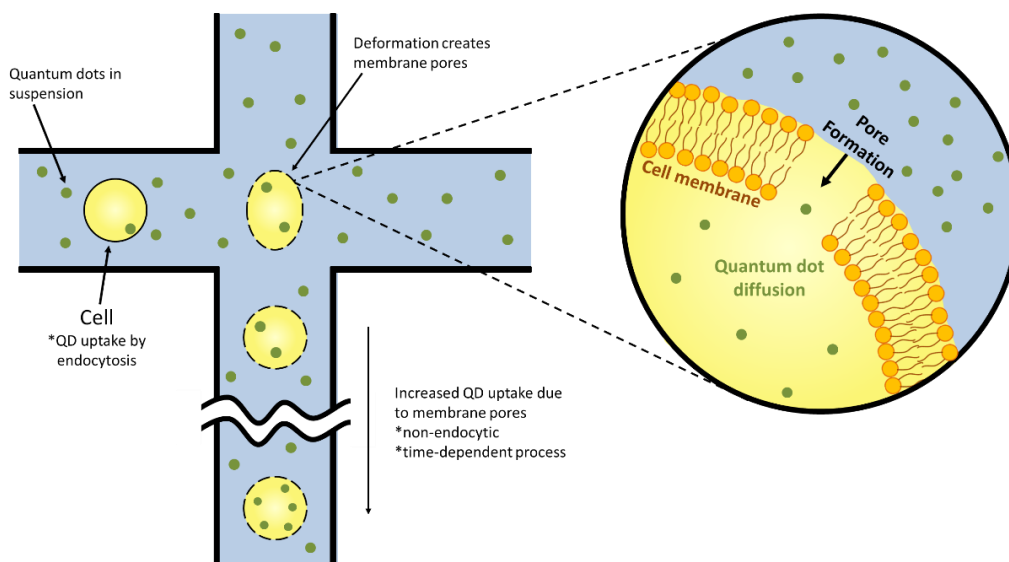


Figure 7.1 Schematic describing the passive diffusion of quantum dots through transient membrane pores in cells, due to deformation at the stagnation point of a cross-slot microfluidic device.

7.1.1 Shear Regime

The uptake of CdTe/CdS core/shell QDs was studied after cross-slot deformation in a shear-dominant regime ($\mu \approx 33$ cP) over a range of flow rates. Section 3.7.2 outlines the microfluidic uptake protocol. This involved suspending the MCF7 cells with QDs at a final concentration of 100 nM before passing them through the microfluidic device. After collection, samples were left to incubate for ~ 20 mins to allow passive diffusion of QDs through any transient membrane pores. Excess QDs were then washed by centrifugation, and QD uptake was measured using confocal fluorescence microscopy.

The deformation index DI was measured over the range of flow rates which is shown by Figure 7.2. Here, no velocity threshold was applied as all cells passed through the device were used for subsequent fluorescence measurements. The dataset is fitted with an exponential function (shown in red) which tends towards a maximum deformation index of $DI_{max} = 2.05 \pm 0.06$.

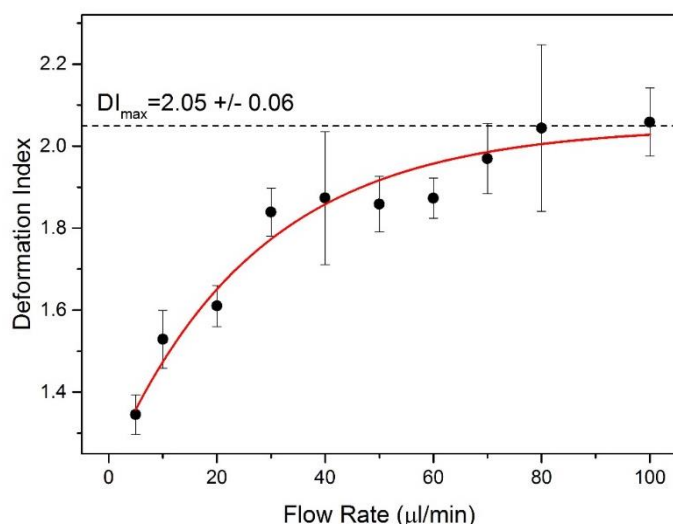


Figure 7.2 The deformation index DI of MCF7 cells as a function of flow rate in a shear-dominant regime ($\mu \cong 33$ cP), fitted with an exponential function.

The amount of QD uptake was quantified by taking confocal fluorescence images of samples measuring the fluorescence intensity of each cell, the image analysis was done as described in section 3.7.3. The total intensity was measured for samples over the range of flow rates, the experiment was then repeated ($N=3$) to obtain the mean average fluorescence per cell. Figure 7.3a shows a plot of mean fluorescence per cell as a function of flow rate which shows a linear trend, thus uptake increases as a function of flow rate. Comparatively, the deformation index as a function of flow rate was fitted with an exponential (Figure 7.2), and DI remained approximately constant for flow rates ≥ 75 $\mu\text{l}/\text{min}$. Interestingly, fluorescence intensity continued to increase linearly for > 75 $\mu\text{l}/\text{min}$. This suggests that even at maximum stretch increasing the flow rate continues to improve uptake, suggesting that more transient pores are formed or bigger or longer lasting pores are formed.

Figure 7.3b shows that cell viability is $>80\%$ for flow rates up to <125 $\mu\text{l}/\text{min}$. However, a significant viability drop occurs for flow rates >125 $\mu\text{l}/\text{min}$ with only 62.4% viability for 175 $\mu\text{l}/\text{min}$. Thus, 100 $\mu\text{l}/\text{min}$ was able to achieve most uptake without a resulting significant drop in viability. Figure 7.3c shows density scatter plots of fluorescence intensity as a function of cell area ($\sim \frac{A^2}{2}$) comparing the incubated control sample (i) with the sample deformed at the optimum condition 100 $\mu\text{l}/\text{min}$ (ii). The incubated control (i) shows a linear relationship between fluorescence intensity and cell size and is fitted with a straight line (black line). The deformed sample shows deviation from the initial linear fit (shown in black), with the majority of the population having increased fluorescence intensity, and a general increase in scattering can be seen. A linear fit to the deformed sample (shown in red) further highlights the increased uptake due to microfluidic deformation. The majority of the deformed cell population shows increased fluorescence intensity compared to the control, which suggests good QD uptake

efficiency. Such that, if efficiency was low we may expect to see a subpopulation similar to the distribution shown by the incubated control (i).

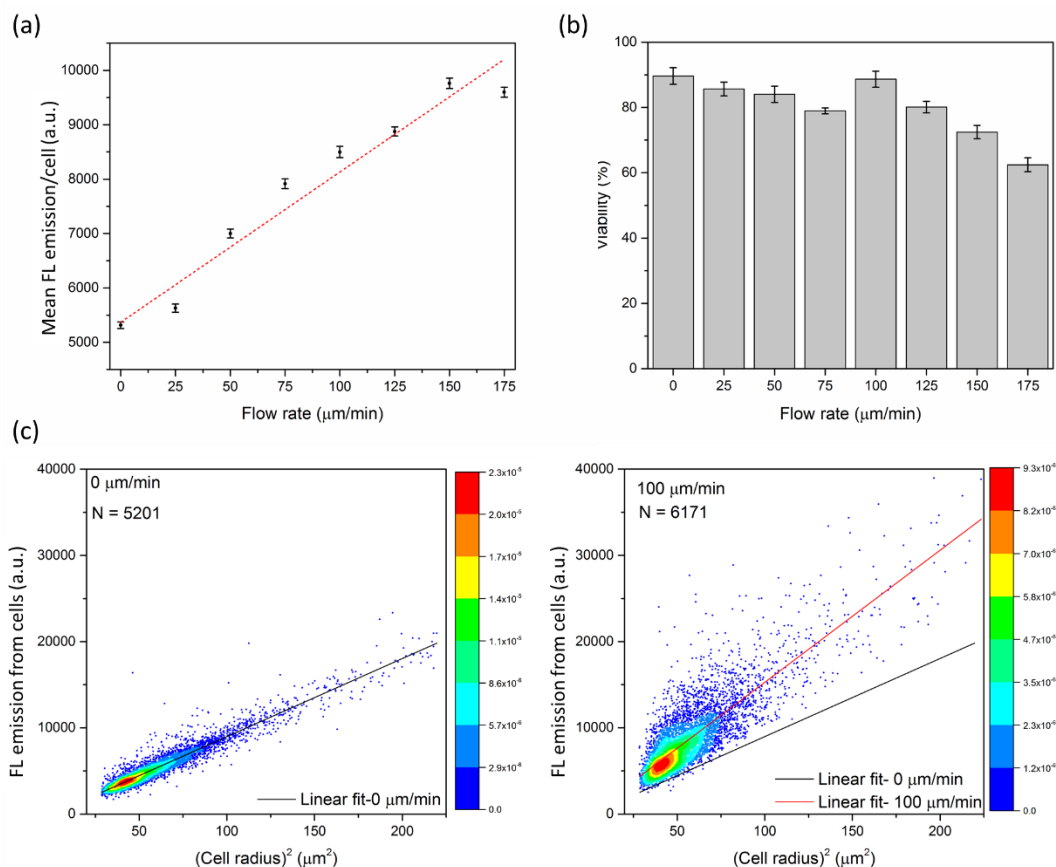


Figure 7.3 QD uptake analysis of MCF7 cells microfluidically deformation whilst suspended with 100 nM of QDs in a shear-dominant regime ($\mu \approx 33$ cP). (a) The average fluorescence emission per cell as a function of flow rate. (b) The cell viability after deformation and incubation with QDs as a function of flow rate using an MTT assay. (c) Density scatter plots of fluorescence emission of uptaken QDs in cells for (i) a control sample which was not deformed (0 μ l/min) and (ii) a sample deformed at 100 μ l/min. Data was acquired and analysed by Abiral Tamang who provided these figures.

Examples of confocal fluorescence images of MCF7 are provided in Figure 7.4. This includes a sample that was deformed in the shear regime at 100 μ l/min whilst incubated with 100 nM of QDs, compared to a control sample which was not treated by the microfluidic device but was also incubated with 100 nM of QDs for the same length of time. The images show a general increase in fluorescence intensity for the deformed sample. Additionally, fluorescence in the control sample is localised to small “dots” which is indicative of uptake occurring via endocytosis. Comparatively, the deformed sample shows more distributed fluorescence throughout the cells which is indicative of cytosolic uptake.

Overall, image analysis showed an increase in the average fluorescence intensity per cell as a function of flow rate indicating that microfluidic deformation in the shear-dominant regime increases QD uptake into cells. Fluorescence imaging provides further evidence that the

increased uptake is due to QDs within the cytoplasm due to the formation of transient membrane pores, in addition to any endocytotic processes.

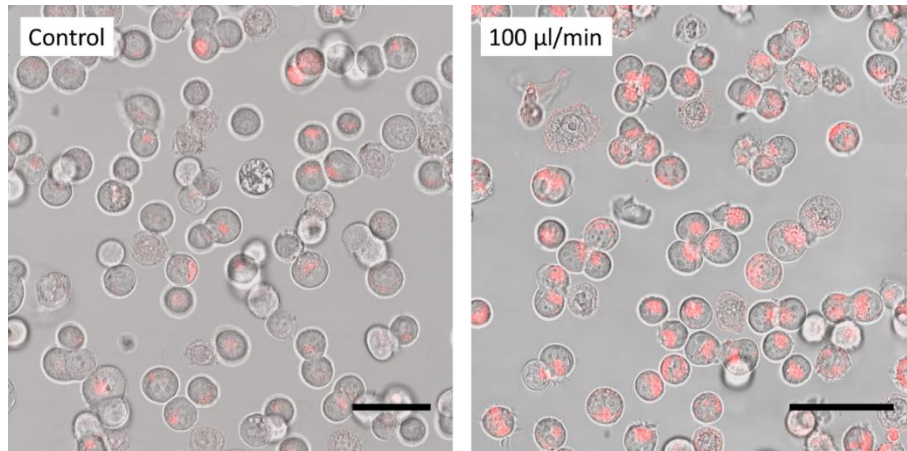


Figure 7.4 Confocal fluorescence images of MCF7 cells with QD uptake, showing QD emission in red overlaid onto bright field images. Comparing a sample which was microfluidically deformed at 100 $\mu\text{l}/\text{min}$ in the presence of QDs (100 nm), and a control sample which was not deformed but was incubated with QDs. Scale bars 100 μm . Images were provided by Abiral Tamang.

7.1.2 Inertial Regime

Cross-slot deformation in the shear-dominant regime showed increased cytosolic uptake of QDs. Uptake was also studied in the inertia-dominant regime at four different flow rates. Based on our previous inertial regime deformation studies (HL60, SW480, HT29, SW620 in sections 4.2.2 and 6.2.2) the apparent *yield stress* of cells occurs at $\sim 300\text{-}400$ $\mu\text{l}/\text{min}$. Thus, for this study flow rates below (100 $\mu\text{l}/\text{min}$), at (400 $\mu\text{l}/\text{min}$) and above (500 and 600 $\mu\text{l}/\text{min}$) were chosen to test cytosolic QD uptake. Figure 7.5 shows the deformation index DI as a function of Q . Results follow the behaviour observed in the inertial regime for HL60 and CRC cell lines, with no significant change in DI above 500 $\mu\text{l}/\text{min}$. This suggests the maximum deformation has been reached and cells could be near to their *failure point*. The DI at 600 $\mu\text{l}/\text{min}$ is $DI = 1.91 \pm 0.07$ which is still less than $DI_{max} = 2.05 \pm 0.06$ in the shear-dominant regime.

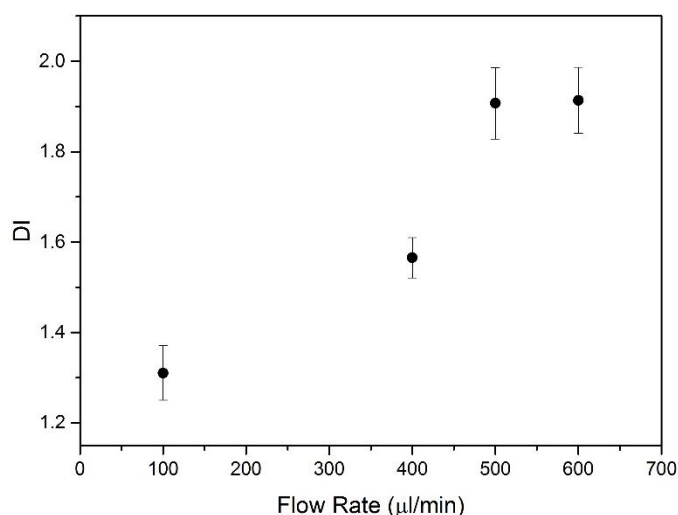


Figure 7.5 The deformation index DI of MCF7 cells as a function of flow rate. Cells were deformed in an inertia-dominant regime where $\mu \sim 1$ cP.

Microfluidic uptake experiments in the inertia-dominant regime were conducted as described in section 4.2.2. Confocal fluorescence was used to collect both bright field and fluorescence images of the cells after incubation with QDs and treatment with on-chip deformation. Uptake was measured by calculating the mean and median fluorescence per cell for deformations at four flow rates and a control sample (same QD incubation time without microfluidic deformation treatment). The median was measured to highlight any skew that may be caused by a small proportion of cells with extremely high fluorescence (i.e. due to dead cells with highly compromised cell membranes). The experiment was repeated ($n=3$) and the average of the mean and median values were plotted as a function of flow rate, shown by Figure 7.6.

Both the mean average (Figure 7.6a) and median average (Figure 7.6b) fluorescence per cell are essentially constant as a function of flow rate, both graphs are fitted with a linear fit with the gradient set at 0 (shown in red). These results suggest that inertia-dominant deformation of MCF7 did not increase cytosolic uptake of QDs, and that uptake was dominated by endocytosis. Comparatively, the shear-dominant regime did show increased cytosolic uptake as a function of flow rate, which may indicate shear forces and deformation at lower strain rates is more efficient at forming transient membrane pores.

Figure 7.7a shows example density scatter plots of the fluorescence intensity per cell as a function of cell area, for MCF7 microfluidically deformed at 500 $\mu\text{l}/\text{min}$ compared to the purely incubated control sample. Both graphs show a linear relationship between uptake and cell size, similar to in the shear regime (Figure 7.2), and linear fits are shown in red. The control sample shows more scatter and higher number of outliers with high fluorescence. This is partly due to the larger sample size for the control compared to the deformed sample (>4 fold). Additionally, dead cells with compromised membranes are known to uptake a large

amount of the QDs, the 500 $\mu\text{l}/\text{min}$ condition may have destroyed these cells during treatment with the microfluidic device. The slope of the control sample was 46.9 ± 1.9 and of the deformed sample was 45.0 ± 2.0 . Further, both fluorescence intensity datasets are plotted as histograms which show a single peak and are fitted with Lognormal functions ($R^2 \approx 0.97$). The peak of the control sample was 2577 ± 21 and of the deformed sample was 2644 ± 26 . This data corroborates that microfluidic deformation in the inertial regime did not significantly increase QD uptake in MCF7 cells.

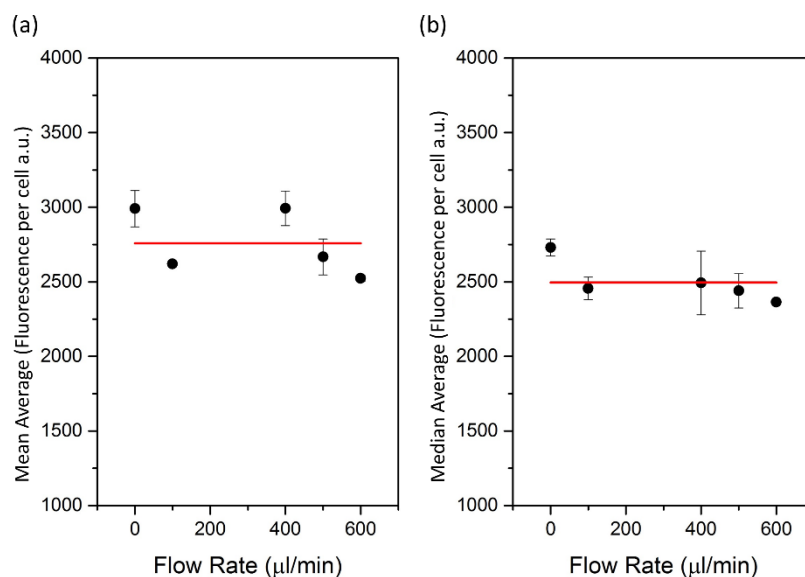


Figure 7.6 Uptake of QDs in MCF7 cells deformed in a cross-slot device whilst suspended in media ($\mu\sim 1$ cP) with 100 nM QDs, the fluorescence of each cell was then measured to quantify QD uptake as a function of deformation. (a) The experiment was repeated $n=3$ and an average of the mean values for each experiment was plotted as a function of flow rate. (b) For the same datasets the median fluorescence per cell was found, then the average of the median values was plotted as a function of flow rate.

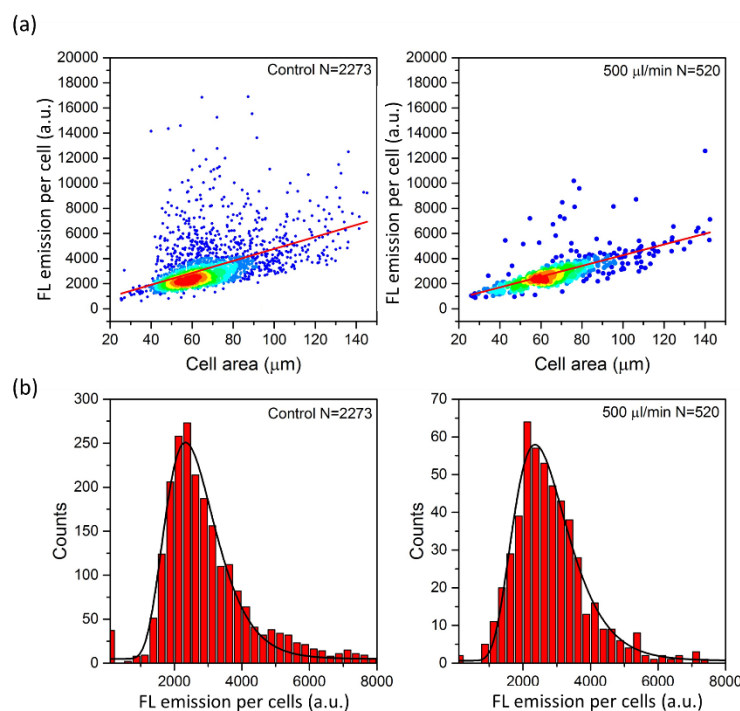


Figure 7.7 Analysis of uptake of MCF7 cells deformed in a cross-slot whilst suspended with 100 nM of QDs ($\mu\approx 1$ cP). (a) Density scatter plots of fluorescence intensity in cells due to QD uptake for a control sample which was not deformed (0 $\mu\text{l}/\text{min}$) and a sample deformed at 500 $\mu\text{l}/\text{min}$. (b) Histograms of the fluorescence intensity per cell for a control sample and a sample deformed at 500 $\mu\text{l}/\text{min}$.

7.1.3 Constriction channel control

The cross-slot geometry used throughout the thesis was described in detail in section 3.2.1, before deforming at the SP cells travel through a channel with a width of 35 μm . At higher flow rates in the shear-regime, shear forces due to confinement in the channel can induce bullet-like cell deformations (similar to those used by the Guck group in RTDC [33]). An example image of this can be found in Figure 7.8bi. Additionally, increased cytosolic uptake of QDs has been seen for constriction channel geometries (where channel width is smaller than initial cell diameter) [65]. Thus the cytosolic uptake seen in the shear-regime may be partly due to the bullet-like deformations before/after extensional flow junction. Also, deformation at the SP did not lead to cytosolic uptake in the inertial-regime which suggests shear forces dominate transient pore membrane formation.

To decouple shear-induced deformation by confinement and extensional flow deformation at the SP, a serpentine channel was designed to replicate our devices without the extensional flow junction. This device was described in detail in section 3.2.2, cells travel through a serpentine with the same inlet/outlet dimensions of the cross-slot including being the same length. This device was then used to measure QD uptake at three flow rates compared to a control (incubated without microfluidic device treatment). Considering the initial cross-slot design had one inlet port which separated into two orthogonal channels to create the

extensional flow junction, the equivalent volumetric flow rates set on the syringe driver were half for the serpentine compared to the cross slot. For example, the largest flow rate tested on the serpentine was 75 $\mu\text{l}/\text{min}$ which is equivalent to using 150 $\mu\text{l}/\text{min}$ on the cross-slot device to achieve the same flow velocity.

The deformations in the serpentine channel were measured using high speed imaging at three flow rates. As deformations were asymmetrical, deformability was characterised by two parameters the deformation index DI and the circularity D_C . These were first introduced in section 3.5.3 and are also shown in schematics in Figure 7.8a. Figure 7.8b shows DI at a function of flow rate and is fitted with an exponential function. This suggests that stretching in the direction of flow tends to a maximum value. Figure 7.8c shows D_C as a function of flow rate, which is fitted with a linear fit. This shows that even though stretching has reached a maximum the circularity continues to deviate over this flow range. This is likely due to the bullet-like shape, at higher flows the back of the cell can become concave which would further increase D_C .

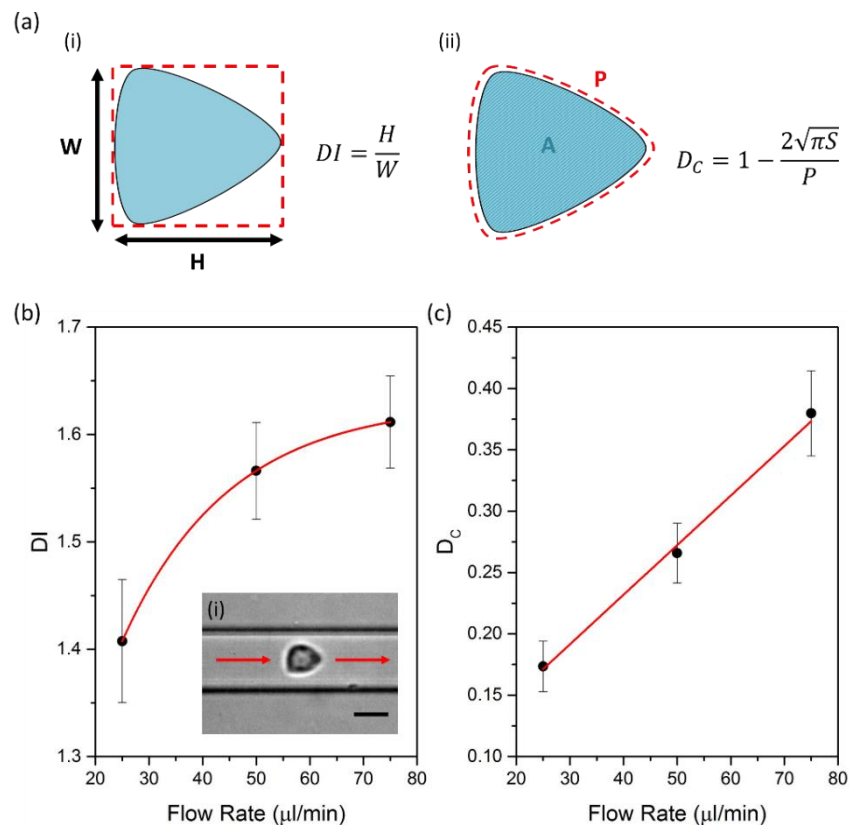


Figure 7.8 Shape analysis of cells deformed in a constriction channel. (a) Diagrams showing how the deformation due to shear in a constriction channel was quantified. Using both deformation index and the circularity. (b) A graph of DI at a function of flow rate for MCF7 cells deformed by shear in a constriction channel ($\mu \approx 33$ cP). (i) An example of image of the bullet-like deformation. (c) A graph of D_C as a function of flow rate for the same dataset.

Uptake experiments using the serpentine device were conducted following the same protocols as the cross slot device. Cells treated microfluidically and a control sample were then imaged using confocal fluorescence microscopy, and a customised Matlab code measured the fluorescence of individual cells (section 3.7.3). The mean and median fluorescence per cell was measured, the experiment was repeated ($n=3$) and the average of the mean and median values was calculated and plotted as a function of flow rate (Figure 7.9).

The mean average (Figure 7.9a) and the median average (Figure 7.9b) show no significant change in fluorescence per cell as a function of flow rate. Both graphs are fitted linearly with the slope fixed at 0 (shown in red). These results suggest that bullet-like deformations due to shear confinement are not sufficient to increase cytosolic uptake of quantum dots. Thus, it is the extensional flow induced deformation of the cross-slot which led to increased cytosolic uptake in the shear-dominant regime (Figure 7.3).

Figure 7.10a shows density scatter plots of the fluorescence intensity per cell as a function of cell size, for cells microfluidically deformed in a serpentine channel at $75 \mu\text{l}/\text{min}$ compared to an undeformed control sample. Both graphs show a linear relationship between intensity and cell size, with no noticeable changes or increase in uptake for the deformed sample. The fluorescence intensity datasets are also plotted as histograms (Figure 7.10b), which are both fitted with a single peak Lognormal. The peak center of the control sample was 499.9 ± 1.6 and the deformed sample was 430 ± 1.5 . These results also indicate no significant improvement in uptake due to constriction deformation using a high viscosity buffer ($\mu \approx 33 \text{ cP}$).

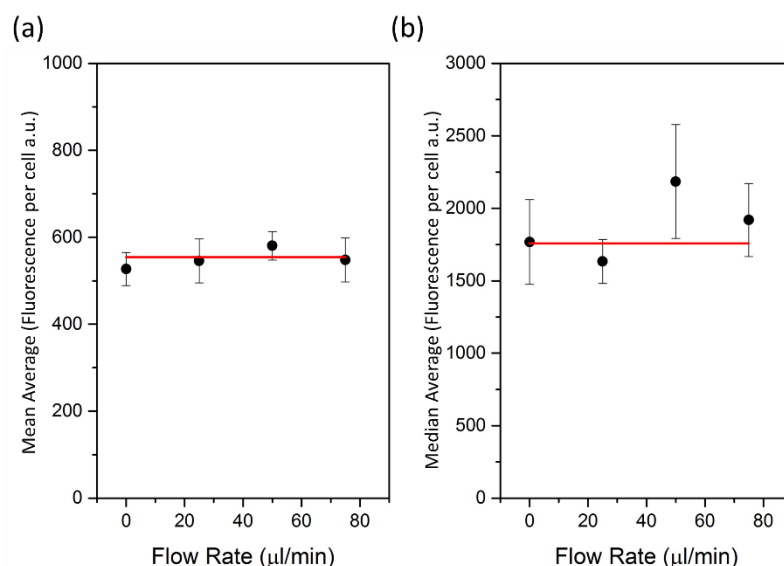


Figure 7.9 Uptake of QDs into MCF7 cells deformed in a constriction channel ($\mu \approx 33 \text{ cP}$) with 100 nM QDs, the fluorescence of each cell was then measured to quantify QD uptake as a function of deformation. (a) The experiment was repeated ($n=3$) and an average of the mean values was plotted as a function of flow rate. (b) The median fluorescence per cell was also found, then the average of the median values was plotted as a function of flow rate.

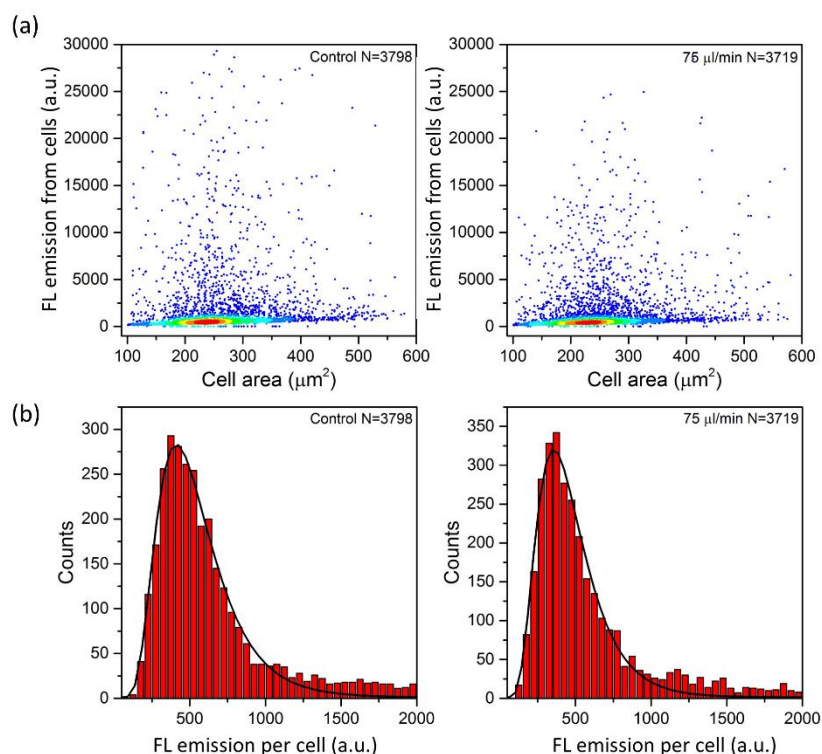


Figure 7.10 Analysis of uptake of QDs in MCF7 cells deformed in a constriction channel whilst suspended with 100 nM of QDs ($\mu \approx 33$ cP). (a) Density scatter plots of fluorescence intensity in cells due to QD uptake for a control sample which was not deformed (0 μ l/min) and a sample deformed at 75 μ l/min. (b) Histograms of the fluorescence intensity per cell for a control sample and a sample deformed at 75 μ l/min.

7.1.4 Uptake by incubation

Sections 7.1.1 and 7.1.2 presented results for QD uptake as a function of flow rate in shear-dominant and inertia-dominant regimes in a cross-slot device. These results were compared to undeformed control samples which were suspended in the high viscosity PBS-MC buffer ($\mu \approx 33$ cP) for the shear regime or suspended in media for the inertial regime ($\mu \sim 1$ cP). It was noticed from these that the control sample in the shear regime appeared more fluorescent than the control for the inertial regime. This effect was further investigated. MCF7 were incubated in media or PBS-MC with 100 nM of QDs for 20 mins. Cell suspensions were then washed by repeated centrifugation at 100 g for 5 mins ($n=3$) to remove excess QDs, as described in section 3.7.2. Samples were then imaged using confocal fluorescence and the fluorescence per cell was measured, similar to the procedure in 7.1.1 and 7.1.2. The sample originally incubated in media will be referred to as the *inertial control*, and the sample incubated in PBS-MC referred to as the *shear control*.

Figure 7.11 a(i) and b(i) show low magnification fluorescent images of QD uptake in the *shear control* and *inertial control*. These images show a large number and were taken using the same image settings and have not been adjusted for brightness or contrast. It is apparent that the

shear control shows increased fluorescent intensity compared to the *inertial control*. Figure 7.11 a(ii) and b (ii) show higher magnification images of both samples where the fluorescent images are overlaid onto bright field images. Fluorescence in the *inertial control* image is mostly showed as bright dots which is indicative of QDs localised in endosomes. The *shear control* image also shows bright dots but also some more diffuse fluorescence is present which may represent QDs in the cytoplasm.

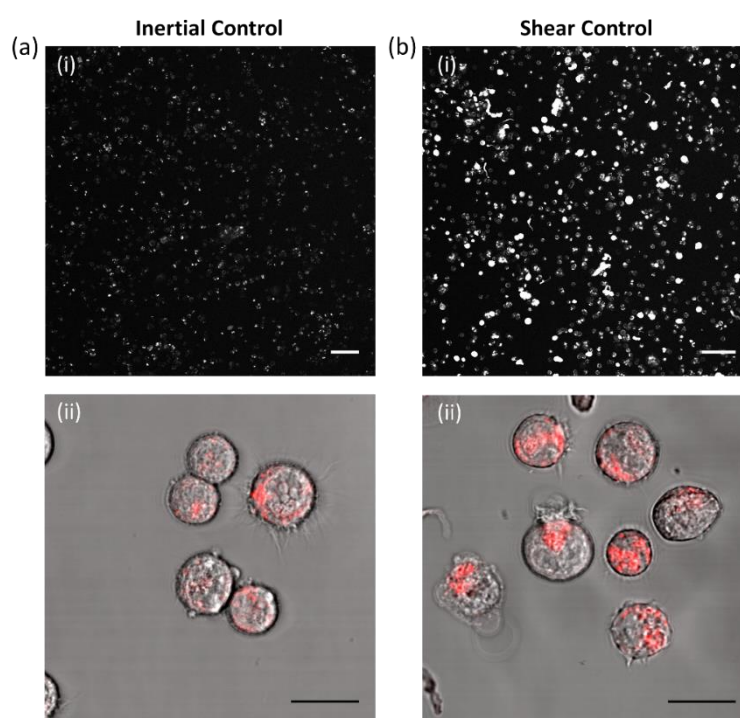


Figure 7.11 Confocal images of QD uptake in MCF7 cells of the inertial and shear controls. (a i) A low magnification fluorescent image of QD uptake in the inertial control sample. Scale bar is 100 μm . (ii) An overlaid fluorescent image of uptake in the inertial control sample, the bright spots are indicative of endocytic uptake. Scale bar is 20 μm . (b i) A low magnification image of uptake in the shear control sample (scale bar 100 μm). (ii) An overlaid fluorescent image of uptake in the shear control sample, bright spots indicating endocytic uptake are present but also some diffuse fluorescence more likely to be cytosolic uptake.

The fluorescence per cell was measured from low magnification fluorescence images of the *inertial control* and the *shear control*. Statistical measurements were done to quantify any significant changes in QD uptake between the samples, including histograms and boxplots (Figure 7.12). Experiments were repeated to obtain mean average and median average values of fluorescence per cell (N=4 for the *inertial control*) and (N=3 for the *shear control*). Figure 7.14a shows histograms of both samples which are fitted by Lognormals. The peak center of the *inertial control* was 2794 ± 14 and of the *shear control* was 3160 ± 51 , showing a ~ 1.1 fold increase in peak fluorescence per cell in the shear control. Additionally, the shear control

showed a wider distribution as the standard deviation of the fit was $w = 0.473 \pm 0.014$ compared to $w = 0.361 \pm 0.004$ for the inertial control.

Figure 7.12b shows a box-plot of the fluorescence per cell of the inertial control and shear control. Here, the box extends the 25th to 75th percentiles and the whiskers extend the 10th-90th percentile. The line through box shows the mean fluorescence per cell and the square shows the median value. The box-plot shows a small increase in the median value of the *shear control* and a much larger increase in the mean value. It also shows a much wider distribution for the *shear control*, which is skewed towards much higher values of fluorescence per cell. This can be seen in the fluorescent images as a small number of cells appear significantly brighter in the *shear control* (Figure 7.11). Figure 7.12b (i) shows a table of mean average and median average values of fluorescence per cell taken from the experimental repeats of the *inertial control* (N=4) and *shear control* (N=3). The mean average of the shear control shows a ~2.1 fold increase compared to the inertial control, and the median also shows a ~1.3 fold increase. Overall, the consensus shows that the *shear control* has higher fluorescence indicating increased uptake of QDs.

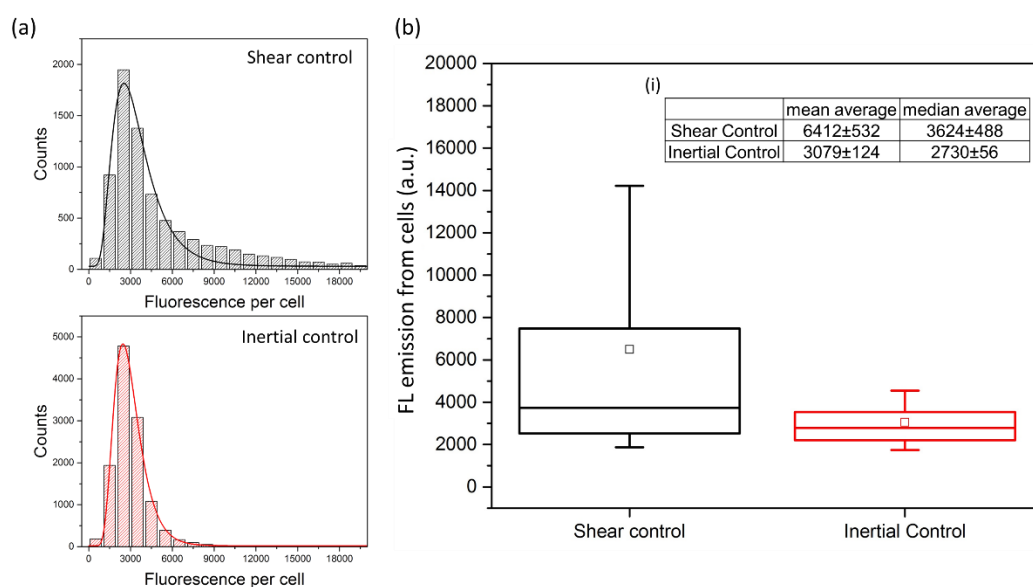


Figure 7.12 (a) Histograms of the fluorescence per cell for the inertial control and the shear control, showing the distribution of QD uptake in MCF7 cells. (b) A boxplot of the fluorescence per cell for the inertial control and the shear control. Where the box extends the 25th to 75th percentile with a line representing the mean and square representing the median, the whiskers extend the 10th to 90th percentiles. (i) Shows the mean and median average fluorescence per cell from the experimental repeats of the inertial control (N=4) and the shear control (N=3).

Increased uptake in the *shear control* likely indicates that additional stresses on the cells during the incubation and washing steps leads to formation of transient membrane pores and additional QD uptake. As these cells are suspended in a higher viscosity buffer they will

experience increased shear forces during the centrifugation steps for washing and from gentle pipetting to resuspend the cells after pelleting. Figure 7.6 showed that microfluidic deformation using the cross-slot can lead to a further ~1.8 fold increase in the mean fluorescence per cell.

7.1.5 Discussion

Microfluidic deformation was investigated as a method to increase cytosolic uptake of QDs into MCF7 cells. Delivery of QDs into the cytosol, as opposed to endosomes, is important for the development of QDs as redox sensors which has potential applications in cancer diagnosis. Firstly, cells were deformed using a cross-slot device in a shear-dominant regime ($\mu\approx 33$ cP) and this showed a linear increase in uptake as a function of flow rate (Figure 7.3). Confocal fluorescence images suggest QDs located in the cytosol after cell deformation, whereas controls incubated with QDs showed them to be localised to endosomes (Figure 7.4). A flow rate of 100 $\mu\text{l}/\text{min}$ proved optimum as it induced the most uptake without significantly decreasing cell viability. Measurements of the deformation index showed that even through DI_{max} was reached for flow rates $\geq 75 \mu\text{l}/\text{min}$, QD uptake continued to increase linearly up to 150 $\mu\text{l}/\text{min}$. Thus, continued increase of the flow rate further increases the stress on the cell which either creates more pores or increases the size of the pores regardless of the cell being at maximum stretch (DI_{max}).

For the optimum condition of 100 $\mu\text{l}/\text{min}$ the mean fluorescence emission per cell was ~1.7 fold greater than for the control sample. Density scatter plots (Figure 7.3c) show the majority of the population of deformed cells show increased emission compared to the control sample, indicative of high efficiency of cytosolic uptake. However, more robust methods are needed to accurately quantify uptake efficiency. Lee *et al.* 2012 used constriction channels ($W < A$) to achieve cytosolic delivery of QDs into cells. They engineered a nanoparticle which changed emission profile when interacting with the reducing environment of the cytosol, and used this to quantify uptake efficiency. Using flow cytometry they found ~35% of the cells deformed through the constriction channels had successful cytosolic delivery.

The same group delivered a range of materials into 11 cell types, and showed that increased cell speeds, reduced constriction dimensions, and repeating constrictions lead to increased uptake efficiency [66], [67]. They also elucidated the mechanism of uptake by adding 3 kDa dextran beads at varying time points after microfluidic treatment, showing 70-90% of delivery occurs within the first minute, supporting that transient membrane pores allow passive diffusion of material. Further tests were done to support that membrane disruption leads to material exchange both in and out of the cell. Bi-directional transport was investigated by three treatment cycles using dextran beads. Firstly, cells were microfluidically treated in the

presence of dextran and then washed, which showed net diffusion of dextran into the cells. Next, the same cells were microfluidically treated without the presence of dextran in the suspension media which showed a net reduction of dextran out of the cells. Finally, the cells were treated a third time again in the presence of dextran which again showed net uptake. A 2D diffusion COMSOL model was used to replicate these experimental results. Passive diffusion across a porous membrane with a set membrane diffusivity showed good agreement with the three-cycle test. However, this model offers no insight into pore size, number of pores or pore lifetime, additionally the stress on a constrained cell is not homogeneous which may cause heterogeneity in pore location.

The use of a constriction channel (where channel width is less than initial cell size) also resulting in 50-90% of the initial number of cells recovered after microfluidic treatment, contributed by cell sticking and clogging within the device. Additionally, even though increasing constriction length and decreasing width led to increased uptake efficiency it also reduced the number of recovered cells. Therefore, using hydrodynamic deformation does not require such dramatic cell confinement and would likely improve recovery and reduce clogging.

No significant increase of QD uptake into MCF7 cells was seen using a constriction channel (wider than the initial cell size) in a shear-dominant regime (Figure 7.9). This result suggests that the shear stress due to confinement is not sufficient to generate pores for passive diffusion of material, converse to extensional deformation at the cross-slot. Physical confinement was shown to increase uptake of QDs [65], likely due to imparting larger membrane deformations but could also be due to additional friction between the cell membrane and channel walls.

The inertia-dominant regime in the cross-slot device also showed no significant improvements to the uptake of QDs into MCF7 cells. This is in disagreement with other studies which show improved uptake of various macromolecules and nanoparticles using highly inertial microfluidic deformation. Chung's lab developed the inertial microfluidic cell stretcher (iMCS), where cells are deformed using a T-junction and endure direct contact with the channel wall ($Re > 100$) [54]. Uptake efficiency was increased further with the addition of a sharp-tip located where the cell deforms [68]. The use of high-flow speeds and direct contact with the solid channel likely imparts more stress compared to hydrodynamic deformation at the SP. However, more recently this group have opted for a cross-slot device in an inertial flow regime (as introduced by Di Carlo *et al.* [27]) referred to as a *Hydroporator* [231]. The *Hydroporator* study achieved delivery of a range of macromolecules to 10 cell types, including MCF7, with up to 90% delivery efficiency. This included delivery of 2000 kDa Dextran beads (~50 nm) at ~60% delivery, comparatively QDs are ~5 nm in size. Their study

showed correlation between cell deformability and delivery efficiency, and out of the 10 cell lines tested MCF7 proved least deformable and had lowest uptake efficiency of 3-5 kDa beads (~25%). Additionally, surface chemistry of NPs likely affects delivery efficiency and QD uptake has not previously been reported in studies using inertial microfluidics.

Finally, incubated controls of MCF7 with QDs using low viscous cell media (*inertial control*) and high viscosity PBS-MC (*shear control*) showed an increase in QD emission for the *shear control* (Figure 7.12). This result suggested that during incubation, washing and resuspension steps, in a high viscosity environment, additional stresses may lead to passive diffusion of material via transient pores. Centrifugation of the cell samples imparts drag forces whilst the cells sediment into a pellet, the drag force and sedimentation rate can be estimated and compared for the *inertial control* and the *shear control*.

The drag force F_{drag} on a sphere can be calculated using Stokes law equation 7.1, which was used to estimate the shear forces on a cell being centrifuged at 100 g. F_{drag} is proportional to the sedimentation velocity v shown by equation 7.2, when A is the cell diameter, ρ_{cell} is the cell density, ρ_{media} is the media density, μ is the viscosity and g is the gravitational force. For the *inertial control* $\rho_{media} = 1000 \text{ kg/m}^3$ and $\mu = 1 \text{ cP}$, and for the *shear control* $\rho_{media} = 1005 \text{ kg/m}^3$ and $\mu = 33 \text{ cP}$. The diameter of MCF7 was estimated as $18 \text{ }\mu\text{m}$ and the cell density as $\rho_{cell} \approx 1080 \text{ kg/m}^3$ (estimated to be the same as HeLa cells [232]). Thus, the drag force on an MCF7 cell centrifuged at 100 g for the *inertial control* was $F_{drag} = 0.24 \text{ nN}$ and for the *shear control* was $F_{drag} = 0.22 \text{ nN}$. Thus, a similar drag force is experienced in both regimes due to the relatively small change in the density of the medium. However, as sedimentation rate is inversely proportional to viscosity and proportional to the change in density the cells in the inertial regime sediment ~35 times faster than those in the shear regime. This means that for a cell to fall ~1 cm from the top of a sample in an Eppendorf to pellet at the bottom would take ~7 s for the *inertial control* compared to ~4 min for the *shear control*. Thus, the cells in the *shear control* are subject to drag forces for a longer time allowing more opportunity for passive diffusion of the QDs through transient membrane pores.

$$F_{drag} = 6\pi\mu Rv \quad 7.1$$

$$v = \frac{A^2(\rho_{cell} - \rho_{media})g}{18\mu} \quad 7.2$$

This theory could be investigated further by quantifying QD uptake in cells centrifuged as a function of; medium viscosity, centrifugation force and centrifugation time. Additionally, altering sedimentation distance whilst maintaining viscosity would further confirm the theory. The use of centrifugation would have certain advantages over microfluidics due to reduced

time, ease of operation and potential for bulk volumes to be tested. However, as cells would be initially suspended throughout the sample the sedimentation time would always be distributed which may affect uptake efficiency. Thus, microfluidics offers a controlled force environment for each individual cell and has shown potential for high efficiency cytosolic uptake (>90%) [231].

To conclude, the use of a cross-slot microfluidic device in the shear-dominant regime showed increased QD uptake into MCF7 cells with evidence that QDs entered through transient membrane pores and were present throughout the cytosol of cells. Comparatively, these studies showed that a constriction channel geometry and cross-slot inertial-regime did not significantly improve QD uptake. Deformation cytometry for cytosolic uptake is advantageous compared to traditional techniques (such as electroporation, sonoporation or microinjection) due to being; high throughput, label-free, maintaining high viability and requiring no external fields of ultrasound. Further studies are needed to quantify uptake efficiency (such as flow cytometry), however the method shows potential for the study of QDs for measuring redox potential in cells.

7.2 DC for probing the mechanoresponse of Piezo1

Cell membranes contain protein ion channels which are activated under certain stimuli, forming temporary pores allowing ions to pass across the membrane. Mechanical deformation is one such stimuli, and an example of a mechanosensitive ion channel (MSC) is Piezo1 which is a ~286 kDa transmembrane protein. Piezo1 can be stimulated by mechanical force, including membrane tension and actomyosin contractile forces [233], [234], activated Piezo1 are permeable to Na⁺, K⁺, and Ca²⁺. Figure 7.13 shows a simplified schematic of Piezo1 activation. Pathological significance has been noted in Piezo1, including mutations linked to haemolytic anaemia [235] and autosomal recessive congenital lymphatic dysplasia [236], as well as contributing to metastases by facilitating cell escape from a monolayer [237]. Piezo1 can be studied by the agonist Yoda1 (discovered in 2015 [186]), which provides a chemical trigger to open the channel, allowing research into Piezo1 activation without need for mechanical stimuli.

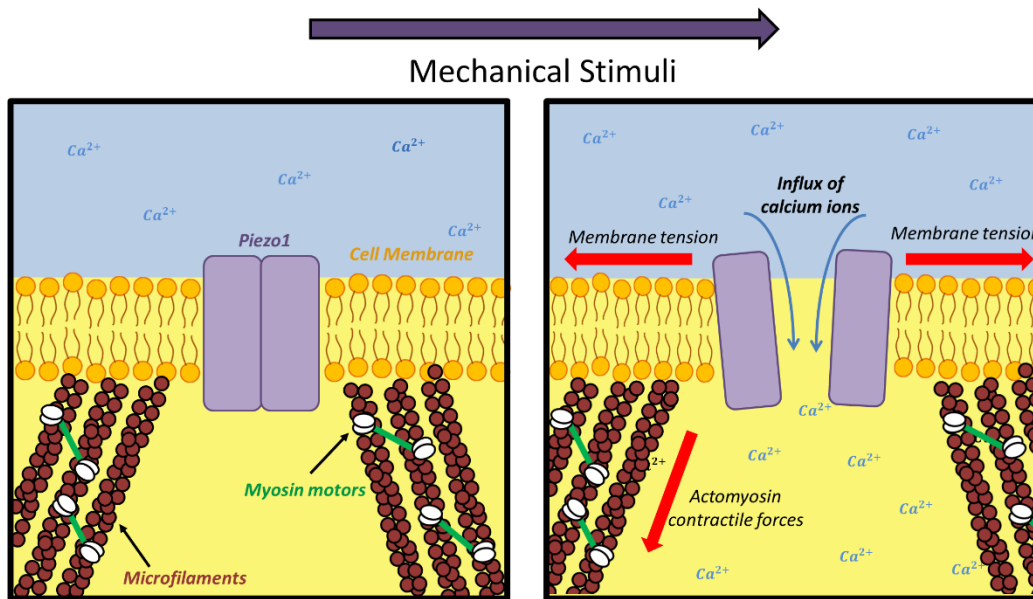


Figure 7.13 Simplified schematic showing the mechanosensitive ion channel Piezo1 which resides in the cell membrane. Mechanical stimulation, via membrane tension or cytoskeletal contractile forces, activates the channel which opens the pore allowing influx of ions.

The previous results sections of the thesis have described the use of deformation cytometry for mechano-phenotyping and increased cytosolic uptake of QDs. This included adapting the technique to probe at low and high strains in two distinct flow regimes (shear and inertia dominant). Thus, this technique may be applicable for studying Piezo1 activation by mechanical force. The applied force can be tailored using flow rate and suspension buffer viscosity, which could potentially infer information on the required forces for activation. This section presents preliminary results for using deformation cytometry to study the MSC Piezo1.

The two cell lines used to investigate Piezo1 activation will be referred to as HEK293 T-REx and Piezo1 T-REx, and were introduced in section 3.6.4. Piezo1 T-REx is a HEK293 cell line with stably incorporated tetracycline-inducible human Piezo1 expression, and show Piezo1 expression after being induced with tetracycline but not without induction. As a control, normal HEK293 T-REx cells (with no incorporated Piezo1) show no response with or without induction by tetracycline. These cells were provided by Elizabeth Evans and the David Beech group (University of Leeds, Faculty of Biological Sciences).

HEK293 cells are an adherent cell line with an epithelial morphology. Figure 7.14a shows phase contrast images of adhered HEK293 T-REx and Piezo1 T-REx, which show no apparent changes in their morphology. For deformation assays and subsequent fluorescence measurements for detecting Piezo1 activation, cells were detached into a rounded morphology. Figure 7.14b includes histograms of the diameter of detached HEK293 T-REx and Piezo1 T-REx, both show a normal distribution and are fitted with a Gaussian. The

Gaussian peak of HEK293 T-REx was $16.5 \pm 0.2 \mu\text{m}$ and of Piezo1 T-REx was $16.4 \pm 0.1 \mu\text{m}$, showing no significant change in size between the two cell lines.

Strain traces were also collected for HEK293 T-REx and Piezo1 T-REx to investigate whether incorporation of Piezo1 into the cell membrane affects the mechanical properties of HEK293 cells.

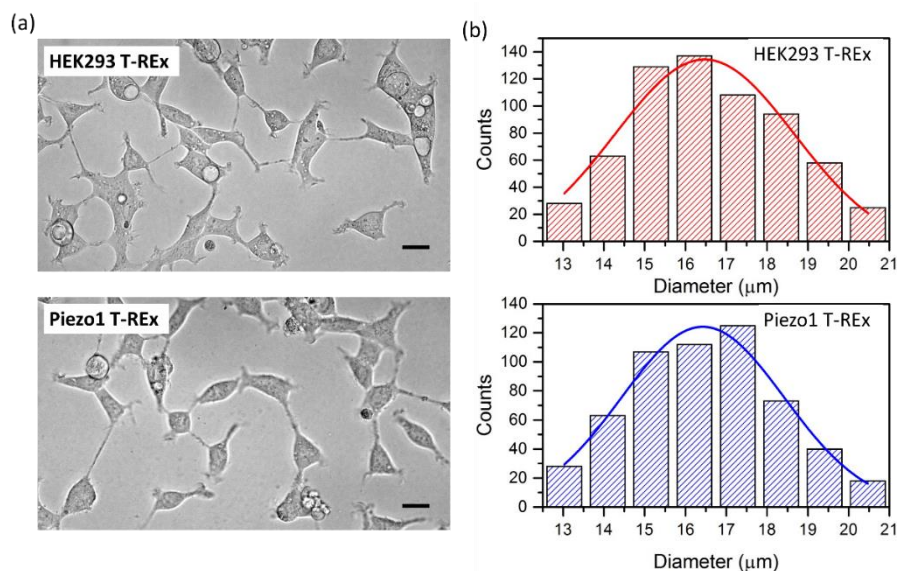


Figure 7.14 (a) Phase contrast images of HEK293 T-REx and Piezo1 T-REx cell lines adhered to a culture flask, scale bars are 20 μm . (b) Histograms of the diameter of HEK293 T-REx and Piezo1 T-REx cell lines when detached into a rounded state, showing normal distributions fitted with Gaussians.

7.2.1 Yoda1 activation

The system was initially tested using the drug Yoda1 to activate Piezo1 and the ratiometric fluorescent dye Fura-2 for detection. A detailed protocol of how cells were loaded with Fura-2 can be found in section 3.6.4. Both cell lines were incubated with 0.1 $\mu\text{g/ml}$ of tetracycline for 24 hr before measurements occurred, tetracycline should induce Piezo1 expression in the Piezo1 T-Rex cell line but not the control cell line. After cells were loaded with Fura2, samples were arranged in a 96 well plate (Costar 96 clear U bottom) with 200 $\mu\text{l/well}$ and $\sim 50,000$ cells per well. Different concentrations of Yoda1 were added to the wells, with five repeating wells for each condition, and a platereader (SpectraMax $\text{\textcircled{R}}$ M2) was then used for fluorescence measurements.

Cells were suspended in SBS (Standard Barths Solution) which contains calcium ions, once Piezo1 is activated calcium ions can pass the cell membrane into the cell. Unbound Fura-2 excites at 380 nm but ones bound to calcium excite at 340 nm. Both excitation wavelengths emit at 510 nm. Thus, the addition of Yoda1 should activate Piezo1 allowing the passage of Calcium ions resulting in increased emission when using 340 nm excitation and reduced emission from excitation at 380 nm. Fluorescence was measured at 340/510 nm (Lm1) and

380/510 nm (Lm2), and the ratio Lm1/Lm2 was used to quantify increased activation of Piezo1 ion channels.

This protocol was based off the work by Evans *et al.* 2018 who tested Yoda1 analogues using these cell lines and the Fura2 ratiometric fluorescence measurements [186]. Their protocol including seeding the cells in the well plate such that they were adhered when Yoda1 was applied. However, for microfluidic deformation the cells are required to be detached and rounded. Therefore, the Yoda1 control was conducted for a range of concentrations on both cell lines in their detached and adhered morphologies.

Figure 7.15 is a graph of fluorescence response Lm1/Lm2 as a function of Yoda1 concentration, where an increase in Lm1/Lm2 indicates increased Piezo1 activation. Results are baseline normalised using Lm1/Lm2 well plate measurements taken before addition of Yoda1. Firstly, results indicate no significant difference in response due to cells being adhered or detached. The Piezo1 T-Rex datasets are fitted with an exponential function, this behaviour is expected as a saturation point will eventually be reached if all Piezo1 channels are fully open. The HEK293 T-Rex datasets show a linear relationship between Yoda1 and Lm1/Lm2, however response is significantly less than the Piezo1 T-REx. HEK T-REx should theoretically not express Piezo1 and so increase in Lm1/Lm2 would be expected due to addition of Yoda1. The presence of endogenous Piezo1 in HEK293 cells is a source of debate and discussed in Dubin *et al.* 2017 [238], thus the data presented by Figure 7.15 would support some endogenous Piezo1 present in the control cell line as there was some response to Yoda1.

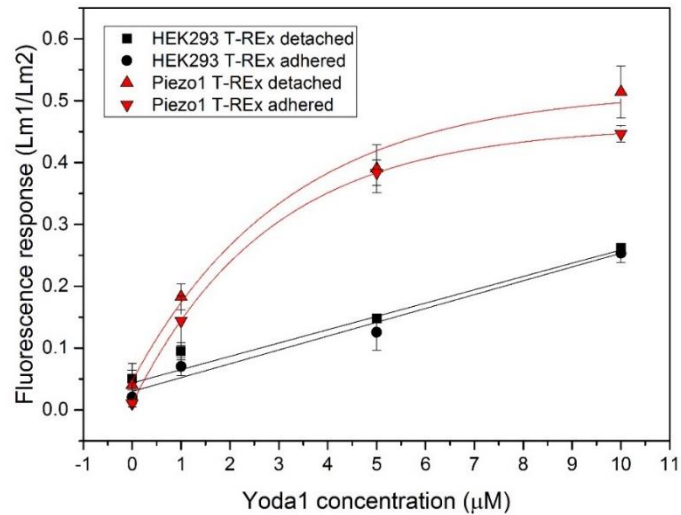


Figure 7.15 The drug Yoda1 was used to activate the mechanosensitive ion channel Piezo1. Activation of Piezo1 allows calcium ions into the cell which then bind to the pre-loaded dye Fura2. Fura2 excites at 340 nm when bound with emission at 510 nm (Lm2), unbound Fura2 excites at 380 nm and also emits at 510 nm (Lm1). Lm1/Lm2 is a measure of Piezo1 activation as fluorescence at Lm1 should increase and Lm2 should decrease. This method was tested on HEK293 T-REx and Piezo1 T-REx cell lines as a function of Yoda1 concentration. This method was also tested on cells adhered to the well surface and detached to a rounded state. Fluorescence intensity was measured across 5 wells for each datapoint and averaged.

7.2.2 Shear Regime Deformation

DC experiments were performed on HEK293 T-REx and Piezo1 T-REx in the shear-dominant regime ($\mu \approx 33$ cP). Cells were deformed on-chip using a range of flow rates, collecting 10s-100s of events for each condition. Experiments were repeated $N=3$ to calculate the average deformation index DI. Cells were deformed between 20 $\mu\text{l}/\text{min}$ and 200 $\mu\text{l}/\text{min}$, the same range used for trying to detect Piezo1 activation due to mechanical force.

Figure 7.16 shows the DI of HEK293 T-REx and Piezo1 T-REx as a function of flow rate, both datasets are fitted with an exponential function. The majority of data points are within error of each other, including the lowest and highest flow rate. This suggests that the incorporation of Piezo1 has little effect on the deformability of HEK293 cells.

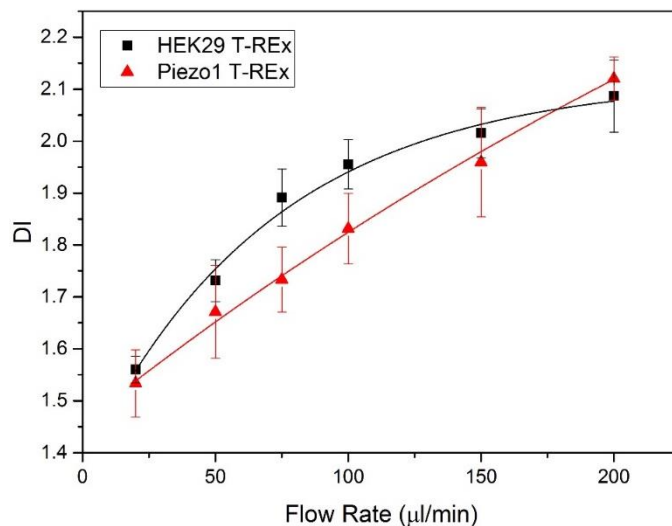


Figure 7.16 The deformation index DI of HEK293 T-REx and Piezo1 T-REx as a function of flow rate. Cells were deformed in a shear-dominant regime (where $\mu \cong 33$ cP) and both datasets are fitted with an exponential function ($n=3$).

The same protocol as described in the previous section was used, however instead of activating Piezo1 using Yoda1 cells were passed through a cross-slot device at different flow rates. This was to test whether the mechanical force imparted on cells at the SP would activate Piezo1.

As before, both cell lines were incubated with 0.1 $\mu\text{g/ml}$ of tetracycline 24 hr in advance and then cells were preloaded with Fura2. The cells were passed through the device until a 300 μl sample was collected, this was then separated into 100 μl into three wells in a 96 well plate. The initial cell density was $5 \cdot 10^5$ cells/ml, to end up with 50,000 cells per well. Fluorescent measurements of Lm1 (380/510 nm) and Lm2 (340/510 nm) were then immediately recorded and the ratio Lm1/Lm2 was used to indicate increased uptake of calcium into the cells. The experiment was repeated three times and from this an average Lm1/Lm2 was found for each flow condition. Figure 7.17a shows Lm1/Lm2 as a function of flow rate for HEK293 T-REx and Piezo1 T-REx. Both cell lines show increased Lm1/Lm2 with flow rate suggesting that microfluidic deformation aids passage of calcium ions across the cell membrane, however Piezo1 T-REx have increased response for all flow rates.

Both data sets are linearly fitted, the slope for HEK293 T-REx was $(8.72 \pm 0.51) \cdot 10^{-4}$ and for Piezo1 T-REx was $(8.61 \pm 0.30) \cdot 10^{-4}$ which are within error of each other, suggesting a systematic increase in response. This is further confirmed by Figure 7.17b which shows the Piezo1 T-REx dataset normalised by the HEK293 T-REx dataset. This is fitted with a linear fit with a set gradient of 0, and shows the Piezo1 T-REx dataset showed a ~ 1.4 fold increase in response for all flow rates.

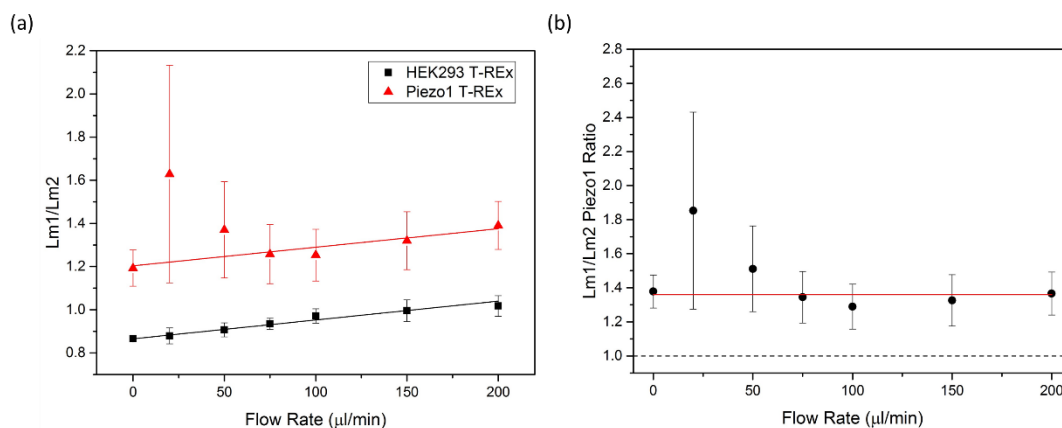


Figure 7.17 (a) The fluorescence intensity $Lm1/Lm2$ of HEK293 T-REx and Piezo1 T-REx cell lines as a function of flow rate through a cross-slot microfluidic device. A higher ratio is indicative of calcium ions getting inside the cell and bonding with the pre-loaded dye Fura2, increasing the emission of $Lm1$ and decreasing the emission of $Lm2$. Both data sets have a linear fit with a positive gradient. (b) The ratio of $(Lm1/Lm2)_{HEK293\ T-REx} / (Lm1/Lm2)_{Piezo1\ T-REx}$ to show the relative change in fluorescence intensity between the cell lines. A ratio of ~ 1 would indicate no change.

Figure 7.17 highlights that the control samples (no microfluidic deformation) also show a ~ 1.4 fold increase in $Lm1/Lm2$ of the Piezo1 T-REx compared to HEK293 T-REx. This suggests that some Piezo1 activation occurs without any microfluidic deformation. As shown in the previous section, cells suspended in higher viscosity media showed increased QD uptake after centrifugation compared to cells suspended in low viscosity media (Figure 7.12). Similarly, in this instance the cells were resuspended in SBS with 0.5% methyl cellulose by 5 min centrifugation at 100 g before performing deformation cytometry. Additionally, during the protocol gentle mixing of the samples occurring by pipetting. These steps will impart some force onto the cells which could result in Piezo1 activation or transient pore formation, the ~ 1.4 increase in Piezo1 T-REx compared to HEK293 T-REx response indicates that *Piezo1* activation must be at least partly responsible.

These results remain inconclusive whether deformation cytometry increased Piezo1 activation. The increase in Piezo1 T-REx response is systematic as a function of flow rate, suggesting Piezo1 activation occurred before microfluidic deformation. The increase in $Lm1/Lm2$ response as a function of flow rate is likely caused instead by transient pore formation, as previously seen for QD uptake in MCF7 cells. An additional artefact of the method is the time delay between deformation and fluorescent measurement. For instance, to collect 300 μl of sample at a flow rate of 20 $\mu\text{l}/\text{min}$ takes 15 minutes. The Yoda1 results in Evans *et al.* 2018 show that after treatment the ion channels activate instantly and $Lm1/Lm2$ increased within seconds and began to decrease exponentially again within a few minutes [186].

7.2.3 Strain Traces

The strain ε of HEK293 T-REx and Piezo1 T-REx was tracked as cells deformed and recovered through an extensional flow junction of a cross-slot device. A flow rate of 5 $\mu\text{l}/\text{min}$ was used in a shear dominant flow regime ($\mu \cong 33 \text{ cP}$). These conditions were used as a low strain shear-regime has previously shown to be most sensitive to cytoskeletal changes, and the addition of Piezo1 may affect the membrane which is coupled to the cytoskeleton.

Figure 7.18 shows the averaged strain traces of N=95 HEK293 T-REx and N=60 Piezo1 T-REx cells. These were used to extract multiple parameters including; the initial strain ε_0 , the maximum strain ε_{max} , the deformation time τ_d , the relaxation time τ_r and the final strain ε_∞ . Deformation and relaxation times were acquired by fitting of exponential functions to the deformation and recovery regions of the traces, and the final strain was then extrapolated by the exponential fit to the recovery region. These parameters are summarised in Table 7.1, showing that ε_0 , ε_{max} and τ_d are within error of each other for the two cell lines. The Piezo1 T-REx show a relatively small increase in τ_r compared to HEK293 T-REx, whereas there was a ~ 3 fold increase in ε_∞ of HEK293 T-REx compared to Piezo1 T-REx. These results show that Piezo1 T-REx recovers its initial shape ($\varepsilon_0 = \varepsilon_\infty$) whereas HEK293 T-REx does not ($\varepsilon_\infty > \varepsilon_0$). This is highlighted by the blue shaded region of the graph which is equivalent to $|2\varepsilon_0|$, as ε_0 is a vector.

Figure 7.19 shows the average velocity profiles of both cell lines as they traversed the extensional flow junction, both profiles are fitted with *sine* functions (shown in red). This was used to fit the Kelvin-Voigt model (section 2.3.4) to the average strain traces of HEK293 T-REx (a) and Piezo1 T-REx (b), also shown in red. From this, the elastic modulus of HEK293 T-REx was found to be $E=144\pm 18 \text{ Pa}$ and of Piezo1 T-REx was found to be $E=167\pm 22 \text{ Pa}$. These values are within error of each other, which suggests that the incorporation of Piezo1 into HEK293 does not alter the stiffness of the cells.

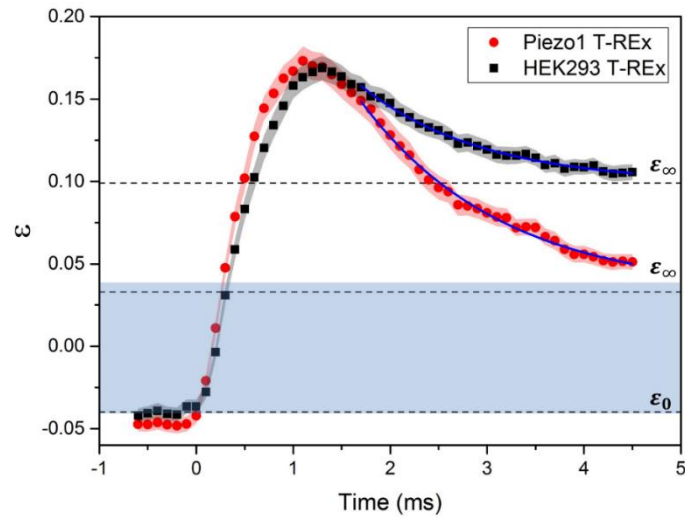


Figure 7.18 The averaged strain trace for HEK293 T-REx ($N = 95$) and Piezo1 T-REx ($N=60$) as a function of time, with the standard error shown by the red and grey shaded areas. The flow rate was $5 \mu\text{l}/\text{min}$, and the suspension medium viscosity was 33 cP . The recovery is fitted with an exponential function and the dashed lines represent the extrapolated final strain ϵ_{∞} for both samples.

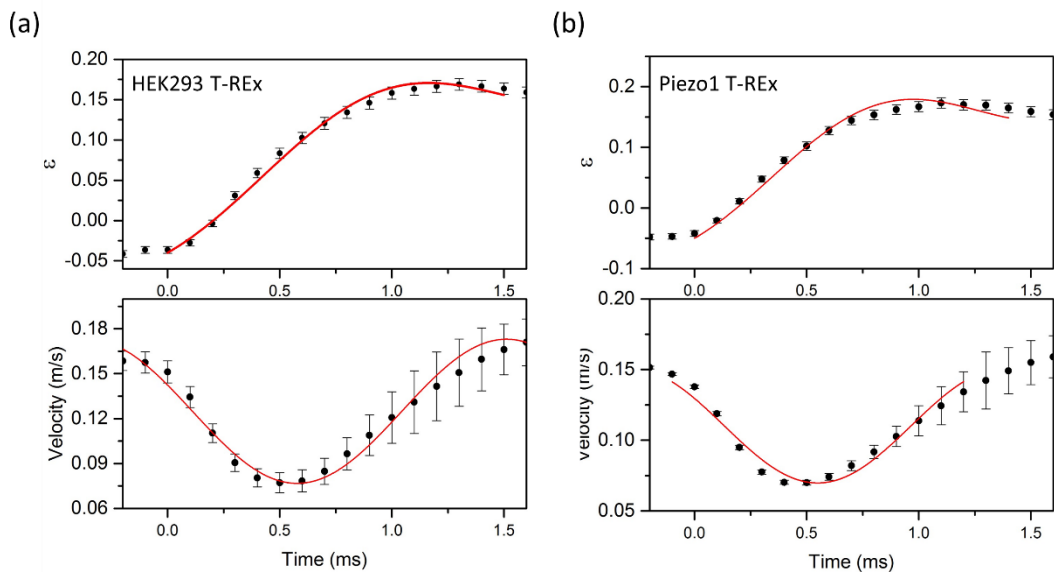


Figure 7.19 Averaged strain traces and velocity profiles of (a) $N=95$ HEK293 T-Rex cells and (b) $N=60$ Piezo1 T-Rex cells. Strain traces are fitted with the Kelvin-Voigt model and velocity profiles fitted with a sine function. Cells were deformed in a shear-dominant regime where $Q = 5 \mu\text{l}/\text{min}$ and $\mu \cong 33 \text{ cP}$.

As discussed in section 4.4.1 cell populations are heterogeneous and bulk measurements can often miss information, such as subpopulations within a sample. Thus, single cell analysis (SCA) was also performed on the $N=90$ HEK293 T-REx cells and $N=65$ Piezo1 T-REx cells, in the same manner as described in results section 4.4.1. Table 7.1 compares the parameters extracted from the ‘‘Averaged Strain Trace’’ to those found by taking the mean average of values from individual strain traces (SCA).

The values of ε_0 are within error of each of for both cell lines using both analysis methods, as are the values of ε_{max} . The relaxation times τ_r are within error of each other for each of the two cell lines using SCA, however both values are greater than their corresponding averaged strain trace values. This suggests outliers may skew the value reported for the averaged trace, showing the importance of investigations at the single cell level. The reported values of ε_∞ using SCA are also marginally higher than those from the averaged strain traces, which is likely coupled to the increase in τ_r .

Table 7.1 Multiple characteristic parameters extracted from the strain traces of N=95 HEK293 T-REx cells and N=60 Piezo1 T-REx cells. Including the initial cell diameter A, the initial strain ε_0 , the final strain ε_∞ , the maximum strain ε_{max} , the deformation time τ_d , the relaxation time τ_r , and the elastic modulus E. Values were found from the ‘‘Averaged Strain Trace’’ and also using single cell analysis ‘‘SCA’’ of individual traces which were then averaged with $\pm SE$.

	HEK293 T-REx		Piezo1 T-REx	
	Averaged trace	SCA	Averaged trace	SCA
A (μm)	N/A	14.114 \pm 0.2	N/A	13.1 \pm 0.2
ε_{max}	0.17 \pm 0.01	0.18 \pm 0.01	0.17 \pm 0.01	0.17 \pm 0.01
ε_0	0.0409 \pm 0.0005	0.0399 \pm 0.0042	0.0477 \pm 0.0003	0.0477 \pm 0.004
ε_∞	0.099 \pm 0.001	0.086 \pm 0.005	0.033 \pm 0.003	0.027 \pm 0.004
τ_d (ms)	1.35 \pm 0.49	N/A	0.75 \pm 0.14	N/A
τ_r (ms)	1.25 \pm 0.08	1.77 \pm 0.38	1.46 \pm 0.11	2.37 \pm 0.78
E (Pa)	144 \pm 18	N/A	167 \pm 22	N/A

Two sample t-tests were used to measure the statistical significance between the different parameters of HEK293 T-REx and Piezo1 T-REx. This was measured using their *p-values*, where smaller *p-values* indicate a higher significance in difference between two datasets. Figure 7.20 shows bar graphs of the average *A*, ε_{max} , ε_∞ , τ_r and ε_0 acquired from SCA of the two cell lines. The level of significance is labelled on the graphs, and raw p-values are also shown in a table in Figure 7.20.

Results show that there is no significant difference between ε_{max} , τ_r and ε_0 between HEK293 T-REx and Piezo1 T-REx and some significance between the initial size *A* of the two datasets (**). The final strain ε_∞ shows an extremely significant difference between the two cell lines (****), showing that the incomplete shape recovery of the HEK293 T-REx is the best physical parameter to distinguish the two cell lines.

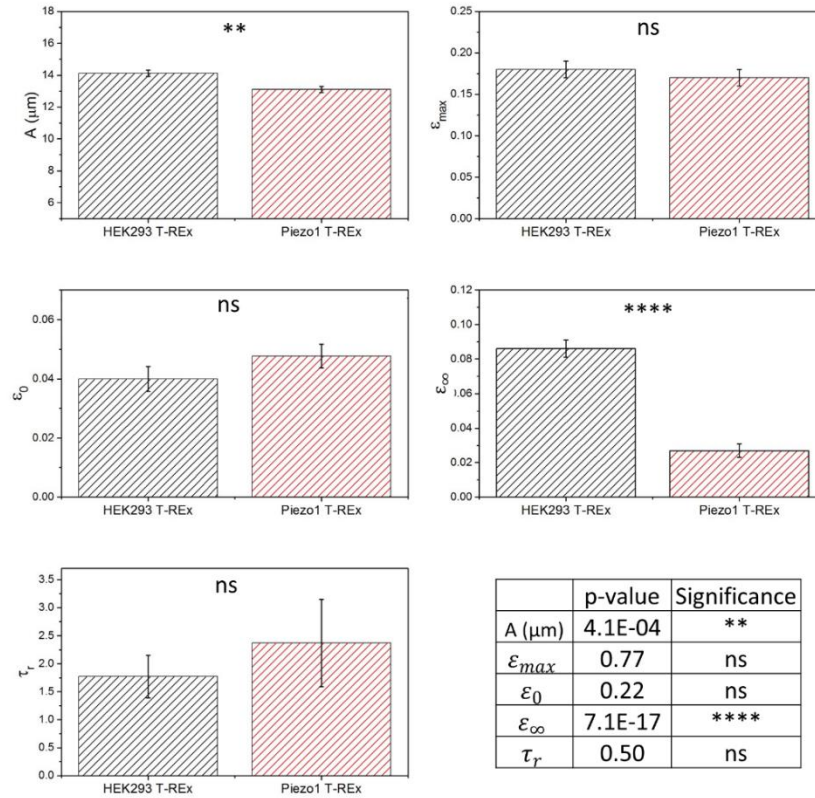


Figure 7.20 SCA was performed on individual strain traces of HEK293 T-Rex and Piezo1 T-Rex. The plots show the average values of the cell diameter A , maximum strain ϵ_{max} , initial strain ϵ_0 , the relaxation time τ_r and the final strain ϵ_{∞} . The error bars denote the standard error SE. Statistical t -tests were done to determine the level of significance, where $p > 0.05$ is not significant (ns), $0.01 < p < 0.05$ is significant (*), $0.001 < p < 0.01$ is very significant (**), $0.0001 < p < 0.001$ is extremely significant (***) and $p < 0.0001$ (****).

Figure 7.21 shows histograms of ϵ_{∞} for HEK293 T-REx and Piezo1 T-REx. The histogram of Piezo1 T-REx shows that most cells have $\epsilon_{\infty} = 0$, indicating full shape recovery after deformation. The histogram of HEK293 T-REx shows a single main peak at $\epsilon_{\infty} = 0.095 \pm 0.003$ found from the peak centre of a fitted Gaussian curve, a smaller population of cells have $\epsilon_{\infty} = 0$ and recover initial shape. The histograms provide more visual information than the averages, by showing the general shift in ϵ_{∞} for HEK293 T-REx as well as the small subpopulation which show similar behaviour to Piezo1 T-REx.

Overall results indicate that the deformation properties (ϵ_{max} , τ_d and E) were the same for HEK293 T-REx and Piezo1 T-REx, showing that incorporation of Piezo1 does not alter whole cell stiffness. However, incomplete shape recovery of HEK293 T-REx compared to Piezo1 T-REx was identified by both averaged strain trace and SCA and further confirmed from Histogram plots and calculation of the p -value. This suggests that the recovery process of HEK293 is potentially altered by incorporation of Piezo1.

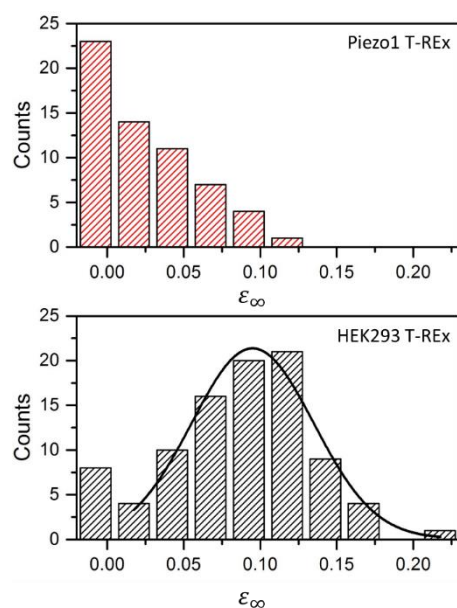


Figure 7.21 Histograms showing the final strain ϵ_{∞} of HEK293 T-REx ($N=95$) and of Piezo1 T-REx ($N=60$).

7.2.4 Discussion

Deformation cytometry was investigated as a potential method for studying activation of the MSC Piezo1 by mechanical force. This was done by deforming cells over a range of flow rates in the shear-dominant regime and measuring the fluorescence response Lm1/Lm2, where an increase is indicative of calcium ions entering the cells and bonding to the dye Fura2. The response of control HEK293 T-REx (no incorporated Piezo1) was compared to Piezo1 T-REx (tetracycline inducible expression of Piezo1).

Results showed a linear relationship between fluorescence response and flow rate for both cell lines (Figure 7.17a), with a systematic increase in the Piezo1 T-REx including the control which was not treated microfluidically (Figure 7.17b). The gradients of the linear fits were within error, which suggests the increase in Lm1/Lm2 was due to pore formation (as discussed in section 7.1). We may expect a critical applied stress to activate Piezo1, thus the systematic increase between the control does not indicate any specific response due to *Piezo1*. This could indicate that the range of applied stresses are already too high and *Piezo1* MSCs are fully activated, or that the dominant response is due to pore formation and the system is not sensitive enough to separate the purely Piezo1 response.

Piezo1 MSCs open via direct gating on the microsecond timescale [239], which can happen via two methods; force transduction through cytoskeletal tethers, or force transduction through membrane tethers. Traditionally, MSC dynamics have been studied using patch clamp electrophysiology adapted for applying mechanical force. Typically, a tight electrical seal is formed between a glass micropipette and the cell membrane where a negative pressure can be

applied to induce membrane tension. The electric potential across the membrane due to the ionic current across the ion channels is then measured. Piezo1 activation in HEK293 cells using this method showed a T50 (half maximal tension) value of 1.4 mN/m, showing Piezo1 can be gated through membrane tension [234]. An alternate path clamp method involves indenting the top surface of the cell whilst measuring the current. Gottlieb *et al.* 2012 showed that actin cytoskeleton disruption using Cytochalasin D lead to a reduced current, this suggests the cytoskeleton also plays a role in transmitting mechanical stimuli to the Piezo1 channels [240]. Comparatively, Retailleau *et al.* 2015 knocked out filamin (which acts as a scaffold between actin and membrane proteins) and found this made the channel easier to activate, suggesting the presence of the cytoskeleton offers some mechoprotection [241]. Finally, Piezo1 activity has also been shown to occur in the absence of external mechanical stimuli suggesting that internal acto-myosin contractile forces can also induce activity, which was confirmed by inhibition of Myosin II resulting in reduced spontaneous Piezo1 activity [242]. Spontaneous Piezo1 activity due to acto-myosin may explain the increase in Lm1/Lm2 shown in our control (undeformed) sample for Piezo1 T-REx compared to HEK293 T-REx (Figure 7.17).

Many techniques are emerging to study Piezo1 activation due to mechanical stress, including the use of indentation, membrane stretch, shear flow and osmotic stress [239]. Gaub and Muller 2017 used AFM to stimulate activation of Piezo1 under pushing and pulling conditions and with attachment of different ECM proteins to the cantilever [243]. They found Piezo1 activation at a pushing force of ~200 nN which was unchanged by altering ECM proteins. However, pulling was dependent on the ECM protein and was more sensitive and activated at ~33 nN. These results show that force directionality elicits different Piezo1 responses. This may lend itself to the cross-slot system, as we can tailor a shear or compressive dominant force regime. Comparatively, we estimate the microfluidic force on cells in the shear regime to be on the 0.1-1.25 μ N range (Figure 4.15). Thus, we may have covered a range of forces already eliciting maximum Piezo1 response and missing the critical range where we see Piezo1 “switch on”. Additionally, the whole cell deformation using a microfluidic cross-slot may differently affect Piezo1 compared to localised AFM probing.

A major artefact in this experimental set-up was the time delay between collection of the microfluidically deformed cells and subsequent fluorescent measurement, which was also affected by flow rate. A sample of 300 μ l was required, which took 15 minutes using 20 μ l/min but only 1.5 minutes using 200 μ l/min. Fluorescence measurements were taken within 2-5 minutes of sample collection. Evans *et al.* 2018 showed that Piezo1 is activated instantly by Yoda1 with Lm1/Lm2 reaching a maximum value within seconds which then decreases exponentially again within a few minutes. Thus, fluorescence measurements need to ideally

be acquired in real time. Figure 7.17 shows much larger errors for Piezo1 T-REx, particularly in the 25-50 $\mu\text{l}/\text{min}$, which may be indicative of the time-dependence of response due to Piezo1.

Combining microfluidic fluorescence with high speed fluorescence could allow force to be applied and fluorescence to be measured on-chip at the point of applied force, and immediately after. Additionally, performing measurements on-chip would allow much lower stresses to be applied which may be able to activate Piezo1 without creating transient membrane pores. For example, in section 7.1.3 we showed that a constriction channel was not sufficient to increase QD uptake in to MCF7 cells, additionally Rosendahl *et al.* 2018 combined a similar deformation geometry with flow cytometry to simultaneously collect mechanical properties and 1D fluorescence data on the single cell level [69].

Strain traces were also collected for HEK293 T-REX and Piezo1 T-REx deformed in the shear-dominant regime ($\mu \approx 33$ cP) at 5 $\mu\text{l}/\text{min}$. Results show no significant changes in the deformation parameters of the two cell lines, including deformation time τ_d , maximum strain ε_{max} and elastic modulus E . However, there were significant differences in the recovery parameters including the relaxation time τ_r and final strain ε_∞ . The main finding was that HEK293 T-REx do not recover their initial shape whereas Piezo1 T-REx did. Incomplete shape recovery was seen in section 6.3.1, where HL60 and SW480 previously showed complete shape recovery whereas HT29 and SW620 did not. These results indicate that incorporation of Piezo1 into HEK293 can alter their recovery process post deformation, and that mechanophenotyping can be used to study these cell processes.

Just as the cytoskeleton effects Piezo1 activation through tethered force transduction, current works are investigating a potential feedback mechanism where Piezo1 activity can also effect cytoskeletal structure. Mchugh *et al.* 2009 showed that knockdown of Piezo1 in Hela cells reduced activation of integrin B, where integrin is a membrane protein which facilitates binding to the extracellular matrix [244], which resulted in reduced cell adhesion. The orientation of stress fibers of endothelial cells lining blood vessels, which tend to align in the direction of blood flow was also investigated [245], [246]. They found that in the absence of Piezo1 activation, stress fibers did not reorient with shear slow and showed a thicker morphology. This feedback mechanism may be responsible for the changes in τ_r and ε_∞ shown in Piezo1 T-REx which may have altered cytoskeletal structure compared to HEK293 T-REx. For instance, in results chapter 5 we showed that the relaxation dynamics of SW480 were affected by destabilisation of the actin using the drug Latrunculin A (LatA). Untreated SW480 recovered its initial shape whereas the treated cells did not.

The study of Piezo1 also has diagnostic application as Piezo1 function has been recently linked to a number of cancers. Jiang *et al.* 2015 found that inhibiting Piezo1 reduced proliferation and invasion of osteosarcoma cells [247]. Li *et al.* 2017 reported upregulation of Piezo1 in the breast cancer cell lines MCF7 compared to normal epithelial cell line MCF-10A, and blocking of Piezo1 in MCF7 also lead to decreased motility [248]. Mchugh 2012 *et al.* proposed that depleted Piezo1 expression could increase migration and metastasis of small cell lung cancer [249]. Cells are known to change their mechanical properties with cancer progression (discussed in section 2.2.4 and chapter 6), thus mechanophenotyping of cells with and without expression of Piezo1 may offer more insight into their relation to cancer progression.

Overall, microfluidics could offer a novel approach to the study of the response of Piezo1 to applied stress. Compared to techniques such as patch clamp physiology, and more recently AFM, microfluidics is high-throughput and requires no pre-selection of each cell. Additionally, the cross-slot device is capable of two distinct regimes where either shear or inertial forces dominate which may offer further insight into the force mechanisms which activate Piezo1. Preliminary results indicate that real-time fluorescence combined with microfluidic deformation would be more applicable, as fluorescence response is nearly instantaneous and may decrease drastically within minutes. Results also suggest that lower flow rates may be required to impart smaller stresses to ensure the critical activation force of Piezo1 is not missed. Gentler microfluidic deformations which do not cause pore formation should also be explored, to confirm that fluorescence response is significantly due to activation of Piezo1. Finally, comparison of strain traces between Piezo1 T-REx and control HEK293 T-REx showed they could be distinguished by their recovery parameters including relaxation and shape recovery. This could be of huge interest as Piezo1 expression has been shown to be coupled to cytoskeletal structure and also is a biomarker of some cancers. Thus, mechanophenotyping of cells with and without Piezo1 could begin to identify structural changes with disease state

8 Conclusions and Future Work

8.1 Chapter by Chapter Overview

Chapter 4 (page 70) detailed optimisation of a cross-slot microfluidic device for measuring the deformation and relaxation properties of single cells, including extracting multiple parameters and comparing bulk measurements with single cell analysis.

HL60 cells were deformed in two distinct flow regimes; the shear-dominant regime and the inertia-dominant regime, which showed highly different mechanical responses. Cells deformed via cross-slot extensional flow experience a shear force due to the viscosity of the suspension fluid and a compressive force due to velocity of the fluid flow. By tailoring the fluid velocity and suspension viscosity a shear-dominant regime (typically low velocity and high viscosity) or inertia-dominant regime (typically high velocity and low viscosity) were achieved. This was also defined using the Reynolds number, where $Re \approx 40$ was defined as the end of the shear regime and the beginning of the inertial regime. Cells deformed in a shear-dominant regime as a function of flow rate showed an increase in deformation index DI which then asymptotically tended towards a maximum value denoted DI_{max} . In the inertia-dominant regime, for flow rates $\leq 400 \mu\text{l}/\text{min}$ the DI tended towards a plateau value DI_{max} . For $Q \geq 400 \mu\text{l}/\text{min}$, DI increased nonlinearly until $Q=600 \mu\text{l}/\text{min}$ and above this cells began to rupture and visibly break apart. The onset of the non-linear increase was defined as an apparent *yield stress* associated with internal breakdown of the subcellular structure (i.e. cytoskeleton), the onset of cell rupture was defined as the cell *failure point*. Viability measurements confirmed that cells remained viable post-deformation in both cell regimes, except beyond the failure point there was a significant drop in viability ($<40\%$). Thus, cells mechanically phenotyped in a regime below the failure point could be used for further experiments such as chemical phenotyping or genotype measurements.

Tracking cell deformation and recovery was used to collect individual “strain traces” of 50 HL60 cells in a low-strain and shear-dominant regime, from these traces multiple characteristic parameters were extracted. These included the initial cell diameter A , initial strain before deformation ε_0 and the maximum strain at the SP ε_{max} . An exponential was fitted to the deformation area of the strain trace (as the cell moves from the inlet to the SP) to extract the deformation time τ_d , and an exponential was fitted to the recovery area (as the cell moves from the SP to the outlet) to extract a relaxation time τ_r and extrapolate the final strain ε_∞ . Comparison of initial strain to final strain allowed quantification of shape-recovery post deformation, where $|\varepsilon_0| = |\varepsilon_\infty|$ indicative cells recovered their original shape and $|\varepsilon_0| < |\varepsilon_\infty|$ showed a permanent deformation or secondary relaxation mechanism not identified over our field of view. Single cell measurements showed that the majority of HL60 underwent shape

recovery whereas a smaller population did not, an average value however showed $|\varepsilon_0| < |\varepsilon_\infty|$ which showed the importance of single cell measurements over bulk averaging. Finally, the Kelvin-Voigt model was fitted to the averaged strain trace to find the elastic modulus of HL60 cells to be $E = 301 \pm 29 Pa$. This value was on the same order of magnitude to those reported in the literature using AFM [34], [190], optical trapping [192] and microfluidic constrictions [34], [250].

The recovery of HL60 after high-strain deformations was also investigated in both shear and inertial regimes. This was done by measuring the average DI of cells before the SP, at the SP, and at various distances through the outlet post deformation. The cell recovery was fitted with an exponential to extrapolate the recovered DI_∞ , showing incomplete shape recovery in shear and inertial regimes ($DI_\infty > 1$) which is indicative of a permanent “plastic” deformation due to disruption of subcellular structure. Histograms identified multiple subpopulations of DI_∞ representing cells which did recover their initial shape and others which underwent an apparent “permanent” deformation, this again showed that single cell analysis is a more powerful tool to utilise.

Chapter 5 (page 105) applied the optimised cross-slot conditions to test changes to the mechanical properties of cells treated with various drugs to alter the subcellular structure. This included Latrunculin A (LatA) to depolymerise actin filaments, Combretastatin A4 (CA4) to destabilise microtubules, and Trichostatin A (TA) to decondense nuclear chromatin. Actin changes were tested on HL60 cells and SW480 cells. LatA treated and untreated cells were deformed in shear and inertia-dominant flow regimes over a range of flow rates. In the shear-regime, results showed that HL60 cells treated with LatA were significantly more deformable than those not treated at low-strain (low flow rates). At high strain (increasing flow rate) the LatA treated and untreated cells had a comparable deformation indices. SW480 cells treated with LatA showed increased DI for the range of flow rates, however the relative increase in DI decreased exponentially with flow rate. In the inertial regime, treated HL60 could not be distinguished from untreated cells at any flow condition. For SW480, the treated cells had increased DI again at low-strains below the *yield stress*. These results indicated that deformation cytometry is most sensitive to changes to the actin cytoskeleton in the low-strain, and shear dominant regime. Strain traces were also collected for SW480 and SW480 LatA in a low-strain, shear regime. From this, the elastic modulus of SW480 was found to be $E = 542 \pm 66$ and the LatA treated cells to be $E = 419 \pm 54$ confirming that disrupting the actin cytoskeleton reduces cell stiffness. Single cell multiparameter analysis showed that ε_{max} and ε_∞ were the only parameters to significantly distinguish the samples. LatA treated cells showed incomplete shape recovery $|\varepsilon_0| < |\varepsilon_\infty|$, whereas normal SW480 did recovery initial shape $|\varepsilon_0| = |\varepsilon_\infty|$. This may be indicative of increased plasticity due to actin destabilisation.

CA4 disrupts the microtubules. Both HL60 and SW480 cells treated with CA4 were studied in the shear-and inertia-dominant flow regimes. Treated and untreated SW480 showed no significant changes in DI as a function of flow rate. Similarly, no change in DI was seen for treated and untreated HL60 in the inertia-dominant regime. However, a systematic decrease in DI was seen for treated cells across all flow rates in the shear-dominant regime. This result was counter-intuitive such that we would expect destabilising the microtubules would make the cells softer. Strain traces were collected for HL60 treated with CA4 to extract multiple deformation and recovery parameters. The elastic modulus of the CA4 treated cells was $E = 598 \pm 66$ (a ~ 2 -fold increase of that of the untreated cells) confirming that CA4 increased cell stiffness. Significant changes were also seen for ϵ_{max} , ϵ_{∞} and τ_r . Interestingly, even though CA4 increased stiffness this was also accompanied by incomplete shape recovery. Viability tests confirmed that the increased stiffness was unlikely to be caused by cell apoptosis or mitotic catastrophe. Thus, changes are likely due to a secondary mechanism such as the cell overcompensating for microtubule destruction by enhancing the actin cytoskeleton [50], [214], [215].

TSA is known to decondense nuclear chromatin, and thereby reduce nuclear stiffness [49], [87], [88]. In the shear-dominant regime no significant changes in the DI of HL60 were seen across the entire range of flow rates. In the inertia-dominant regime, a small increase in DI was seen for flow rates below the *yield stress* (~ 1.1 -fold increase in DI). For flow rates above the *yield stress* a larger relative increase in DI was seen (~ 1.3 fold at the *yield stress*), indicating that a high-strain and inertia-dominant flow regime is most sensitive to such nuclear changes. Previous results using LatA indicated that cytoskeletal breakdown occurs above the *yield stress*, thus at low-strain nuclear changes may be shielded by the mechanics of the cytoskeleton. Therefore, high strains are more useful for probing the nuclear properties which is in accordance with results by Gossett *et al.* 2012 [27].

Chapter 6 (page 154) used Deformation Cytometry to explore changes in mechanical properties of different colorectal cancer (CRC) cell lines, using three cell lines as a model of CRC progression. This included; primary tumour cell lines SW480, an advanced primary tumour cell line HT29, and the lymph node secondary tumour cell line SW620. The three cell lines were probed in the shear-dominant flow regime and inertia-dominant flow regimes over a range of flow rates.

For these measurements, the deformation index was normalised by the initial size of the cell (DI/A) as this better accounts for size-dependence in applied stress [48]. Below the *yield stress* in the inertia-dominant regime, DI/A was largest for SW620 cells and lowest for SW480 cells with HT29 showing intermediate behaviour. Above the *yield stress* the cell lines no longer

showed significant differences in DI/A . The *yield stress* is thought to be associated with breakdown of the actin cytoskeleton. These results suggest that cytoskeletal changes associated with progression are apparent below the yield stress, however actin breakdown above the yield stress results in no changes to deformability under these flow conditions. The shear-dominant regime showed the largest DI/A for SW620 for the entire range of flow rates, and SW480 had the lowest. At low flow rates, the DI/A of HT29 was comparable to SW620 but as flow rate increased the DI/A approached those of SW480. A larger DI/A is likely indicative of increased deformability, these results correlated previous works using AFM which showed the metastatic SW620 cells to be softer than the primary tumour SW480 cells [222], [251].

It was noted that using DI without adjusting for cell size, mostly resulted in no significant changes between cell types in either flow regime. This suggested that multiparameter measurements of deformation and relaxation may better characterise mechanical changes between the different CRC cell lines. Strain traces were found for the different cell types and the Kelvin-Voigt model was used to extract an elastic modulus, offering a mechanical parameter which accounts for initial cell size. The elastic modulus of SW480 was $E = 542 \pm 66$, of HT29 was $E = 309 \pm 50$ and of SW620 was $E = 372 \pm 98$. These results confirmed that SW620 (cells from later stages of disease progression) were softer than SW480, and that HT29 have comparable stiffness to SW620.

The relaxation of the CRC cell lines showed that SW480 underwent complete shape recovery, whereas HT29 and SW620 did not suggesting a permanent induced deformation and increased plasticity. HT29 and SW620 showed similar deformation and relaxation properties, even though the initial size of HT29 and SW480 was similar compared to smaller SW620 cells. These results indicate that as CRC progresses from Dukes stage B (SW480) to stage C (HT29), which involves cells migrating to the outer lining of the bowel, sub-structural changes occur increasing cell deformability. Then as cells metastasis from the outer lining to a lymph node (secondary site), mechanical changes are less essential. Statistical t-tests were done on HL60, SW480, HT29 and SW620 using the parameters A , ϵ_{max} , ϵ_0 , τ_r and ϵ_∞ to quantify their significance for characterisation. Results showed that no single parameter could significantly distinguish all the cell types, highlighting the need for multiparameter mechanical phenotyping. Further, Linear Discriminant Analysis (LDA) was used on the datasets to perform k-fold validation tests. The resulting classification rates were; ~82% for HL60, ~71% for SW480, ~85% for SW620 and ~36% for HT29. HT29 had a significantly lower classification rate with ~39% incorrectly classified as SW480 and ~20% as SW620, this result may be indicative of HT29 showing intermediate properties between the other two CRC cell lines. An average classification rate of ~69% shows promise for the method, however

increased sample size would likely further enhance results (current datasets included $46 < N < 56$ strain traces).

Chapter 7 (page 179) investigated other applications of Deformation Cytometry. Firstly, deformation cytometry tested toward increasing cytosolic uptake of quantum dots (QDs) into MCF7 cells through generating transient membrane pores through microfluidic deformations [227]. QDs have diagnostic potential for sensing redox potential which is a marker for disease [230], however this requires a method for non-endocytic delivery into cells. Cells were deformed with QDs in a cross-slot device using shear and inertial regimes, confocal fluorescence was then used to observe QD uptake. The shear-dominant regime showed a linear increase in uptake with flow rate, and confocal and TEM images confirmed increased cytosolic uptake. An optimum flow rate of 100 $\mu\text{l}/\text{min}$ was found to offer most improved uptake whilst maintaining cell viability. Comparatively, deformation using an inertial regime did not show significant changes in uptake compared to an undeformed sample over a range of flow rates (up to 600 $\mu\text{l}/\text{min}$), with comparable deformation DI to the shear regime. This result is contradictory to reports of a cross-slot inertial regime for cytosolic uptake of various macromolecules and nanoparticles to the cytosol [68], [231]. Deformation using a constriction channel and high viscosity suspension buffer ($\mu \approx 33$ cP) was also tested for increasing uptake, where the constriction channel was slightly wider than the cell size and induced bullet-like dimensions (similar to RT-DC [96]). The length and dimensions of the channel were comparable to the inlet and outlet of the cross-slot devices. This also showed no significant improvements to uptake over a range of flow rates comparable to the cross-slot shear-regime. The use of a constriction with dimensions smaller than initial cell size has been shown to increase cytosolic uptake of QDs into cells [65]. These results show that shear forces are more efficient for generating transient membrane pores, as is extensional deformation compared to constriction deformation.

Deformation in a cross-slot device in a shear-dominant regime was also tested for activating the mechanosensitive ion channel Piezo1. The Piezo1 T-REx cell line was used (which has incorporated tetracycline inducible Piezo1) was compared to control cell line HEK293 T-REx. The mechanical properties of the two cell lines were compared, with mostly no changes between DI seen in the shear-regime across a range of flow rates. Strain traces collected for both cell lines also indicated no changes in the deformation properties (ϵ_{max} and elastic modulus). However significant changes were seen for relaxation properties (ϵ_{∞} and τ_r), Piezo1 T-REx showed complete shape recovery whereas HEK293 did not. Piezo1 is known to have pathological significance [236], [252] and its function has been recently linked to a number of cancers [247]–[249]. Additionally, Piezo1 activation is partially caused by tethers to the cytoskeleton and in turn Piezo1 functionality can affect cytoskeletal structure [239],

[245], [246], [249]. Thus, microfluidics shows potential for studied the response of Piezo1 to applied stress and how Piezo1 incorporation may alter mechanical phenotype which could potentially be correlated to disease state (discussed further in the next steps section 8.3.3).

The ratiometric dye Fura2 was used to assess activation of Piezo1. Results showed increased fluorescence response as a function of flow rate for both cell lines, with a systematic increase in Piezo1 T-REx. However, the origin of this increase remained inconclusive (i.e. could also be due to pore formation), thus, further testing and improvements to the experimental method are needed which are discussed in the next steps section 8.3.

8.2 MRC Project

The work in this thesis was initially part of a joint project between the University of Leeds and Leeds Teaching Hospitals toward development of a microfluidic platform to integrate different phenotyping methods. These methods were first to be developed separately. Whilst this thesis developed the mechanical phenotyping method, another PhD student Julia Gala De Pablo worked towards chemical phenotyping of cells on-chip using Raman Spectroscopy. Some of her results of chemical phenotyping of CRC cell lines, including SW480, HT29 and SW620, were published in the Journal of Raman Spectroscopy (2018) [2]. Results showed that Raman spectra could distinguish cell lines with high confidence, with a 98.7% classification rate between SW480 and SW620 using principal component analysis combined with linear discriminant analysis. Thus, our results combined provide an overview of the mechanical (chapter 6) and chemical phenotype of CRC. A future aim is to combine the techniques into a joint microfluidic platform, allowing mechanical and chemical phenotype on a single cell level.

Some comparisons can be made between the chemical and mechanical phenotypes of HL60, SW480, HT29 and SW620 cells. Firstly, measurement of the nuclear ratio ($A_{ratio} = A_{nucleus}/A_{cell}$) showed that HL60 had the smallest nuclear diameter, followed by SW620, HT29 and SW480 respectively (Table 4.1). Raman results showed that the 782 cm^{-1} and 810 cm^{-1} show the DNA contents of the cell followed a trend inverse to the nuclear ratio. This may indicate that these peaks are sensitive to how compressed the nuclear material is and that higher DNA content correlates to a more compressed (i.e. smaller) nucleus.

Table 8.1 Confusion Matrix of PCA/LDA results from Raman spectra of the three CRC cell lines, where each column corresponds to the predicted members of a class, and each row corresponds to the actual membership of the class. Results adapted from Julia Gala De Pablo's PhD thesis [253].

	SW480	HT29	SW620
SW480	91.7±1.0	7.8±0.9	0.2±0.2
HT29	9.0±1.0	90.0±1.0	0.5±0.2
SW620	0.8±0.3	1.9±0.5	96.2±0.7

Multiple parameters were extracted from strain traces of the CRC cell lines, and showed that HT29 (primary, Duke's stage C) and SW620 (metastatic, Duke's stage C) had similar deformation and recovery properties (including maximum strain, elastic modulus and final strain). Whereas SW480 showed different deformation and recovery and was generally stiffer than SW620 cells. These results suggested HT29 acquired a metastatic mechanical phenotype before leaving the primary tumour site. Interestingly, HT29 and SW480 cells appear to have more similar Raman signatures compared to SW620. The confusion matrix shown by Table 8.1, adapted from the PhD thesis of Julia Gala De Pablo, shows a summary of this, ~8% of SW480 were incorrectly classified as HT29 and ~9% of HT29 as SW480. Comparatively, SW620 had the highest classification rate of ~96% [253]. Overall, results point towards HT29 cells being an intermediate state between SW480 and SW620 cells, where the chemical phenotype matches the primary cells but the mechanical phenotype matches the metastatic cells.

8.3 Next Steps

8.3.1 Further optimisation

Multiparameter analysis of strain traces showed promise for single-cell mechanical phenotyping and classification, however sample sizes were relatively low ($50 < N < 100$) compared to other microfluidic assays ($N > 1000$). The current limiting factor is that strain traces require a larger field of view, compared to just measuring DI at the SP, which vastly increases the processing time required to save already large high-speed videos ($N > 10,000$ s of frames per sample). Theoretically, using a flow rate of 5 $\mu\text{l}/\text{min}$ and a cell density of $1 \cdot 10^6 \text{ cells}/\text{ml}$ is equivalent to a throughput of ~800 cells/s. Thus, implementation of real-time analysis or a more powerful operating system (capable of processing data at faster speeds), would allow utilisation of this throughput. This would lead to collection of larger sample sizes with more statistical significance.

The upper-end of the range of flow rates in both regimes was limited due to back-pressure in the device, thus the failure point of stiffer cells (i.e. the CRC cell lines) could not be measured. Fabrication of a glass microfluidic device may allow these measurements in the future.

To accurately compare between samples, only cells which deformed at the SP were included in deformability measurements to ensure all cells deformed under the same applied stress. The velocity profile of cells was tracked, and a *velocity threshold* was defined to discard cells which did not enter the extensional flow junction centrally. The velocity threshold was defined as $\Delta v = \frac{v_{inlet} - v_{min}}{v_{inlet}}$, a of $\Delta v \geq 0.75$ was found to be a sufficient threshold as further increasing the threshold did not alter the average *DI* of a sample.

Further optimisation to the technique would be to implement a microfluidic focusing technique to ensure all cells enter the extensional flow junction centrally, this would mean no cells are discarded from calculations and further improve throughput. Sheath flows are commonly used to push particles into the channel centre, achieved by joining two outer flowing channels to the central channel [96]. However, this would add further complexity to the device requiring additional inlets and a second syringe pump to be used for measurements. Also, the addition of the sheath fluid essentially dilutes the sample which would reduce throughput. Sheath-less methods of focusing include, viscoelastic focusing [29] and inertial focusing [254]. Inertial focusing involves implementing curved channels to manipulate inertial forces acting on particles in flow ($1 < Re$). Curving channels induce a secondary rotational flow due to the inertia of the fluid itself, known as Dean flow, which can change to equilibrium position of flowing particles. Di Carlo *et al.* 2007 used asymmetric curbing geometries to focus particles to a single central stream, which has since been implemented in the group deformation cytometry experiments [27], [165]. Although a highly accurate focusing method, it depends highly on coupling channel geometry and flow rate. Thus, our experiments worked to probe cell deformations across a wide range of flow conditions using the same cross-slot geometry and it would be time-consuming to alter the design for each flow rate to test.

8.3.2 DC to study other subcellular alterations

Chapter 5 investigated mechanical changes to cells treated with drugs which changed the structure of actin, microtubules and the nucleus, and these results were compared to other cell mechanics studies. However, currently significantly less work has been done on the role of intermediate filaments and how changes to their structure affects whole cell mechanics. Understanding the mechanobiology of intermediate filaments has many applications because their structural changes have been linked to various diseases such as cancer [255], and also drugs targeting intermediate filaments may offer new cancer therapies [256].

Intermediate filaments are the least stiff of the three cytoskeletal filaments, however they can withstand much higher strains than microfilaments and microtubules [82]. In the thesis, we showed apparent yield stress behaviour that may be associated with actin breakdown at high

strains. Thus, a high strain inertia-dominant regime may be more sensitive to changes to intermediate filaments. This would differ from actin and microtubule changes which favoured a low-strain and shear-dominant regime. Gossett *et al.* 2012 used a compound to reorganise networks of the intermediate filament Keratin using deformability cytometry in a high strain inertial regime, results showed no significant change due to treatment [174]. The same group later reported an inertia-dominant pinched flow deformation, which was able to detect increased deformability of cells with disrupted vimentin intermediate filaments using Calyculin A [30]. Gladilin *et al.* 2014 used microfluidic optical stretching to show increased cell deformability due to vimentin disruption using Withaferin A [257]. These results highlight that different types of intermediate filaments have different mechanical roles within the cell, and detecting these changes may require different strains, flow regime and multiparameter analysis of deformation and recovery profiles. Additionally, lamins are a type of intermediate filament which make up the nuclear lamina, which along with chromatin add mechanical integrity to the cell nucleus. The nucleus structure is mediated by lamins and loss of lamins has been coupled to cytoskeletal changes and shown reduced cell stiffness [89].

Various other subcellular changes could be probed using deformation cytometry, including inhibition of molecular motors. Various studies have studied mechanical changes of cells due to inhibition of the actin dwelling motor protein myosin II, using drugs such as blebbistatin [52], [174] or ML7 [44]. Chan *et al.* 2015 studied the deformability of multiple adherent and non-adherent cell lines deformed in a suspended state using microfluidic optical stretching, RT-DC and advection time through microconstrictions [52]. They found that cells showed increased stiffness with myosin II inhibition using the range of techniques. Comparatively, Ahmmed *et al.* 2018 showed decreased stiffness in MCF7 with myosin II inhibition using a similar microfluidic constriction induce deformation [44]. Thus, the role of myosin II and its relationship to mechanical integrity remains unclear in suspended cells. Additionally, changes to motor proteins could affect the cells ability to recovery post deformation and may show significant changes to relaxation time τ_r and final strain ϵ_∞ . Mechanophenotyping cells with inhibition of microtubule motor proteins Kinesin and Dynein could also be of interest. Microtubule motor proteins are heavily involved in mitosis, thus alterations in their expression can lead to carcinogenesis [258].

8.3.3 DC for studying Piezo1

Future work could investigate using deformation cytometry to detect Piezo1 MSCs in cells and elucidate how activation is coupled to the cytoskeleton and whole cell mechanics. Currently unpublished work to be included in the PhD thesis of Judith Valluru (University of Leeds) investigated links between Piezo1 functionality in colorectal cancer cells lines. HT29 and SW480 cell types were found to have functionally active Piezo1, confirmed using tests

with the agonist Yoda1. Piezo1 siRNA transfection was used to knockdown Piezo1, which was used to test the responses of the CRC cell lines with and without Piezo1 functionality. Results showed that Piezo1 knockdown reduced proliferation without cell death in both cell lines. A migration assay through a porous membrane towards a chemo-attractive substrate, showed that Piezo1 aids migration. Additionally, Piezo1 also showed increased G2M arrest and cell cycle stages are known to have distinct mechanophenotypes. These results imply mechanical changes may accompany Piezo1 knockdown in CRC cell lines, which could be studied using deformation cytometry. Our results in section 7.2 show that the recovery of HEK293 with incorporated Piezo1 was significantly different to a control without Piezo1. Additionally, our results showed mechanical differences between SW480 and the more advanced CRC cell lines HT29 and SW620 which could potentially be correlated to Piezo1 functionality.

8.3.4 DC and high speed fluorescence

Results throughout the thesis showed that subcellular structural changes cause measurable changes to whole cell mechanical properties. Additionally, *yield stress* behaviour was noted and may be indicative of subcellular breakdown. Recent mechanophenotyping methods are working towards combining bright field and fluorescence measurements. The Guck group recently combined RT-DC with 1D fluorescence measurements, to try to match flow cytometry throughput, however this offers no 2D structural information [69]. Combined fluorescent labelling and bright field imaging during deformation would allow direct correlation between deformability changes and substructural changes (described by the schematics in Figure 8.1). For example, by staining the nucleus the nuclear deformability and whole cell deformability could be tracked. Also, at high-strains above the yield stress it may be possible to visualise cytoskeletal breakdown of nuclear rupture. Finally, real-time fluorescence imaging combined with microfluidics would be ideal for quantifying Piezo1 activation as it is known to occur instantaneously after force is applied. The method could also be used to study transient pore formation and resealing after deformation at the SP, by loading the cells with a fluorescent dye such as Calcein.

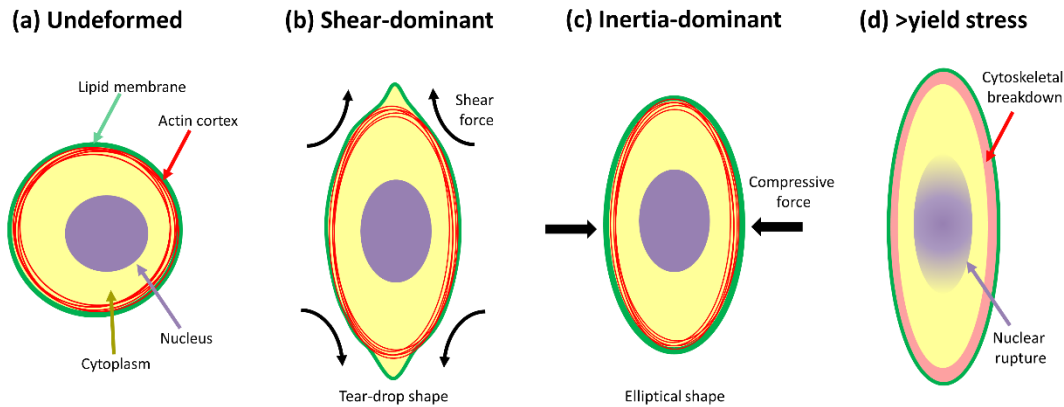


Figure 8.1 Schematic showing structural information that could be gained from combining deformation cytometry and fluorescence imaging. Including visualising (a) the lipid membrane, actin cortex and nucleus. (b)-(d) show examples of how this could be regime dependent, including how high strains could elicit cytoskeletal breakdown and nuclear rupture.

Development of high-speed fluorescence microscopes able to resolve cell structure when travelling at high speeds, have been limited by the fluorescence lifetime of fluorophores. The Goda research group developed the FDM (frequency division multiplexing) confocal microscope that achieved a frame rate higher than the limiting fluorescence lifetime [70]. Combined high speed confocal and light-sheet fluorescence can resolve cells travelling >1 m/s down a straight microfluidic channel, including using 2 fluorescent channels with a DNA stain [259]. This allowed multiple parameter analysis of physical parameters including whole cell and nuclear shape. Future work will collaborate with Goda's lab to combine their fluorescence microscopy with deformation cytometry, allowing single-cell multiparameter analysis including direct relation to whole cell deformability and subcellular structure. Preliminary work successfully deformed cells in a cross-slot in the shear regime with two-channel cytoplasmic and nuclear staining, and current work is being done toward processing and analysing this data.

Appendix

COMSOL model from Chapter 4

COMSOL Multiphysics simulates fluid flow by solving a set of equations for known boundary conditions including inlets, outlets and walls. The fluid velocity and pressure can be predicted for a given geometry by solving the Navier-Stokes (NS) equation (equation 2.14), which represents momentum conservation, and the continuity equation (equation 2.15), which represents conservation of mass. A model was built to calculate the flow velocity in the inlet and outlet channels of the cross-slot device, to compare to the measured velocity of beads and cells in flow (section 4.1.1) in the same device geometry. The Model Navigator below outlines how the model was built and how data was extracted from it.

Model Navigator

From the File menu, choose New.

NEW

1 In the New window, click Model Wizard.

MODEL WIZARD

1 In the Model Wizard window, click 3D.

2 In the Select physics tree, select Fluid Flow >Single-Phase Flow >Laminar Flow. Click Add.

3 Click Study.

4 Click Done.

PARAMETERS

1 In the Global Definitions window, select Parameters.

2 Add a Parameter labelled *FR* (flow rate) with an initial value of $5 \mu\text{l}/\text{min}$.

GEOMETRY

1 In the Model Builder window, under Component 1 (comp1) click Geometry 1.

2 In the Settings window for Geometry, locate the Units section, from the length unit list, choose μm .

3 On the Geometry toolbar, click Primitives and choose Rectangle. Set the Width to 500 and Height to 35.

4 Go to Draw and select Extrude and extrude Work Plane 1 (wp1) by 25.

5 On the Home toolbar, click Build All.

MATERIALS

1 In the Model Builder window, under Component 1 (comp1) right-click Materials and choose Water.

LAMINAR FLOW

- 1 In the Model Builder window, under Component 1 (comp1) click Laminar Flow.
- 2 Select All Domains. Select Equations from Study Controlled, Study 1 Stationary.
- 3 Set Compressibility to incompressible fluid. 4 Under Fluid Properties, select both density ρ and viscosity μ as from Material.
- 5 Under Wall 1 select domains 2, 3, 4 and 5.
- 6 On the Laminar Flow toolbar, click Inlet 1. Select domain 1, Laminar inflow as the boundary condition and in the Flow Rate text field type *FR*.
- 8 On the Laminar Flow toolbar, click Outlet. Select domain 6, select Pressure=0 as the Boundary Condition and select Suppress Backflow.

MESH GENERATOR

- 1 Select Physics Controlled Mesh and select Finer from the predefined mesh sizes list.
- 2 Click the Initialize Mesh button in the toolbar to generate the mesh.

STUDY

- 1 In the Model Builder window, under Component 1 (comp1) click Study.
- 2 Locate the Parametric Sweep section. Set Name of parameter to *FR* (flow rate) and List of parameter values to range (2.5 [$\mu\text{l}/\text{min}$], 5 [$\mu\text{l}/\text{min}$], 10 [$\mu\text{l}/\text{min}$], 25 [$\mu\text{l}/\text{min}$], 40 [$\mu\text{l}/\text{min}$]).
- 3 On the Home toolbar, click Compute.

RESULTS

- 1 In the Model Builder window, under Component 1 (comp1) click Results.
- 2 On the Data Sets toolbar, click Cut Line. For Point 1 set: $x=100$, $y=0$, $z=12.5$. For Point 2 set: $x=100$, $y=35$, $z=12.5$.
- 3 On the Velocity toolbar, click and add Slice and select the x-y plane.
- 4 On the Velocity toolbar, click and add Streamline and select uniform density and a separating distance of 0.01.
- 5 Under 1D Group Plot select Cut Line 1, for Parameter Selection (*FR*) select All.
- 6 Click Plot.
- 7 On the Export toolbar, click add data. Select Cut Line 1 and click Export.

Supplementary Figures for Chapter 4

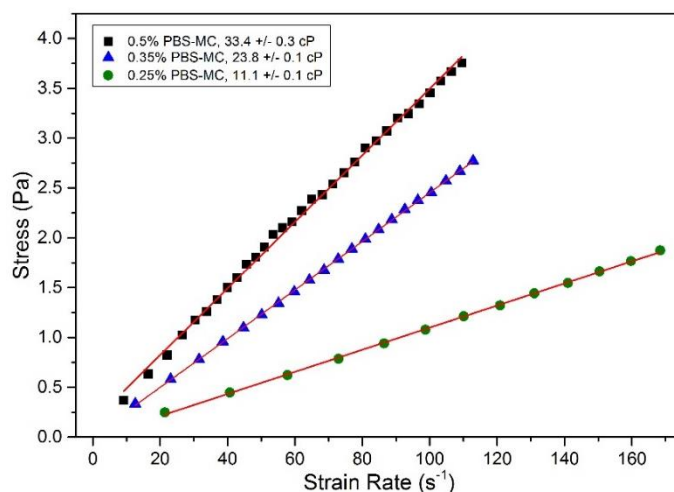


Figure S1 Viscosity data for PBS with different amounts of methyl cellulose (0.25%, 0.35% and 0.5% w/v). Viscosity was measured using a Rheometrics SR-500 Dynamic Stress Rheometer in the parallel plate configuration (diameter of 25 mm). The graph shows a plot of strain rate as a function of stress, each dataset has a linear fit where the gradient is equivalent to the viscosity. Rheometry measurements were taken by Matthew Hughes.

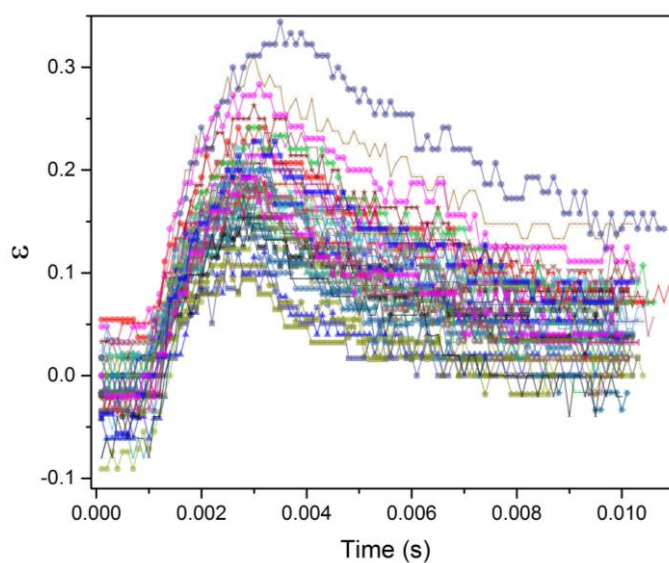


Figure S2 The raw data of the $N=50$ strain traces of HL60 cells deformed in a shear-dominant regime ($\mu = 33$ cP) at a flow rate of $5 \mu\text{l}/\text{min}$.

Supporting Videos for Chapter 4

Video 1: HL60 cells deforming in the shear-dominant flow regime ($\mu \approx 33$ cP) at a flow rate of 80 $\mu\text{l}/\text{min}$.

Video 2: HL60 cells deforming in the inertia-dominant flow regime ($\mu \approx 1$ cP) at a flow rate of 200 $\mu\text{l}/\text{min}$, which is below the cells *yield stress*.

Video 3: HL60 cells deforming in the inertia-dominant flow regime ($\mu \approx 1$ cP) at a flow rate of 400 $\mu\text{l}/\text{min}$, which is equivalent to the cells *yield stress*.

Video 4: HL60 cells deforming in the inertia-dominant flow regime ($\mu \approx 1$ cP) at a flow rate of 600 $\mu\text{l}/\text{min}$, which above the cells *yield stress* and at the *critical strain* (flow rates above this surpass the cell *failure point* leading to on-chip cell rupture).

Video 5: HL60 cells deforming in the shear-dominant flow regime ($\mu \approx 33$ cP) at a flow rate of 5 $\mu\text{l}/\text{min}$. An example of the maximised field of view used to track cell deformation and relaxation and extract multiple parameters.

Supplementary Figures for Chapter 5

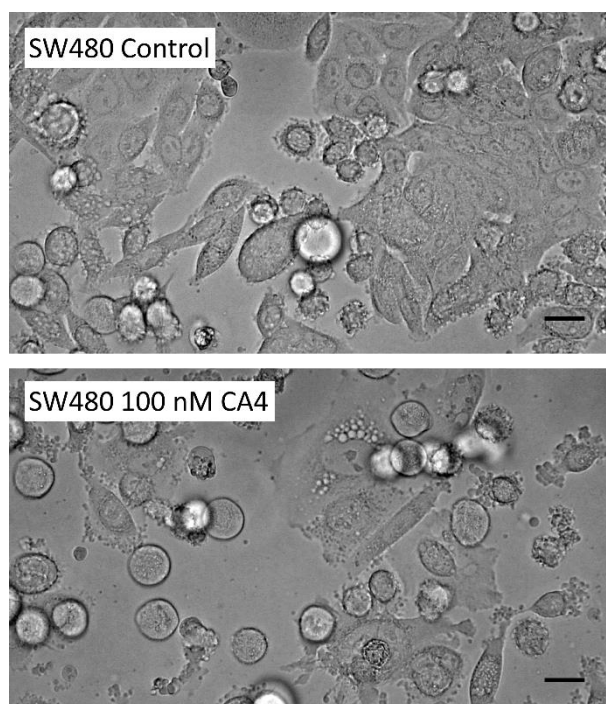


Figure S3 Phase contrast images of SW480 cells treated with 100 nM of CA4 for 24 hr compared to a control same seeded on the same day. A 40 x objective was used, scale bars are 20 μm .

Supplementary Figures for Chapter 6

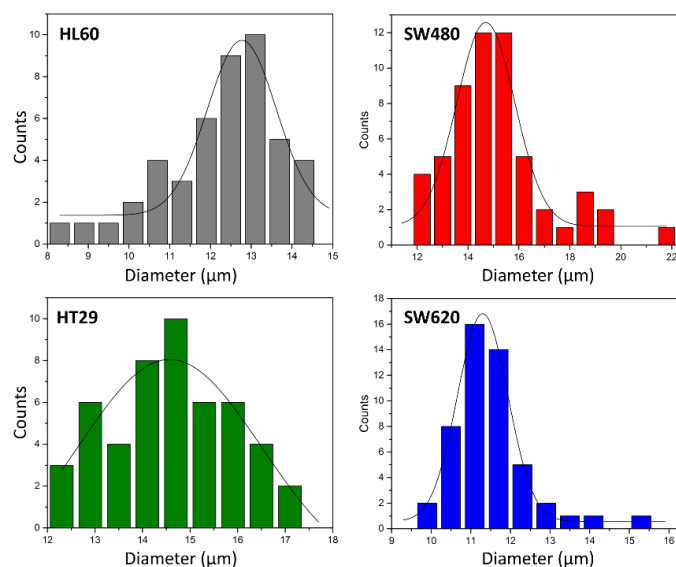


Figure S4 Histograms showing the initial diameter A of four cell lines. Found using image analysis as cells approached the SP of an extensional flow junction. The flow regime was shear-dominant ($\mu \approx 33$ cP, $Q = 5$ $\mu\text{l}/\text{min}$).

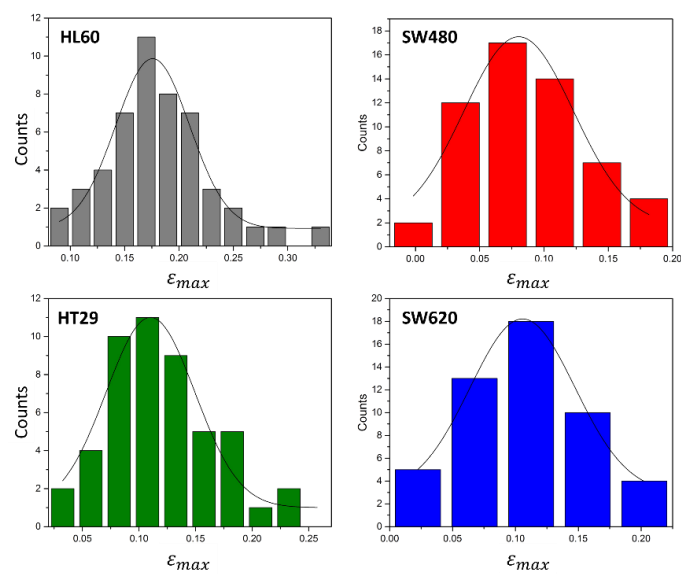


Figure S5 Histograms showing the maximum strain ϵ_{max} of four cell lines. Found using image analysis as deformed at the SP of an extensional flow junction. The flow regime was shear-dominant ($\mu \approx 33$ cP, $Q = 5$ $\mu\text{l}/\text{min}$).

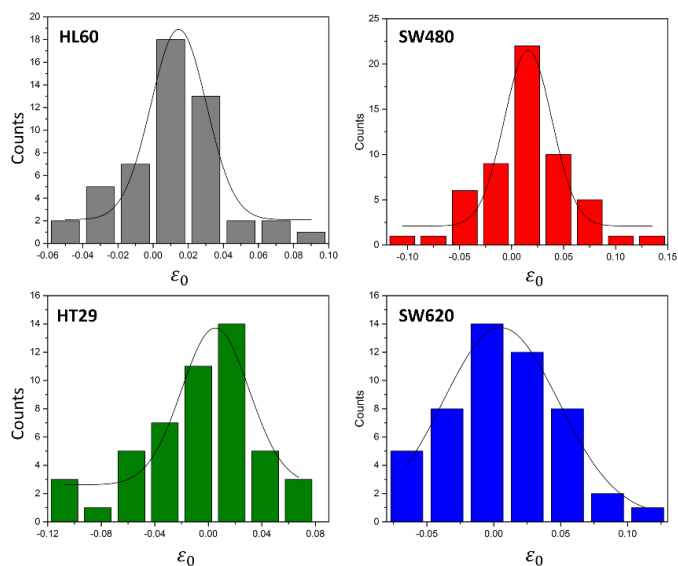


Figure S6 Histograms showing the initial strain ϵ_0 of four cell lines. Found using image analysis as cells approached the SP of an extensional flow junction. The flow regime was shear-dominant ($\mu \approx 33$ cP, $Q = 5 \mu\text{l}/\text{min}$).

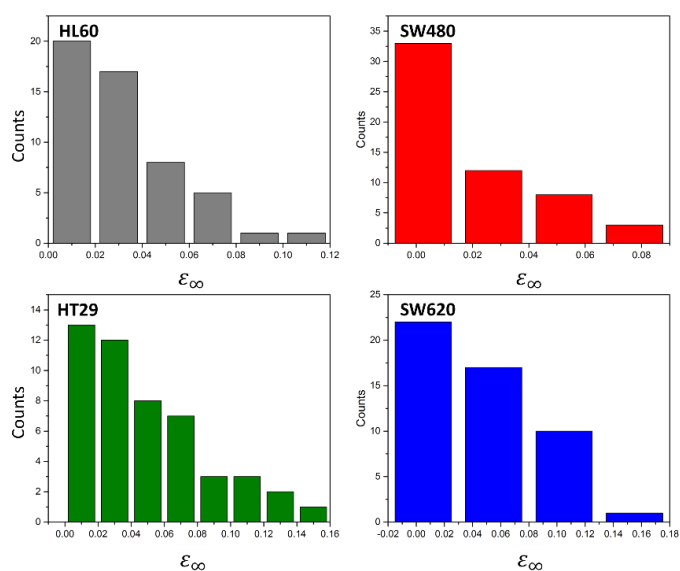


Figure S7 Histograms showing the final strain ϵ_∞ of four cell lines. Found using image analysis as cells recovered after deformation at the SP of an extensional flow junction. The flow regime was shear-dominant ($\mu \approx 33$ cP, $Q = 5 \mu\text{l}/\text{min}$).

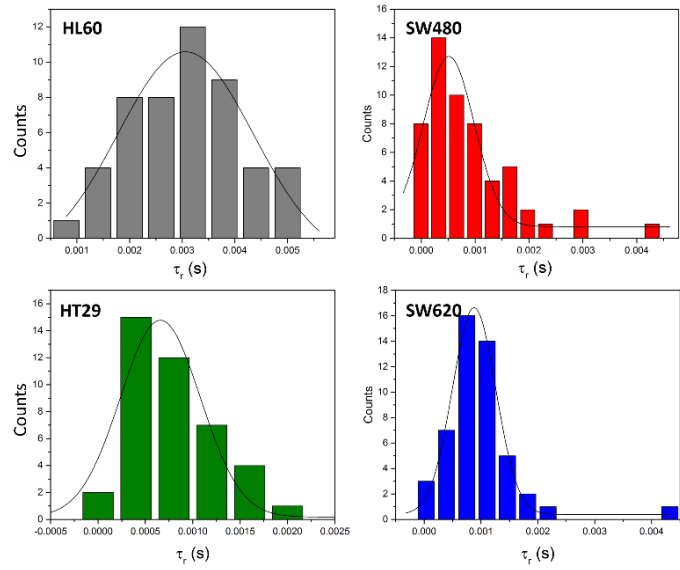


Figure S8 Histograms showing the relaxation time τ_r of four cell lines. Found using image analysis as cells recovered after deformation at the SP of an extensional flow junction. The flow regime was shear-dominant ($\mu \approx 33$ cP, $Q = 5 \mu\text{l}/\text{min}$).

References

- [1] F. J. Armistead, J. Gala De Pablo, S. A. Peyman, H. Gadêlha, and S. D. Evans, “Cells Under Stress: An Inertial-Shear Microfluidic Determination Of Cell Behaviour,” *Biophys. J.*, pp. 1–9, 2019.
- [2] J. G. De Pablo, M. Lones, S. Smith, and S. D. Evans, “Biochemical fingerprint of colorectal cancer cell lines using label - free live single - cell Raman spectroscopy,” no. December 2017, pp. 1–10, 2018.
- [3] M. Kærn, T. C. Elston, W. J. Blake, and J. J. Collins, “Stochasticity in gene expression: From theories to phenotypes,” *Nat. Rev. Genet.*, vol. 6, no. 6, pp. 451–464, 2005.
- [4] L. S. Tsimring, “Noise in biology,” *Reports Prog. Phys.*, vol. 77, no. 2, 2014.
- [5] J. Picot, C. L. Guerin, C. Le Van Kim, and C. M. Boulanger, “Flow cytometry: Retrospective, fundamentals and recent instrumentation,” *Cytotechnology*, vol. 64, no. 2, pp. 109–130, 2012.
- [6] G. Bao and S. Suresh, “Cell and molecular mechanics of biological materials,” *Nat. Mater.*, vol. 2, no. 11, pp. 715–725, 2003.
- [7] S. Suresh, “Biomechanics and biophysics of cancer cells,” *Acta Mater.*, vol. 55, no. 12, pp. 3989–4014, 2007.
- [8] C. Rotsch and M. Radmacher, “Drug-induced changes of cytoskeletal structure and mechanics in fibroblasts: An atomic force microscopy study,” *Biophys. J.*, vol. 78, no. 1, pp. 520–535, 2000.
- [9] S. Kumar and J. L. Mackay, *Measuring the Elastic Properties of Living Cells with Atomic Force Microscopy Indentation.*, 931st ed. Totowa, NJ: Humana Press, 2012.
- [10] K. J. Van Vliet, G. Bao, and S. Suresh, “The biomechanics toolbox: Experimental approaches for living cells and biomolecules,” *Acta Mater.*, vol. 51, no. 19, pp. 5881–5905, 2003.
- [11] F. H. C. Crick and A. F. W. Hughes, “The physical properties of the cytoplasm: A study by means of the magnetic particle method,” *October*, 1949.
- [12] M. Puig-De-Morales, M. Grabulosa, J. Alcaraz, J. Mullol, G. N. Maksym, J. J. Fredberg, and D. Navajas, “Measurement of cell microrheology by magnetic twisting cytometry with frequency domain demodulation,” *J. Appl. Physiol.*, vol. 91, no. 3, pp. 1152–9, 2001.
- [13] J. Guck, R. Ananthakrishnan, H. Mahmood, T. J. Moon, C. C. Cunningham, and J. Käs, “The optical stretcher: A novel laser tool to micromanipulate cells,” *Biophys. J.*, vol. 81, no. 2, pp. 767–784, 2001.
- [14] R. M. Hochmuth, “Micropipette aspiration of living cells,” *J. Biomech.*, vol. 33, no. 1, pp. 15–22, 2000.
- [15] E. Evans and A. Yeung, “Apparent viscosity and cortical tension of blood granulocytes determined by micropipet aspiration,” vol. 56, no. July, pp. 151–160, 1989.
- [16] S. Usami, H. H. Chen, Y. Zhao, S. Chien, and R. Skalak, “Design and construction of a linear shear stress flow chamber,” *Ann. Biomed. Eng.*, vol. 21, no. 1, pp. 77–83, 1993.
- [17] R. J. Pelham and Y. Wang, “Cell locomotion and focal adhesions are regulated by substrate flexibility,” *Proc. Am. Thorac. Soc.*, vol. 94, pp. 13661–13665, 1997.
- [18] H. M. Wyss, “Cell Mechanics: Combining Speed with Precision,” *Biophysj*, vol. 109, no. 10, pp. 1997–1998, 2015.
- [19] Y. Zheng, J. Nguyen, Y. Wei, and Y. Sun, “Recent advances in microfluidic techniques for single-cell biophysical characterization,” *Lab Chip*, vol. 13, no. 13, pp. 2464–83, 2013.
- [20] J. P. Shelby, J. White, K. Ganesan, P. K. Rathod, and D. T. Chiu, “A microfluidic model for single-cell capillary obstruction by Plasmodium falciparum-infected erythrocytes,” *Proc. Natl. Acad. Sci. U. S. A.*, vol. 100, no. 25, pp. 14618–14622, 2003.
- [21] Y. Zheng, E. Shojaei-Baghini, A. Azad, C. Wang, and Y. Sun, “High-throughput biophysical measurement of human red blood cells,” *Lab Chip*, vol. 12, no. 14, pp. 2560–2567, 2012.
- [22] A. Adamo, A. Sharei, L. Adamo, B. Lee, S. Mao, K. F. Jensen, J. P. Shelby, J. White, K. Ganesan, P. K. Rathod, and D. T. Chiu, “Microfluidic-based assessment of cell deformability,” *Proc. Natl. Acad. Sci. U. S. A.*, vol. 100, no. 25, pp. 14618–14622, 2003.

- [23] V. Faustino, D. Pinho, T. Yaginuma, R. C. Calhelha, I. C. F. R. Ferreira, and R. Lima, "Extensional flow-based microfluidic device: deformability assessment of red blood cells in contact with tumor cells," *BioChip J.*, vol. 8, no. 1, pp. 42–47, 2014.
- [24] T. Yaginuma, M. S. N. Oliveira, R. Lima, T. Ishikawa, and T. Yamaguchi, "Human red blood cell behavior under homogeneous extensional flow in a hyperbolic-shaped microchannel.," *Biomicrofluidics*, vol. 7, no. 5, p. 54110, 2013.
- [25] Y. Zheng, J. Nguyen, C. Wang, and Y. Sun, "Electrical measurement of red blood cell deformability on a microfluidic device.," *Lab Chip*, vol. 13, no. 16, pp. 3275–83, 2013.
- [26] S. S. Lee, Y. Yim, K. H. Ahn, and S. J. Lee, "Extensional flow-based assessment of red blood cell deformability using hyperbolic converging microchannel," *Biomed. Microdevices*, vol. 11, no. 5, pp. 1021–1027, 2009.
- [27] D. R. Gossett, H. T. K. Tse, S. A. Lee, Y. Ying, A. G. Lindgren, O. O. Yang, J. Rao, A. T. Clark, and D. Di Carlo, "Hydrodynamic stretching of single cells for large population mechanical phenotyping," *Proc. Natl. Acad. Sci.*, vol. 109, no. 20, pp. 7630–7635, 2012.
- [28] D. Di Carlo, D. Irimia, R. G. Tompkins, and M. Toner, "Continuous inertial focusing, ordering, and separation of particles in microchannels.," *Proc. Natl. Acad. Sci. U. S. A.*, vol. 104, no. 48, pp. 18892–18897, 2007.
- [29] S. Cha, T. Shin, S. S. Lee, W. Shim, G. Lee, S. J. Lee, Y. Kim, and J. M. Kim, "Cell Stretching Measurement Utilizing Viscoelastic Particle Focusing," 2012.
- [30] J. S. Dudani, D. R. Gossett, H. T. Tse, and D. Di Carlo, "Pinched-flow hydrodynamic stretching of single-cells," *Lab Chip*, vol. 13, no. 18, pp. 3728–3734, 2013.
- [31] E. M. Darling and D. Di Carlo, *High-Throughput Assessment of Cellular Mechanical Properties*. 2015.
- [32] H. T. K. Tse, D. R. Gossett, Y. S. Moon, M. Masaeli, M. Sohsman, Y. Ying, K. Mislick, R. P. Adams, J. Rao, and D. Di Carlo, "Quantitative diagnosis of malignant pleural effusions by single-cell mechanophenotyping.," *Sci. Transl. Med.*, vol. 5, no. 212, p. 212ra163, 2013.
- [33] O. Otto, P. Rosendahl, S. Golfier, A. Mietke, M. Herbig, A. Jacobi, N. Töpfner, C. Herold, D. Klaue, S. Girardo, M. Winzi, and J. Guck, "Real - Time Deformability Cytometry as a Label - Free Indicator of Cell Function *," pp. 1861–1864, 2015.
- [34] A. Mietke, O. Otto, S. Girardo, P. Rosendahl, A. Taubenberger, S. Golfier, E. Ulbricht, S. Aland, J. Guck, and E. Fischer-Friedrich, "Extracting Cell Stiffness from Real-Time Deformability Cytometry: Theory and Experiment," *Biophys. J.*, vol. 109, no. 10, pp. 2023–2036, 2015.
- [35] L. Guillou, J. B. Dahl, J. G. Lin, A. I. Barakat, J. Husson, and S. J. Muller, "Measuring Cell Viscoelastic Properties Using a Microfluidic Extensional Flow Device," *Biophysj*, vol. 111, no. 9, pp. 2039–2050, 2016.
- [36] J. Guck, S. Schinkinger, B. Lincoln, F. Wottawah, S. Ebert, M. Romeyke, D. Lenz, H. M. Erickson, R. Ananthakrishnan, D. Mitchell, J. Käs, S. Ulvick, and C. Bilby, "Optical Deformability as an Inherent Cell Marker for Testing Malignant Transformation and Metastatic Competence," *Biophys. J.*, vol. 88, no. 5, pp. 3689–3698, 2005.
- [37] Q. Guo, S. Park, and H. Ma, "Microfluidic micropipette aspiration for measuring the deformability of single cells," *Lab Chip*, vol. 12, no. 15, pp. 2687–2695, 2012.
- [38] I. L. Ahmad and M. R. Ahmad, "Technological advancements in characterizing single cell's stiffness properties- A review," *IECBES 2014, Conf. Proc. - 2014 IEEE Conf. Biomed. Eng. Sci. "Miri, Where Eng. Med. Biol. Humanit. Meet."*, pp. 187–192, 2014.
- [39] O. K. Baskurt, D. Gelmont, and H. J. Meiselman, "Red blood cell deformability in sepsis," *Am J Respir Crit Care Med*, vol. 157, no. 2, p. 421–7., 1998.
- [40] Q. Guo, S. J. Reiling, P. Rohrbach, and H. Ma, "Microfluidic biomechanical assay for red blood cells parasitized by *Plasmodium falciparum*," *Lab Chip*, vol. 12, no. 6, p. 1143, 2012.
- [41] D. E. McMillan, N. G. Utterback, and J. La Puma, "Reduced erythrocyte deformability in diabetes," *Diabetes*, vol. 27, no. 9, pp. 895–901, 1978.
- [42] J. Stuart and G. B. Nash, "Red cell deformability and haematological disorders," *Blood Rev.*, vol. 4, no. 3, pp. 141–147, 1990.

- [43] S. E. Cross, Y.-S. Jin, J. Rao, and J. K. Gimzewski, “Nanomechanical analysis of cells from cancer patients.,” *Nat. Nanotechnol.*, vol. 2, no. 12, pp. 780–3, 2007.
- [44] S. M. Ahmmed, S. S. Bithi, A. A. Pore, N. Mubtasim, C. Schuster, L. S. Gollahon, and S. A. Vanapalli, “Multi-sample deformability cytometry of cancer cells,” *APL Bioeng.*, vol. 2, no. 3, p. 32002, 2018.
- [45] A. V. Nguyen, K. D. Nyberg, M. B. Scott, A. M. Welsh, A. H. Nguyen, N. Wu, S. V. Hohlbauch, N. A. Geisse, E. A. Gibb, A. G. Robertson, T. R. Donahue, and A. C. Rowat, “Stiffness of pancreatic cancer cells is associated with increased invasive potential,” *Integr. Biol. (United Kingdom)*, vol. 8, no. 12, pp. 1232–1245, 2016.
- [46] M. Xavier, P. Rosendahl, M. Herbig, M. Kräter, D. Spencer, M. Bornhäuser, R. O. C. Oreffo, H. Morgan, J. Guck, and O. Otto, “Mechanical phenotyping of primary human skeletal stem cells in heterogeneous populations by real-time deformability cytometry.,” *Integr. Biol. (Camb.)*, pp. 10–12, 2016.
- [47] Z. S. Khan and S. A. Vanapalli, “Probing the mechanical properties of brain cancer cells using a microfluidic cell squeezer device,” *Biomicrofluidics*, vol. 7, no. 1, pp. 1–15, 2013.
- [48] M. Masaeli, D. Gupta, S. O. Byrne, H. T. K. Tse, D. R. Gossett, P. Tseng, A. S. Utada, H. Jung, S. Young, A. T. Clark, and D. Di Carlo, “Multiparameter mechanical and morphometric screening of cells,” *Nat. Publ. Gr.*, no. October 2015, pp. 1–11, 2016.
- [49] A. C. Hodgson, C. M. Verstreken, C. L. Fisher, U. F. Keyser, and K. J. Chalut, “A microfluidic device for characterizing nuclear deformations,” *Lab Chip*, vol. 17, pp. 805–813, 2017.
- [50] S. Golfier, P. Rosendahl, A. Mietke, M. Herbig, J. Guck, and O. Otto, “High-throughput cell mechanical phenotyping for label-free titration assays of cytoskeletal modifications,” *Cytoskeleton*, vol. 74, no. 8, pp. 283–296, 2017.
- [51] S. Pagliara, K. Franze, C. R. McClain, G. W. Wylde, C. L. Fisher, R. J. M. Franklin, A. J. Kabla, U. F. Keyser, and K. J. Chalut, “Auxetic nuclei in embryonic stem cells exiting pluripotency.,” *Nat. Mater.*, vol. 13, no. 6, pp. 638–44, 2014.
- [52] C. J. Chan, A. E. Ekpenyong, S. Golfier, W. Li, K. J. Chalut, and O. Otto, “Myosin II Activity Softens Cells in Suspension,” vol. 108, no. April, pp. 1856–1869, 2015.
- [53] L. Reymond, E. D. Este, A. Masharina, F. Göttfert, H. Ta, A. Güther, M. Fournier, S. Rizzo, H. Waldmann, C. Blaukopf, C. Sommer, D. W. Gerlich, H. Arndt, S. W. Hell, and K. Johnsson, “Fluorogenic probes for live-cell imaging of the cytoskeleton,” vol. 11, no. 7, 2014.
- [54] N. R. C. Mechanotyping, Y. Deng, S. P. Davis, F. Yang, K. S. Paulsen, M. Kumar, R. S. Devaux, X. Wang, D. S. Conklin, A. Oberai, J. I. Herschkowitz, and A. J. Chung, “Inertial Microfluidic Cell Stretcher (iMCS): Fully Automated ,” pp. 1–11, 2017.
- [55] D. Schaffert and E. Wagner, “Gene therapy progress and prospects: Synthetic polymer-based systems,” *Gene Ther.*, vol. 15, no. 16, pp. 1131–1138, 2008.
- [56] B. Leader, Q. J. Baca, and D. E. Golan, “Protein Therapeutics: a summary and pharmacological classification,” *Nat. Rev. Drug Discov.*, vol. 7, no. January, pp. 21–39, 2008.
- [57] Z. X. Jiang and Z. Y. Zhang, “Targeting PTPs with small molecule inhibitors in cancer treatment,” *Cancer Metastasis Rev.*, vol. 27, no. 2, pp. 263–272, 2008.
- [58] A. M. Derfus, W. C. W. Chan, and S. N. Bhatia, “Intracellular delivery of quantum dots for live cell labeling and organelle tracking,” *Adv. Mater.*, vol. 16, no. 12, pp. 961–966, 2004.
- [59] S. S. Gambhir and S. Weiss, “Quantum Dots for Live Cells, in Vivo Imaging, and Diagnostics,” *Science (80-.)*, vol. 307, no. January, pp. 538–545, 2005.
- [60] M. Dahan, S. Lévi, C. Luccardini, P. Rostaing, B. Riveau, and A. Triller, “Diffusion Dynamics of Glycine Receptors Revealed by Single-Quantum Dot Tracking,” *Science (80-.)*, vol. 302, no. 5644, pp. 442–445, 2003.
- [61] M. P. Stewart, R. Langer, and K. F. Jensen, “Intracellular Delivery by Membrane Disruption : Mechanisms , Strategies , and Concepts,” *Chem. Rev.*, vol. 118, pp. 7409–7531, 2018.
- [62] A. Verma, U. Oktay, Y. Hu, Y. Hu, H.-S. Han, N. Watson, S. Chen, D. J. Irvine, and S. Francesco, “Surface Structure-Regulated Cell Membrane Penetration by Monolayer Protected Nanoparticles Ayush,” *NIH-PA*, vol. 7, no. 7, pp. 588–595, 2008.
- [63] S. Yoon, M. G. Kim, C. T. Chiu, J. Y. Hwang, H. H. Kim, Y. Wang, and K. K. Shung, “Direct

- and sustained intracellular delivery of exogenous molecules using acoustic-transfection with high frequency ultrasound,” *Sci. Rep.*, vol. 6, no. July 2015, pp. 1–11, 2016.
- [64] Y. Zhang and L. C. Yu, “Microinjection as a tool of mechanical delivery,” *Curr. Opin. Biotechnol.*, vol. 19, no. 5, pp. 506–510, 2008.
- [65] J. Lee, A. Sharei, W. Y. Sim, A. Adamo, R. Langer, K. F. Jensen, and M. G. Bawendi, “Nonendocytic delivery of functional engineered nanoparticles into the cytoplasm of live cells using a novel, high-throughput microfluidic device,” *Nano Lett.*, vol. 12, no. 12, pp. 6322–6327, 2012.
- [66] A. Sharei, J. Zoldan, A. Adamo, W. Young, N. Cho, E. Jackson, S. Mao, R. Langer, and K. F. Jensen, “A vector-free microfluidic platform for intracellular delivery,” *PNAS*, vol. 110, no. 6, 2013.
- [67] G. L. Szeto, D. Van Egeren, H. Worku, A. Sharei, B. Alejandro, C. Park, K. Frew, M. Brefo, S. Mao, M. Heimann, R. Langer, K. Jensen, and D. J. Irvine, “Microfluidic squeezing for intracellular antigen loading in polyclonal B-cells as cellular vaccines,” *Sci. Rep.*, vol. 5, no. April, pp. 1–13, 2015.
- [68] Y. Deng, M. Kizer, M. Rada, J. Sage, X. Wang, D. J. Cheon, and A. J. Chung, “Intracellular Delivery of Nanomaterials via an Inertial Microfluidic Cell Hydroporator,” *Nano Lett.*, vol. 18, no. 4, pp. 2705–2710, 2018.
- [69] P. Rosendahl, K. Plak, A. Jacobi, M. Kraeter, N. Toepfner, O. Otto, C. Herold, M. Winzi, M. Herbig, Y. Ge, S. Girardo, K. Wagner, B. Baum, and J. Guck, “Real-time fluorescence and deformability cytometry,” *Nat. Methods*, vol. 15, no. 5, pp. 355–358, 2018.
- [70] H. Mikami, J. Harmon, H. Kobayashi, S. Hamad, Y. Wang, O. Iwata, K. Suzuki, T. Ito, Y. Aisaka, N. Kutsuna, K. Nagasawa, H. Watarai, Y. Ozeki, and K. Goda, “Ultrafast confocal fluorescence microscopy beyond the fluorescence lifetime limit,” *Optica*, vol. 5, no. 2, p. 117, 2018.
- [71] C. Lei, H. Kobayashi, Y. Wu, M. Li, A. Isozaki, A. Yasumoto, H. Mikami, T. Ito, N. Nitta, T. Sugimura, M. Yamada, Y. Yatomi, D. Di Carlo, Y. Ozeki, and K. Goda, “High-throughput imaging flow cytometry by optical time-stretch microscopy,” vol. 13, no. July, 2018.
- [72] B. Chance, P. Mueller, D. De Vault, and L. Powers, “Biological membranes,” *Phys. Today*, vol. 33, no. 10, pp. 32–38, 1980.
- [73] Y. Nematbakhsh and C. T. Lim, “Cell biomechanics and its applications in human disease diagnosis,” *Acta Mech. Sin. Xuebao*, vol. 31, no. 2, pp. 268–273, 2015.
- [74] M. B. Omary, N. O. Ku, G. Z. Tao, D. M. Toivola, and J. Liao, “‘Heads and tails’ of intermediate filament phosphorylation: multiple sites and functional insights,” *Trends Biochem. Sci.*, vol. 31, no. 7, pp. 383–394, 2006.
- [75] K. A. Michie and J. Löwe, “Dynamic Filaments of the Bacterial Cytoskeleton,” *Annu. Rev. Biochem.*, vol. 75, no. 1, pp. 467–492, 2006.
- [76] S. Mostowy, “Multiple Roles of the Cytoskeleton in Bacterial Autophagy,” *PLoS Pathog.*, vol. 10, no. 11, pp. 1–7, 2014.
- [77] A. Wegner and J. Engel, “Kinetics of the cooperative association of actin to actin filaments,” *Biophys. Chem.*, pp. 215–225, 1975.
- [78] A. Manuscript, “Polymer physics of the cytoskeleton,” pp. 1–13, 2012.
- [79] A. G. Clark, K. Dierkes, and E. K. Paluch, “Monitoring actin cortex thickness in live cells,” *Biophys. J.*, vol. 105, no. 3, pp. 570–580, 2013.
- [80] S. Petry and R. D. Vale, “Microtubule nucleation at the centrosome and beyond,” *Nat. Cell Biol.*, vol. 17, no. 9, pp. 1089–1093, 2015.
- [81] K. Albers, E. Fuchs, J. C. Biol, S. R. Gill, P. C. Wong, M. J. Monteiro, J. C. Sci, E. Rosevear, R. D. Goldman, and P. Natl, “Kinesin and Dynein Superfamily Proteins and the Mechanism of Organelle Transport,” vol. 279, no. January 1998, 2005.
- [82] Z. Qin, M. J. Buehler, and L. Kreplak, “A multi-scale approach to understand the mechanobiology of intermediate filaments,” *J. Biomech.*, vol. 43, no. 1, pp. 15–22, 2010.
- [83] P. A. Janmey, U. Euteneuer, P. Traub, and M. Schliwa, “Viscoelastic properties of vimentin compared with other filamentous biopolymer networks,” *J. Cell Biol.*, vol. 113, no. 1, pp. 155–

- 160, 1991.
- [84] J. Lammerding, “Mechanics of the Nucleus,” vol. 1, no. 2, pp. 783–807, 2015.
- [85] A. L. Rynearson and C. R. Sussman, “Nuclear structure, organization, and oncogenesis,” *J. Gastrointest. Cancer*, vol. 42, no. 2, pp. 112–117, 2011.
- [86] J. D. Pajerowski, D. E. Discher, F. L. Zhong, K. N. Dahl, and P. J. Sannak, “Physical plasticity of the nucleus in stem cell differentiation,” *Proc. Natl. Acad. Sci.*, vol. 104, no. 40, pp. 15619–15624, 2007.
- [87] K. J. Chalut, M. Höpfler, F. Lautenschläger, L. Boyde, C. J. Chan, A. Ekpenyong, A. Martinez-Arias, and J. Guck, “Chromatin decondensation and nuclear softening accompany Nanog downregulation in embryonic stem cells,” *Biophys. J.*, vol. 103, no. 10, pp. 2060–2070, 2012.
- [88] M. Krause, J. Te Riet, and K. Wolf, “Probing the compressibility of tumor cell nuclei by combined atomic force-confocal microscopy,” *Phys. Biol.*, vol. 10, no. 6, 2013.
- [89] J. S. H. Lee, C. M. Hale, P. Panorchan, S. B. Khatau, J. P. George, Y. Tseng, C. L. Stewart, D. Hodzic, and D. Wirtz, “Nuclear lamin A/C deficiency induces defects in cell mechanics, polarization, and migration,” *Biophys. J.*, vol. 93, no. 7, pp. 2542–2552, 2007.
- [90] N. Caille, O. Thoumine, Y. Tardy, and J. Meister, “Contribution of the nucleus to the mechanical properties of endothelial cells,” vol. 35, pp. 177–187, 2002.
- [91] A. Vaziri and M. R. K. Mofrad, “Mechanics and deformation of the nucleus in micropipette aspiration experiment,” *J. Biomech.*, vol. 40, no. 9, pp. 2053–2062, 2007.
- [92] K. N. Dahl, A. J. Engler, J. D. Pajerowski, and D. E. Discher, “Power-law rheology of isolated nuclei with deformation mapping of nuclear substructures,” *Biophys. J.*, vol. 89, no. 4, pp. 2855–2864, 2005.
- [93] J. Lammerding, K. N. Dahl, D. E. Discher, and R. D. Kamm, “Nuclear Mechanics and Methods,” *Methods Cell Biol.*, vol. 83, no. 7, pp. 269–294, 2007.
- [94] J. Schäpe, S. Prauße, M. Radmacher, and R. Stick, “Influence of lamin A on the mechanical properties of amphibian oocyte nuclei measured by atomic force microscopy,” *Biophys. J.*, vol. 96, no. 10, pp. 4319–4325, 2009.
- [95] C. GM, *The Cell: A Molecular Approach.*, 2nd Editio. Sinauer Associates, 2000.
- [96] O. Otto, P. Rosendahl, A. Mietke, S. Golfier, C. Herold, D. Klaue, S. Girardo, S. Pagliara, A. Ekpenyong, A. Jacobi, M. Wobus, N. Töpfner, U. F. Keyser, J. Mansfeld, E. Fischer-Friedrich, and J. Guck, “Real-time deformability cytometry: on-the-fly cell mechanical phenotyping,” *Nat. Methods*, vol. 12, no. 3, 2015.
- [97] P. Kunda and B. Baum, “The actin cytoskeleton in spindle assembly and positioning,” *Trends Cell Biol.*, vol. 19, no. 4, pp. 174–179, 2009.
- [98] Cancer Research UK, “Cancer incidence for common cancers.” [Online]. Available: <https://www.cancerresearchuk.org/health-professional/cancer-statistics/incidence/common-cancers-compared#heading-Zero>. [Accessed: 28-May-2019].
- [99] Cancer Research UK, “Bowel cancer statistics.” [Online]. Available: <https://www.cancerresearchuk.org/health-professional/cancer-statistics/statistics-by-cancer-type/bowel-cancer#heading-Zero>. [Accessed: 28-May-2019].
- [100] “Colorectal Cancer Survival by Stage- NCIN Data Briefing.” [Online]. Available: http://www.ncin.org.uk/publications/data_briefings/colorectal_cancer_survival_by_stage. [Accessed: 28-May-2019].
- [101] S. D. Markowitz and M. M. Bertagnolli, “Molecular Origins of cancer,” *N. Engl. J. Med.*, vol. 361, no. 25, pp. 2449–2460, 2010.
- [102] B. Vogelstein and K. W. Kinzler, “Cancer genes and the pathways they control,” *Nat. Med.*, vol. 10, no. 8, pp. 789–799, 2004.
- [103] L. Sompayac, *How Cancer Works*. Jones and Bartlett.
- [104] R. J. Davies, R. Miller, and N. Coleman, “Colorectal cancer screening: Prospects for molecular stool analysis,” *Nat. Rev. Cancer*, vol. 5, no. 3, pp. 199–209, 2005.
- [105] K. O. Alfarouk, C. M. Stock, S. Taylor, M. Walsh, A. K. Muddathir, D. Verduzco, A. H. H. Bashir, O. Y. Mohammed, G. O. Elhassan, S. Harguindey, S. J. Reshkin, M. E. Ibrahim, and C. Rauch, “Resistance to cancer chemotherapy: Failure in drug response from ADME to P-gp,”

Cancer Cell Int., vol. 15, no. 1, pp. 1–13, 2015.

- [106] R. E. Hewitt, A. Mcmarlin, D. Kleiner, R. Wersto, P. Martin, M. Tsoskas, G. W. H. Stamp, and W. G. Stetler-stevenson, “Validation of a model of colon cancer progression,” vol. 9896, pp. 446–454, 2000.
- [107] A. Leibovitz, J. C. Stinson, W. B. McCombs, C. E. McCoy, K. C. Mazur, and N. D. Mabry, “Human Colorectal Adenocarcinoma Cell Lines,” *Cancer Res.*, vol. 36, no. December, pp. 4562–4569, 1976.
- [108] E. Buck, A. Eyzaguirre, S. Barr, S. Thompson, R. Sennello, D. Young, K. K. Iwata, N. W. Gibson, P. Cagnoni, and J. D. Haley, “Loss of homotypic cell adhesion by epithelial-mesenchymal transition or mutation limits sensitivity to epidermal growth factor receptor inhibition,” *Mol. Cancer Ther.*, vol. 6, no. 2, pp. 532–541, 2007.
- [109] J. Fogh, *Human Tumor Cells in Vitro*. Boston: MA: Springer US, 1975.
- [110] D. Ahmed, P. W. Eide, I. A. Eilertsen, S. A. Danielsen, M. Eknæs, M. Hektoen, G. E. Lind, and R. A. Lothe, “Epigenetic and genetic features of 24 colon cancer cell lines,” *Oncogenesis*, vol. 2, no. 424, 2013.
- [111] K. Cai, K. Mulatz, R. Ard, T. Nguyen, and S. H. Gee, “Increased diacylglycerol kinase zeta expression in human metastatic colon cancer cells augments Rho GTPase activity and contributes to enhanced invasion,” *BMC Cancer*, vol. 14, no. 1, p. 208, 2014.
- [112] D. Ghosh, H. Yu, X. F. Tan, T. K. Lim, R. M. Zubaidah, H. T. Tan, M. C. M. Chung, and Q. Lin, “Identification of key players for colorectal cancer metastasis by iTRAQ quantitative proteomics profiling of isogenic SW480 and SW620 cell lines,” *J. Proteome Res.*, vol. 10, no. 10, pp. 4373–4387, 2011.
- [113] M. Katayama, H. Nakano, A. Ishiuchi, W. Wu, R. Oshima, J. Sakurai, H. Nishikawa, S. Yamaguchi, and T. Otsubo, “Protein pattern difference in the colon cancer cell lines examined by two-dimensional differential in-gel electrophoresis and mass spectrometry,” *Surg. Today*, vol. 36, no. 12, pp. 1085–1093, 2006.
- [114] E. Foran, P. McWilliam, D. Kelleher, D. T. Croke, and A. Long, “The leukocyte protein L-plastin induces proliferation, invasion and loss of E-cadherin expression in colon cancer cells,” *Int. J. Cancer*, vol. 118, no. 8, pp. 2098–2104, 2006.
- [115] X. L. Zhu, L. Liang, and Y. Q. Ding, “Overexpression of FMNL2 is closely related to metastasis of colorectal cancer,” *Int. J. Colorectal Dis.*, vol. 23, no. 11, pp. 1041–1047, 2008.
- [116] A. Elfick, D. Tsikritis, H. Shi, Y. Wang, S. Velugotla, and V. Sr, “Label-Free Biomarkers of Human Embryonic Stem Cell Differentiation to Hepatocytes se n,” pp. 575–584, 2016.
- [117] V. Palmieri, D. Lucchetti, A. Maiorana, M. Papi, G. Maulucci, F. Calapa, G. Ciasca, and R. Giordano, “Soft Matter primary tumor and lymph node metastasis cells,” pp. 5719–5726, 2015.
- [118] J. M. Northcott, I. S. Dean, J. K. Mouw, and V. M. Weaver, “Feeling Stress: The Mechanics of Cancer Progression and Aggression,” *Front. Cell Dev. Biol.*, vol. 6, no. February, pp. 1–12, 2018.
- [119] S. Kumar and V. M. Weaver, “Mechanics, malignancy, and metastasis: The force journey of a tumor cell,” *Cancer Metastasis Rev.*, vol. 28, no. 1–2, pp. 113–127, 2009.
- [120] H. Sato and M. Suzuki, *Deformability and viability of tumor cells by transcapillary passage with reference to organ affinity of metastasis in cancer*. 1976.
- [121] K. A. Ward, W. I Li, S. Zimmer, and T. Davis, *Viscoelastic properties of transformed cells: Role in tumor cell progression and metastasis formation*, vol. 28. 1991.
- [122] J. Roche, “The epithelial-to-mesenchymal transition in cancer,” *Cancers (Basel)*, vol. 10, no. 2, pp. 10–13, 2018.
- [123] P. Dey, “Cancer Nucleus: Morphology and Beyond,” *Diagn. Cytopathol.*, vol. 0, no. 0, pp. 1–5, 2011.
- [124] W. Xu, R. Mezencev, B. Kim, L. Wang, J. McDonald, and T. Sulchek, “Cell Stiffness Is a Biomarker of the Metastatic Potential of Ovarian Cancer Cells,” *PLoS One*, vol. 7, no. 10, 2012.
- [125] S. Suresh, “Biomechanics and biophysics of cancer cells,” *Acta Mater.*, vol. 55, no. 12, pp. 3989–4014, 2007.
- [126] C. R. Ethier and C. a. Simmons, *Introductory Biomechanics From Cells to Organisms*. 2007.

- [127] A. R. Bausch, F. Ziemann, A. A. Boulbitch, K. Jacobson, and E. Sackmann, “Local measurements of viscoelastic parameters of adherent cell surfaces by magnetic bead microrheometry.,” *Biophys. J.*, vol. 75, no. 4, pp. 2038–2049, 1998.
- [128] S. Moreno-Flores, R. Benitez, M. D. M. Vivanco, and J. L. Toca-Herrera, “Stress relaxation and creep on living cells with the atomic force microscope: A means to calculate elastic moduli and viscosities of cell components,” *Nanotechnology*, vol. 21, no. 44, 2010.
- [129] A. Cartagena and A. Raman, “Local viscoelastic properties of live cells investigated using dynamic and quasi-static atomic force microscopy methods,” *Biophys. J.*, vol. 106, no. 5, pp. 1033–1043, 2014.
- [130] K. B. Roth, C. D. Eggleton, K. B. Neeves, and D. W. M. Marr, “Measuring cell mechanics by optical alignment compression cytometry.,” *Lab Chip*, vol. 13, no. 8, pp. 1571–7, 2013.
- [131] T. Tiffert, R. Seear, V. L. Lew, A. Esposito, C. F. Kaminski, J. M. A. Mauritz, F. Lautenschläger, and J. Guck, “Detection of Plasmodium falciparum-infected red blood cells by optical stretching,” *J. Biomed. Opt.*, vol. 15, no. 3, p. 30517, 2010.
- [132] G. Tomaiuolo, M. Barra, V. Preziosi, A. Cassinese, B. Rotoli, and S. Guido, “Microfluidics analysis of red blood cell membrane viscoelasticity.,” *Lab Chip*, vol. 11, no. 3, pp. 449–454, 2011.
- [133] J.-F. Berret, “Local viscoelasticity of living cells measured by rotational magnetic spectroscopy,” *Nat. Commun.*, vol. 7, p. 18, 2015.
- [134] E. A. López-Guerra and S. D. Solares, “Modeling viscoelasticity through spring-dashpot models in intermittent-contact atomic force microscopy,” *Beilstein J. Nanotechnol.*, vol. 5, no. 1, pp. 2149–2163, 2014.
- [135] Y. Guo, X. Zhang, T. Wang, Y. Zheng, S. Chen, H. Lin, Y. Shen, X. Chen, and Y. Zhu, “Analyzing and modeling rheological behavior of liver fibrosis in rats using shear viscoelastic moduli,” *J. Zhejiang Univ. Sci. B*, vol. 15, no. 4, pp. 375–381, 2014.
- [136] B. Carmichael, H. Babahosseini, S. N. Mahmoodi, and M. Agah, “The fractional viscoelastic response of human breast tissue cells,” *Phys. Biol.*, vol. 12, no. 4, 2015.
- [137] G. W. Schmid-Schönbein, K. L. Sung, H. Tözere, R. Skalak, and S. Chien, “Passive mechanical properties of human leukocytes,” *Biophys. J.*, vol. 36, no. 1, pp. 243–256, 1981.
- [138] R. Tran-Son-Tay, D. Needham, A. Yeung, and R. M. Hochmuth, “Time-dependent recovery of passive neutrophils after large deformation,” *Biophys. J.*, vol. 60, no. October, pp. 856–866, 1991.
- [139] A. R. Bausch, F. Ziemann, A. A. Boulbitch, K. Jacobson, and E. Sackmann, “Local measurements of viscoelastic parameters of adherent cell surfaces by magnetic bead microrheometry.,” *Biophys. J.*, vol. 75, no. 4, pp. 2038–2049, 1998.
- [140] V. M. Laurent, R. Fodil, P. Cañadas, S. Féréol, B. Louis, E. Planus, and D. Isabey, “Partitioning of cortical and deep cytoskeleton responses from transient magnetic bead twisting,” *Ann. Biomed. Eng.*, vol. 31, no. 10, pp. 1263–1278, 2003.
- [141] S. Moreno-Flores, R. Benitez, M. d. M. Vivanco, and J. L. Toca-Herrera, “Stress relaxation microscopy: Imaging local stress in cells,” *J. Biomech.*, vol. 43, no. 2, pp. 349–354, 2010.
- [142] H. Babahosseini, B. Carmichael, J. S. Strobl, S. N. Mahmoodi, and M. Agah, “Sub-cellular force microscopy in single normal and cancer cells,” *Biochem. Biophys. Res. Commun.*, vol. 463, no. 4, pp. 587–592, 2015.
- [143] P. Kollmannsberger and B. Fabry, “Linear and Nonlinear Rheology of Living Cells,” *Annu. Rev. Mater. Res.*, vol. 41, pp. 75–97, 2011.
- [144] B. D. Hoffman, G. Massiera, K. M. Van Citters, and J. C. Crocker, “The consensus mechanics of cultured mammalian cells.,” *Proc. Natl. Acad. Sci. U. S. A.*, vol. 103, no. 27, pp. 10259–10264, 2006.
- [145] B. D. Hoffman and J. C. Crocker, “Cell mechanics: dissecting the physical responses of cells to force.,” *Annu. Rev. Biomed. Eng.*, vol. 11, pp. 259–288, 2009.
- [146] B. Fabry, G. N. Maksym, J. P. Butler, M. Glogauer, D. Navajas, and J. J. Fredberg, “Scaling the microrheology of living cells,” *Phys. Rev. Lett.*, vol. 87, no. 14, pp. 1–4, 2001.
- [147] L. Wolff, P. Fernández, and K. Kroy, “Resolving the Stiffening-Softening Paradox in Cell

- Mechanics,” *PLoS One*, vol. 7, no. 7, p. e40063, Jul. 2012.
- [148] P. a Janmey, S. Hvidt, J. Lamb, and T. P. Stossel, “Resemblance of actin-binding protein/actin gels to covalently crosslinked networks,” *Nature*, vol. 345, no. 6270, pp. 89–92, 1990.
- [149] P. Sollich, “Rheological constitutive equation for model of soft glassy materials,” *Phys. Rev. E*, vol. 58, no. 1, pp. 738–759, 1998.
- [150] D. E. Ingber, “Tensegrity I. Cell structure and hierarchical systems biology.,” *J. Cell Sci.*, vol. 116, no. Pt 7, pp. 1157–1173, 2003.
- [151] C. Sultan, D. Stamenovic, and D. E. Ingber, “{A} computational tensegrity model predicys dynamic reological behaviors in living cells.,” *Ann Biomed Eng*, vol. 32, no. 4, pp. 520–530, 2004.
- [152] E. H. Zhou, F. D. Martinez, and J. J. Fredberg, “Cell rheology: Mush rather than machine,” *Nat. Mater.*, vol. 12, no. 3, pp. 184–185, 2013.
- [153] E. Moeendarbary, L. Valon, M. Fritzsche, A. R. Harris, D. a Moulding, A. J. Thrasher, E. Stride, L. Mahadevan, and G. T. Charras, “The cytoplasm of living cells behaves as a poroelastic material.,” *Nat. Mater.*, vol. 12, no. 3, pp. 253–61, 2013.
- [154] K. Haase, T. N. Shendruk, and A. E. Pelling, “Rapid dynamics of cell-shape recovery in response to local deformations,” *Soft Matter*, vol. 13, no. 3, pp. 567–577, 2017.
- [155] N. Bonakdar, R. Gerum, M. Kuhn, M. Spörrer, A. Lippert, W. Schneider, K. E. Aifantis, and B. Fabry, “Mechanical plasticity of cells,” vol. 15, no. October, 2016.
- [156] K. K. Y. Ho, Y. L. Wang, J. Wu, and A. P. Liu, “Advanced Microfluidic Device Designed for Cyclic Compression of Single Adherent Cells,” *Front. Bioeng. Biotechnol.*, vol. 6, no. October, pp. 1–13, 2018.
- [157] A. Manz, N. Graber, and H. M. Widmer, “Miniturized Total Chemical Analysis Systems: A Novel Concept for Chemical Sensing,” *Sensors and Actuators*, vol. 1, no. 1–6, pp. 244–248, 1990.
- [158] D. J. Acheson, *Elementary Fluid Dynamics*. 1990.
- [159] E. M. Purcell, “Life at low Reynolds number,” *Am. J. Phys.*, vol. 45, no. 1, pp. 3–11, 1977.
- [160] D. J. Beebe, G. a Mensing, and G. M. Walker, “Physics and applications of microfluidics in biology.,” *Annu. Rev. Biomed. Eng.*, vol. 4, pp. 261–286, 2002.
- [161] H. A. Stone, A. D. Stroock, and A. Ajdari, “Engineering Flows in Small Devices,” *Annu. Rev. Fluid Mech.*, vol. 36, no. 1, pp. 381–411, 2004.
- [162] K. Avila, D. Moxey, A. De Lozar, M. Avila, D. Barkley, and B. Hof, “The onset of turbulence in pipe flow,” *Science (80-.)*, vol. 333, no. 6039, pp. 192–196, 2011.
- [163] J. P. Abraham, E. M. Sparrow, and W. J. Minkowycz, “Internal-flow Nusselt numbers for the low-Reynolds-number end of the laminar-to-turbulent transition regime,” *Int. J. Heat Mass Transf.*, vol. 54, no. 1–3, pp. 584–588, 2011.
- [164] D. Di Carlo, “Inertial microfluidics,” *Lab Chip*, vol. 9, no. 21, p. 3038, 2009.
- [165] D. Di Carlo, D. Irimia, R. G. Tompkins, and M. Toner, “Continuous inertial focusing, ordering, and separation of particles in microchannels.,” *Proc. Natl. Acad. Sci. U. S. A.*, vol. 104, no. 48, pp. 18892–7, 2007.
- [166] J. Che, V. Yu, M. Dhar, C. Renier, M. Matsumoto, K. Heirich, E. B. Garon, J. Goldman, J. Rao, W. George, M. D. Pegram, S. Sheth, S. S. Jeffrey, R. P. Kulkarni, E. Sollier, and D. Di Carlo, “Classification of large circulating tumor cells isolated with ultra- high throughput microfluidic Vortex technology,” vol. 7, no. 11.
- [167] S. Asmolov, Evgeny, “The inertial lift on a spherical particle in a plane Poiseuille flow at large channel Reynolds number,” *J. Fluid Mech.*, vol. 381, pp. 63–87, 1999.
- [168] X. Xu, P. Sarder, Z. Li, and A. Nehorai, “Optimization of microfluidic microsphere-trap arrays,” *Biomicrofluidics*, vol. 7, no. 1, pp. 1–16, 2013.
- [169] “Cytoskeleton This article has been accepted for publication and undergone full peer review but has not been through the copyediting , typesetting , pagination and proofreading process which may lead to differences between this version and the Version of R,” 2017.
- [170] J. Lin, D. Kim, H. T. Tse, P. Tseng, L. Peng, M. Dhar, S. Karumbayaram, and D. Di Carlo,

- “High-throughput physical phenotyping of cell differentiation,” no. November 2016, 2017.
- [171] J. Che, V. Yu, E. B. Garon, J. W. Goldman, and D. Di, “Lab on a Chip circulating tumor cells †,” *Lab Chip*, vol. 17, pp. 1452–1461, 2017.
- [172] O. Scrivener, C. Berner, R. Cressely, R. Hocquart, R. Sellin, and N. S. Vlachos, “Dynamical behaviour of drag-reducing polymer solutions,” *J. Nonnewton. Fluid Mech.*, vol. 5, no. C, pp. 475–495, 1979.
- [173] S. J. Haward, M. S. N. Oliveira, M. A. Alves, and G. H. McKinley, “Optimized cross-slot flow geometry for microfluidic extensional rheometry,” *Phys. Rev. Lett.*, vol. 109, no. 12, pp. 1–5, 2012.
- [174] D. R. Gossett, H. T. K. Tse, S. a. Lee, Y. Ying, a. G. Lindgren, O. O. Yang, J. Rao, a. T. Clark, and D. Di Carlo, “Hydrodynamic stretching of single cells for large population mechanical phenotyping,” *Proc. Natl. Acad. Sci.*, vol. 109, no. 20, pp. 7630–7635, 2012.
- [175] P. P. Brown and D. F. Lawler, “Sphere Drag and Settling Velocity Revisited,” *J. Environ. Eng.*, vol. 129, no. 3, pp. 222–231, 2003.
- [176] S. Matter, S. J. Haward, T. J. Ober, S. N. Oliveira, A. Alves, and G. H. Mckinley, “Extensional rheology and elastic instabilities of a wormlike micellar solution in a microfluidic cross-slot device †‡,” pp. 536–555, 2012.
- [177] J. M. Kim, “Kinematic analyses of a cross-slot microchannel applicable to cell deformability measurement under inertial or viscoelastic flow,” vol. 32, no. 12, pp. 2406–2411, 2015.
- [178] S. Bhattacharya, “Plasma bonding of poly(dimethyl) siloxane and glass surfaces and its application to microfluidics,” A Thesis in Mechanical Engineering, Texas Tech University, 2003.
- [179] A. Kapur, S. H. Medina, W. Wang, G. Palui, X. Ji, J. P. Schneider, and H. Mattoussi, “Enhanced Uptake of Luminescent Quantum Dots by Live Cells Mediated by a Membrane-Active Peptide,” *ACS Omega*, vol. 3, no. 12, pp. 17164–17172, 2018.
- [180] S.R. Sternberg, “Biomedical Image Processing,” *Computer (Long. Beach. Calif.)*, vol. 16, pp. 22–34, 1983.
- [181] T. W. Ridler and S. Calvard, “Picture Thresholding Using,” *IEEE Trans. Syst. Man Cybern.*, vol. smc-8, no. 8, pp. 630–632, 1978.
- [182] T. Geis, “DropletTracker,” *ImageJ*, 2013.
- [183] P. Harris and P. Ralph, “Human leukemic models of myelomonocytic development: A review of the HL-60 and U937 cell lines,” *J. Leukoc. Biol.*, vol. 37, no. 4, pp. 407–422, 1985.
- [184] N. Shimizu and H. Utiyama, “Loss of Amplified c-myc Genes in the Spontaneously Differentiated HL-60 Cells,” 1994.
- [185] P. Orth, D. Schnappinger, W. Hillen, W. Saenger, and W. Hinrichs, “Structural basis of gene regulation by the tetracycline inducible Tet repressor – operator system,” pp. 215–219, 2000.
- [186] E. L. Evans, K. Cuthbertson, N. Endesh, B. Rode, N. M. Blythe, A. J. Hyman, S. J. Hall, H. J. Gaunt, M. J. Ludlow, R. Foster, and D. J. Beech, “Yoda1 analogue (Dooku1) which antagonizes Yoda1-evoked activation of Piezo1 and aortic relaxation,” 2018.
- [187] M. Mak and D. Erickson, “A serial micropipette microfluidic device with applications to cancer cell repeated deformation studies,” *Integr. Biol. (United Kingdom)*, vol. 5, no. 11, pp. 1374–1384, 2013.
- [188] A. E. Pelling, F. S. Veraitch, C. P. K. Chu, C. Mason, and M. A. Horton, “Mechanical dynamics of single cells during early apoptosis,” *Cell Motil. Cytoskeleton*, vol. 66, no. 7, pp. 409–422, 2009.
- [189] M. N. Starodubtseva, “Mechanical properties of cells and ageing,” *Ageing Res. Rev.*, vol. 10, no. 1, pp. 16–25, 2011.
- [190] M. J. Rosenbluth, W. A. Lam, and D. A. Fletcher, “Force Microscopy of Nonadherent Cells : A Comparison of Leukemia Cell Deformability,” vol. 90, no. 1762, pp. 2994–3003, 2006.
- [191] S. H. Kleinman, K. D. Nyberg, M. J. Butte, A. C. Rowat, K. H. Hu, and D. B. Khismatullin, “Quantitative Deformability Cytometry: Rapid, Calibrated Measurements of Cell Mechanical Properties,” *Biophys. J.*, vol. 113, no. 7, pp. 1574–1584, 2017.
- [192] Z. L. Zhou, T. H. Hui, B. Tang, and A. H. W. Ngan, “Accurate measurement of stiffness of

- leukemia cells and leukocytes using an optical trap by a rate-jump method,” *RSC Adv.*, vol. 4, no. 17, pp. 8453–8460, 2014.
- [193] J. E. Cooper and W. S. Evans, “Latrunculins: Novel Marine Toxins That Disrupt Microfilament Organization in Cultured Cells,” vol. 5932, no. February, pp. 493–496, 1983.
- [194] S. L. Brenner and D. Korn, “Inhibition of actin polymerization by latrunculin A,” *FEBS Lett.*, vol. 2, no. 2, pp. 316–318, 1987.
- [195] J. M. Maloney and K. J. Van Vliet, “Chemoenvironmental modulators of fluidity in the suspended biological cell,” *Soft Matter*, vol. 10, no. 40, pp. 8031–8042, 2014.
- [196] S. Nawaz, P. Sánchez, K. Bodensiek, S. Li, M. Simons, and I. A. T. Schaap, “Cell Visco-Elasticity Measured with AFM and Optical Trapping at Sub-Micrometer Deformations,” *PLoS One*, vol. 7, no. 9, 2012.
- [197] Y. Abidine, V. M. Laurent, R. Michel, A. Duperray, and C. Verdier, “Local mechanical properties of bladder cancer cells measured by AFM as a signature of metastatic potential,” *Eur. Phys. J. Plus*, vol. 130, no. 10, 2015.
- [198] H. Kubitschke, J. Schnauss, K. D. Nnetu, E. Warnt, R. Stange, and J. Kaes, “Actin and microtubule networks contribute differently to cell response for small and large strains,” *New J. Phys.*, vol. 19, no. 9, 2017.
- [199] N. H. Reynolds, W. Ronan, E. P. Dowling, P. Owens, R. M. McMeeking, and J. P. McGarry, “On the role of the actin cytoskeleton and nucleus in the biomechanical response of spread cells,” *Biomaterials*, vol. 35, no. 13, pp. 4015–4025, 2014.
- [200] W. Lam, M. J. Rosenbluth, and D. A. Fletcher, “Chemotherapy exposure increases leukemia cell stiffness,” *Blood*, vol. 109, no. 8, pp. 3505–8, 2007.
- [201] B. R. Stevenson and D. A. Begg, “Concentration-dependent effects of cytochalasin D on tight junctions and actin filaments in MDCK epithelial cells,” *J. Cell Sci.*, vol. 107 (Pt 3, pp. 367–75, 1994.
- [202] L. M. Lee and A. P. Liu, “A microfluidic pipette array for mechanophenotyping of cancer cells and mechanical gating of mechanosensitive channels,” *Lab Chip*, vol. 15, no. 1, pp. 264–273, 2015.
- [203] J. Kim, S. Han, A. Lei, M. Miyano, J. Bloom, V. Srivastava, M. R. Stampfer, Z. J. Gartner, M. A. LaBarge, and L. L. Sohn, “Characterizing cellular mechanical phenotypes with mechanonode-pore sensing,” *Microsystems Nanoeng.*, vol. 4, no. July 2017, p. 17091, 2018.
- [204] G. R. Pettit, S. B. Singh, E. Hamel, C. M. Lin, D. S. Alberts, and D. Garcia-Kendal, “Isolation and structure of the strong cell growth and tubulin inhibitor combretastatin A-4,” *Experientia*, vol. 45, no. 2, pp. 209–211, 1989.
- [205] G. R. Pettit, S. B. Singh, M. R. Boyd, E. Hamel, R. K. Pettit, J. M. Schmidt, and F. Hogan, “Antineoplastic Agents. 291. Isolation and Synthesis of Combretastatins A-4, A-5, and A-6,” *J. Med. Chem.*, vol. 38, no. 10, pp. 1666–1672, 1995.
- [206] G. M. Tozer, C. Kanthou, and B. C. Baguley, “Disrupting tumour blood vessels,” *Nat. Rev. Cancer*, vol. 5, no. 6, pp. 423–435, 2005.
- [207] V. Mico, A. Charalambous, S. A. Peyman, R. H. Abou-saleh, A. F. Markham, P. L. Coletta, and S. D. Evans, “Evaluation of lipid-stabilised tripropionin nanodroplets as a delivery route for combretastatin A4,” *Int. J. Pharm.*, vol. 526, no. 1–2, pp. 547–555, 2017.
- [208] L. M. Greene, S. M. Nathwani, S. A. Bright, D. Fayne, A. Croke, M. Gagliardi, A. M. Mcelligott, L. O. Connor, M. Carr, N. O. Keely, N. M. O. Boyle, P. Carroll, B. Sarkadi, E. Conneally, D. G. Lloyd, M. Lawler, M. J. Meegan, and D. M. Zisterer, “The Vascular Targeting Agent Combretastatin-A4 and a Novel cis- Restricted β -Lactam Analogue , CA-432 , Induce Apoptosis in Human Chronic Myeloid Leukemia Cells and Ex Vivo Patient Samples Including Those Displaying Multidrug Resistance,” vol. 335, no. 2, pp. 302–313, 2010.
- [209] R. Martinez Vazquez, G. Nava, M. Vegliione, T. Yang, F. Bragheri, P. Minzioni, E. Bianchi, M. Di Tano, I. Chiodi, R. Osellame, C. Mondello, and I. Cristiani, “An optofluidic constriction chip for monitoring metastatic potential and drug response of cancer cells,” *Integr. Biol. (United Kingdom)*, vol. 7, no. 4, pp. 477–484, 2015.
- [210] G. M. Tozer, C. Kanthou, C. S. Parkins, and S. A. Hill, “The biology of the combretastatins as

- tumour vascular targeting agents,” *Int. J. Exp. Pathol.*, vol. 83, no. 1, pp. 21–38, 2002.
- [211] G. Dark, S. A. Hill, M. Tozer, R. Pettit, and D. J. Chaplin, “Advances in Brief Combretastatin A-4 , an Agent That Displays Potent and Selective Toxicity toward Tumor Vasculature ’,” *Comp. Gen. Pharmacol.*, pp. 1829–1834, 1834.
- [212] A. S. Boehle, B. Sipos, U. Kliche, H. Kalthoff, and P. Dohrmann, “Combretastatin A-4 prodrug inhibits growth of human non-small cell lung cancer in a murine xenotransplant model,” *Ann. Thorac. Surg.*, vol. 71, no. 5, pp. 1657–1665, 2001.
- [213] M. A. Tsai, R. E. Waugh, and P. C. Keng, “Cell Cycle-Dependence of HL-60 Cell Deformability,” vol. 70, no. April 1996, 2000.
- [214] B. A. Danowski, “Fibroblast contractility and actin organization are stimulated by microtubule inhibitors,” *J. Cell Sci.*, vol. 93 (Pt 2), no. 3280, pp. 255–66, 1989.
- [215] A. D. Verin, A. Birukova, P. Wang, F. Liu, P. Becker, K. Birukov, and J. G. N. Garcia, “Microtubule disassembly increases endothelial cell barrier dysfunction: role of MLC phosphorylation,” *Am. J. Physiol. Cell. Mol. Physiol.*, vol. 281, no. 3, pp. L565–L574, 2017.
- [216] M. A. Tsai, R. E. Waugh, and P. C. Keng, “Passive mechanical behavior of human neutrophils: Effects of colchicine and paclitaxel,” *Biophys. J.*, vol. 74, no. 6, pp. 3282–3291, 1998.
- [217] M. Yoshidas, “Potent and specific inhibition of mammalian in vivo and in vitro by trichostatin A,” *October*, vol. 265, no. 28, pp. 17174–17179, 1990.
- [218] M. Panagiotakopoulou, M. Bergert, A. Taubenberger, J. Guck, D. Poulidakos, and A. Ferrari, “A Nanoprinted Model of Interstitial Cancer Migration Reveals a Link between Cell Deformability and Proliferation,” *ACS Nano*, vol. 10, no. 7, pp. 6437–6448, 2016.
- [219] Y. P. Ninios, K. E. Sekeri-Pataryas, and T. G. Sourlingas, “Differential sensitivity of human leukemic cell lines to the histone deacetylase inhibitor, trichostatin A,” *Leuk. Res.*, vol. 34, no. 6, pp. 786–792, 2010.
- [220] F. J. Davis, J. B. Pillai, M. Gupta, and M. P. Gupta, “Concurrent opposite effects of trichostatin A, an inhibitor of histone deacetylases, on expression of α -MHC and cardiac tubulins: implication for gain in cardiac muscle contractility,” *Am. J. Physiol. Circ. Physiol.*, vol. 288, no. 3, pp. H1477–H1490, 2004.
- [221] F. Zhang, Q. Huang, J. Yan, X. Zhang, and J. Li, “Assessment of the effect of trichostatin a on hela cells through FT-IR spectroscopy,” *Anal. Chem.*, vol. 87, no. 4, pp. 2511–2517, 2015.
- [222] D. Tsikritis, S. Richmond, P. Stewart, A. Elfick, and A. Downes, “living human primary and secondary tumour cells,” pp. 5162–5168, 2015.
- [223] R. Gautam, S. Vanga, F. Ariese, and S. Umopathy, “Review of multidimensional data processing approaches for Raman and infrared spectroscopy,” *EPJ Tech. Instrum.*, vol. 2, no. 1, 2015.
- [224] A. Boccaccio, L. Lamberti, M. Papi, S. Arndt, A. Russell, J. Tomas, A. Boccaccio, A. E. Uva, and M. Papi, “Nanoindentation characterisation of human colorectal cancer cells considering cell geometry , surface roughness and hyperelastic constitutive behaviour.”
- [225] N. Tomita, W. Jiang, H. Hibshoosh, D. Warburton, S. M. Kahn, and I. B. Weinstein, “Isolation and Characterization of a Highly Malignant Variant of the SW480 Human Colon Cancer Cell Line,” *Cancer Res.*, vol. 52, no. 24, pp. 6840–6847, 1992.
- [226] A. Downes, “living human primary and secondary tumour cells,” pp. 5162–5168, 2015.
- [227] A. Sharei, N. Cho, S. Mao, E. Jackson, R. Pocevicute, A. Adamo, J. Zoldan, and R. Langer, “Cell Squeezing as a Robust , Microfluidic Intracellular Delivery Platform,” no. November, pp. 1–7, 2013.
- [228] W. Ma, L. X. Qin, F. T. Liu, Z. Gu, J. Wang, Z. G. Pan, T. D. James, and Y. T. Long, “Ubiquinone-quantum dot bioconjugates for in vitro and intracellular complex i sensing,” *Sci. Rep.*, vol. 3, pp. 1–9, 2013.
- [229] A. J. Harvie, “Quantum Dot Redox Sensors: Understanding Excited State Dynamics,” University of Leeds, 2018.
- [230] J. H. Ostrander, C. M. McMahon, S. Lem, S. R. Millon, J. Q. Brown, V. L. Seewaldt, and N. Ramanujam, “Optical redox ratio differentiates breast cancer cell lines based on estrogen receptor status,” *Cancer Res.*, vol. 70, no. 11, pp. 4759–4766, 2010.

- [231] M. E. Kizer, Y. Deng, G. Kang, P. E. Mikael, X. Wang, and A. J. Chung, “Hydroporator: A hydrodynamic cell membrane perforator for high-throughput vector-free nanomaterial intracellular delivery and DNA origami biostability evaluation,” *Lab Chip*, vol. 19, no. 10, pp. 1747–1754, 2019.
- [232] R. Milo and R. Phillips, *Cell biology by the numbers*. New York: Garland Science, Taylor and Francis group, 2016.
- [233] R. Syeda, M. N. Florendo, C. D. Cox, J. M. Kefauver, J. S. Santos, B. Martinac, and A. Patapoutian, “Piezo1 Channels Are Inherently Mechanosensitive,” *Cell Rep.*, vol. 17, no. 7, pp. 1739–1746, 2016.
- [234] A. H. Lewis and J. Grandl, “Mechanical sensitivity of Piezo1 ion channels can be tuned by cellular membrane tension,” *Elife*, vol. 4, no. December2015, pp. 1–17, 2015.
- [235] R. Zarychanski, V. P. Schulz, B. L. Houston, Y. Maksimova, D. S. Houston, B. Smith, J. Rinehart, and P. G. Gallagher, “Mutations in the mechanotransduction protein PIEZO1 are associated with hereditary xerocytosis,” *Blood*, vol. 120, no. 9, pp. 1908–1915, 2012.
- [236] V. Lukacs, J. Mathur, R. Mao, P. Bayrak-Toydemir, M. Procter, S. M. Cahalan, H. J. Kim, M. Bandell, N. Longo, R. W. Day, D. A. Stevenson, A. Patapoutian, and B. L. Krock, “Impaired PIEZO1 function in patients with a novel autosomal recessive congenital lymphatic dysplasia,” *Nat. Commun.*, vol. 6, pp. 1–7, 2015.
- [237] G. T. Eisenhoffer, P. D. Loftus, M. Yoshiga, H. Otsuna, C.-B. Chien, P. A. Morcos, and J. Rosenblatt, “Crowding induces live cell extrusion to maintain homeostatic cell numbers in epithelia,” *Mol Psychiatry.*, vol. 20, no. 6, pp. 1588–1595, 2015.
- [238] A. E. Dubin, S. Murthy, A. H. Lewis, L. Brosse, S. M. Cahalan, J. Grandl, B. Coste, and A. Patapoutian, “Endogenous Piezo1 Can Confound Mechanically Activated Channel Identification and Characterization,” *Neuron*, vol. 94, no. 2, p. 266–270.e3, 2017.
- [239] J. L. Nourse and M. M. Pathak, “How cells channel their stress: Interplay between Piezo1 and the cytoskeleton,” *Semin Cell Dev Biol.*, vol. 72, no. 3, 2017.
- [240] P. A. Gottlieb, C. Bae, and F. Sachs, “Gating the mechanical channel Piezo1: A comparison between whole-cell and patch recording,” *Channels*, vol. 6, no. 4, pp. 282–289, 2012.
- [241] K. Retailleau, F. Duprat, M. Arhatte, S. S. Ranade, R. Peyronnet, J. R. Martins, M. Jodar, C. Moro, S. Offermanns, Y. Feng, S. Demolombe, A. Patel, and E. Honoré, “Piezo1 in Smooth Muscle Cells Is Involved in Hypertension-Dependent Arterial Remodeling,” *Cell Rep.*, vol. 13, no. 6, pp. 1161–1171, 2015.
- [242] M. M. Pathak, J. L. Nourse, T. Tran, J. Hwe, J. Arulmoli, D. T. T. Le, E. Bernardis, L. A. Flanagan, and F. Tombola, “Stretch-activated ion channel Piezo1 directs lineage choice in human neural stem cells,” *Proc. Natl. Acad. Sci.*, vol. 111, no. 45, pp. 16148–16153, 2014.
- [243] B. M. Gaub and D. J. Müller, “Mechanical Stimulation of Piezo1 Receptors Depends on Extracellular Matrix Proteins and Directionality of Force,” *Nano Lett.*, vol. 17, no. 3, pp. 2064–2072, 2017.
- [244] B. J. McHugh, R. Buttery, Y. Lad, S. Banks, C. Haslett, and T. Sethi, “Integrin activation by Fam38A uses a novel mechanism of R-Ras targeting to the endoplasmic reticulum,” *J. Cell Sci.*, vol. 123, no. 1, pp. 51–61, 2009.
- [245] J. Li, B. Hou, S. Tumova, K. Muraki, A. Bruns, M. J. Ludlow, A. Sedo, A. J. Hyman, L. McKeown, R. S. Young, N. Y. Yuldasheva, Y. Majeed, L. A. Wilson, B. Rode, M. A. Bailey, H. R. Kim, Z. Fu, D. A. L. Carter, J. Bilton, H. Imrie, P. Ajuh, T. N. Dear, R. M. Cubbon, M. T. Kearney, K. R. Prasad, P. C. Evans, J. F. X. Ainscough, and D. J. Beech, “Piezo1 integration of vascular architecture with physiological force,” *Nature*, vol. 515, no. 7526, pp. 279–282, 2014.
- [246] S. S. Ranade, Z. Qiu, S.-H. Woo, S. S. Hur, S. E. Murthy, S. M. Cahalan, J. Xu, J. Mathur, M. Bandell, B. Coste, Y.-S. J. Li, S. Chien, and A. Patapoutian, “Piezo1, a mechanically activated ion channel, is required for vascular development in mice,” *Proc. Natl. Acad. Sci.*, vol. 111, no. 28, pp. 10347–10352, 2014.
- [247] L. Jiang, Y. Zhao, and W. Chen, “The Function of the Novel Mechanical Activated Ion Channel Piezo1 in the Human Osteosarcoma Cells,” *Med. Sci. Monit.*, vol. 23, pp. 5070–5082, 2017.
- [248] C. Li, S. Rezanian, S. Kammerer, A. Sokolowski, T. Devaney, A. Gorischek, S. Jahn, H. Hackl,

- K. Groschner, C. Windpassinger, E. Malle, T. Bauernhofer, and W. Schreibmayer, "Piezo1 forms mechanosensitive ion channels in the human MCF-7 breast cancer cell line," *Sci. Rep.*, vol. 5, pp. 1–9, 2015.
- [249] B. J. McHugh, A. Murdoch, C. Haslett, and T. Sethi, "Loss of the integrin-activating transmembrane protein Fam38A (Piezo1) promotes a switch to a reduced integrin-dependent mode of cell migration," *PLoS One*, vol. 7, no. 7, 2012.
- [250] K. D. Nyberg, M. B. Scott, S. L. Bruce, A. B. Gopinath, D. Bikos, T. G. Mason, W. Kim, H. Sung, and A. C. Rowat, "Lab on a Chip for rapid, single cell mechanotyping †," *Lab Chip*, vol. 16, pp. 3330–3339, 2016.
- [251] V. A. Online, V. Palmieri, D. Lucchetti, A. Maiorana, M. Papi, G. Maulucci, F. Calapa, G. Ciasca, and R. Giordano, "Soft Matter primary tumor and lymph node metastasis cells," pp. 5719–5726, 2015.
- [252] C. Bae, R. Gnanasambandam, C. Nicolai, F. Sachs, and P. A. Gottlieb, "Xerocytosis is caused by mutations that alter the kinetics of the mechanosensitive channel PIEZO1.," *Proc. Natl. Acad. Sci. U. S. A.*, vol. 110, no. 12, pp. E1162-8, 2013.
- [253] J. Gala De Pablo, "Biochemical phenotyping of live single cells using confocal Raman spectroscopy," University of Leeds, 2019.
- [254] D. R. Gossett and D. Di Carlo, "Particle focusing mechanisms in curving confined flows," *Anal. Chem.*, vol. 81, no. 20, pp. 8459–8465, 2009.
- [255] M. J. C. Hendrix, E. A. Seftor, Y. W. Chu, K. T. Trevor, and R. E. B. Seftor, "Role of intermediate filaments in migration, invasion and metastasis," *Cancer Metastasis Rev.*, vol. 15, no. 4, pp. 507–525, 1996.
- [256] E. Gladilin, P. Gonzalez, and R. Eils, "Dissecting the contribution of actin and vimentin intermediate filaments to mechanical phenotype of suspended cells using high-throughput deformability measurements and computational modeling," *J. Biomech.*, vol. 47, no. 11, pp. 2598–2605, 2014.
- [257] E. Gladilin, P. Gonzalez, and R. Eils, "Dissecting the contribution of actin and vimentin intermediate filaments to mechanical phenotype of suspended cells using high-throughput deformability measurements and computational modeling," *J. Biomech.*, vol. 47, no. 11, pp. 2598–2605, 2014.
- [258] Y. Yu and Y. M. Feng, "The role of kinesin family proteins in tumorigenesis and progression," *Cancer*, vol. 116, no. 22, pp. 5150–5160, 2010.
- [259] T. A. M. Iura, H. I. M. Ikami, A. K. I. Sozaki, T. A. I. To, Y. A. O. Zeki, and K. E. G. Oda, "On-chip light-sheet fluorescence imaging flow cytometry at a high flow speed of 1 m / s," vol. 9, no. 7, pp. 14474–14480, 2018.